Manipulation of Dirac Cones and Edge states in Polariton Honeycomb Lattices

Marijana Milicevic

THÈSE DE DOCTORAT

De l'université Pierre et Marie Curie en Sciences Physiques

ÉCOLE DOCTORALE : Physique et Chimie de Matériaux

présentée par
Marijana MILIĆEVIĆ

Manipulation of Dirac Cones and Edge states in Polariton Honeycomb Lattices

Manipulation de cônes de Dirac et états de bord
dans des réseaux de polaritons en nid d'abeilles

Dirigée par Jacqueline BLOCH

Soutenance le 15 Juin 2018 devant le jury composé de :

Jacqueline BLOCH	Directrice de thèse
Alberto AMO	Encadrant de thèse
Mark GOERBIG	Rapporteur
Dimitrii KRIZHANOVSKII	Rapporteur
Jean DALIBARD	Examinateur
Hannah PRICE	Examinateur
Mathieu Bellec	Examinateur

CONTENTS

INTRODUCTION

The connection between the fundamental understanding of nature and the engineering of materials with the desired characteristics has revolutionized the way we live and coexist with nature. The design and manipulation of the mechanical and chemical properties of materials has led to the creation of various ceramics, metallic alloys and plastics, which have marked the eras when they were created.

Development of modern physics, particularly the application of quantum mechanics to the area of solid state physics, allowed manipulating the electronic properties of materials. Investigation of bulk and surface transport properties of semiconductors like silicon and germanium by Bardeen, Brattain and Shockley lead to what is considered to be the biggest discovery of 20th century, the creation of the transistor.

During this progress of material science, light has been mostly used as a tool to probe materials properties. Various spectroscopic techniques were developed, based on the response of a material to an electromagnetic field, whether it absorbs, reflects or transmits light in certain frequency range. Eventually, it finally became possible to also engineer the optical properties of materials: the field of photonics was born. The result is the development of technologies such as lasers, light emitting diodes or optical fibers.

Most interestingly, these advances led to a new paradigm, at the heart of many recent efforts in the scientific community. The goal is to create entirely new types of states of light and matter, with novel exciting properties, by inter crossing different disciplines, like solid state physics, photonics, particle physics or mathematics. On this route, it is not unusual to surpass the fundamental differences between elementary particles, and designed materials in which (effective) particles show interesting features that combine the properties of both electrons and photons for example.

Historically, concepts from solid state physics have been regularly transfered to the area of photonics. In crystals, collective behavior of electrons is determined by the periodic potential. This principle has inspired periodic arrangements of materials with different index of refraction, that is, photonic crystals. In these structures the light dispersion can be engineered, and photonic gaps can be created in a desired frequency range. [1].

More recently, the field of topological photonics is being developed [2, 3]. The idea is to implement in the photonic world the analogous of topologically non trivial phases of mater, similar to those achieved in electronic topological insulators [4]. In this way robust propagation of light, with low losses could to be achieved. The envisioned applications range from creation of integrated non-reciprocal devices such as optical isolators [5], robust delay lines [6], or generation of topologically robust correlated photon pairs [7].

On the other side, the fact that light can be controlled with high levels of precision has inspired efforts to build photonic simulators of various complex physical phenomena. For example, new topological effects that are hard, or even impossible to realize in solid state systems have been implemented in photonic systems including Floquet physics [8], 4D quantum Hall physics [9], or Type II Weyl points [10].

One of the established ways to manipulate light, and even introduce photon-photon interactions is by strongly coupling it to matter. In fact, light-matter interaction is not an intrinsic characteristic of a given material, but can be artificially controlled. In 1964, Purcell demonstrated that the emission rate of a quantum system can be enhanced or inhibited by modifying its environment [11]. This idea was successfully applied on quantum emitters [12, 13] and particularly in the optical range thanks to developments of techniques for confinement of light. The modern epitaxial growth allows confining light inside semiconductor cavities of different shapes (planar cavity, micropillars, microdisc, photonic crystal cavities) but also the excitonic modes in semiconductor quantum wells or quantum dots [14]. In these structures, photons can be emitted, reabsorbed and re-emitted again by quantum well excitons several times before escaping the cavity. If losses are weaker than the light matter coupling strength, the strong coupling regime is achieved and the system is described by quasi-particles with hybrid light-matter nature, called microcavity exciton polaritons [15].

These are bosonic quasi-particles that combine properties inherited from their photonic component, such as small effective mass, with those inherited from electrons, such as the possibility to interact. Polaritons allow direct visualization of their dispersion and spatial wave functions, as well as information on the phase by analyzing photons escaping the cavity. They can be probed under resonant and non-resonant excitation and can propagate over long distances.

Because of these properties, polaritons represent a system of choice to investigate quantum fluids of light [16]. The possibility to optically control their momentum, density, phase and spin allowed the observation of superfluid motion [17], the generation of topological defect like solitons [18, 19], and the observation of the optical spin Hall effect [20].

Recently, polaritons emerged as an extraordinary photonic platform to emulate 1D and 2D Hamiltonians. Engineering of desired potential landscape for polaritons is possible by imposing deep lateral confinement in the desired form. The techniques for lateral etching of microcavities developed at Centre de Nanosciences et Nanotechnologies (former Laboratorie de Photonique et Nanostructures), allowed designing 0D structures such as micropillars (photonic atoms) [21] and benzene molecule [22], 1D wires [23, 24], modulated wires [25, 26] and 1D or 2D lattices [27, 28].

In 2013, a 2D honeycomb lattice of coupled micropillars was fabricated in our group [28]. In that structure the lowest two bands arise from the coupling of the lowest energy, $s-$modes of each micropillar, and emulate the π and π^* bands of graphene. As in graphene, around isolated points in momentum space, called Dirac points, the bands have a linear dispersion analogous to the one describing massless fermions.

Most interestingly, the polariton honeycomb lattice allows going beyond what is already known about the physics of graphene. It provides a way to study the orbital degree of freedom and its interplay with the geometry of the honeycomb lattice. This degree of freedom has been known to play an important role in the properties of certain complex lattice systems such as transition metal dichalcogenides [29] or topological insulators [30].

In the polariton honeycomb lattice, the system first excited states of each micropillar resonator have a P-orbital geometry. When coupled in the honeycomb lattice, they give rise to orbital bands, inaccessible in actual solid state materials and which have attracted significant attention [31, 27, 32, 33, 34].

In the present thesis, we engineered new lattice geometries of the polariton lattice can to explore two main topics. One is the experimental study of the lattice edge states. The other one is the manipulation and creation of new types of Dirac dispersions and corresponding quasi-particles in deformed lattices.

In the **first chapter**, we will provide a short introduction to Dirac physics. In the first part we will give some insights on how the original Dirac equation was formulated in order to describe relativistic massless fermions. In the second part we will consider the first solid state system in which Dirac quasi-particles have been observed, the 2D graphene. We will also discuss topological properties of Dirac points and define the concept of "winding" that will be used throughout the thesis to characterize the topological properties of different lattices.

In the **second chapter** we will address the physics of polaritons, how they are formed and what are their main properties. A particular attention will be paid to explain how polaritons can be studied experimentally, and how information on their properties is retrieved in a photoluminescence experiment. Then, we will describe how polariton structures are designed and fabricated, particularly that of the honeycomb lattice, which will be the subject of study in the rest of the thesis. We will explore its main characteristics as a simulator: lattice effective dispersion, propagation and tunability.

The **third chapter** is the first devoted to edge states. There, we review the properties of edge states predicted to appear in a honeycomb lattice, as well as their connection to the bulk properties, that is topological winding. This study provides the first direct visualization of edge states, both in real and reciprocal space. The momentum space dispersion of the edge states associated to the zig-zag and bearded type of edges is proved to feature unidimensional quasi-flat bands. Intensity of the emission in real space reveals the localized character of the observed edge states.

In the **fourth chapter** we first introduce polariton orbital graphene, a hexagonal lattice in which each lattice site holds degenerate anisotropic p_x and p_y orbitals. We then focus on exploring the edge states in this lattice using the theoretical and experimental tools presented in the previous chapter. We experimentally find novel edge states with properties different from the π and π^* bands of graphene. We also present a theoretical study of their topological origin realized in collaboration with theoreticians G. Montambaux and T. Ozawa.

In the **fifth chapter**, we switch to the study of the lattice bulk properties, and how they can be manipulated. In particular, we propose a method to implement strain in order to tailor Dirac dispersions and create new types of hybrid Dirac particles which combine zero, finite and infinite effective masses. By engineering the strain in the structure, we trigger topological phase transitions. In $s-$ bands, Dirac cones with opposite windings merge and open a gap, while a pair of new Dirac cones with equal winding numbers is created at new positions in the 1st Brillouin zone. Along this phase transition, we evidence, for the first time, the hybrid dispersion of a photonic semi-Dirac quasi-particle, characterized by a finite mass for the transport along one direction of reciprocal space and massless-propagation along the orthogonal one.

Even more remarkably, in $p-$ bands, we can tune the tilt of the Dirac cones and create strongly tilted cones. A quasi-particle with flat-Dirac dispersion is observed experimentally for the first time.

We will conclude the manuscript with a section devoted to conclusions and new directions and perspectives open by the work presented here.

INTRODUCTION TO DIRAC HAMILTONIANS

One of the most surprising results of modern solid state physics is the emergence of materials whose elementary excitations are governed by Dirac, Weyl and Majorana equations, originally introduced in the context of relativistic physics. Materials as graphene, topological insulators or superconductors [35] offer plethora of novel and exciting transport properties, promising for creation of future robust miniaturized electronic devices or implementation of quantum computing [36, 37].

Many physical phenomena behind these properties, such as Klein tunneling or appearance of edge states in graphene, or topologically protected transport in Chern insulators, can be captured by models in tight-binding approximation. Experimental realization and manipulation of corresponding Hamiltonians emerged as a powerful approach for studying these phenomena. Throughout this thesis we will experimentally address Dirac Hamiltonians in the context of half-light half matter polaritons.

The aim of this chapter is to review the main aspects of "Dirac physics", particularly in two dimensional lattices. Dirac and Weyl equations in their original form, as used to describe relativistic fermions in particle physics are introduced in sections 2.1.1, 2.1.2.

In order to define the notion of Dirac matter, a brief summary of band theory of solids is given in 2.2.1, followed by a review of the main properties of the most celebrated Dirac material, graphene in 2.2.2.

Some general features of Dirac Hamiltonians are presented in section 2.3, as they have important consequences on the physical properties of the materials they describe. These include symmetries, 2.3.1, and topological properties, 2.3.2.

2.1 RELATIVISTIC FERMIONS

2.1.1 *Dirac equation*

The Dirac equation was developed by Paul Maurice Dirac in 1928. in order to describe the dynamics of electrons at relativistic speeds [38]. His goal was to develop a quantum mechanical description compatible with the special theory of relativity, a theory already accepted at the time.

To understand the challenge he faced, let us first remind how an isolated free particle is described. Classically its dynamics is given by the following Hamiltonian [39]:

$$H = \frac{p^2}{2m},\tag{1}$$

where p and m are the particle momentum and mass, respectively. To obtain a quantum mechanical physical observables are exchanged by operators description of the dynamics of the electron, we can write the Shrödinger equation in $x-$ representation:

$$i\hbar\frac{\partial\psi(x)}{\partial t} = \frac{-\hbar^2\nabla^2}{2m}\psi(x),\tag{2}$$

where $\psi(x)\psi^*(x)$ describes the probability density of detecting a particle at a given place. This equation is however, not applicable for particles moving with a speed comparable to the speed of light. Changing the inertial system, that is, applying a Lorentz boost with a certain speed, will affect differently the left-hand side of equation 2.1.1, which is first order in time derivative and the right- hand side, which has second order space-derivatives. This means that the equation is not Lorentz invariant and that the solution will change when the inertial system is changed, contrary to the postulates of special relativity.

In the context of special relativity both total energy and momenta transform as components of contravariant four-vector:

$$\mathbf{P} = (p^0, p^1, p^2, p^3) = (\frac{E}{c}, p_x, p_y, p_z) \tag{3}$$

Even more this vector has invariant length, which determines the energy-momentum relation of the relativistic particle :

$$\mathbf{P} \cdot \mathbf{P} = \frac{E^2}{c^2} - \mathbf{p} \cdot \mathbf{p} = m^2 c^2 \quad \rightarrow \quad E^2 = p^2 c^2 + m^2 c^4, \tag{4}$$

where m is the rest mass of the particle and c is the velocity of light in vacuum.

In order to write an equation consistent with the theory of relativity Dirac proposed to write the right-hand side of the Shrödinger equation using only the first order derivatives. He introduced a Hamiltonian in the form:

$$H_D = -i \sum_{j=1}^{3} \hbar c \alpha_j \partial_j + \beta m c^2 \tag{5}$$

where i enumerates the three space coordinates, and α_i and β are dimensionless coefficients. Crucially, Dirac concluded that the coefficients α_i and β cannot simply be numbers if we want to keep invariance to spatial rotation and to properly define probability density as a positive value. He proposed to write the wave function ψ as a column matrix and the coefficients as matrices. The necessary matrix algebra followed from the energy momentum relation given by eq. 4, and the postulate of quantum mechanics that a Hamiltonian must be a Hermitian operator. It reads:

$$\alpha_i^2 = \beta^2 = 1, \quad \{\alpha_i, \beta\} = 0, \quad \{\alpha_i, \alpha_j\} = 2\delta_{i,j}, \tag{6}$$

where $\{,\}$ denotes anti commutator. Interestingly, matrices that satisfy these conditions are the three Pauli matrices, already used in formalizing the theory of electron spin. Still, 4 matrices are needed, if we want to solve the problem in 3+1 time-space dimensions. It is thus convenient to use the tensor product between Pauli matrices σ_i and define the standard representation of the so called γ matrices $(\gamma^0, \gamma^1, \gamma^2, \gamma^3) \equiv (\beta, \alpha_i)$ as:

$$\alpha_i = \sigma_i \otimes \sigma_1 = \begin{pmatrix} 0 & \sigma_i \\ -\sigma_i & 0 \end{pmatrix}, \quad \beta = \sigma_0 \otimes \sigma_3 = \begin{pmatrix} \sigma_0 & 0 \\ 0 & -\sigma_0 \end{pmatrix} \tag{7}$$

and

$$\sigma_1 = \begin{pmatrix} 0 & 1 \\ 1 & 0 \end{pmatrix}, \quad \sigma_2 = \begin{pmatrix} 0 & -i \\ i & 0 \end{pmatrix}, \tag{8}$$

$$\sigma_3 = \begin{pmatrix} 1 & 0 \\ 0 & -1 \end{pmatrix}, \quad \sigma_0 = \begin{pmatrix} 1 & 0 \\ 0 & 1 \end{pmatrix} \tag{9}$$

and σ_0 is the 2×2 unit matrix. The newly obtained γ matrices satisfy the Clifford algebra:

$$\{\gamma^\mu, \gamma^\nu\} = 2\eta^{\mu\nu} \tag{10}$$

where $\eta^{\mu\nu}$ is the Minkowski metric tensor.

Finally, using these matrices Dirac wrote the famous equation describing fermions at relativistic speeds in the covariant form:

$$(i\hbar\gamma^\mu\partial_\mu - mc^2)\Psi = 0, \tag{11}$$

where ∂_μ is the so called four gradient $\partial_\mu = (\partial_0, \partial_x, \partial_y, \partial_z)$. The beauty of this equation lies not only in its elegant form but also in its profound physical consequences. We can unveil some of them simply by considering the number of solutions corresponding to an electron in rest. In that case Dirac equation reduces to:

$$(i\hbar\gamma^0\partial_t - mc^2)\Psi = 0. \tag{12}$$

The four solutions we obtain are:

$$\psi^1 = e^{-\frac{imc^2}{\hbar}t}u^1 \quad \psi^2 = e^{-\frac{imc^2}{\hbar}t}u^2 \quad \psi^3 = e^{+\frac{imc^2}{\hbar}t}u^3 \quad \psi^4 = e^{+\frac{imc^2}{\hbar}t}u^4, \tag{13}$$

with:

$$u^1 = \begin{pmatrix} 1 \\ 0 \\ 0 \\ 0 \end{pmatrix} \quad u^2 = \begin{pmatrix} 0 \\ 1 \\ 0 \\ 0 \end{pmatrix} \quad u^3 = \begin{pmatrix} 0 \\ 0 \\ 1 \\ 0 \end{pmatrix} \quad u^4 = \begin{pmatrix} 0 \\ 0 \\ 0 \\ 1 \end{pmatrix} \tag{14}$$

The four component column vectors we obtained can accommodate four states. We can easily verify that the first two have positive energy $E = mc^2$ and the other two negative one $E = -mc^2$, still in agreement with dispersion relation eq. 4. As it can be rigorously demonstrated, the two states for each energy value, describe two spin projections of a spin 1/2 particle [39]. The above solutions are thus called Dirac spinors. Positive definite probability density can be calculated as $\rho = \psi^\dagger\psi$.

At the time the theory was developed, the interpretation of the negative energy solutions represented an important problem. Their existence meant that electrons could always radiate energy by falling into one of them. An arbitrarily big amount of energy could be obtained in that way.

To solve the apparent paradox Dirac imagined all negative energy states are already occupied, forming the negatively charged "see" that fills the universe [40]. No new electrons could then occupy these states due to the Pauli principle of exclusion. At the same time, one of the negative energy electrons from the sea could be excited to a positive energy state. In that case it would leave "a hole" at the negative energy, which would have positive charge.

This interpretation represents the famous theoretical prediction of antiparticles which had a crucial role in the development of the standard model as well as many concepts of solid state physics. Still, the explanation wasn't without its own problems: it implied an infinite negative charge of the universe. It was only later, when quantum field theory was developed, capable of explaining inelastic processes and creation of particle-antiparticle pairs, that the negative energy solutions were understood completely.

2.1.2 *Weyl equation and chirality*

Before starting the journey of the use of the Dirac equation in solid state physics and photonics, lets introduce a slightly different representation of it, convenient for describing ultra-relativistic or massless particles. It is called the chiral or spinor representation, for the reasons we will see below.

Let us redefine the matrices α_i and β in the following way:

$$\alpha_i = \sigma_i \otimes \sigma_3 = \begin{pmatrix} \sigma_i & 0 \\ 0 & -\sigma_i \end{pmatrix} \qquad \beta = \sigma_0 \otimes \sigma_1 = \begin{pmatrix} 0 & \sigma_0 \\ -\sigma_0 & 0 \end{pmatrix} \tag{15}$$

In this representation the Dirac spinor can be written as $\Psi = (\Psi_L, \Psi_R)$, where two component spinors Ψ_L, Ψ_R are solutions of the two coupled equations:

$$(i\sigma_0 \partial_t + ic\sigma_i \partial_i)\Psi_R = (mc^2/\hbar)\Psi_L \tag{16}$$

$$(i\sigma_0 \partial_t + ic\sigma_i \partial_i)\Psi_L = (mc^2/\hbar)\Psi_R \tag{17}$$
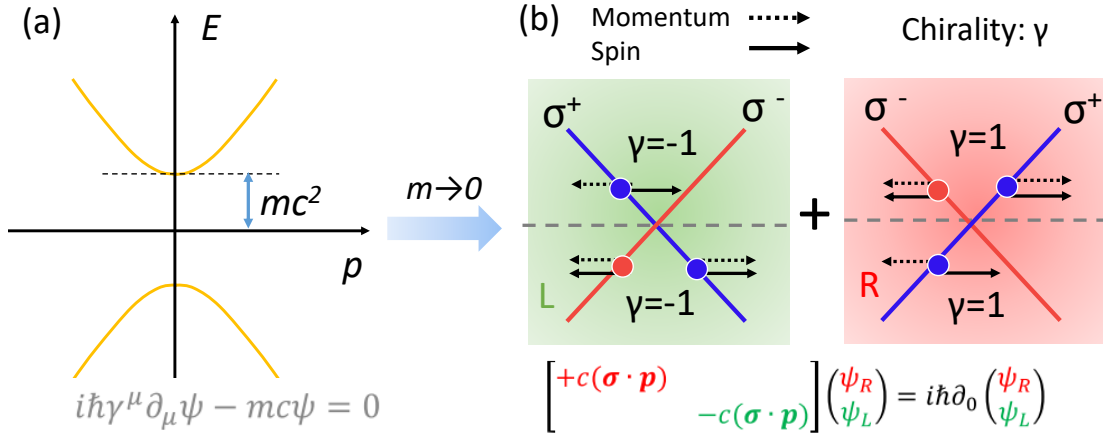
Figure 1: **Dirac and Weyl particles** (a) Parabolic energy-momentum relation of a particle described by Dirac equation. Both positive and negative energy solution exist. (b) When $cp >> mc^2$, dispersion becomes linear and particle spin is tied to its momentum . Two types of solutions, left-handed and right-handed exist, depending on alignment between momentum and spin.

This form allows us to examine easily the physics of the system in the case when the kinetic energy dominates the rest energy mc^2, that is when $cp >> mc^2$. In that case the two equations become decoupled, and can be written using only the identity and Pauli matrices:

$$(\sigma_0 \partial_t + c\boldsymbol{\sigma} \cdot \partial_{\mathbf{r}})\Psi_R = 0 \tag{18}$$

$$(\sigma_0 \partial_t - c\boldsymbol{\sigma} \cdot \partial_{\mathbf{r}})\Psi_L = 0 \tag{19}$$

These equations also define the massless Dirac Hamiltonian:

$$\hat{H} = c\boldsymbol{\sigma} \cdot \hat{\mathbf{p}} \tag{20}$$

which is also called Weyl Hamiltonian, by the name of Herman Weyl. He was the first to notice the two very interesting features of the spinor solutions Ψ_L, Ψ_R. First, their energy-momentum relation is linear, $E = \pm c\boldsymbol{\sigma} \cdot \mathbf{p}$ and second, the particle's spin is always tied with its momentum [41].

To understand this, lets define an operator that projects the spin along the direction of the momentum:

$$\hat{h} = \frac{\boldsymbol{\sigma} \cdot \hat{\mathbf{p}}}{|\mathbf{p}|} \tag{21}$$

This operator is called helicity and its eigen values are $h = 1$, for the so called right-handed solutions, where the spin vector is parallel to the momentum vector, and $h = -1$, for the so called left-handed solutions, where the spin vector is anti parallel to momentum vector.

While it can be also defined for massive particles, helicity is not Lorentz invariant in that case. For that reason another operator, which fulfills this request is introduced. It is called chirality and can be defined using γ matrices:

$$\gamma^5 \equiv i\gamma^0\gamma^1\gamma^2\gamma^3 = \begin{pmatrix} 0 & I \\ I & 0 \end{pmatrix} \tag{22}$$

Chirality is not strictly speaking a symmetry, as it anti-commutes with the Hamiltonian. It has well defined eigen vectors:

$$\gamma^5 u_R = u_R \quad \gamma^5 v_R = -v_R \tag{23}$$
$$\gamma^5 u_L = -u_L \quad \gamma^5 v_L = v_L \tag{24}$$

with eigenvalues 1 and -1 (u and v represent particle, and antiparticle spinor, similarly to the case in eq. 13). Right handed solutions are particles with chirality $+1$ and antiparticles with chirality -1, while the opposite stands for the left handed ones.

In the case of zero mass they construct solutions Ψ_L, Ψ_R of the decoupled equations 19. In fig. 1, a schematic representation of all possible solutions and their chirality,γ, is presented. We see that the "rigt-hand" and "left-hand" solutions are not identical, but represent a mirror image of each other in terms of spin. Such feature is the essence of chirality. It is also worth noting that in the case of massless particles eigenstates of the helicity operator and chirality operator are the same.

The necessary condition for massless Dirac equation to be applied, a negligible mass with respect to kinetic energy, restricted its use in astrophysics and particle physics for a long time. On the scale of condensed matter physics the electron mass of $\approx 0.5 MeV$ is considerable and the formation of massless Dirac fermions is not intuitive. However, Dirac-like dispersions can appear when we consider electronic quasi-particles in crystalline lattices in solids.

To understand their emergence in crystals, let us review the main ideas of one of the most successful theories in the solid state physics: the band theory of solids.

2.2 DIRAC MATTER: THE CASE OF GRAPHENE

2.2.1 *Basic notions of band theory of solids*

The band theory of solids was created in response to the question why some materials conduct heat and electricity better than others [42]. Its starting point is the fact that atoms in some solids are arranged in ordered and periodic manner. These solids are called crystals.

While electrons in isolated atoms occupy discrete, separate energy levels, when many atoms are close together orbitals overlap and hybridize into extend states. Interestingly, the resulting bands often have an energy momentum relation which is parabolic, such that electrons in each of them can be approximated by an electron moving freely in space, but with an effective mass, possibly very different form the free electron mass.

The situation when complex interactions of particles in many body systems can be approximated by a free particle with some new effective properties, leads to the concept of quasi particle. As this concept will be repeatedly used in this thesis we reproduce here a memorable explanation from a many body physics textbook, written by Mattuck [43]. It states that, as a particle moves in a many body system, it affects, and is being affected by other particles, and what we observe is the combination of these effects. The situation is similar to that of a horse surrounded by the dust he agitated by galloping fig. 2.
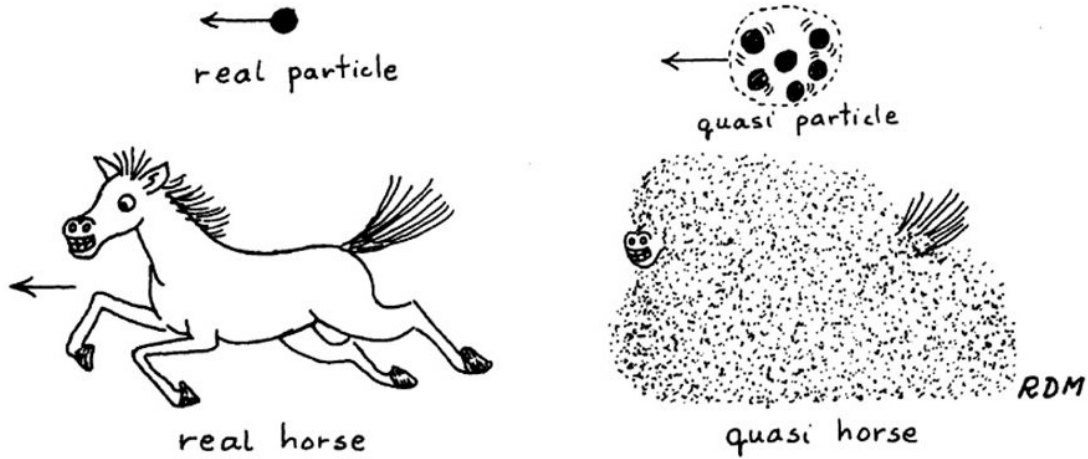
Figure 2: **Quasiparticles.** A particle interacting with other particles in a complex medium can be approximated by a free particle with new physical properties. Taken from [43]

In the case of crystals, periodic potential permits to classify allowed energy bands and calculate their effective masses. Inside a Brillouin zone of reciprocal space, allowed energy bands exist, $E_n(\mathbf{k})$, separated by regions where electronic states are forbidden: the gaps [42].

Electron's wave functions corresponding to these bands have the form of Bloch waves:

$$\psi_{n,\mathbf{k}}(\mathbf{r}) = e^{i\mathbf{k}\cdot\mathbf{r}}u_{n,\mathbf{k}}(\mathbf{r}) \tag{25}$$

where the function $u_{n,\mathbf{k}}(\mathbf{r})$ is periodic over the lattice: $u_{n,\mathbf{k}}(\mathbf{r}+\mathbf{R}) = u_{n,\mathbf{k}}(\mathbf{r})$. Here, $\mathbf{R}$ is the lattice vector which determines its periodicity, $\mathbf{r}$ is the position inside a periodic unit cell, and $\mathbf{k}$ is the momentum in a Brillouin zone.

In the absence of significant electron-electron interactions, the number of electrons determines the electronic properties of the crystal. In the case when this number is such that the crystal contains only fully filled bands, and fully empty bands, we will obtain a semiconductor or an insulator, depending on the width of the gap. If partially filled bands exist, the material is a conductor. The last fully filled band is called the valence band, and the partially filled one, the conduction band.

It may occur in some materials that the width of the gap is small, such that the valence and conduction bands touch or even overlap. Such materials are called semi-metals. A very particular example of this situation arises in the two dimensional lattice of graphene.

2.2.2 *Graphene*

Graphene is a single layer of carbon atoms arranged in a hexagonal (honeycomb) lattice fig. 3. Atomically thin, with the thickness of only $0.035nm$, it represents the first two dimensional (2D) material that was discovered. It was isolated in 2004 by A. Geim and K. Novoselov in Manchester University [44] who, in this way proved wrong the theorem that claimed that 2D materials cannot exist due to destabilizing thermal fluctuations in the third dimension [45].

The researchers of the Manchester group also experimentally proved that graphene is a Dirac material: its elementary excitations behave as massless fermions described by a 2D Weyl equation [46].

This particular dispersion, in which bands linearly cross around isolated points of momentum space is ultimately the consequence of the lattice geometry and the electronic configuration of carbon atoms [47]. Four out of six electrons in this atom lie in half filled orbitals, configuration energetically favorable due to Pauli principle. In this way one $s-$ and three $p-$ half filled orbitals are available to form bonds in carbon, which is the reason it can create numerous compounds and allotrope modifications.

In graphene, which represents one of the carbon allotrope modifications, the $s-$ and two p orbitals (p_x and p_y) hybridize, and create the strong covalent in plane carbon-carbon bonds, forming the 2D hexagonal lattice depicted in 3. The "free" electrons in the last, p_z orbital of each atom, stay perpendicular to the lattice plane structure, and are responsible for the material electronic properties.

2.2.3 *Graphene band structure*

To calculate the material band structure we can profit from the fact that the hexagonal lattice is periodic if we define a unit cell that consists of two atoms (gray area in fig. 3). This means the lattice is composed of two inter penetrating triangular lattices (we can

label them with A and B) a property that will turn out very important for the material. This distinction is purely geometrical, as the atoms in sub lattices A and B are identical carbon atoms.

We can capture a big part of graphene physics if we describe hopping of electrons between atoms in the lattice using the tight binding approximation. In this model crystal wave functions can be described as superpositions of electron wave functions of isolated atoms. The overlap of the wave functions between the nearest or the next nearest neighbor atoms in the lattice can be interpreted as the probability amplitude that an electron hops from one atom to another. Even though it doesn't take the electron-electron interaction into account, this model is very useful for the description of electrons in lattices [42].

As, in graphene, p_z orbitals are responsible for material electronic properties, we will use them as a basis, and write the tight binding Hamiltonian taking into account the hopping between nearest neighbors atoms in the lattice. A convenient way to write this Hamiltonian is by using the so called creation and annihilation operators, introduced in the formalism of second quantization [48].We find:

$$H = -t \sum_{\mathbf{r}_A} \sum_{i=1}^{3} (\hat{b}^\dagger(\mathbf{r}_A + \delta_i)\hat{a}(\mathbf{r}_A) + H.c.) \tag{26}$$

where $a(a^\dagger)$ annihilates (creates) an electron sublattice A (equivalent definition is used for sublattice B), and summation goes over all A sites positions $\mathbf{r}_A$ and their three nearest neighbor B sites given by the vectors δ_i (see fig. 3), defined as:

$$\delta_1 = a(0, -1), \quad \delta_2 = (-\sqrt{3}/2, 1/2), \quad \delta_3 = (\sqrt{3}/2, 1/2) \tag{27}$$

The parameter t represents the overlap between the p_z orbitals of two adjacent carbon atoms, and it is measured to be $t_s \approx 2.7 eV$ in graphene [47].
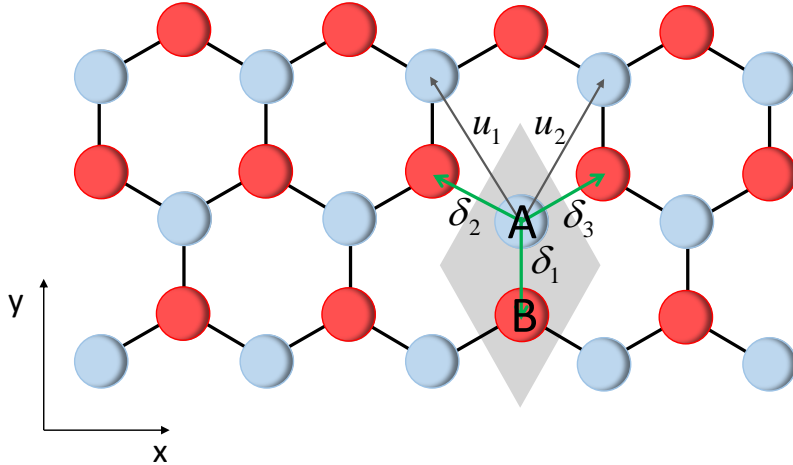

Figure 3: **Honeycomb lattice** Schematic illustration of the lattice. Red and blue sites represent two inter penetrating sub-lattices A and B. In graphene these atoms on all sites are identical. Unit cell is given by gray area.

By imposing periodic boundary conditions we can simulate an infinite lattice, in which case momentum $\mathbf{k} = (k_x, k_y)$ is a good quantum number [42]. Then, by Fourier transforming creation and annihilation operators, $\hat{a}(\mathbf{r}_i) = \frac{1}{\sqrt{N}} \sum_{\mathbf{k}} e^{-i\mathbf{k}\cdot\mathbf{r}_i} \hat{a}(\mathbf{k})$ (and equivalent for $\hat{a}^\dagger, \hat{b}$ and $\hat{b}^\dagger$), we obtain a simple 2×2 momentum space Hamiltonian, written in the basis of A and B sub-lattice:

$$H(\mathbf{k}) = -t \begin{pmatrix} 0 & 1 + e^{-i\mathbf{k}\cdot\mathbf{u}_1} + e^{-i\mathbf{k}\cdot\mathbf{u}_2} \\ c.c & 0 \end{pmatrix} \tag{28}$$

$$\equiv -t \begin{pmatrix} 0 & f_s \\ f_s^* & 0 \end{pmatrix} \tag{29}$$

Electronic spectrum, obtained by solving the eigen problem of this Hamiltonian, is plotted in fig. 4. It consists of two bands, as expected for the system with 2 sites per unit cell, which are symmetric around zero energy: $E_\pm(\mathbf{k}) = \pm t_s \left| \sum_{i=1}^3 e^{i\mathbf{k}\cdot\delta_i} \right|$.

Most importantly the two bands intersect linearly at the corners of the hexagonal reciprocal unit cell (Brillouin) zone, called Dirac points. There are only two such inequivalent points $\mathbf{K}$ and $\mathbf{K'}$ at positions $\mathbf{k} = \pm\mathbf{K} = (\pm 4\pi/3\sqrt{3}a, 0)$, and others can be obtained by translation with the unit vectors in reciprocal space.

In pristine graphene the two bands are half filled and the Fermi level lyes exactly at zero energy. To study the low energy excitations it is useful thus to expand the Hamiltonian around the touching points, that is to take $\mathbf{k} = \xi\mathbf{K} + \mathbf{q}$. Here we introduce the valley index $\xi = \pm 1$ to keep track of the two inequivalent Dirac points. In first order in $\mathbf{q}$ we obtain [47]:

$$H(\mathbf{q}) = \hbar v_F \begin{pmatrix} 0 & \xi q_x - i q_y \\ \xi q_x + i q_y & 0 \end{pmatrix} = \hbar v_F \boldsymbol{\sigma} \cdot \mathbf{q} \tag{30}$$

where $\boldsymbol{\sigma} = (\sigma_x, \sigma_y)$ are the first two Pauli matrices and $v_F = -\frac{3at}{2}$ is the Fermi velocity (a being the distance between the carbon atoms).

This is exactly the form of the 2D Weyl Hamiltonian, we have obtained in section 2.1.2 meaning that electrons indeed behave like massless relativistic particles. One important difference with respect to equation 20, is that the speed of light is replaced with the Fermi velocity, which is approximately 300 times smaller. The other important difference is that the role of the spin in Weyl Hamiltonian is played by the lattice isospin or pseudospin, a degree of freedom related to the existence of A and B sub-lattices. The wave function still has the form of a spinor, representing the components of the wavefunction on each sub-lattice:

$$\psi_{\mathbf{k}\pm, \mathbf{K}}(\mathbf{q}) = \frac{1}{\sqrt{2}} \begin{pmatrix} 1 \\ \pm e^{-i\theta_{\mathbf{q}}} \end{pmatrix} \tag{31}$$

with $\theta_{\mathbf{q}} = \arctan\left(\frac{q_x}{q_y}\right)$, and the $\pm$ sign corresponds to the eigen energies $E = \pm\hbar v_f |q|$. Remarkably, relativistic-like behavior of electrons in graphene is not the consequence of strong spin-orbit coupling, but of the particular lattice geometry. Sublattice isospin couples to momentum and results in a Weyl Hamiltonian. At the same time, spin-orbit interaction
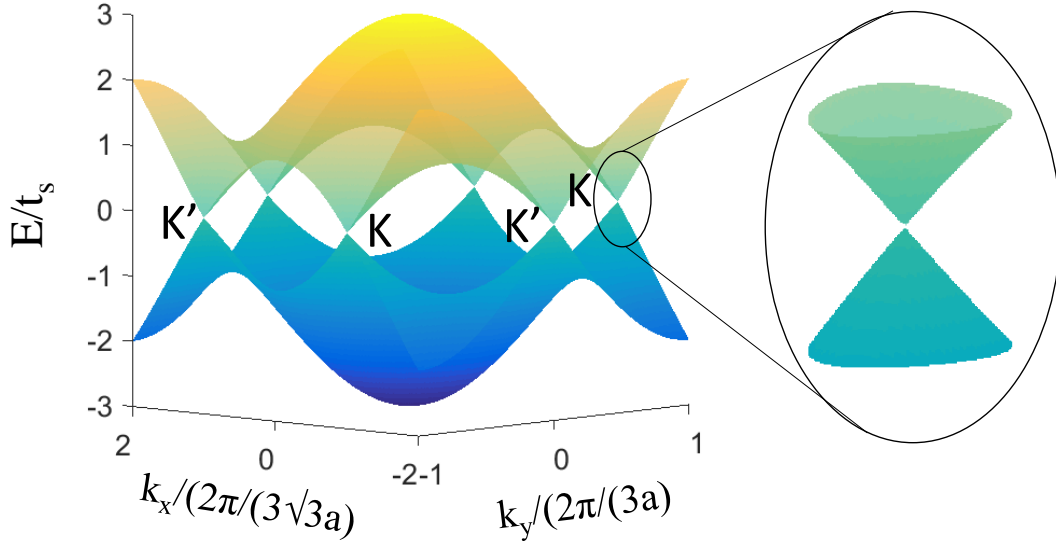
Figure 4: **Energy-momentum relation in the first Bz. of graphene** Valence and conduction band touch in two inequivalent point, around which dispersion has linear character, as seen in the zoom.

in graphene itself is very small, which is the reason why we did not consider spin in our calculation.

It is also important to note that in graphene, there are no real negative energy solutions, as in the case of relativistic particles. The full Hamiltonian of the system requires contribution from other electrons, which in the approximation we used results in a constant. Nevertheless, electrons in graphene are analogous to massless Dirac fermions as their spectrum is symmetric around the certain energy level, and they have spinor wave fuctions.

The experimental realization of graphene deeply changed the field of solid state physics. Not only a new way to for studying relativistic effects was created, but unprecedented electronic properties have been evidenced in the material. Electrons in graphene move with a constant speed independently of their energy, and interact weakly with the lattice phonons. Record electron mobility and conductivity have been measured, along with the possibility to change the nature of charge carriers between electrons and holes by tuning the Fermi level using a gate voltage or dopants [49]. Another impressive transport property, the conservation of the pseudospin prevents back scattering against a potential barrier at normal incidence [50]. This effect, known as Klein tunneling, was predicted for high energy particles and has been observed experimentally in graphene [51]. Unconventional quantum Hall effect was measured at room temperature [52] and understood to be a direct consequence of the massless Dirac nature of graphene carriers [53]

Those, as well as mechanical, thermal and optical properties made graphene a competitive candidate for a broad range of applications. It has been shown to improve batteries, solar cells, electronic transistors, flexible displays or gas sensors, which are expected to be industrialized in the close future, with the advancement of methods for scalable production of the material [54, 55, 56, 57] .

Following the discovery of graphene, important questions both from fundamental and practical point of view arose. Which properties of the lattice govern the conditions necessary to obtain linear Dirac dispersion [58]? How robust are these features with respect to the change of lattice geometry or defects?

Usually when bands in crystals are about to cross, a gap opens that is, an avoided crossing appears due to Bragg scattering of the lattice that mix different states. However, it was found that certain lattice symmetries can restrict the form of the Hamiltonian allowing the bands to intersect in isolated points. This is the case of graphene [59, 60, 61]. Even more, Dirac cones are found not to be only band degeneracies, but stable discontinuity points in the dispersion with particular topological features. Symmetry, and topological arguments determine not only the dispersion, but also other important physical properties such as the shape of the wavefunctions, existence of edge states and the behavior of the bands under lattice deformation, as we are going to see throughout this thesis.

2.3 GENERAL FEATURES OF DIRAC HAMILTONIANS

2.3.1 *The role of symmetries*

It is useful for these reasons to discuss the symmetries of the honeycomb lattice. The first we can notice is inversion symmetry. It imposes that the Hamiltonian is invariant under the exchange of the two sublattices $A \to B$ while interchanging $\mathbf{k} \leftrightarrow -\mathbf{k}$.

Another important symmetry is time reversal symmetry. This very fundamental symmetry in physics is formally represented with an anti unitary operator $\mathcal{T}$, which satisfies $\mathcal{T}\mathcal{H}(\mathbf{k})\mathcal{T}^{-1} = \mathcal{H}(-\mathbf{k})$. It is not necessary, for the use in the band theory, that such symmetry corresponds to the physical time reversal symmetry. For example, we can notice that graphene Hamiltonian is invariant under the simultaneous operations of complex conjugation and $\mathbf{k} \to -\mathbf{k}$. This means we can identify complex conjugation $\mathcal{K}$ as $\mathcal{T}$.

It can be shown, using simple mathematical arguments[61], that the combination inversion and time reversal symmetry allows the appearance of stable Dirac points in a two dimensional crystal. It constrains the Hamiltonian in such a way that a solution holding band degeneracies is allowed to exist.

The obtained form of the Hamiltonian is:

$$H(\mathbf{k}) = \sum_{i=0}^{3} f(\mathbf{k})^i \boldsymbol{\sigma}^i = \begin{pmatrix} 0 & f(\mathbf{k}) \\ f(\mathbf{k}) & 0 \end{pmatrix}, \quad = f(\mathbf{k})^x - i f(\mathbf{k})^y \tag{32}$$

In addition to time-reversal and inversion symmetry graphene also possesses chiral symmetry. Mathematically, this symmetry is defined as a unitary matrix which anticommutes with the Hamiltonian:

$$\Gamma^\dagger H(\mathbf{k})\Gamma = -H(\mathbf{k}) \tag{33}$$

We have already introduced this symmetry in the same way in the section on the Weyl equation 2.1.2, to distinguish left-hand and right hand Weyl fermions. While the mathematically equivalent Hamiltonian possessing chiral symmetry also describes graphene lattice, as we mentioned, the role of spin is played by the lattice pseudo-spin. This means that

spin-momentum locking present in particle physics translates in graphene as sub-lattice pseudospin-momentum locking.

In solid state physics, this symmetry is known as the sub-lattice symmetry or the symmetry of bipartite systems. These are systems which can be divided in two parts, and the hopping exists only between sites belonging to different parts, as is the case for graphene described in nearest neighbor tight binding approximation Hamiltonian.

This symmetry has several important consequences on the physics of graphene. It assures that the spectrum of graphene is symmetric with respect to zero energy. As a result wavefunctions describing edge states can be supported only on one sub-lattice, as we will see in the chapter 4.

Additionally, Hatsugai [62] has shown that the existence of a chiral symmetry implies not only the feasibility of contact points in the band structure but also the fact that they appear in pairs without requiring an additional symmetry such as time reversal symmetry . However, in such a case, the pair of contact points is not necessarily at $\mathbf{K}_D$ and $-\mathbf{K}_D$. In addition, he showed that the contact points within a pair have opposite chiralities. This is the 2D version of the more general Nielsen-Ninomiya theorem which has fundamental importance when simulating standard model phenomena with crystals [63, 64]

Graphene is thus quite exceptional material as it has many symmetries among which inversion, time-reversal, sublattice (chiral) and particle hole symmetry. The last three have a special status in solid state physics as they are used to identify and classify crystals with particular topological properties [65]. Actually, an interesting property of graphene Hamiltonian is that it presents topological features. For example its Dirac cones are characterized by winding numbers, and the existence of its edge states can be connected to its bulk properties (bulk-edge correspondence).

2.3.2 *Topology in physics*

In general, topology is a mathematical discipline which deals with properties of objects conserved under continuous deformations. If two objects cannot be transformed one into the other by any continuous deformation we say that they belong to different topological classes [66]. For example the surface of a sphere cannot be transformed into that of a the torus without "tearing" it and "gluing" it again, thus they are topologically different.

Further more mathematics teaches us that the topology of a space can have consequences on objects existing in it, such as vectors. If we want to place vectors all over the surface of a sphere, we will necessarily create defect-like patterns i.e. vortices fig. 5(a). This is not needed in the case of a thorus, which is topologically different surface than a sphere. [67].

Conveniently, mathematics also equipes us with recipes to quantify this behavior and calculate a quantity which labels different topological classes. These quantity is called a topological invariant, and it can take only integer values [68]. By definition it doesn't change with continuous deformations, meaning that it quantifies global properties of the object in question. In the case of a vortex we can calculate the winding number, which describes how many times it loops around a central point, and in which direction, fig 5(b).

In the 1980's topological concepts were successfully transfered to abstract spaces of particle wave functions. At the time, Thouless and his coworkers tried to understand the robust quantization of the transverse conductivity plateaus of a 2D electron gas under

magnetic field, phenomenon known as quantum Hall effect. They realized that magnetic field changes the topology of momentum space [69]. The robust conductivity quantization, which showed no dependence on a sample disorder, could be explained in terms of the so called Chern number, that represents the number of vortices induced by the magnetic field in each Landau level.
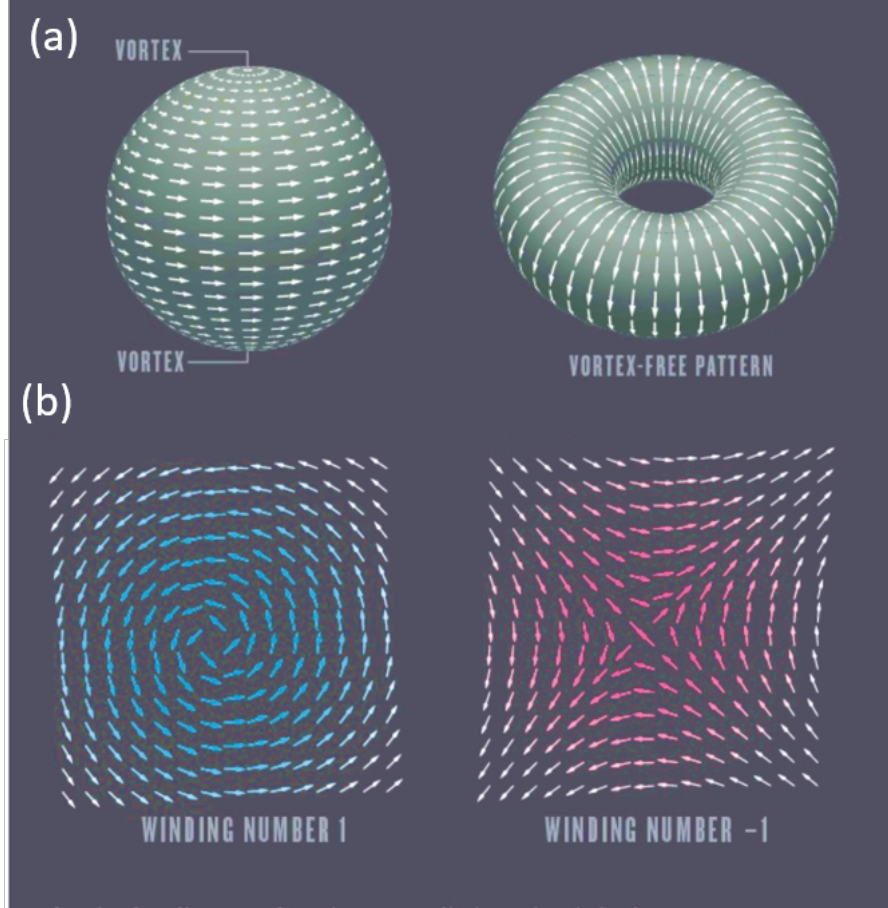
Figure 5: **Topology** (a) Surfaces of a sphere and of a torus cannot be deformed one into another by continuous change, they are topologically nonequivalent . (b) Topological objects are characterized by an integer number called topological invariant. Vortex as a topological object is described by winding number, which quantifies how many times it turns around a point in its center. Such an object can be removed only by annihilation with vortex of opposite sign. Taken from [67]

Topological arguments are now used to establish new classification of phases of matter (given by topological invariants) and explain numerous phenomena in areas of physics like superconductivity and magnetism [70, 71, 72].

In band theory of solids it was shown for the first time that to capture the physics of a system, it is not only necessary to know its dispersion but also information about the structure of the wave function in momentum space. The global evolution of the k-dependent wave function over the Brillouin zone, quantified by topological invariants,

determines certain local properties of the system. In lattices, a very important topological invariant is the Chern number. It can be defined in gapped spectrum for each band as:

$$C = \frac{1}{2\pi} \int \nabla_{\mathbf{k}} \times \langle u(\mathbf{k}) | \, i\nabla_{\mathbf{k}} \, | u(\mathbf{k}) \rangle \cdot d\mathbf{s} \tag{34}$$

where $u(\mathbf{k})$ is the spatially periodic part of the Bloch wave function, and $<>$ denotes the inner product in real space. Materials with nonzero Chern numbers are called topological insulators, and their physics is closely related to that of Quantum hall [73, 74].

The interesting situation happens when topologically inequivalent insulators are placed right next to each other. As the two Hamiltonians cannot be continuously connected gap will need to close, and reopen on their interface so that the topological invariant can changed. In that way, additional states will be created in gap, whatever are the local properties of the interface. Creation of these type of edge states has been the objective of numerous studies, particularly in 2D systems where such conductive channels assures unidirectional transport protected from back scattering on defects.

2.3.3   *Topological properties of Dirac matter*

Recently, topological properties of gapless systems, have been intensively studied and better understood [62, 75, 76, 77]. Its main representative in 2D, graphene, is interesting as it shows topological features even without spin orbit coupling or breaking of time reversal symmetry, as is the case in topological insulators. As we mentioned in section 2.2.3, it is a particular isospin-orbit interaction that result in particular properties of its wave function.

The ensemble of touching points in graphene is attributed the zero Chern number. Thus, we cannot apply theory of topological insulators in this case. However, there is another relevant non zero bulk invariant, the winding number. We will see throughout this thesis that important aspects of graphene physics are determined by its topological properties, that is, they can be related to bulk invariants.

Winding number in graphene describes the winding of the phase of the wave function around the Dirac point. It's non zero value makes Dirac point a topological object in two dimensions [61]. While other quantities are sometimes used to express graphene topological features (such as Berry phase, or Berry curvature) winding number represent a most convenient choice as it is gauge invariant [78].

More precisely, winding number of Dirac cone can be found from the behavior of the spinor wave function around the Dirac point. Let us write the wave function in the basis of two pseudo spin states

$$\psi = \frac{1}{\sqrt{2}} \begin{pmatrix} e^{-i\phi(q_x, q_y)/2} \\ \pm e^{-i\phi(q_x, q_y)/2} \end{pmatrix} \tag{35}$$

Then, for each value of $\mathbf{q} = (q_x, q_y)$ the relative phase of the two components defines the direction of the 2D pseudo spin vector $\mathbf{h}$, fig. 6. The number of rotations that a pseudospin vector undergoes when the electronic wave vector rotates fully one time around the Dirac point is called the (pseudo spin) winding number:

$$\omega = \frac{1}{2\pi} \int \nabla\phi(\mathbf{q}) d\mathbf{q}. \tag{36}$$
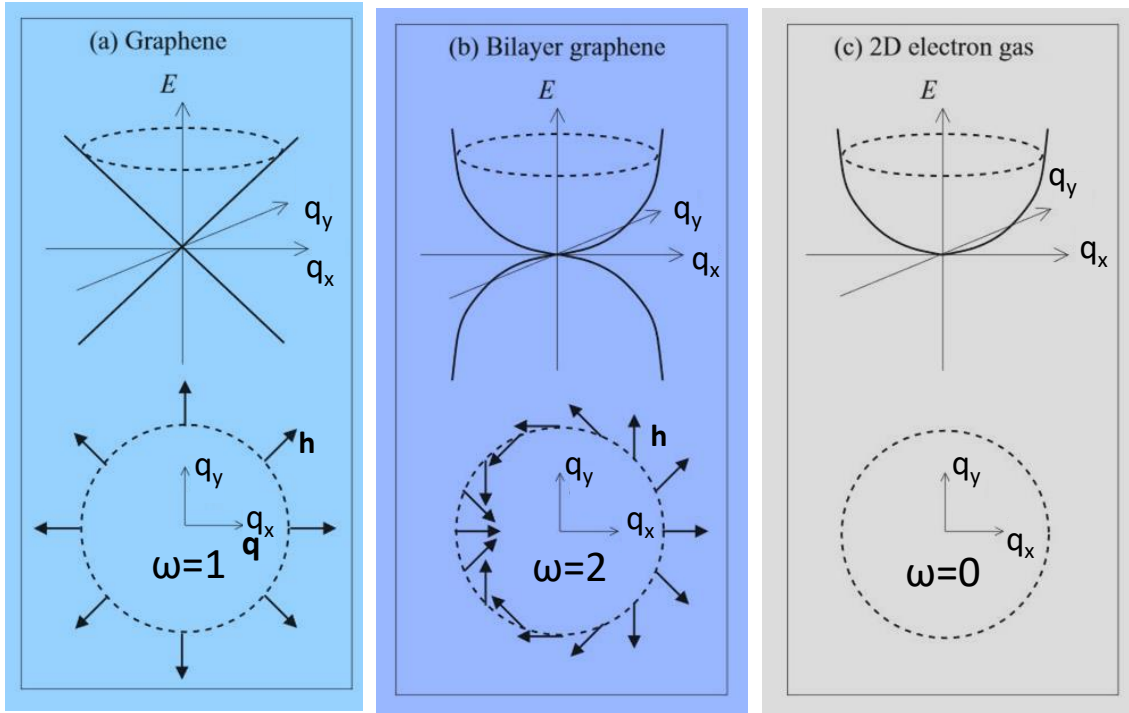
Figure 6: **Winding of pseudo spin vector** (a) Around Dirac point the vector winds once. This situation occurs in graphene. (b) In the case of bilayer graphene, wavefunction is also a spinor, with the winding 2 around the quadratic band touching. (c) 2D electron gas has winding zero. Figure taken from [78]

This quantity is gauge invariant (it does not depend on the overall phase of a quantum state) and thus can be directly calculated from the Hamiltonian, which contains information on the pseudospin vector $\mathbf{h}$. By rewriting Dirac Hamiltonian as :

$$H(\mathbf{q}) = \hbar v_F \mathbf{h} \cdot \boldsymbol{\sigma} = h_x(\mathbf{q})\sigma_x + h_y(\mathbf{q})\sigma_y \tag{37}$$

we can easily parametrize $\mathbf{h}$:

$$h_x = \mathbf{h} \cdot \mathbf{e}_x = \epsilon \cos \phi(\mathbf{q}) \tag{38}$$

$$h_y = \mathbf{h} \cdot \mathbf{e}_y = \epsilon \sin \phi(\mathbf{q}) \tag{39}$$

$$\rightarrow \tan \phi = \frac{h_x}{h_x} \tag{40}$$

and find the winding:

$$\omega = \frac{1}{2\pi} \int \nabla \phi(\mathbf{q}) d\mathbf{q} = \frac{1}{2\pi} \int_0^{2\pi} \frac{\partial \phi(q, \theta)}{\partial \theta} d\theta, \tag{41}$$

where $\theta = \arctan(q_y/q_x)$ goes around the Dirac cone. In the case of graphene, where we simply have $h_x = \hbar v_f q_x$ and $h_x = \hbar v_f q_y$, we get:

$$h_x = v_F q \cos \theta \qquad\qquad h_y = v_F q \sin \theta \tag{42}$$

and

$$\omega = \frac{1}{2\pi} \int_0^{2\pi} 1 d\theta = 1. \tag{43}$$

Winding number around $\mathbf{K}'$ point can be also calculated using definition 36, by taking $\xi = -1$. The obtained value $\omega = -1$ means that the pseudo spin vector winds in other direction around K' point.

We have thus obtained that Dirac cones are characterized by non zero windings 6(a). This result is important in the physics of graphene. The quantity, also called the topological charge, reflects the stability of Dirac point. As a sort of topological vortex in momentum space, it can be moved by deformation of the lattice, but cannot be easily destroyed. While chiral and time-reversal symmetry of the lattice are preserved, the only way for a Dirac cone to disappear is through a topological phase transition, by merging with Dirac cone of opposite topological charge.

In chapter 6 we will see under which conditions merging of two Dirac cones with opposite winding number can happen and how it can be used to tune transport properties in honeycomb lattice.

Winding numbers also govern the existence of lattice edge states [79]. While edge states in graphene are not unidirectional like in 2D Chern topological insulators, their existence and behavior under lattice deformations can be determined by topological arguments. A detailed review on this subject and the discovery of new weakly topological edge states are presented in chapters 4 and 5.

Finally, winding number quantity is crucial for understanding the behavior of graphene under gauge fields. It explains the appearance of half integer quantum Hall effect under magnet field [78] as well as the emergence of artificial gauge fields when suitably deforming the lattice [80].

Winding number can be equally calculated for other systems described by the two component spinor wave function. For example, quadratic band touching in the spectrum of low energy Hamiltonian of bilayer graphene also has a non zero winding. The Hamiltonian reads [81]:

$$H = \begin{pmatrix} 0 & (q_x - iq_y)^2 \\ ((q_x - iq_y)^*)^2 & 0 \end{pmatrix} \tag{44}$$

In that case the components of the pseudospin vector are:

$$h_x = \frac{q_x^2}{2m} - \frac{q_y^2}{2m} = \frac{q^2}{2m}(\cos\theta^2 - \sin\theta^2) = \frac{q^2}{2m}(\cos 2\theta) \tag{45}$$

$$h_y = \frac{q_x q_y}{2m} = \frac{q^2}{m}(\cos\theta\sin\theta = \frac{q^2}{2m}(\sin 2\theta) \tag{46}$$

The angle ϕ, given by $\tan\phi = h_y/h_x = 2\tan 2\theta$ is $\phi = 2\theta$ and the winding:

$$\omega = \frac{1}{2\pi} \int_0^{2\pi} 2d\theta = 2 \tag{47}$$

This means that the pseudo spin vector winds twice around the band touching 6(b). The obtained value explains, for example the absence of the first Hall plateau in bilayer graphene [82, 83, 78].

2.4 DIRAC HAMILTONIANS BEYOND CONDENSED MATTER

As a material, graphene represents a valuable playground for exploring interesting phenomena of relativistic fermions, or topological concepts in a relatively simple geometry. In parallel to the research activities on its properties, a radically different question was posed after its discovery. Can we transfer those properties to other physical systems, different from that of condensed matter, or even surpass them in that way? Can it be done with neutral particles such as photons, in order to design and control the behavior of light in a new way?

In the last decade the idea of creation of artificial systems for Hamiltonian simulation allowed fast development in that direction. Artificial systems offer advantages such as the possibility to tune the lattice geometry, but also easier access to the properties of the wave functions, all that without the need to match the Fermi energy with the desired energy region. The study of graphene physics in new regimes became possible with access to a range of parameters unavailable in natural electronic lattice. Topological phase transitions, creation of artificial gauge fields as well as realization of exotic topological models with graphene became experimentally reachable.

In the next chapter we will review some of the successful realizations of graphene simulators. Then, we will present polaritons, half-light half matter particles and the way they can be used to simulate graphene. The final goal of this thesis is to discover new physics is this analogue simulator and the way it can be used to design new properties of light.

A POLARITON GRAPHENE SIMULATOR

In the previous chapter, we have learned that electrons in graphene lattice acquire particular properties of massless Dirac fermions. The experimental discovery of this material allowed to study many phenomena related to these exceptional particles, but also raised numerous questions about the extension of Dirac physics beyond the original framework of special relativity. How stable are Dirac points in a crystal, can the Dirac dispersion be modified? Many of these questions remained opened due to the difficulties to manipulate and access graphene.

The goal of this chapter is to introduce a polariton hexagonal lattice as a platform of interacting photons which can be used to create a physical analogue of graphene and address challenges in Dirac physics in the photonic context.

In the first part of the chapter we will briefly review the main ideas behind analogue simulation and present state of the art platforms to which graphene physics has been transposed.

In the second part we will present general properties of the system we use to simulate graphene. These are microcavity polaritons, mixed light-matter quasi particles obtained via strong coupling of quantum well excitons and cavity photons. Their main properties will be presented, especially focusing on their photonic character and how it can be used to engineer a 2D potential landscape.

In the third part we will introduce the polariton graphene lattice as a system of choice to implement Dirac physics in the photonics context. In particular, we will show how the lattice is created by confining polaritons in three dimensions, and how it can be directly accessed to provide imaging of wavefunctions in both real and momentum space. We will also explain how lattice parameters, such as the geometry and hopping, can be controllably tuned in such structure, a feature that will be used throughout the thesis.

Details on the samples used in the thesis and experimental setup will be given in the last section .

3.1 ARTIFICIAL SYSTEMS

In the first chapter we have seen that an interesting analogy has been provided by nature between the free relativistic fermions on one side, and charge carriers in graphene on the other. What makes such phenomenon possible essentially is the fact that all particles, within a quantum mechanical description, behave as waves. Indeed, free like propagation of electrons in lattices is possible due to formation of extended states -waves- in periodic potentials. This is how electrons in particular in a hexagonal lattice can acquire properties of free particles such as Dirac fermions.

In the last few decades the idea to use this fact and develop artificial analogues (or simulators) has being intensively developed in different systems, including photonic ones [84, 85]. The objective of these efforts is to create in a controlled way, systems with desired physical

properties which can be directly manipulated and accessed. As such, simulators offer the possibility to experimentally study complex phenomena, or systems that are hard to access or manipulate. Importantly, they also offer the opportunity to explore how properties of matter and light can be modified or even to design new ones.

What are the main requirements for the realization of a simulator? In principle, it is sufficient to create a system well described by the same Hamiltonian that describes the system we desire to simulate. Engineering potential landscape with high precision is thus a very important task towards this goal. Another ingredient is the interaction between the particles.

At first, using light to create simulators doesn't seem like an obvious solution. Photonic system are fundamentally different from solid state lattices, where the basic constituents, the electrons, obey Fermi statistics, interact strongly and are most often examined at equilibrium states at low temperature. On the contrary i) the basic constituent of light, namely photon obeys Boson statistic, ii) photons do not interact and iii) they can reside in any realistic device only for a finite time, and some external driving is needed to inject them in a steady state.

Nevertheless, photons have proved a particularly interesting platform for realization simulation [86]. This is certainly due to their fundamental properties: photons propagate very fast and can be precisely controlled in relatively simple experiments. Various techniques to confine photons and impose the desired potential landscape have been developed while significant interactions can be introduced through non-linear media. Additionally, photon spin (polarisation) degree of freedom can also be well controlled and can be used as a building block for information manipulation, making them important even in the domains of quantum simulation and quantum computing.

Simulation allows transposing newly discovered physical phenomena from other areas into photonics. It allows controling propagation and localization of photons, and engineer photonic dispersions which are some of the central goals in photonics. Historically, the first class of materials in which modification of optical properties was achieved was inspired by electronic lattices. These are photonic crystals, structures with a periodic change of dielectric constant (or equivalently periodic index of refraction). In these structures photonic gaps are engineered such that light waves of certain range of frequencies are reflected while others are transmitted [87, 1]. Highly reflective dielectric mirrors made in this way are commercially used to increase the efficiency of certain LEDs as well as the reflectivity of mirrors in laser microcavities, for example.

More recently various systems of coupled photonic resonators have been used to further design properties of light. Particularly, numerous efforts have been made to implement topological effects in photonics [2]. The possibility to create unidirectional propagation of light in these structures is expected to bring new solutions for the creation of optical isolators and delay lines [3], crucial for development of integrated optic devices.

Graphene is a material which displays numerous interesting physical properties, including topological, as well as the potential for many other applications. This is why its hexagonal lattice has been proposed as a geometry for several artificial systems. Let us shortly review how these analogues meet the simulation requirements and the main results achieved using them.

3.2 STATE OF THE ART GRAPHENE SIMULATORS

3.2.1 *Photonic honeycomb lattices*

One of the first graphene simulators was created as an array of evanescentlly-coupled waveguides arranged in a honeycomb lattice (HCL) fig. 7(a). The equation describing the diffraction of light in such structure, the paraxial wave equation, is mathematically equivalent to the Schrödinger equation describing time evolution of electrons. Graphene wave dynamics can thus be probed in this system by observing propagation of monochromatic light through this waveguide array, which allows observation of the wavefunction (including phase). The system was successfully employed to address several aspect of graphene physics and its implications in optics. Edge states in graphene have been observed [88] and manipulated [89], and artificial gauge fields have been introduced by implementing nonuniform strain [90]. The lack of possibility to access the eigenvalue spectrum stays the biggest limitation of this system.
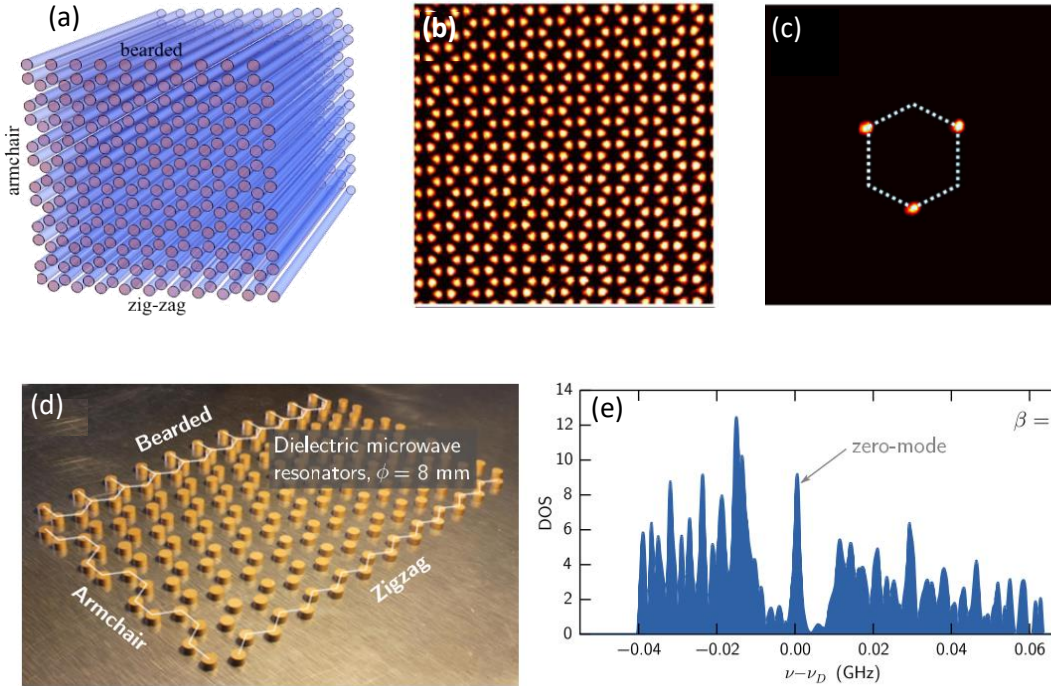
Figure 7: **Photonic graphene structures** (a) A scheme of a periodic array of waveguides that are evanescently coupled to one another fabricated using the femtosecond laser-writing technique which locally increases the refractive index in the silica sample [90]. (b) Honeycomb lattice made by changing refractive index in photorefractive nonlinear crystal by by optical induction. (c)vThe k-space spectrum of the input beam in the structure in fig.(b) matching the three marked Dirac points. Selective excitation of Dirac points allowed experimental observation of pseudospin-mediated vortex generation. (d) Implementation of HCL with microwave resonators. (e)Density of states directly measured in structure in fig.(d) allows to detect edge states.

A similar platform, based on a nonlinear crystal in which index of refraction is varied in hexagonal geometry has been used to experimentally study the pseudo spin degree of freedom, demonstrating that it is not merely for theoretical elegance but rather physically measurable quantity [91]. In fig. 7(b) we see an optically induced honeycomb lattice in this material and in fig. 7(c) the k-space spectrum of the input beam matching the three selectively marked Dirac points.

Another very successful platform has been created in the microwave regime using cylindrical resonators to create graphene lattice sites [92, 93, 94]. The dielectric cylinders are coupled by an evanescent magnetic field, so that the wave propagation between the resonators is well described by a tight-binding-like hopping term fig. 7(d). The setup allows for direct access to the local density of states through the reflected signal measured via a movable loop-antenna, fig 7(e). Moreover, the setup allows visualizing the wave function associated with each eigen frequency. We will see in the next chapters how this system was used to study edge states and phase transitions in graphene.

Apart from photonic other systems have also been used to realize analogues of graphene. They include (i) Optical lattices for cold atoms [95], (ii) nanopatterning of ultrahigh-mobility 2D electron gases (2DEGs) [96], (iii) molecule-by-molecule assembly of honeycomb lattices on metal surfaces by scanning probe methods [97], (iv) mechanical graphene [98] and others [99].

The most interesting results in terms of topics discussed in this thesis have been achieved with optical lattices for cold atoms and this is why we would like to mention some of them.

3.2.2 *Cold atom honeycomb lattices*

Ultracold gases in optical lattices present one of the most advanced platforms for quantum simulation [100]. Within this setting, potential landscape for atoms and ions can be created by interfering multiple laser beams. A very important milestone in the field of quantum simulation has been achieved in cold atom systems with the experimental creation of one of the basic models for interacting particles in lattices, the so called Bose- (or Fermi-) Hubbard model [101] and with the observation of the superfluid-Mott transition.

The first cold atoms honeycomb lattice has been realized and investigated using a Bose-Einstein condensate [102], but no signatures of Dirac points were observed. In later experiments by L.Tarruel in T. Esslinger group a honeycomb lattice has been implemented for fermionic K atoms [95]. The hexagonal geometry is provided by interferences of three retro-reflected laser beams as schematically depicted and explained in fig. 8(a). Minima in the potential (white regions in fig. 8(b)) could be arranged in different geometries, including hexagonal by tuning the relative intensity of the three beams.

It is interesting to understand how Dirac cones were detected in this system. This was done by probing the energy splitting between the resulting two lowest-energy bands through Landau-Zener oscillations. The atom cloud is first prepared in the lowest energy band of graphene and then accelerated using magnetic field up to the point when it reaches the edge of the Brillouin zone and is Bragg reflected (making thus one full oscillation in momentum space). The oscillations for quasi momenta close to the Dirac points differ from those which are far for them. Figure 8(c) shows data obtained before and after one oscillation for these two cases. Close to the Dirac cone (green empty circle in the

figure 8(c), atoms are partly transfered from the first band to the second because of the vanishing energy splitting at the linear band crossing. Those transfered atoms appear in the second Brillouin zone, where they are detected. No such transfer is observed far from the Dirac point (full blue line).

In a more recent work graphene-type hexagonal optical lattice loaded with bosonic atoms was used to detect the Berry flux localized at each Dirac point [103]. Finally, ultra-cold atoms in optical lattices periodically modulated in time allowed creation of complex hopping amplitudes and realization of Haldane model in honeycomb lattice [104].
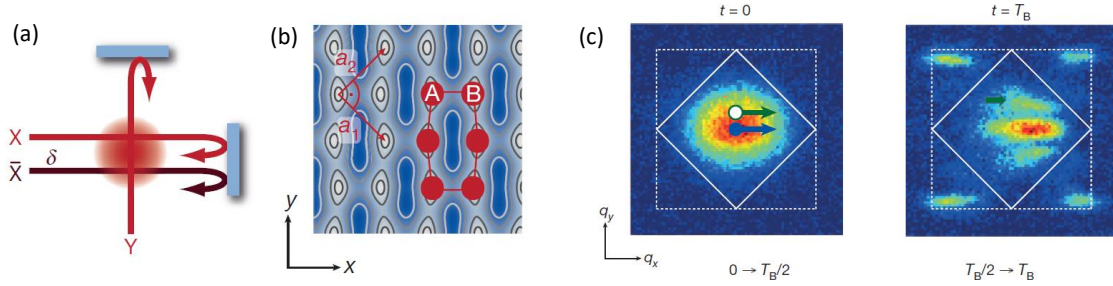
Figure 8: **HCL with cold atoms** (a)Three retro-reflected laser beams of wavelength l51nm create the two-dimensional lattice potential. Beams X and Y interfere and produce a checker-board pattern, and beam $\overline{X}$ creates an independent standing wave. (b) HCL potential can be realized by adjusting intensities of the lattice beams. White regions correspond to lower potential energies and blue regions to higher potential energies.(c) Quasi-momentum distribution of the atoms before and after one Bloch oscillation, of period TB (color scale, column density of the absorption image in arbitrary units). The cloud explores two trajectories in quasi-momentum space simultaneously, close to the Dirac point (green open circle) and far from it (blue filled circle).

3.3 INTRODUCTION TO MICROCAVITY EXCITON POLARITONS

In this section we will present microcavity exciton-polaritons as a system suitable for creation of analogue simulators of Hamiltonians, and particularly that of a honeycomb lattice. Exciton-polaritons are mixed light-matter particles that arise from the strong interaction of quantum well excitons and cavity photons in semiconductor microcavities.

Similarly to photonic architectures, potential landscape can be designed at will by creating structures with periodic change of index of refraction. Different from other photonic systems, polaritons provide combined information on real, momentum, and energy spaces needed to reconstruct the band dispersion and the eigenfunctions. At the same time, the out of equilibrium nature of the system allows its visualization in luminescence experiments at temperatures on the order of 10K. Additionally, transport properties of the lattice can be probed thanks to the property of polaritons to propagate in 2D. Finally, polaritons interact through their excitonic component and thus present a great potential in accessing the nonlinear domain which is unfeasible in electronic graphene systems.

For these reasons, polaritons provide an extraordinary photonic platform to emulate 1D and 2D Hamiltonians, as well as to transpose to the photonic world some of the properties

of electrons in solid state systems, and to engineer Hamiltonians with novel transport properties.

3.3.1 *General introduction to polaritons*

Interaction between light and matter is the main mechanism behind our perception of the world, dominated by vision. Interestingly, it is also one of the main tools of scientific investigation, as optical spectroscopy methods are widely used to reveal structure and properties of matter ranging from cosmological objects to nanomaterials. Conversely, material structures have enabled us to discover the general laws governing the dynamics of light, e.g. refraction, reflection, and diffraction.

Classically, light-matter interaction is described by the macroscopic Maxwell equations which determine the degree of polarization induced in the material in the presence of an electro-magnetic field [105]. Quantum mechanical theories give us more details on how excited atoms emit light. Two regimes of light-matter interaction are possible. In the first, the so called weak coupling regime, the emission of light by matter is an irreversible process. Excited atom spontaneously emits a photon and the probability that it gets reabsorbed is exponentially small. The reason is that the single excited state is coupled to a continuum of final states, constituted by the atom in a lower energy level and a photon with a direction and polarization which can take a continuum of possible values [106]. In this case light and matter behave as separate entities, and this is why we can learn about one by probing it with the other.

However, particular conditions can be created such that light and matter interact strongly and mix to an extent that we cannot separate one from each other. This is the, so called strong coupling regime. The most efficient way to achieve it is by confining light in an optical microcavity and putting an atom, or other two level systems inside of it [12]. It this case one matter mode can be coupled to just one light mode, and a photon can be absorbed and re-emitted several times by the atom before leaving the cavity. The probability to find the atom in the excited state does not decrease exponentially. The system oscillates in time between two states: 1) atom in the excited state and 2) atom in the ground state plus one photon. These oscillations are called Rabi oscillations.

While the strong-coupling regime in semiconductors was first achieved in the bulk *GaAs*, without the use of a cavity [107, 108], an important breakthrough arrived in 1992, when C.Weisbuch and collaborators attained it for the first time in semiconductor microcavities [109]. In this, and many other works that followed, strong coupling is obtained by embedding a semiconductor quantum well inside a microcavity, in which one longitudinal optical mode is resonant with the excitonic transition in the quantum well. If the typical lifetimes of the photon and the exciton are long enough as compared to the typical interaction strength, the system is in the strong coupling regime. Similarly to their atomic counterpart, semiconductor microcavities in the strong coupling regime are characterized by mixed half light-matter eigen states, which are called microcavity exciton-polaritons.

Polaritons inherit properties from both components. From their photonic component they inherit low mass, about five orders of magnitude smaller then the one of excitons, and eight orders of magnitude smaller that of electrons. It is thanks to this property that polaritons in microcavities can propagate at distances up to hundreds of microns, and that

arbitrary potential landscape on the microscale can be imposed to them, as we will see in the next sections.

Thank to their excitonic component, polaritons inherit the possibility to via Coulomb interaction between their fermionic component, but also with the external magnetic field. Important results in the area of physics of interacting bosons have been achieved in this system. They include condensation in a single macroscopic state (Bose Einstein condensation) at temperatures much higher then that necessary in atomic gases, as well as superfluid behavior [16]. More recently, strong tunable artificial gauge potentials for two-dimensional microcavity exciton polaritons was created by application of orthogonal electric and magnetic fields [110].

In the next section we are going to review some details on how strong coupling regime can be achieved in microcavities. We will start by recalling the main techniques of confining photons in a microcavity, as well as excitons in quantum wells.

3.3.2 *Confinement of light*

Confinement and manipulation of light can be achieved by designing different cavities [14]. In order to enhance light matter interaction, a small mode volume is required and solid state structures with dimensions typically of the same order of magnitude as the wavelength are used. Additionally, long lifetime of photons is achieved by using highly reflective interferential semiconductor mirrors, rather than metallic ones in which absorption is considerable.

Cavities of various geometries, like planar microcavities, microdiscs or micropillars have been created with nanometer precision, thanks to the great progress of epitaxial growth and etching techniques. Behavior of light in those structures can be simply understood in terms of two main light phenomena. The first is reflection (and refraction) of light on a single surface between two media with different indexes of refraction, fig. 9(a). The other important phenomena is the interference produced by such reflections on multiple interfaces periodically arranged on the scale of the wavelength of light, fig. 9(b).
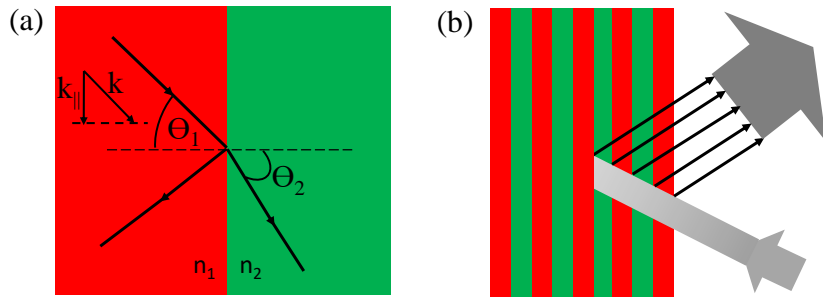
Figure 9: (a)Schematic representation of reflection and refraction of light on the interface between two media with different index of refraction. (b) multiple interfaces periodically arranged on the scale of the wavelength of light produce interference effect which significantly change the way light is reflected and transmitted.

In the first limit, reflection and refraction on a single surface are usually given in therms of Snell's law: $n_1 \sin(\theta_1) = n_2 \sin(\theta_2)$, (or in more general form by Fresnel equations).

These laws are the consequence of continuous translation symmetry and conservation of momenta in the plane of the interface. A particular phenomenon, important for confining the light, occurs in case when $n_1 > n_2$. If $\theta_1 > \sin(n_2/n_1)^{-1}$ the law gives $\sin(\theta_2) > 1$, which is not possible, and the light is totally reflected. This phenomenon, called total internal reflection, will have important role when patterning a microcavity into a honeycomb lattice, as we will see later.

Before going in that direction, we will apply these basic laws on propagation of light onto structures in which index of refraction changes at distances similar to the desired resonant wavelengths. This will allow us to understand how a planar (2D) single mode microcavity, with high quality factor can be designed using dielectric materials. We will start by the most simple case, a Fabry Perot cavity, then extend its principle of work to Bragg mirrors, and finally describe a complete semiconductor microcavity.

3.3.2.1 *Fabry-Perot cavity*

Two transparent plates with reflective surfaces separated by the distance L_{cav}, as in the fig. 10(a), make a Fabry-Perot cavity, or an etalon, as this structure is called due to its particular, well defined transmission properties. These properties are the consequence of interferences between multiple transmitted and reflected waves that appear when light is incident on such a structure. Their exact form depends on the parameters of the cavity: values of reflectivity and transmission coefficients of the plates, r_1, r_2 and t_1, t_2 respectively, cavity width L_{cav} and its refractive index n_{cav}
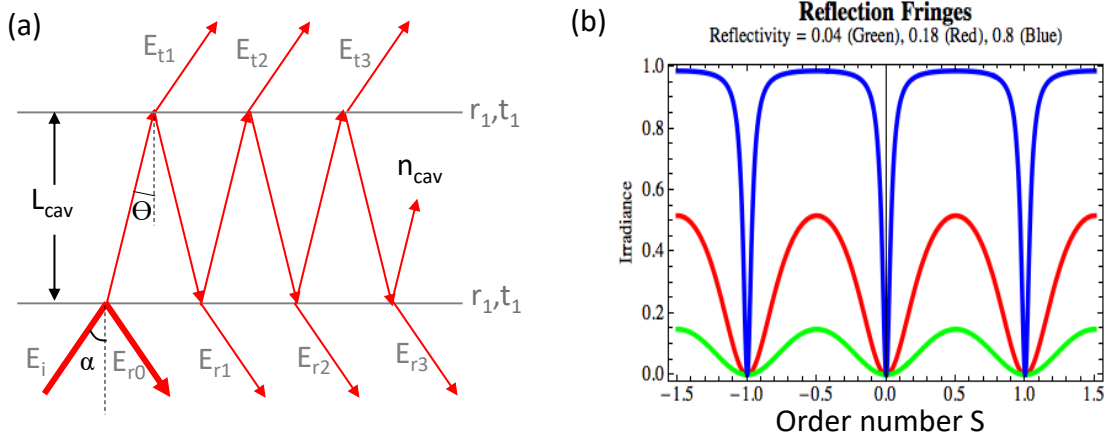
Figure 10: (a)Fabry Perot cavity's scheme with metallic mirrors. (b) Reflectance of a Fabry-Perot cavity as a function of order number and reflectivity of the mirrors.

Let us consider how a monochromatic plane wave, incident on the surface of the cavity with angle α is transmitted through the structure. We will take $n_{cav} > n_{air}$. The angle of propagation inside the cavity will be $n_{air} \sin(\alpha) = n_{cav} \sin(\theta) \rightarrow \theta = \sin^{-1}(\frac{n_{air}}{n_{cav}} \sin(\alpha))$. Assuming an incident external field with (complex) amplitude E_i, as in fig. 10(a), the transmitted field is composed of an infinite number of components of decreasing magnitude which can be obtained by simply tracing the trajectories of the ray in the figure and

accounting for reflections and transmissions. In each round trip inside the cavity the wave gains a phase of $\phi = 2\pi(n_{cav}L_{cav}\cos(\theta)/\lambda)$. Then, for the transmitted wave we can write:

$$E_t = E_i t_1 e^{i\phi} t_2 + E_i t_1 e^{i\phi}(r_2 e^{i\phi} r_1 e^{i\phi})...E_i t_1 e^{i\phi}(r_2 e^{i\phi} r_1 e^{i\phi})^n t_2 + ... \tag{48}$$

$$E_t = E_i t_1 t_2 e^{i\phi}\left(\frac{1}{1 - r_1 r_2 e^{2i\phi}}\right) \tag{49}$$

For the transmission coefficient we obtain:

$$T = \left|\frac{E_t}{E_i}\right| = \frac{(t_1 t_2)^2}{1 + (r_1 r_2)^2 - 2r_1 r_2 \cos(\phi_{tot})}, \tag{50}$$

where $\phi_{tot} = 2\phi$. In the case when there is no absorption in the mirrors or diffusion at the interface reflectance the coefficient R can be found from $R + T = 1$. In fig. 10(b) we see that the reflectivity drops to zero whenever $\phi_{tot} = S \times 2\pi$, where S is an integer value. For the simple case of normal incidence ($\alpha = 0$), resonance in transmission is attained under condition $n_{cav}L_{cav} = S\lambda/2$. This means Fabry Perot cavity provides a convenient way to select particular wavelength, in the case when highly reflective surfaces (mirrors) are used.

The quality factor of the cavity is the measure of the resonant enhancement of the mode. It is simply defined as the ratio of a resonant cavity frequency, ω_c, and the line width of the cavity mode $\delta\omega_c$ (full width at the half maximum-FWHM of the reflectance minimum):

$$Q = \frac{\omega_c}{\delta\omega_c}. \tag{51}$$

The Q-factor is a measure of the rate at which optical energy decays from the cavity . It also gives the cavity photon lifetime $\tau = \frac{\hbar Q}{\omega_c}$. The quality factor depends on the cavity mode (and cavity length) we are considering. In the case of Fabry-Perot we have:

$$Q = \frac{S\pi\sqrt{r_1 r_2}}{1 - r_1 r_2} \tag{52}$$

3.3.2.2 *The effective photon mass*

When the cavity is excited not at normal incidence but at a certain angle α with respect to the normal, the interference condition defining the cavity mode resonance changes slightly. Let us write the wave vector of the incident wave as $\mathbf{k} = \mathbf{k}_{||} + \mathbf{k}_z$. Upon the change of index of refraction in $z-$direction $n_{air} \to n_{cav}$, k_z component will change while the parallel one will be conserved. Taking into account that we have $k_{cav} = n_{cav}k_{air} = n_{cav}E/\hbar c$, where E is now the energy of the mode and $\mathbf{k}_{||}^2 + \mathbf{k}_z^2 = (2\pi n_{cav}/\lambda)^2$, we can impose the resonance condition for the mode S and get:

$$k_z^{cav} \cdot L_{cav} = S\pi \tag{53}$$

$$\sqrt{\left(\frac{n_{cav}E}{\hbar c}\right)^2 - k_{||}^2} = \frac{S\pi}{L_{cav}} \tag{54}$$

The dispersion relation of the optical modes is then given by:

$$E^C(k_{||}) = \hbar c \sqrt{\left(\frac{\pi}{L_{eff} n_{cav}}\right)^2 + k_{||}^2} \tag{55}$$

For the small incident angles $k_{||} << k_z$ this dispersion can be approximated by a parabola:

$$E^C(k_{||}) = \frac{\hbar c \pi}{L_{eff} n_{cav}} + \frac{\hbar^2 k_{||}^2}{2 m_{ph}}, \tag{56}$$

with $m_{ph} = \frac{\hbar \pi}{c L_{eff} n_{cav}}$. This is a very interesting result, as it suggests that confinement of the photons between two parallel mirrors results in a finite mass to the photon for photon in-plane motion.

3.3.2.3 *Bragg mirrors*

As we pointed out earlier, in order to realize a cavity with high quality factor and high finesse the use of highly refractive mirrors is needed. Distributed Bragg mirrors (DBRs) are semiconductor heterostructures which can provide reflectivity coefficient near 100%.

They consist of periodically arranged layers with different index of refraction n_1, and n_2 and widths L_1 and L_2 such that $n_1 L_1 = n_2 L_2$. Similarly to the case of Fabry Perot cavity, radiation incident on the DBR will be subjected to multiple reflections (transmissions) as it propagates along the structure, giving rise to an interference process which will be globally constructive or destructive depending on the radiation wavelength and incidence angle. One can show that, for a given wavelength λ_{Bragg}, the periodic structure will present an enhanced reflectivity for normal incidence when the optical thickness $(n_i \cdot L)$ of each layer is equal to $\lambda_{Bragg}/4$.

In the case of a large number of layers N and normal incidence the reflectivity at the wavelength $\lambda_{Bragg} = \frac{2\pi c}{\omega_{Bragg}}$ is given by:

$$R(\lambda_{Bragg}) \approx 1 - 4 \frac{n_{out}}{n_{sub}} \left(\frac{n_1}{n_2}\right)^{2N} \tag{57}$$

with n_{out} the optical index of the external medium and n_{sub} the one of the substrate on which the structure is grown. The reflectivity increases with the number of pairs and with the index contrast between layers. Reflectivity curves of Bragg mirrors with $7, 15$ and 25 pairs, as a function of the normalized frequency ω/ω_{Bragg} are shown in fig. 11(b). The region of high reflectivity, centered symmetrically around λ_{Bragg}, is called the stop band. For the DBRs typically used in our experiments, made of alternating layers of $GaAs/AlAs$, with indices of refraction $n_{GaAs} = 3.54$ and $n_{AlAs} = 2.96$, 25 pairs are enough to reach values of reflectivity very close to one ($R \approx 0.9997$).

3.3.2.4 *Bragg mirror microcavity*

We can now create a cavity consisting of two DBRs with a layer in between (a spacer) of width $L_{cav} = S\lambda_c/2$ and index n_{cav}, fig. 11(c). Such a cavity will have a sharp resonance in the middle of the wide stop band, at wavelength λ_c. The corresponding reflectivity spectrum showing a narrow dip corresponding to this mode is shown in fig. 11(d)
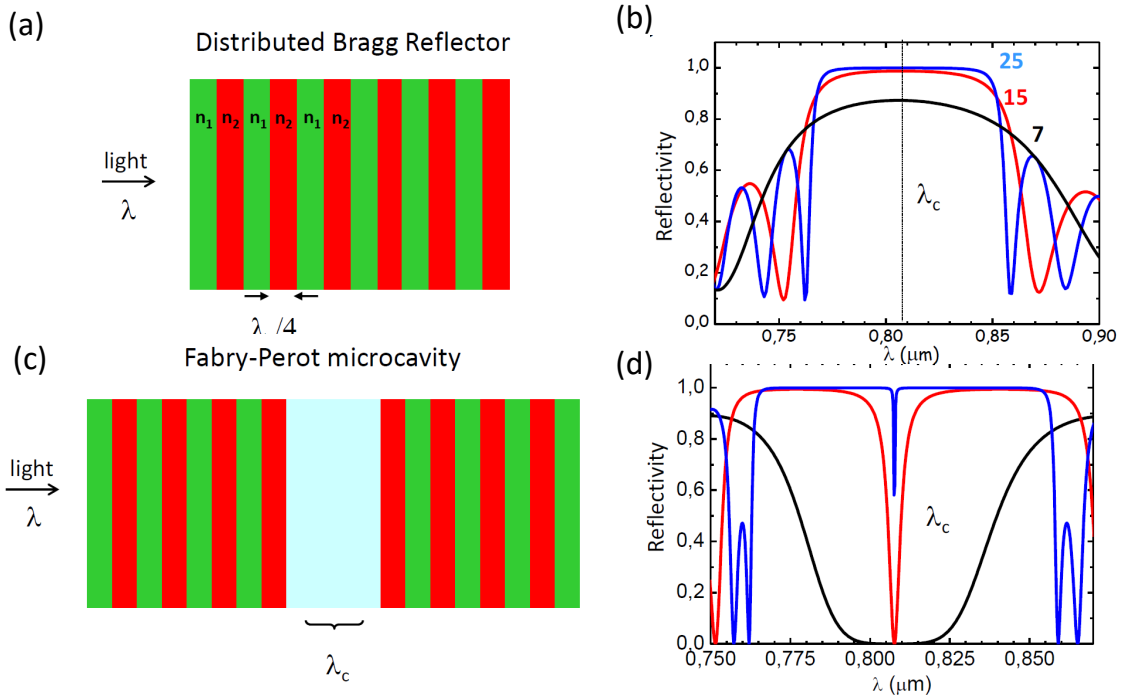
Figure 11: **Bragg reflector cavity** (a) Schematic representation of a Distributed Bragg Reflector (DBR). (b) Typical DBR reflectivity spectrum for three different numbers of (n1, n2) pairs. (c) Schematic representation of a Fabry-Perot microcavity made by coupling two DBRs. (d) Reflectivity spectrum of the microcavity, displaying a dip at the center of the stop-band, corresponding to the optical mode resonant with the cavity. Taken from [111].

As the cavity has a separation in energy between the modes inversely proportional to L_{cav}, for cavity widths on the order of λ_c the structure operates as a single mode cavity for longitudinal modes.

The high reflectivity of DBRs at the stop-band makes semiconductor microcavities with Q factors up to 100000, corresponding to photonic lifetimes of up to 40ps. The corresponding effective mass for photons in such structures is of the order of $m_{ph} \approx 10^{-5} m_e$ where m_e is the electron mass.

DBRs can be used to efficiently confine photons assuring both increased photonic lifetime and single mode operation. Now we are interested in understanding how light in microcavities can be strongly coupled to matter to create quasi particles called polaritons. In particular, we will consider the case in which we insert a quantum well inside the cavity such that resonant the mode couples to excitonic two-level transitions of the quantum well.

3.3.3   *Quantum well excitons*

3.3.3.1   *Excitons in semiconductors*

In the short introduction to band theory of solids presented in chapter 2, we discussed that the ground state of any semiconductor is characterized by a completely occupied valence band and empty conduction band, separated by the gap.

The fundamental excitation in a semiconductor consists in the promotion of an electron from the top of the valence band to the bottom of the conduction band. In this way all the valence band states except one remain occupied. It is convenient, to picture this empty state as a positive charge in an empty valence band. This is the definition of a hole and its description as a positive charge enables us to consider the valence band masses as positive in all practical calculations, despite the fact that from the single electron picture they have negative curvature.

As the excited electron and all the remaining charges in the valence band interact, the energy of the excited state is lowered. We can describe it in a picture in which the electron and the hole undergo Coulomb attraction and a bound state called exciton is created in the gap. The following Hamiltonian can describe the system:

$$H\Psi(r_e, r_h) = \left[\frac{(p_e)^2}{2m_e} + \frac{(p_h)^2}{2m_h} + E_g - \frac{e^2}{\epsilon|r_e - r_h|} \right] \Psi(r_e, r_h) = E\Psi(r_e, r_h), \qquad (58)$$

where r_e, r_h, p_e, p_h and m_e, m_h are respectively position, momentum vector, and effective mass of an electron and a hole in the crystal. The value of the dielectric constant ϵ accounts for the screening effect of the Coulomb interaction due to all the other electrons in the valence band.

Excitons are somehow analogues to hydrogen atoms, holes playing the role of protons. The Hamiltonians of both systems have the same expression and the structure of the energy levels and eigenmodes is the same, resulting in exciton levels $1s, 2s, 2p$ and so on. The energy of the excitonic ground state can be written as:

$$E_{exc} = E_{gap} - E_b + \frac{\hbar^2 K^2}{2m}, \qquad (59)$$

where E_b is the electron-hole binding energy, $4.2 meV$ in bulk $GaAs$, $\hbar K$ is the exciton momentum, defined as the momentum of the center of mass of the electron-hole pair, and m is the exciton effective mass, given by the sum of the effective masses of electron and hole, which gives to the exciton its own parabolic band.

The lowest energy exciton wavefunction is the $n = 1$ (1s) state that reads:

$$\Phi(r)\frac{1}{\sqrt{\pi a_B}}e^{-r/a_B}, \tag{60}$$

with $a_B = \frac{\hbar^2 \epsilon}{\mu e^2}$ the exciton Bor radius, that characterizes the spatial extension of the exciton.

It is also worth mentioning that the exciton, made of two fermionic quasi-particles, behaves as a boson for low particle density. Electronic spin, with spin projections on the z quantization axis $J(e)_z = \pm 1/2$ combines with hole spin $J(h) = \pm 3/2$, to give two possible values for the excitonic spin $J(exc) = 1$ and $J(exc) = 2$. Note that the fundamental state of the crystal has $J = 0$. This picture is valid for particle densities below the so called Mott density limit, corresponding to the disappearance of a well defined excitonic bound state. For GaAs QWs this values corresponds approximately to a density of 10^{11} excitons per cm^2 [112, 113]

3.3.3.2   *Confined excitons in quantum wells*

Both energy and spatial extension of an exciton are changed if it is confined. In general, excitons can be confined along one (quantum well), two (quantum wire) or three (quantum dot) dimensions. In this work we will consider the case of quantum wells, a semiconductor quantum heterostructure where excitons result to be confined in the growth direction z, while they are free to move in the (x, y) 2D plane, perpendicular to z.

A quantum well can be fabricated by growing a sequence of three thin 2D layers of semiconductors, where a material B, with a typical thickness of $\approx 10 nm$ is sandwiched between two layers of a material A characterized by a higher energy gap. Figure 12 shows the extrema of the valence and conduction bands as a function of the growth direction z, displaying an abrupt discontinuity, when crossing the A-B interfaces. This heterostructure creates a quantum well in which excitons are confined. The thickness of the B layer is chosen on the order of the size of the exciton.

As a consequence of confinement the overlap between electron and hole wavefunctions is increased and the exciton binding energy is larger. In the in-plane direction, the dispersion curve for quantum well excitons can be written:

$$E_{K_{||}} = E_{exc} + \frac{\hbar^2 K_{||}^2}{2m_{exc}}, \tag{61}$$

with $E_{exc} = E_{gap}^B + E_{conf}^e + E_{conf}^h - E_b$, were E_{conf}^e and E_{conf}^h are the confining energies of the first electron and hole levels, fig. 12. $K_{||}$ is the in-plane momentum and m_{exc} is the effective in-plane mass of the exciton, given by the sum of the free electron and hole effective in-plane masses. In GaAs based quantum wells, the exciton effective mass is of the order of $m_{exc} \approx 10^{-1} m_e$, where m_e is the electron mass. Also, the value of the Bohr
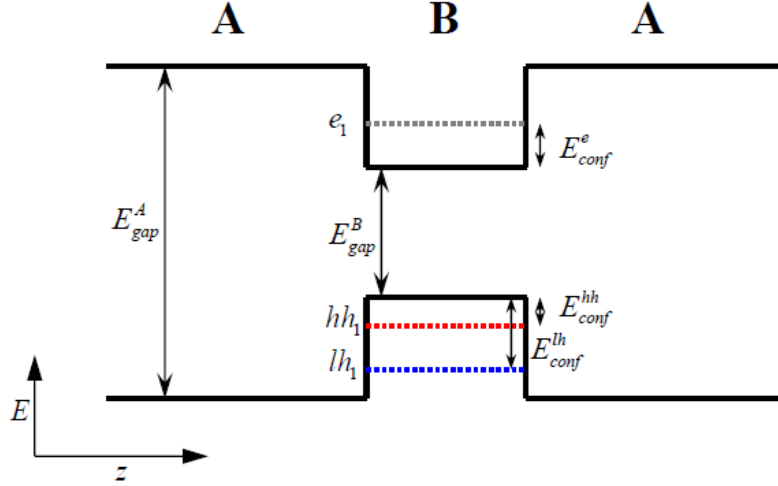
Figure 12: Semiconductor quantum well. (a) Extrema of the valence and conduction bands as a function of the growth direction z. The first confined energy levels for electrons and holes (light and heavy) are represented by dotted lines. (b) In-plane conduction and valence bands dispersions for a *GaAs/AlGaAs* quantum well, close to the fundamental gap. Taken from [111]

radius is decreased with respect to the bulk case, depending on the width of the QW. These properties are important when coupling an exciton to the cavity mode.

Excitonic transition can be induced optically or electrically. In the context of polaritons, we are interested particularly in optically induced transitions. In particular, a photon whose energy exceeds the bandgap energy $\hbar\omega > E_{gap}^B$, can be absorbed inducing a transition from the fundamental state of the crystal to a state where one exciton is created.

In dipolar approximation, the Hamiltonian of the exciton photon coupling becomes:

$$H \cong -\frac{e}{m_0}\mathbf{A}\cdot\mathbf{p}, \tag{62}$$

with $\mathbf{A}$ the vector potential, $\mathbf{p}$ the momentum operator, $-e$ the electron charge and m_0 electron mass. The absorption of the photon is proportional to the matrix element $\langle\mathbf{K}|\mathbf{A}\cdot\mathbf{p}|0\rangle$ where $|0\rangle$ is the ground state and $\langle\mathbf{K}|$ the excitonic state.

Some selection rules need to be satisfied in order for the optical transition to take place. Fist of all energy must be conserved in the transition. The energy of a photon is given by $\frac{\hbar ck}{n}$. This means that excitons with $K_\parallel > k_{rad}$, where k_{rad} satisfies $\frac{\hbar ck_{rad}}{n} = E_X(K_\parallel = 0 + \frac{2\bar{K}^2}{2M})$, are states not coupled to light.

Additionally, in quantum wells, the selection rule regarding momentum conservation is modified with respect to bulk semiconductors: conservation of the in-plane momentum $\hbar\mathbf{K}_\parallel$ is required, instead of conservation of the total momentum. As a consequence, an exciton is coupled to a continuum of modes of the electromagnetic field, since, once energy, spin and in-plane momentum are conserved, light with any k_z component can excite the system.

Conservation of the total angular momentum is also required. In particular, since photons have total intrinsic angular momentum equal to one, it follows that just excitons with

$J = 1$ can be optically excited. Excitons with $J = 2$ can not interact with light and they are therefore called dark excitons.

3.3.4 *Strong light-matter coupling*

We have presented the two building blocks of a microcavity structure. Both the QWs and the cavity play an analogous role respectively on exciton and photon by breaking the translational symmetry on the z axis and imposing a confinement that discretize the excitonic and photonic levels. We now discuss the case in which the cavity mode is in spectral resonance with the excitonic 1s transition. Once excited exciton can relax via the emission of a photon. This emission can take place in two regimes [114, 115]:

- WEAK COUPLING   The photon emitted has negligible probability of being reabsorbed by the same medium (an irreversible process). The regime is also called perturbative, because the electromagnetic field appears in the Hamiltonian as a perturbative term $\omega \sim \mathbf{A} \cdot \mathbf{p}$ and the first order development gives the spontaneous emission rate (Fermi golden rule):

$$\Gamma = \frac{2\pi}{\hbar} |\langle \mathbf{K} | \omega | 0 \rangle|^2 \rho(E_{ph}) \tag{63}$$

  where E_{ph} is the photon density of states and $\langle \Psi_0 |$ and $| \Psi_1 \rangle$ are the ground and excited state respectively. In this regime the excitation will be dissipated and the population of excited excitons will decay exponentially.

  By acting on the electromagnetic environment, and so on the electromagnetic density of states, one can modify the transition probability given by the Fermi Golden rule: this is the Purcell effect [11] , that consists in an increase or a decrease of the emission probability [116, 117].

- STRONG COUPLING   It is also called non perturbative regime, and corresponds to the case in which the photon emitted can be recaptured and re-excite the medium. In the spectral domain, this oscillations, called Rabi oscillations are revealed by an energy splitting, called Rabi splitting or normal mode splitting, and by the anti-crossing of the energy levels. Excitons and photons are no more the eigenstates of the microcavity but they are replaced by half light half-matter quasi-particles, microcavity polaritons.

  The first theoretical discussion of the strong coupling regime in solid state system was made by Hopfield in 1958 [118], while it was also largely explored in the field of atoms in a cavity, with the theoretical work of Jaymes and Cummings [119].

In our case, the strong coupling regime is obtained by embedding one or more semiconductor quantum wells in a microcavity, with the optical mode quasi-resonant with the excitonic transition. In particular, the quantum wells are placed at the anti-nodes of the electromagnetic field, in order to maximize the coupling, as shown schematically in fig. 13. When we discussed the quantum well excitons, we saw that for a quantum well in the free space, one excitonic transition is coupled to a continuum of modes of the electromagnetic
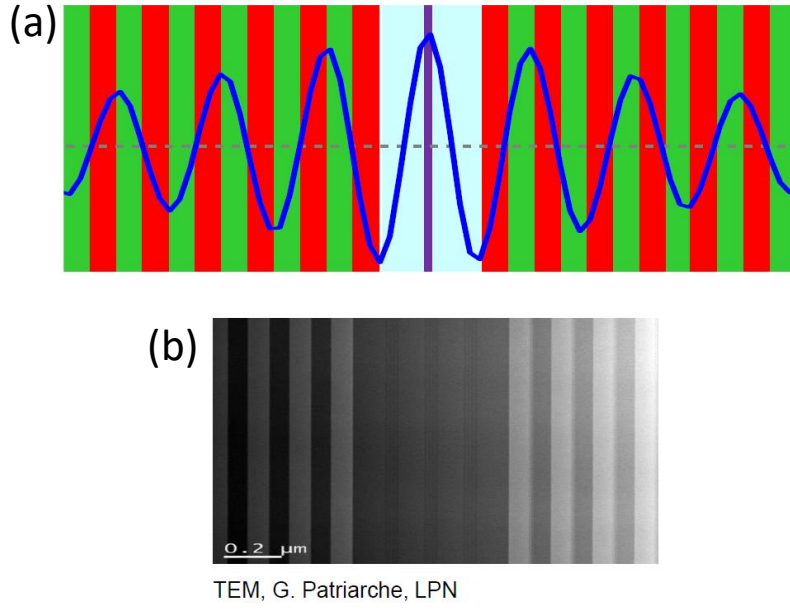
Figure 13: (a) Schematic representation of a semiconductor microcavity with one embedded quantum well. Its position corresponds to an anti-node of the electromagnetic field inside the cavity. (b) TEM image taken from a real microcavity, with three sets of four quantum wells placed inside the cavity. Taken from [111]

field, each mode having a different k_z component. Since the microcavity imposes the quantization of motion in the growth direction z, it selects one specific value of k_z, i.e. just one optical mode. In that way the coupling between two discrete modes is realized. Of course this would be strictly true, only if both exciton and photon had infinite lifetime. The finite lifetime introduces a broadening of the linewidths, meaning that we do not have exactly two single modes. The systems can be viewed in the picture of two coupled Lorentz oscillators which are damped. The strong coupling regime is achieved if damping is smaller then the coupling between the modes.

3.3.4.1 *Hopfield coefficients*

For the moment, we suppose the coupling of two modes with infinite lifetimes, i.e. delta functions in energy. We also suppose that we excite just few particles in the system. This allows neglecting interactions between excitons, i.e. nonlinear terms in the Hamiltonian. We also consider excitons in pure states of spin (normal incidence, for circularly polarized light), which allows to use a scalar theory. Under these approximations, the system is equivalent to two coupled harmonic oscillators, one oscillator being the excitonic transition with wave vector $\mathbf{K}_{||}$, the other a quasi-resonant optical mode with $\mathbf{k}_{||} = K_{||}$. This description will allow us to understand more precisely how polaritonic states are formed and what is their energy. From now on, we will omit the index $||$ to simplify notations, $\mathbf{k} \equiv \mathbf{k}_{||}$. We

write the Hamiltonian using a quantum approach, even if a mean-field classical approach would give equivalent results:

$$H_{\mathbf{k}} = E_{exc}(k)b_{\mathbf{k}}^{\dagger}b_{\mathbf{k}} + E_{cav}(k)a_{\mathbf{k}}^{\dagger}a_{\mathbf{k}} + \frac{\Omega_R}{2}(a_{\mathbf{k}}^{\dagger}b_{\mathbf{k}} + b_{\mathbf{k}}^{\dagger}a_{\mathbf{k}}), \tag{64}$$

where $b_{\mathbf{k}}^{\dagger}, b_{\mathbf{k}}$ and $a_{\mathbf{k}}^{\dagger}, a_{\mathbf{k}}$ are respectively the creation and annihilation operators for an exciton and a photon with wave vector $\mathbf{k}$ in the 2D plane transversal to the growth axis, which satisfy the bosonic commutation relations. $E_{exc}(k)$ and $E_{cav}(k)$ correspond to the energies of excitons and photons, given by the dispersion relations in eq. 61 and eq. 56. The last term in eq. 64 corresponds to the coupling term. In particular, it contains one term corresponding to the simultaneous creation of a photon and annihilation of an exciton (emission term) and a term corresponding to the simultaneous creation of an exciton and annihilation of a photon (absorption term). The coefficient $\Omega_R/2$ is the coupling energy (Ω_R is the Rabi splitting) and it has the expression [120]:

$$\Omega_R = 2g = 2\sqrt{\frac{2c\Gamma_0}{n_{cav}L_{eff}}} \propto \sqrt{\frac{f_{osc}}{L_{eff}}}, \tag{65}$$

where Γ_0 is the radiative lifetime of the excitons at $k = 0$ in the absence of the cavity. L_{eff} is the effective length in which the optical mode is confined, $L_{eff} = L_{cav} + 2L_{Bragg}$, where L_{Bragg} is the length over which the electromagnetic field decays exponentially inside each Bragg mirror (typically $L_{Bragg} \approx \lambda_c$). f_{osc} is the oscillator strength of the excitonic transition, a quantity characterizing the strength of its dipolar coupling to the electromagnetic field. Therefore, the coupling constant depends on one hand on the oscillator strength of the exciton, which is increased in a quantum well, due to the enhanced overlap of the electron and hole wavefunctions, on the other hand on the volume over which the electromagnetic field is confined. This volume is particularly small in semiconductor microcavities. Both contribute to achieve high values of Ω_R typically of the order of $3.5meV$ for a single QW in a $GaAs$ based samples, and even higher for $CdTe$ and GaN based microcavities.

The Hamiltonian 64 is diagonalized in the following way:

$$H_{\mathbf{k}} = E_{UP}(k)p_{\mathbf{k}}^{(UP)\dagger}p^{(UP)} + E_{LP}p_{\mathbf{k}}^{(LP)\dagger}p^{(LP)\mathbf{k}}, \tag{66}$$

where operators $p_{\mathbf{k}}$ can be found by applying to the photon and exciton operators $a_{\mathbf{k}}$ and $b_{\mathbf{k}}$, the unitary transformation

$$\begin{pmatrix} p_{\mathbf{k}}^{(LP)} \\ p_{\mathbf{k}}^{(UP)} \end{pmatrix} = \begin{pmatrix} -C_k & X_k \\ X_k & C_k \end{pmatrix} \begin{pmatrix} a_{\mathbf{k}} \\ b_{\mathbf{k}} \end{pmatrix} \tag{67}$$

C_k and X_k are Hopfield coefficients defined as:

$$X_k^2 = \frac{1}{2}\left(1 + \frac{\delta_k}{\sqrt{4\hbar^2\Omega_R^2 + \delta_k^2}}\right) \tag{68}$$

$$C_k^2 = \frac{1}{2}\left(1 - \frac{\delta_k}{\sqrt{4\hbar^2\Omega_R^2 + \delta_k^2}}\right), \tag{69}$$

where δ_k is the cavity-exciton detuning, given by $\delta_k = E_{cav}(k) - E_{exc}(k)$. The Hopfield coefficients satisfy the relation $X_k^2 + C_k^2 = 1$.

The new eigenstates of the system are called exciton-polaritons. Two branches are obtained, that of the upper polariton (UP) and the lower polariton (LP) and, as explicitly written in eq. 67. They are mixed particles composed by a photonic fraction C_k^2 and an excitonic fraction X_k^2. At zero detuning ($\delta_k = 0$) upper and lower polaritons are both composed by an equal amount of photonic and excitonic components ($X_k^2 = C_k^2 = 1/2$).

The energies of the lower and upper polaritons are given by:

$$E_{UP,LP}(k) = \frac{1}{2}(E_{exc}(k) + E_{cav}(k) \pm \sqrt{\delta_k^2 + \Omega_R^2}), \tag{70}$$

Dispersion curves corresponding to three different values of the cavity-exciton detuning $\delta \equiv \delta_{k=0}$, are shown in fig. 14. At zero detuning (fig. 14 (c)-(d)) and at $k = 0$, where the excitonic transition and the optical mode have the same energy, the coupling lifts the degeneracy of modes, and opens an energy gap between the polaritonic states equal to the Rabi splitting Ω_R.

Close to $k = 0$, for zero or negative detuning the lower polariton dispersion (Fig. 14(c)) is a parabola. Polaritons can be therefore approximated by free particles, moving in the 2D plane of the cavity, characterized by a small effective mass that follows the relation :

$$\frac{1}{m_{pol}} = \frac{X_k}{m_X^*} + \frac{C_k}{m_{ph}}, \tag{71}$$

with m_X^2 the exciton in-plane effective mass and $m_{ph} \approx 10^{-5} m_{el}$ cavity photon mass. Since $m_X^2 >> m_{ph}$, the polariton mass can be approximated by $m_{ph} \approx m_{ph}/C_k$, or for $k = 0$ $m_{ph} \approx m_{ph}/2$.

Figures 14(a)-(b) show the dispersion curves and the corresponding Hopfield coefficients in the case of positive detuning ($\delta_k = -\Omega_R$), while figs. 14(e)-(f) show the case of negative detuning ($\delta_k = -\Omega_R$). We observe that in the case of positive detuning, the upper polariton branch has a higher photonic weight, while the lower polariton branch is mostly excitonic. In the case of negative detuning, the situation is inverted. We also note that, as the detuning between the excitonic transition and the optical mode is increased, the effect of the coupling becomes less and less important, up to a point in which the eigenmodes of the system are the bare cavity and exciton modes.

3.3.4.2 *Polariton lifetime*

Up to now we have considered exciton and photons to have an infinite lifetime. For finite lifetimes, photons and excitons are no more single modes, but they are characterized by a finite homogeneous linewidth in the spectral domain. The comparison of this homogeneous linewidth with the magnitude of the exciton-photon coupling tells us if the system can be with a good approximation described by the two-mode description, i.e. if it is in the strong coupling regime. In particular we can describe the finite lifetime by introducing the complex energies, $E_{cav} - i\gamma_{cav}$ and $E_{exc} - i\gamma_{exc}$. If we insert these expressions into the ones describing the energy of upper and lower polaritons, eq. 70, we will see that two separate energies E_{UP} and E_{LP} exist at zero detuning if $\Omega_R > |\gamma_{cav}(k) - \gamma_{exc}(k)|$. In that case the system is in the strong coupling regime. If Ω_R is smaller than $|\gamma_{cav}(k) - \gamma_{exc}(k)|$, the two

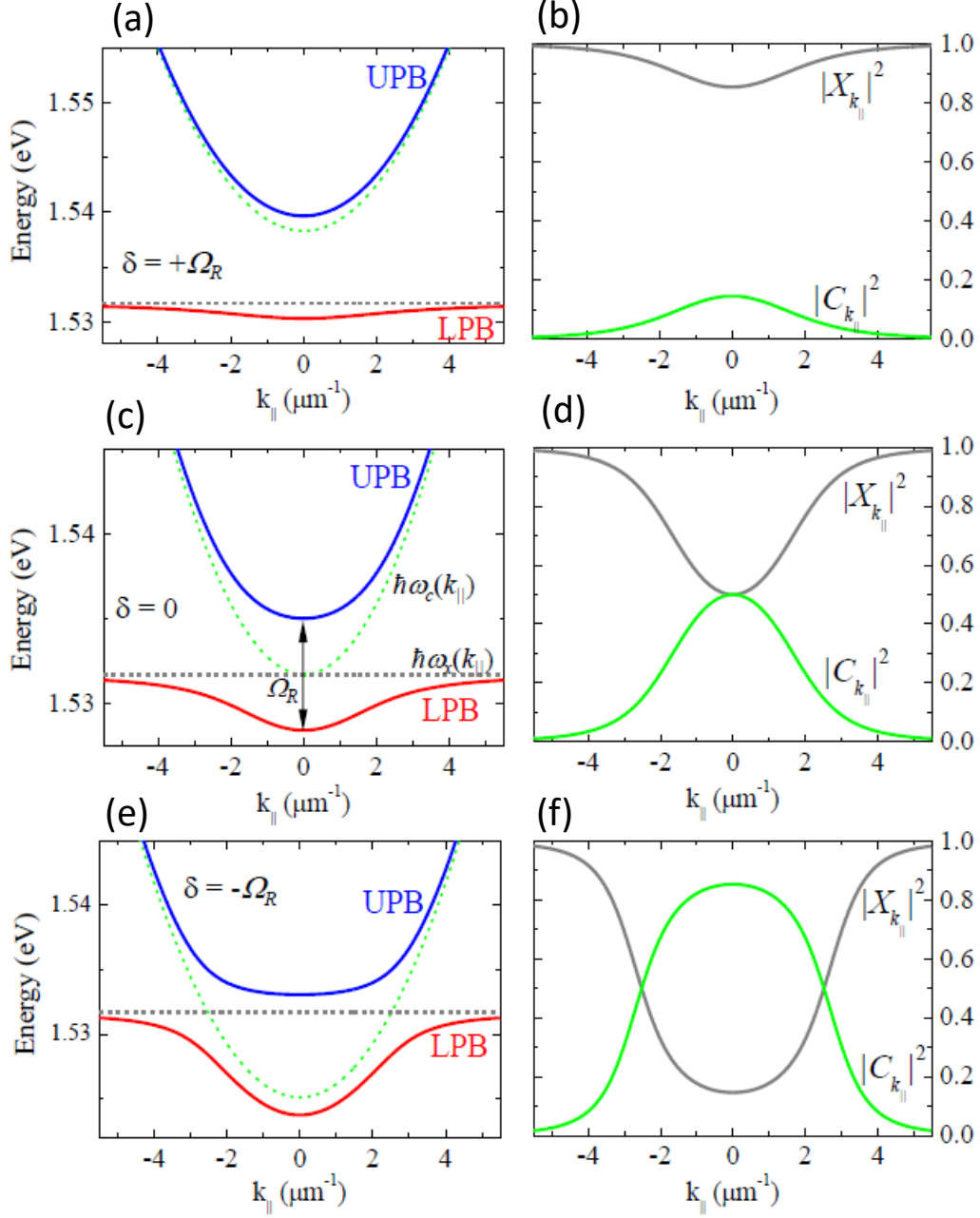Figure 14: Left panels: calculated bare exciton and cavity mode dispersions (dashed lines) as well as polariton dispersions (solid lines) for different cavity-exciton detuning δ in a microcavity with a Rabi splitting $\Omega_R = 6.6 meV$. Right panels: corresponding Hopfield coefficients obtained from Eqs. 68 and 69 Detuning: (a)-(b) $+\Omega_R$, (c)-(d) zero, (e)-(f) $-\Omega_R$. Taken from [111].

energies have the same real part and the degeneracy between photon and exciton is not lifted. In this case the system is in the weak coupling regime.

The imaginary part of complex energies gives the homogeneous linewidths of the upper and lower polaritonic modes, which can be related to the bare photon and exciton homogeneous linewidths through the relations:

$$\gamma_{(LP)}(k) = X_k^2 \gamma_{exc} + C_k^2 \gamma_{cav} \tag{72}$$

$$\gamma_{(UP)}(k) = C_k^2 \gamma_{exc} + X_k^2 \gamma_{cav} \tag{73}$$

Polaritons are characterized by quite short lifetimes, of the order of some tens of ps.

The short polariton lifetime is responsible for some features characterizing specifically polaritonic systems. Most importantly for this work, it defines polaritons as an intrinsically out of-equilibrium system. Upon optical excitation the system is characterized by a continuous decay of the population corresponding to photons leaking out of the cavity fig. 15(b). This property, on one hand is an obstacle for reaching of the thermodynamical equilibrium. On the other hand, it represents a great advantage, since it allows a direct way of detection.

Indeed, when photons are emitted through Bragg mirrors both energy and in-plane momenta are conserved, fig. 15(a), and as consequence they are in a one-to-one correspondence with polariton states inside the cavity. The properties of polaritons can thus be fully reconstructed by analyzing the emitted photons. The form of the polariton wavefunction can be obtained by spatially resolving emission from the cavity. Measurements resolved in angle reveal the in-plane momenta of the emitted photons. Information on energy can be obtained by spectrally resolving the emission.

Depending on the excitation conditions two main experimental schemes for studying polaritonic states can be distinguished.

3.3.5   *Resonant and nonresonant excitation schemes*

- RESONANT EXCITATION   In this experimental scheme the sample is pumped with a laser whose frequency is tuned to match the energy of a polariton state. In-plane component of the wavevector of exciting photons from the laser can also be adjusted to match the in-plane wave vector of polaritons, and make resonant injection efficient by well defining the angle of incidence. This experiment is preformed in transmission geometry in order to avoid strong laser reflection. The light coupled to the desired polariton mode is transmitted through the sample (the cavity and the substrate) and finally collected and analyzed. The transmission trough the $GaAs$ substrate is assured by red-shifting the polariton energy, which is achieved by employing $InGaAs$ instead of $GaAs$ quantum wells. This experimental scheme is very convenient for studying propagation of polaritons (see section 3.5.3) as well as interaction between them [121].

- NON RESONANT EXCITATION Another scheme is achieved via non-resonant excitation. In this case the energy of the excitation laser is set to be $\approx 100 meV$ above the polariton bands, typically in the first reflectivity dip above the stop band. Upon excitation, electron-hole pairs in quantum wells are created. Then, they incoherently relax via longitudinal phonons and create an exciton reservoir, see fig. 15(b). From the exciton reservoir particles further relax and occupy the ensemble of polariton states below the energy of the exciton.
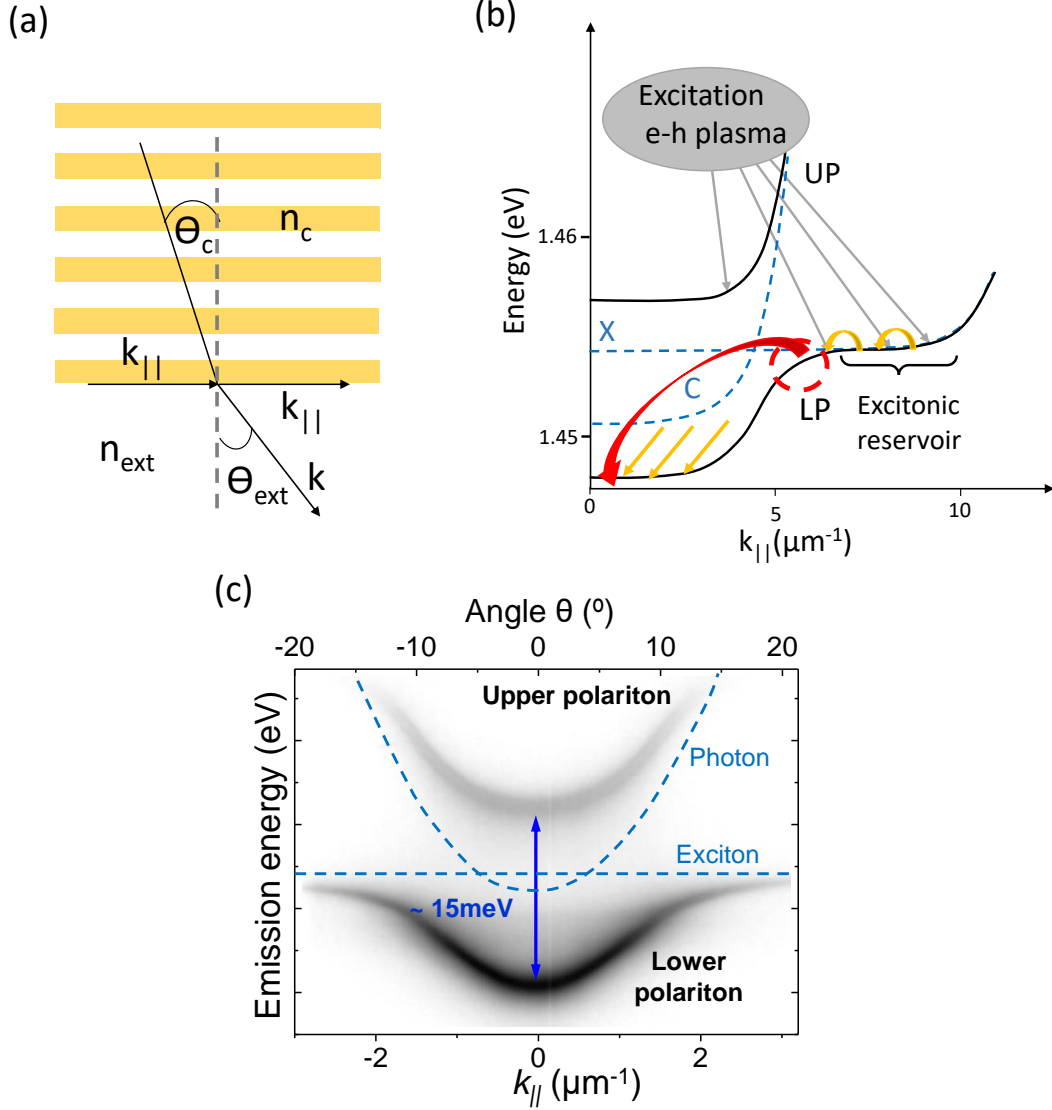
Figure 15: (a) Scheme of the photon emission outside the cavity. In plane momentum is conserved upon the emission. (b) Scheme of non-resonant excitation of microcavity. For excitation power below the threshold all bands all populated. Above threshold stimulated emission takes place at $k|| = 0$. (c) Polariton dispersion obtained by non-resonant excitation of microcavity. At $k_{||} = 0$ anti-crossing between upper and lower polariton branch is observed.

Non-resonant excitation scheme is very advantageous as it allows to simultaneously obtain information on all polariton states. Indeed, using a system of lenses and a monochromator coupled to a CCD camera, emission from the cavity can be resolved in space, momentum and energy. Details on experimental setup are given in section 3.3.6.

Figure 15(c) shows emission from a planar microcavity in strong coupling regime excited non-resonantly, resolved in energy and in angle. We can observe the polariton dispersion consisting of upper and lower polariton branches with characteristic anti-crossing at $k = 0$.

Because of its advantages this experimental scheme will be used throughout this thesis to reveal states of graphene simulator.

3.3.6 *Experimental setup*

We briefly present here the main characteristics of the micro-photoluminescence setup used in the present work. A scheme of such setup is reported on fig. 16(a).

All the experiments are performed at a temperature of $10K$. The sample is therefore pasted on the cold finger of a ST-500 Janis Cryostat mounted on a translational stage. The thermal conduction is assured by the use of a vacuum grease (Apiezon N Grease). A constant flow of Liquid Helium is set in order to maintain the cold

finger at a temperature $T = 10$ K. The chamber is maintained at a high vacuum, at a pressure between 10^{-5} Torr and 10^{-6} Torr thanks to the use of a Turbo Molecular Vacuum Pump.

We excite the sample non resonantly using a CW monomode Ti:Saphire laser at 740nm wavelength. The excitation beam is focused using a high numerical aperture objective (NA=0.65) with the focal length 4mm. It provides a small excitation spot with $FWHM = 2\mu m$. In order to enlarge the size of the excitation laser spot, a telescope consisting of two lenses is added to the path of the incidence beam when needed. The position of the spot on the sample is monitored by an additional CCD camera (CCD2) on figure 16. The same camera was also used to image the surface of the sample under white light illumination in order to choose the desired lattice.

We collect the emitted photons in reflection geometry with the same objective used for the excitation. Two variations of the setup are used in order to distinguish between the real and momentum space imaging.

Fig. 16(b) depicts the collection part of the setup and the optical path when the real space or near field is selected. The signal collected by the objective is imaged on the monochromator slit using the lens L3, whose focal length is adjusted to obtain the appropriate magnification (in this case $30cm$). (An additional telescope with magnification 1 (lenses L1 and L2) is constructed to reduce losses in the long optical path.) In this way a 2D image of the surface of the sample is created at the distance where the monochromator is placed (green arrows). 1D slice of the 2D image is selected by the slit (parallel to the $y-$direction), then dispersed and imaged by a Peltier cooled CCD. Using a motorized translational stage, the position of the imaging lens L3 is progressively shifted along the $x-$ direction such that the image of the whole sample can be reconstructed, revealing the wavefunction distribution at different energies.

A slightly different setup is used to perform the angle resolved measurements and image the momentum space, fig. 16(b). Actually, upon escaping the cavity, all photons emitted
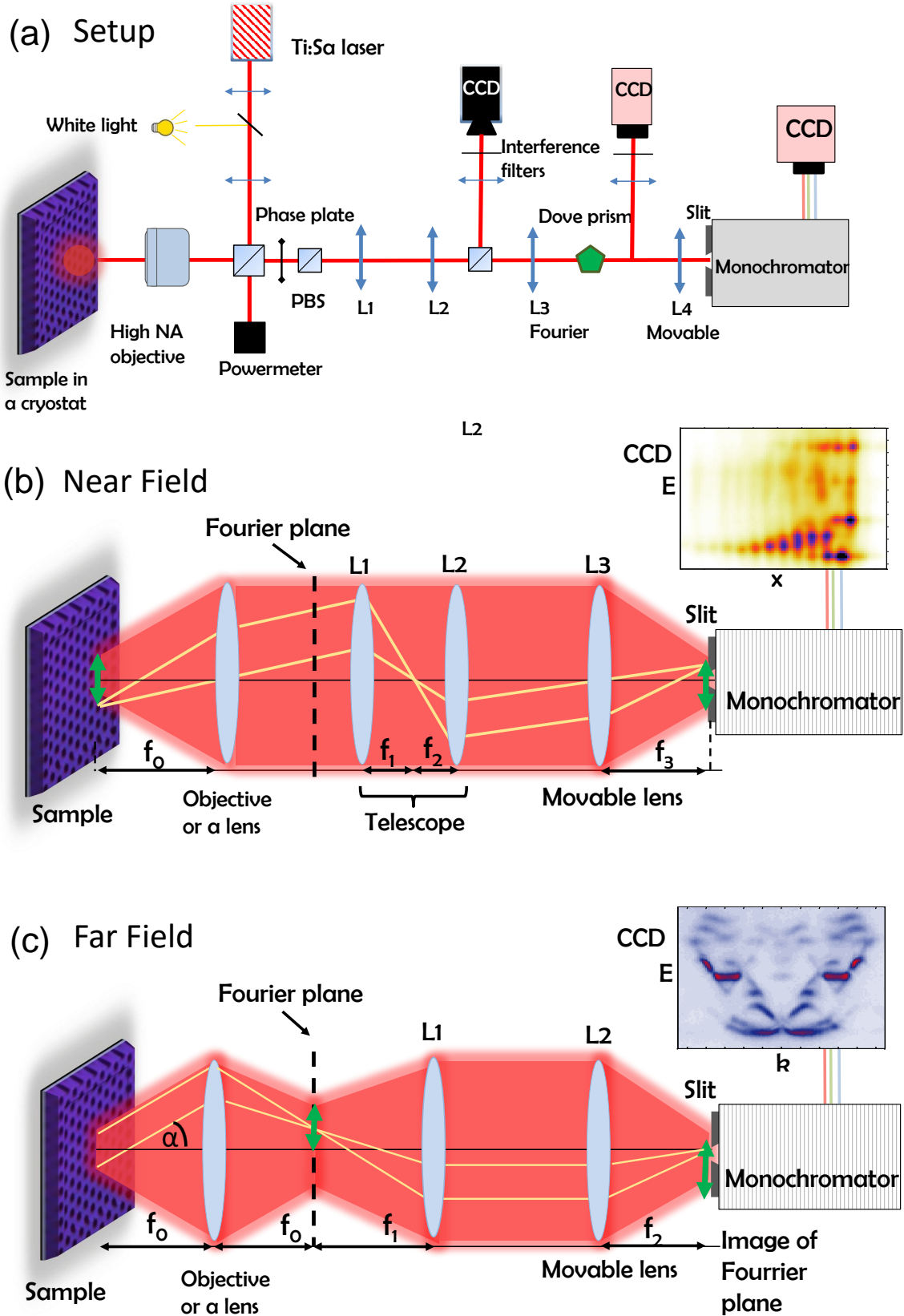
Figure 16: (a)The scheme of the experimental setup (b), (c) Scheme of the optical path for the imaging of real and Fourier space, respectively. Yellow lines represent the paths of two representative rays. Red lines represent visual eye guide. In the case of Fourier imaging all photons emitted at the certain angle are focused in one point in the Fourier plane, which is imaged onto spectrometer. Fourier plane is located at the focal distance in case the emitted light is collected with the lens. In case of a n objective f_1' differs from it focal f_1.

at a certain angle are focused by the collecting objective onto the same point of the so called, "Fourier" plane (black dotted line). As the angle of emission corresponds to the in- plane momentum of polaritons, Fourier plane represents a reconstruction of the 2D momentum space of a cavity (or later a 2D lattice) . By adding lens in the setup, a 2D image of the Fourier plane is projected at the entrance of the monochromator. To preform properly the angle resolved measurements, the lens has to be placed at the distance equal to its focal length from the Fourier plane. Once the full 2D image is projected onto the monochromator, any desired direction of momentum space can be aligned with the slit, by moving the lens L2 in the direction perpendicular to the slit, or by using a dove prism to rotate the image. The desired dispersion is then directly imaged on a CCD coupled to the monochromator. Finally, reconstruction of a 3D matrix whose axis are k_x, k_y and the emission energy can be performed. Each matrix element carries the information about the intensity of the measured signal $I(k_x, k_y, E)$, providing the full information about the dispersion.

We note that the polarization of light was filtered in using a pair of $\lambda/2$ waveplates and a polarizing beam splitter.

3.4 ENGINEERING OF POLARITON HAMILTONIANS

In the previous section we have introduced microcavity polaritons and we discussed some of the properties and advantages of the system. In this chapter we will see how we can impose additional lateral potential to polaritons quasi particles. This will allow to engineer a potential landscape in this system and design of lattices.

First, we will review some of the techniques reported in the literature, and then we will explain the procedure employed in C2N which allowed implementation on polariton honeycomb lattice.

Shaping of potential for polaritons can be achieved by introducing additional, lateral confinement. Two main approaches have been reported in the literature, one of them relies on acting on polariton excitonic component and the other on its photonic component. Different techniques have been developed in different groups following either approach offering various confinement strengths and trapping geometries, as reviewed in [122].

One of the techniques for creating polariton lattices has been developed in the group of P. Santos. It involves the use of the appropriate form of surface acoustic waves which create periodic strain fields, affecting both the photonic and the excitonic component [127, 128]. 1D and 2D lattices with modulation depth of few meV have been created using one or two trains of surface acoustic waves (SAW) which periodically modulate polariton energy, fig. 17(c,d). Polariton condensation in a dynamic acoustic lattice has for example been obtained in these lattices [124].

As for the techniques acting exclusively on the excitonic component they mostly rely on optical manipulation. To explain their underlying mechanism we remind that in the spot region, in the case of non resonant excitation, an excitonic reservoir is created. The repulsive interaction between polaritons and exciton of the reservoir results in a renormalization of the polariton dispersion with a local shift towards the blue. In this way local potential is formed. This effect has allowed to study important aspects of polariton physics [129, 23, 130] but the technique proved to be difficult to scale up and create ex-
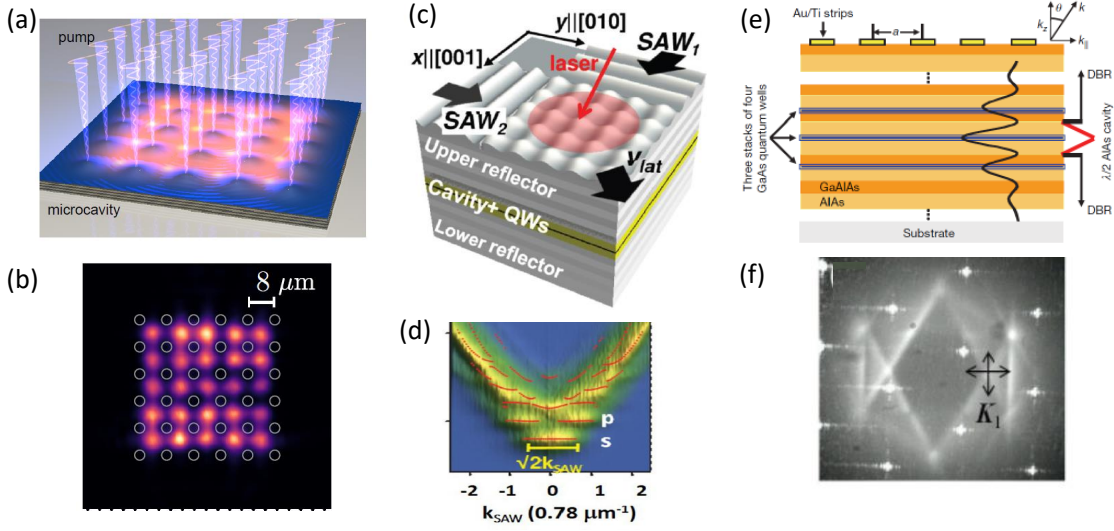
Figure 17: (a) Schematic of condensation in optical lattice potentials (b) Real space emission of synchronized (delocalized) condensate lattice obtained in that way. Both taken from [123] (c) Schematics of two propagating SAWs, forming a square lattice potential on a polariton sample. (d) Dispersion of the polariton gas below the condensation threshold under the 2D SAW potential. Taken from [124] (e) Cavity patterning by metalic layer deposition, [125] (f) Dirac cones in corresponding triangular lattice [126] .

tended 2D potentials. Recently, by spatial modulation of the pumping source, polariton condensates were imprinted into two-dimensional graph configuration [131]. In a similar way, weakly disordered lattices are realized, fig. 17(a) in which polariton condensates have been observed 17(b) [123].

3.4.0.1 *Photonic confining potentials*

Several procedures have been developed to create a potential acting on the polariton photonic component. The first was developed in the group of Y. Yamamoto in Stanford [125, 132]. By depositing a patterned thin metallic layer on top of the sample a local change in the dielectric constant of a cavity is introduced, shifting the polariton energy by about $200\mu eV$, fig. 17(e). While the weakness of the introduced potential remains a limiting factor in this system 2D periodic lattices such as a triagonal, [133] and a Kagome lattice [126] were obtained. The spontaneous build-up of coherence has been observed in different states, including states close to the Dirac point in triangular lattice, fig. 17(f), [133].

Another technique, developed in the group of B. Deveaud in Lausanne, consists in locally changing the thickness of the cavity layer during the growth process, prior to the growth of the upper mirror. 0D confining structures (mesas), have been realized 18(a), [134, 135]. Optical control of the quantized polaritonic modes in a mesa has been reported [136]. More recently square lattice, made by the similar technique was studied in [137], 18(b).

Etching of both upper and lower mirror was implemented in the group of M. Bayer in Dortmund and A. Forchel in Wurzburg for the cavities in the weak coupling regime [87]. For example, a chain of coupled micron sized cavities has been shown to display a characteristic band structure [138].

Recently, the groups of S. Höfling and D. N. Krizhanovski have fabricated lattices by etching the upper mirror of the cavity [32, 33]. Figure18(c) shows a 2D Lieb lattice obtained in this way and the corresponding spectrum in momentum space.
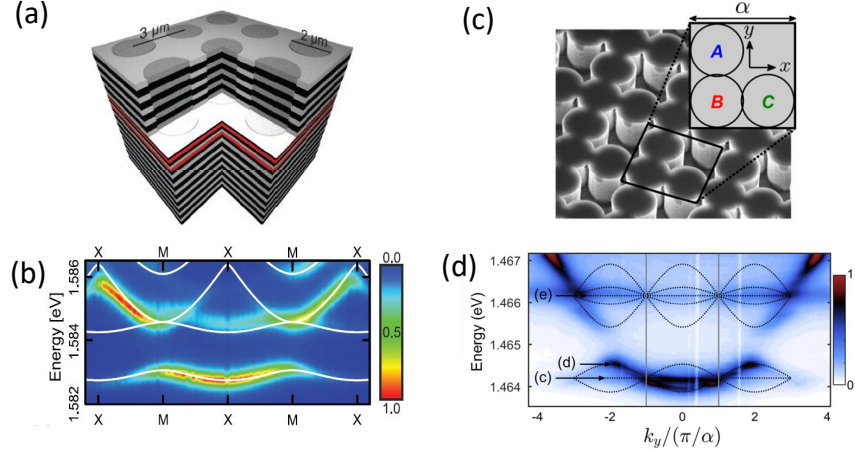
Figure 18: (a) Polariton lattice made by defining shallow mesas in the cavity. (b) Zoom onto the band gap region of such a square lattice [134, 137] (c) SEM image of a Lieb lattice made by etching the cavity upper mirror. (b) Lattice emission in energy-momentum space measured under low-power nonresonant excitation. [33]

3.4.0.2   *Etching technique at C2N*

A technique which allows creation of deep lateral confining potential in a microcavity was developed in C2N (former LPN). It is based on a post growth etching of a *GaAs* based microcavity.

First, the cavity is grown by molecular beam epitaxy. A photo resist layer is then spin coated on top of it. Using an electron beam, the pattern corresponding to our desired design is transfered on the resist before it was developed. The structure is finally realized by inductive coupled plasma etching (ICP). All the layers of the microcavity down to the substrate are etched in every area shined by the e-beam, thus imprinting the desired geometry into the cavity sample.

We would like to emphasize here that the sample fabrication was done by Aristide Lemaitre, Elisabeth Galopin and Carmen Gomez for what concerns the growth of the microcavities, and Luc le Gratiet, Abdelmounaim Harouri and Isabelle Sagnes performed the etching processes.

The technique we used allows to obtain structures with a strong lateral confinement, thanks to the effect of total internal reflection of light on the interface between regions with large refractive index difference, in this case the air and semiconductor. The method does not impose any restrictions on the shape of the structures, except that their lateral dimension should not be too small (typically lateral dimension should be larger than $1.5\mu m$) to avoid non-radiative recombinations on the side walls of the etched structures, which would strongly degrade the optical properties of the system. 0D, 1D and 2D structures can be realized with a high degree of flexibility in the geometry shape. In fig. 19(a) we see a scanning electron microscope (SEM) image of a sample created in C2N facilities, in

which a series of 1D wires of different widths and 0D pillars with various diameters are realized.
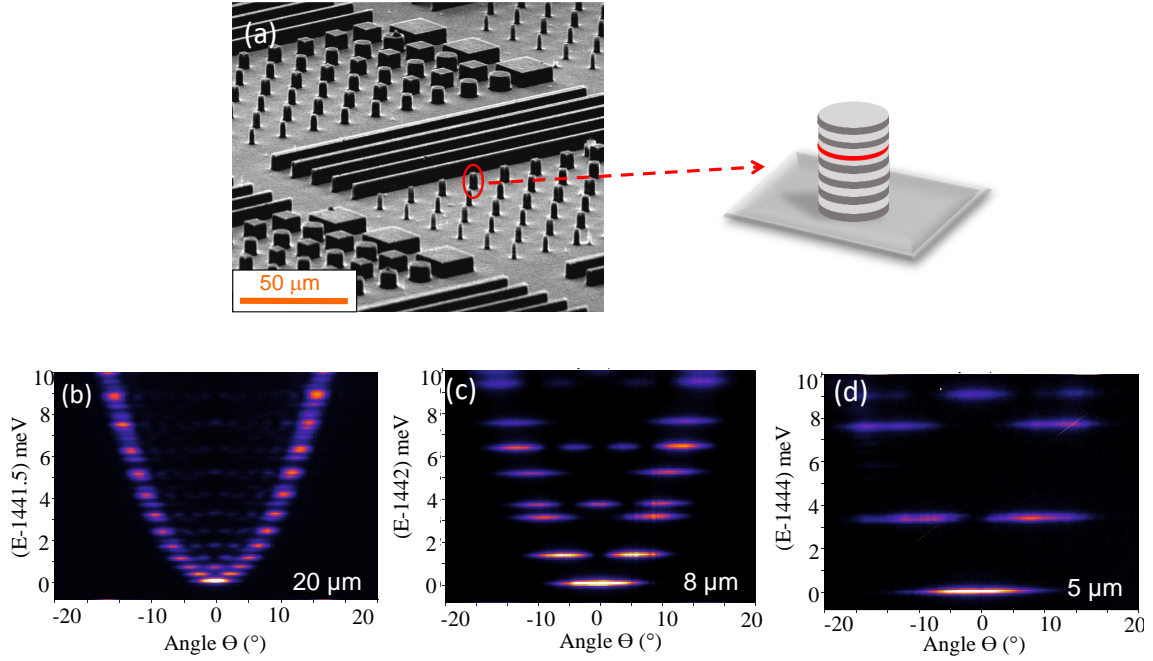
Figure 19: (a) SEM image of an etched sample. 1D wires of various widths as well as rectangular and circular micropillars are present (b-d) Energy spectrum of cylindrical micropillars, for three different pillar diameters:20 ÎŒm, 8 ÎŒm and 5 ÎŒm, respectively.

3.4.0.3 *Micropillars*

Circular micropillars obtained by deep etching represent the building block for creation of polariton lattices with desired geometry. In this quasi-0D structure with a typical lateral size of few μm a strong 3D confinement of the optical mode is obtained: in the longitudinal direction it is obtained thanks to the Bragg mirrors, in the lateral directions thanks to the large difference in refractive index between semiconductor and air.

The 3D confinement of the optical mode results in a full discretization of the polaritonic energy spectrum, since both the in-plane wave vector components k_x and k_y are quantized. Figure 19(b-d) shows the energy spectrum for three different pillar sizes. The energy levels are more separated in energy as we consider pillar of smaller lateral size.

Such quantization effect can be simply understood in terms of a massive particle moving in the infinite cilindrical potential well in 2D of the form:

$$V(r) = \begin{cases} 0 & \text{for} \quad 0 \leq r \leq R \\ \infty & \text{otherwise} \end{cases} \tag{74}$$

Solution of Shrödinger equation with the above potential gives the allowed energy levels:

$$E_{n,l} = z_{n,l}^2 \frac{\hbar^2}{2mR^2}, \tag{75}$$

where $n > 0$ and $-n \leq l \leq n$ are quantum numbers and $z_{n,l}$ are the zeros of spherical Bessel functions. The first energy level corresponds to one mode with radial symmetry $(n = 1, l = 1)$ analogue to the so called $s-$ mode of an atom. The second corresponds to the degenerate p_x and p_y modes $n = 2, l = +1, -1$. In figures 19(b-d) momentum space spectra taken along $x-$direction reveal the single lobe of the $s-$mode and two lobes of the p_x mode confirming this interpretation. Micropillars thus behave like tunable photonic atoms.

Note that excitons do not feel any confinement as Bohr radius is two orders of magnitude smaller than the structure.

3.4.0.4 *Coupled micropillars*

By coupling several micropillars more complex systems can be created. If the cavity is etched in the form of overlapping pillars their optical modes overlap and photonic coupling is introduced. Figure 20(a) shows a SEM image of the diatomic molecule, realized in this way. The spectrum of such a structure reveals two molecular modes, one above and one below the energy of the $1s$ states of each pillar. In fig. 20(b) we show the experimentally obtained spatial profile of these two modes (see section 3.3.6 for explanation of experimental procedure). Like in the case of a natural molecule, they show the bonding and the anti-bonding character: there is zero intensity in between the pillars at the higher energy. These states are thus obtained by the hybridization of the $1s$ states and the energy separation $2J$ of the two orbitals gives the coupling strength J.

Importantly, the magnitude of J can be tuned by changing the inter-pillar distance. Figure 20(c) shows a series of dimer molecules in which this parameter is varied and fig. 20(d) the corresponding dependence of the energies of the bonding and anti-bonding modes. As expected, the splitting between modes increases as pillars overlap more significantly .

The architecture of overlapping pillars was used in our group to design various polaritonic molecules and 1D lattices and observe intriguing physical phenomena. For example, the structure made of six coupled micropillars arranged in a hexagonal geometry, given in fig. 21(a), represents a polaritonic analogue of a benzene molecule. In this structure engineering of spin-orbit coupling effect was achieved [140].

High freedom in the design of the structure allowed to extend the few pillar molecules to 1D chains and 2D lattices. For example, 1D Lieb lattice was created fig. 21(b) in order to study flat band physics and the role of interactions [141]. The staggered 1D chain made of coupled pillars, the so called SSH model, has also been fabricated. Recently, it allowed to demonstrate the first topological laser [27].
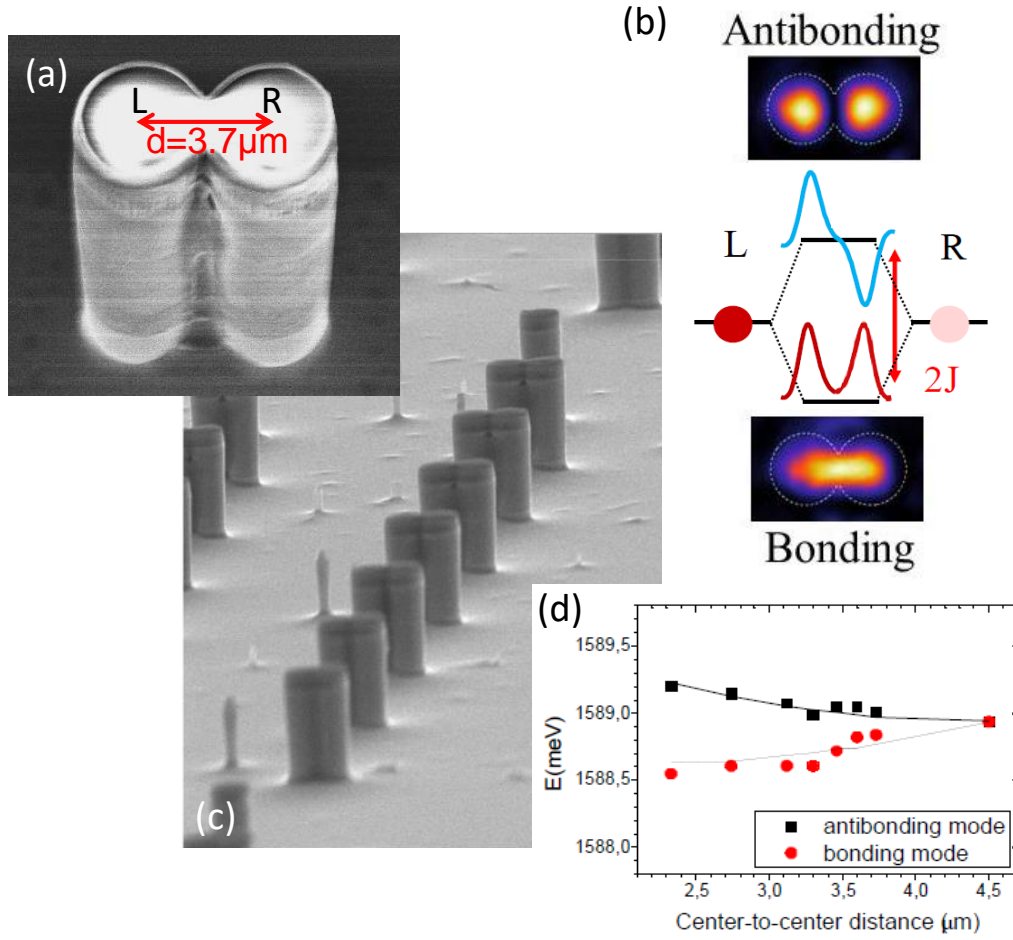
Figure 20: (a) Scanning electron microscope (SEM) image of the diatomic molecule. (b) Sketch showing the bonding-antibonding energy splitting equal to 2J and the real-space image of the first two modes of the molecule, taken by out-of-resonance excitation at low excitation power. (c) SEM image of a sample containing molecules with different inter-pillar distance (d) Energy of the bonding and anti-bonding modes for molecules with different inter-pillar distance from (c) Data taken form [139]
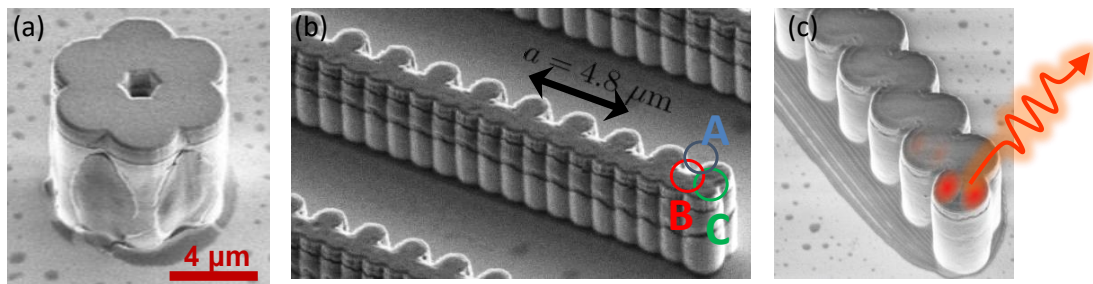
Figure 21: Examples of structures made of coupled micropillars processed at C2N. (a) Benzene molecule, [140] (b) 1D Lieb lattice, [141], (c) SSH lattice, [27]

3.5   A POLARITON HONEYCOMB LATTICE

Prior to my arrival in the group, a polariton graphene simulator had been realized in C2N and studied during the post-doc of T. Jacqmin [28]. The sample was created by etching the microcavity in the form of hundreds of overlapping pillars, arranged in a honeycomb lattice. Figures 22(a,b) show SEM images of such sample close to the two different edges. Pillar diameter is $2.75\mu m$ and inter-pillar distance $2.4\mu m$. It contains around 30 unit cells along the two crystallographic axes. Blue circles in figures indicate the position of six overlapping pillars forming one hexagon, and are there as a guide to the eye. Zoomed views on the lattice edges are given in figures 22(c,d). In all the figures holes between the pillars appear darker (and form triangular lattice).
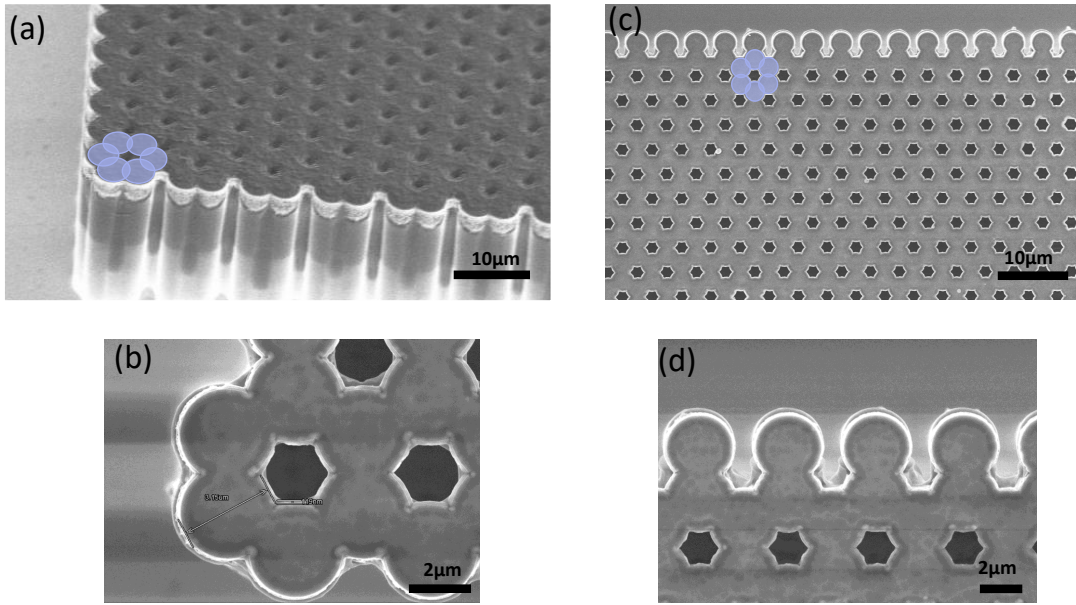
Figure 22: (a) SEM image of the corner of the fist honeycomb lattice sample realized in the group. pillar size iz $2.75\mu m$ and inter-pillar distance $2.4\mu m$ Blue circles design six pillars forming one hexagon of the lattice. (b) Top view of the corner hexagon (c) Top view of the lattice close to the edge. Potential minima are at the center of each pillar belonging to hexagonal lattice. Holes in between pillars, which represent potential maxima, form triangular lattice visible in the image. (d) zoomed view of the lattice edge from (c)

Lateral intersection at the corner of the sample is visible in fig. 22(a). After the etching, in the area between the pillars, the whole cavity (visible as dark gray region) is removed, along with the part of the substrate (light gray region).

In this section we will first provide additional details on the samples, in particular on the structure of the planar microcavity which was the basis of HCL polariton lattices presented in this thesis.

Then we will focus on the main properties of the structure as a graphene simulator. As we have seen in the section 3.4.0.4, coupled pillars are well described by the tight binding approximation, and it is expected that the polariton dispersion in a honeycomb lattice is analogue to the dispersion of electrons in graphene. In order to examine this analogy, we

will first study the sample under non-resonant excitation and comment on the effective dispersion in the structure.

In the third part of the section we will analyze two other important aspects of the polariton graphene simulator which I have explored during my PhD work at C2N. First, we will examine propagation of polaritons in the 2D lattice and demonstrate experimentally that polaritons do propagate with velocity determined by graphene dispersion relation.

Then, we will discuss one of the most important advantages of the artificial lattices, the possibility to tune the nearest neighbor hopping parameter between the lattice sites. Again, this can be achieved by changing the inter pillar distance, a. We will determine the precise values of a that allow to set hopping parameter such that uni-axial strain in the lattice is simulated. This will be done by analyzing experimental data and simulations on coupling strengths in dimer molecules. The obtained parameters are used to create lattices examined in chapter 6. It is that chapter that we will study how the designed lattices performed experimentally and what are the limits of the simulator regarding the tuning of hopping parameter.

3.5.1 *The samples*

The results presented in this manuscript are obtained from two samples. The first, labeled C4T44E, was fabricated before I arrived in the group, and was also investigated during the post doc of Thibaut Jacqmin. Results in chapters 4 and 5 are obtained on this sample. The other, labeled G9X089F, was grown and designed during my thesis, and used for experiments presented in chapter 6.

Both samples have the same nominal parameters, and they are grown in the MBE facilities of C2N by Aristide Lemaitre and coworkers. The table containing the description of each layer in the structure is given in fig. 23. The heterostructure consists of a $Ga_{0.05}Al_{0.95}As$ $\lambda/2$ cavity embedded between two $Ga_{0.05}Al_{0.95}As/Ga_{0.8}Al_{0.2}As$ Bragg mirrors with 28 (40) top (bottom) pairs. The higher number of bottom mirror pairs is used as it increases it's reflectivity, reducing the photon losses into the substrate and allowing efficient photon detection from the top. Nominally, the quality factor of the structure is $Q = 70000$, and resonant wavelength $780nm$. During the growth of the spacer the rotation of the $GaAs$ wafer inside the MBE machine was stopped resulting in a wedge in the layer thickness of the sample. In this way the cavity energy varies by a few meV over the sample (while the energy of the exciton in the thin QWs stays approximately the same), and polaritons with different values of detuning can be probed.

The sample contains 12 $GaAs$ quantum wells, $7nm$ in width. Four of them are inserted in the first maximum of electromagnetic field in the cavity field. The other 8, divided in two groups of four, are placed on the first antinode of the electromagnetic field inside the Bragg mirrors.The high number of quantum wells results in a Rabi splitting between the upper and lower polaritons bands of $\Omega_R = 15meV$.

(a)	Nominal structure		Repetition
	Material	Width	
Upper Mirror	$Ga_{0.8}Al_{0.2}As$	566.0 Å	x 1
	$Ga_{0.5}Al_{95}As$	650.0 Å	x27
	$Ga_{0.8}Al_{0.2}As$	566.0 Å	
	$Ga_{0.5}Al_{95}As$	424.8 Å	x1
	GaAs	70.0 Å	x4
	$Ga_{0.5}Al_{95}As$	30.0 Å	
	$Ga_{0.8}Al_{0.2}As$	369.5 Å	x1
Cavity	$Ga_{0.5}Al_{95}As$	396.0 Å	x1
	GaAs	70.0 Å	x4
	$Ga_{0.5}Al_{95}As$	30.0 Å	
	$Ga_{0.5}Al_{95}As$	366.0 Å	x1
Lower mirror	$Ga_{0.8}Al_{0.2}As$	369.5 Å	x1
	$Ga_{0.5}Al_{95}As$	30.0 Å	x4
	GaAs	70.0 Å	
	$Ga_{0.5}Al_{95}As$	424.8 Å	x1
	$Ga_{0.8}Al_{0.2}As$	566.0 Å	x39
	$Ga_{0.5}Al_{95}As$	650.0 Å	
Substrate	GaAs	-	-

Figure 23: Tabular representation of the microcavity structure

Optical characterization The first characterization of the sample is done by by Fourier Transform Infrared Spectroscopy (FTIR) at room temperature. The sample with a radius of around $5cm$ is scanned and a map of the energy of the cavity mode is deduced from the measured edges of the stop bands. Based on this result the region where exciton-photon detuning is expected to be negative at low temperature is selected, and the wafer is clived along the crystallographic axis to make a $1 \times 2cm$ sample (small enough to be pasted on the cryostat's cold finger and be observed at liquid Helium temperature). The values of negative detuning were selected in order to make sure that a large energy range is available to observe band structure.

Finally the samples were patterned into honeycomb lattices by e-beam and dry ICP etching as discussed in sections 3.4.0.2 and 3.5.4.

3.5.2 *Polariton graphene dispersion*

The band structure of a polariton lattice can be directly imaged in a low temperature luminescence experiment, in the same way as in the case of a microcavity, (see section 3.3.5). The sample is excited from the top of the structure, using out of resonance pump laser. Due to bosonic character of the polaritons, and their out of equilibrium nature, there is no equivalent of a Fermi level and all states are occupied upon relaxation of excitation from excitonic reservoir towards polariton bands. The use of low excitation power, about ten times smaller than threshold power, assures that the sample is probed in the linear regime and the single particle physics is examined. The far field emission along the desired direction in 2D momentum space can be energy resolved and imaged on a CCD revealing the dispersion. The tomography of the entire 2D momentum space resolved in energy can be reconstructed by recording dispersions along multiple directions. The results we will present in this section are obtained in the sample labeled C4T44E-R1, at negative exciton-photon detuning of $-17meV$.

Figure 24 shows the far field emission intensity along the k_x direction, for $k_y = -2\pi/3a$ (red line in the inset in the upper left corner which shows the first Bz). We can observe several groups of bands separated by energy gaps. As we expect from the lattice with two atoms per unit cell there are two lowest bands ($s-$ bands), which arise from the coupling between the fundamental mode of the pillars ($s-$ modes). At higher energy, we observe a group of four bands ($p-$ bands), arising from the coupling between the first excited states of the pillars, which are twice degenerate. The gap between these two groups of bands is $E = 3.2meV$, the energy difference between the two lowest-energy states of the individual pillars. Above those two groups of bands, many others can be seen arising from the hybridization of higher energy modes of the pillars.

In this section we will concentrate on the $s-$ bands. As the fundamental $s-$ modes of the pillars have a cylindrical symmetry similar to that of the carbon P_z electronic orbitals in graphene, we expect the two $s-$ bands to present features analogous to the π and π^* bands of this material, including the six Dirac (contact) points in the first Bz. Indeed, we see in the presented dispersion that the two bands intersect linearly around Dirac points $k_x = 1, -1 * (\pi/3a)$.

The next figure 25(a), shows the measured emitted intensity in momentum space at the Dirac points energy (zero energy in fig. 24(b)). We observe six isolated bright spots
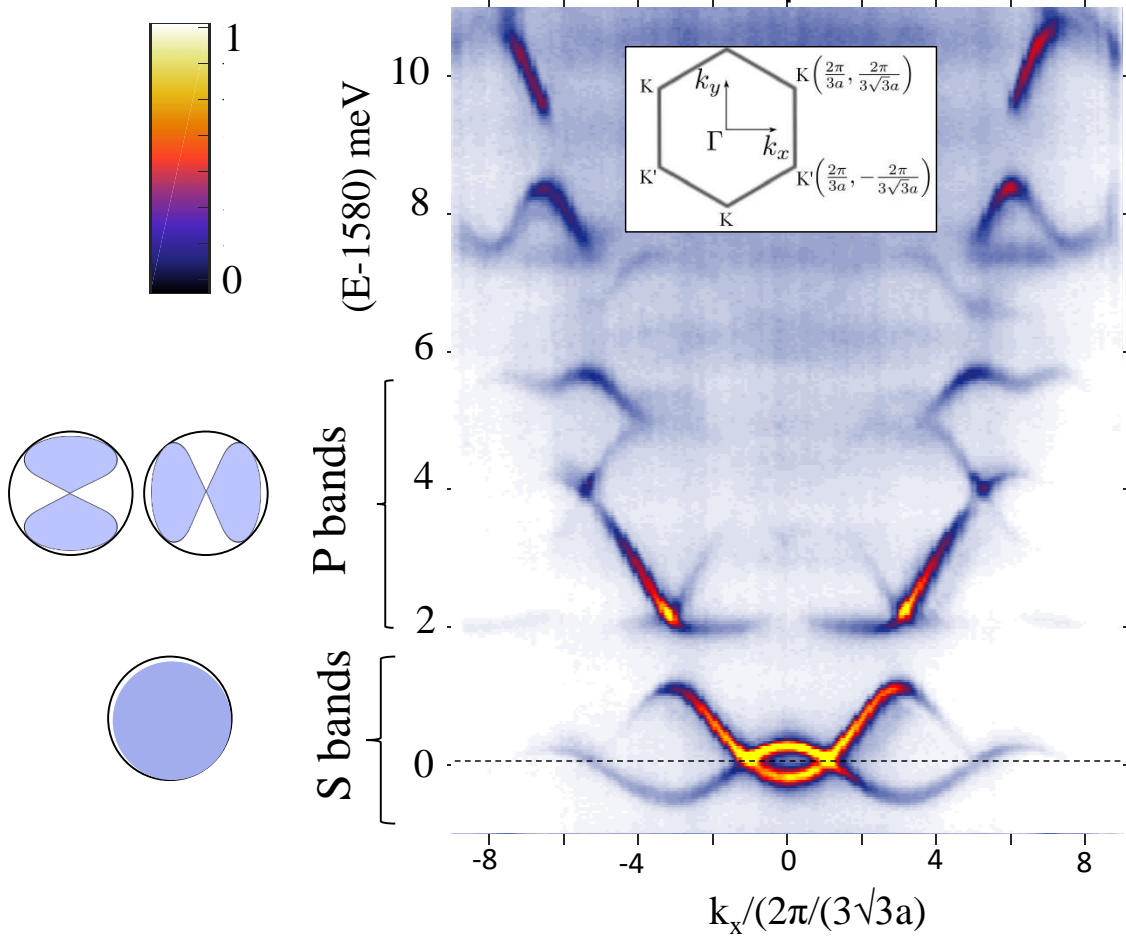
Figure 24: **Dispersion in polariton graphene** Measured momentum space energy resolved photoluminescence at $k_y = -2\pi/3a$ (line 2 in fig. 25), under non-resonant low-power excitation. Inset shows first Brillouin zone. Panel on the left side shows sketch of the real space distribution of $s-$ and $p-$ modes in a single pillar.

at the corners of the 1st Brillouin zones (Bz). These are the points in which upper and lower bands meet. The adjacent Bzs are also seen in the figure. The triangular shape of the points is due to the trigonal warping known to be present in the honeycomb lattice spectrum for non-zero energies [47], visible here because of the finite linewidth.

Figures 25(b) and (c) show the measured energy resolved emission along the two perpendicular directions in momentum space (along lines 1 and 2 indicated in fig. 25(a)). They further confirm the well defined graphene-like dispersion passing through four (line 1) and three (line 2) Dirac intersections.

Importantly, the system is well described by the tight-binding approximation, as the confinement energy on each site of the lattice is much larger than the tunneling energy. We will demonstrate this by fitting the experimentally obtained dispersions with the theoretical expression. In the calculation we will include both nearest- and second-nearest neighbor tunnelings, t and t^{NN}, respectively, in order to account for the asymmetry between the upper and the lower band, visible in fig. 25(b). Indeed, it is known from graphene literature [47] that non zero value of t^{NN} breaks particle-hole symmetry in graphene such that bulk bands become asymmetric. The following dispersion is obtained in this approximation:

$$E(\mathbf{k}) = \pm t\sqrt{3 + f(\mathbf{k})} - t^{NN}f(\mathbf{k}), \tag{76}$$

where

$$f(\mathbf{k}) = 2\cos\sqrt{3}k_x a + 4\cos\frac{\sqrt{3}}{2}k_x\cos\frac{3}{2}k_y a \tag{77}$$

The fit we obtain using 76 is given with black dashed line in fig. 25(b). It allows to extract the value of $t = 0.25 meV$ and $t^{NN} = -0.02 meV$ for the lattice. In this way the group velocity around the Dirac points can be found: $v = 3at/2\hbar = 1.3 \times 10^6 m/s$.

We have thus confirmed that the polaritons in honeycomb lattice show graphene-like dispersion and thus feel a potential analogous to electrons in graphene.

In the previous analysis you could note that the data shown in fig. 25(b) do not belong to the first Bz. If we perform the same measurement along line 3 in fig. 25(a), which does go through the first Bz, we obtain the result shown in fig. 25(d). We see that the emission is absent in the upper band (dashed line) within the first Bz, and in the lower band (solid line) within the second Bz. This phenomenon arises from destructive interference effects already known in literature. They appear along the high symmetry directions in momentum space, when the states of the lattice with two (or more) atoms per unit cell are probed with light. The origin of this effect are different path-lengths from the two atoms in the unit cell to the detector, combined with the relative phase of the wavefunctions in the unit cell. Such interference effects have been already considered theoretically and experimentally for photo-electron spectroscopy (ARPES) of graphene [142, 143] and were reported in polariton graphene in [28]. In the chapter 5 dedicated to the $p-$ bands of the polariton honeycomb lattice we will see that this inhomogeneities in the intensity are well reproduced by calculations solving 2D Schrödinger equation.
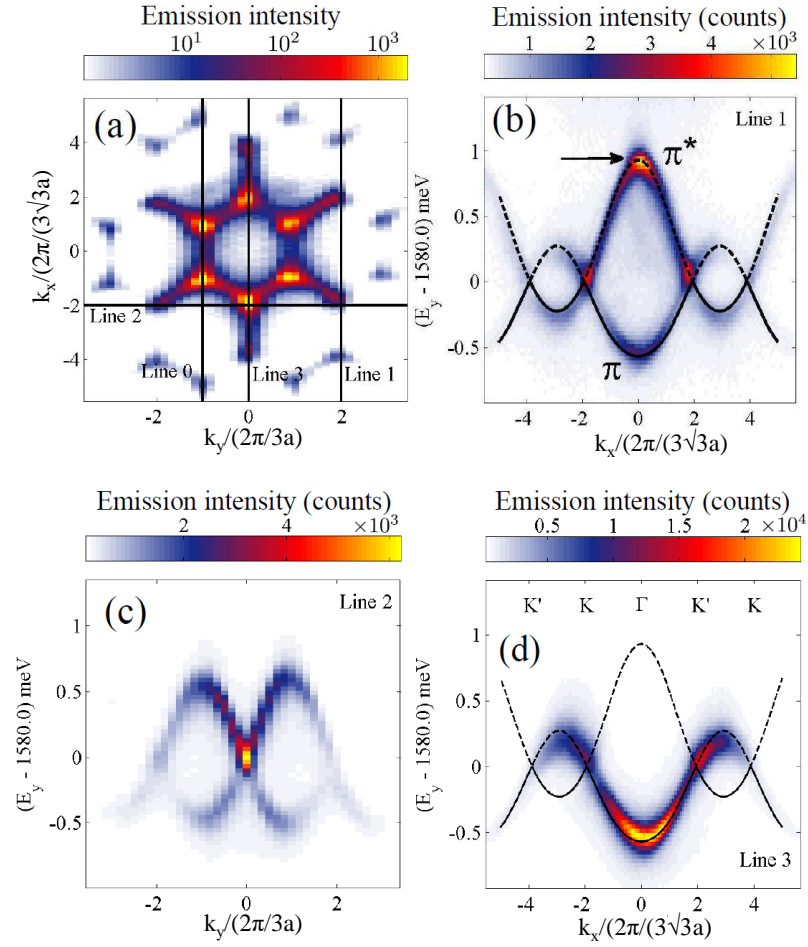
Figure 25: (a) Measured photoluminescence intensity in momentum space at the energy of the Dirac points. (b) Spectrally resolved far field emission along line 1 in (a). The black line is a fit to Eq. 76. (c) Same as (b) along line 2 in (a). (d) Spectrally resolved far field emission along line 3 in (a), passing through the first Bz. Figure extracted from [28]

3.5.3 *Propagation in polariton graphene*

Up to now we have demonstrated that microcavity polaritons represent a powerful platform to a graphene simulator and to access its spectrum in momentum space. An additional advantage of the system is the fact that polaritons with non zero wave vector can propagate away from the excitation region in a ballistic way over long distances. $GaAs$ based cavities proved to be the most suitable to study propagation effects, as propagation lengths longer than $40\mu m$ were observed in numerous works, in our group years before my arrival [23, 25] as well as in other groups [20, 130]. These results required the use of high quality factor cavities, up to $Q = 10^5$, corresponding to polariton lifetimes longer than 50 ps [20, 25].

Propagation effects can be studied in various experimental schemes. Very often the resonant excitation scheme is chosen as it allows to properly control the propagation velocity by injecting polaritons with a chosen wave-vector [144, 145, 146].

Alternatively, propagation has also been studied by the means of non resonant excitation as it was demonstrated in works by E. Wertz in our group [23, 24].

Propagation is a key potential feature of polariton graphene simulator. It opens the way to probe and study, for instance Klein tunneling [147].

We have thus performed an experiment with the goal to examine polariton propagation in graphene samples. The exact same lattice used in the previous section was excited non-resonantly, using a small laser spot, $2\mu m$ FWHM. The power applied was again below the condensation threshold, such that all the bands are populated. By collecting and resolving the emission from the lattice in energy, but also in two space dimensions, x and y, information about the propagation for each value of energy is obtained.

In figure 26(a) we report the emission intensity resolved along the x and y spatial directions for the value of energy $1585 meV$ (marked by the white dashed line in figure 26(c)). We can observe that the signal intensity decreases radially with distance from the excitation region(in $x = y = 0$).

If, indeed, the propagation is the origin of the signal we observe away from the excitation spot, it is expected to decrease with an exponential law $I = \frac{I_0}{r} e^{-r/r_0}$. Here, r_0 is the propagation length which depends on the group velocity v_g at the observed energy and the polariton lifetime τ: $r_0 = v_g \cdot \tau$. We can thus find the propagation length for each energy from the experimental data, and, by assuming a constant polariton lifetime, deduce the group velocity v_{g-exp}. Then, this experimentally obtained v_{g-exp} can be compared to the graphene v_g found analytically, which depends only on the lattice constant a and tunneling t.

To extract the propagation length we measure the emission intensity as a function of the distance from the spot. We select the region along $x-$ direction (white rectangle in fig. 26(a)), and analyze the real space spectrum, fig. 26(b). For each energy, we take the maximum of the signal on each pillar and fit the data with an exponential decay. In figure 26(c) we plot the measured dependence (black dots) and the corresponding exponential fit (red line) of the intensity at the energy $1584.5 meV$, given by the white dashed line in fig. 26(b). The obtained propagation length at this energy is $x_0 = 10\mu m$.

Before continuing the quantitative analysis we note some qualitative properties of the spectrum fig. 26(b). The usual signature of propagation is that x_0 is larger for polaritons with higher group velocity (for higher values of wavevector k) and very small around
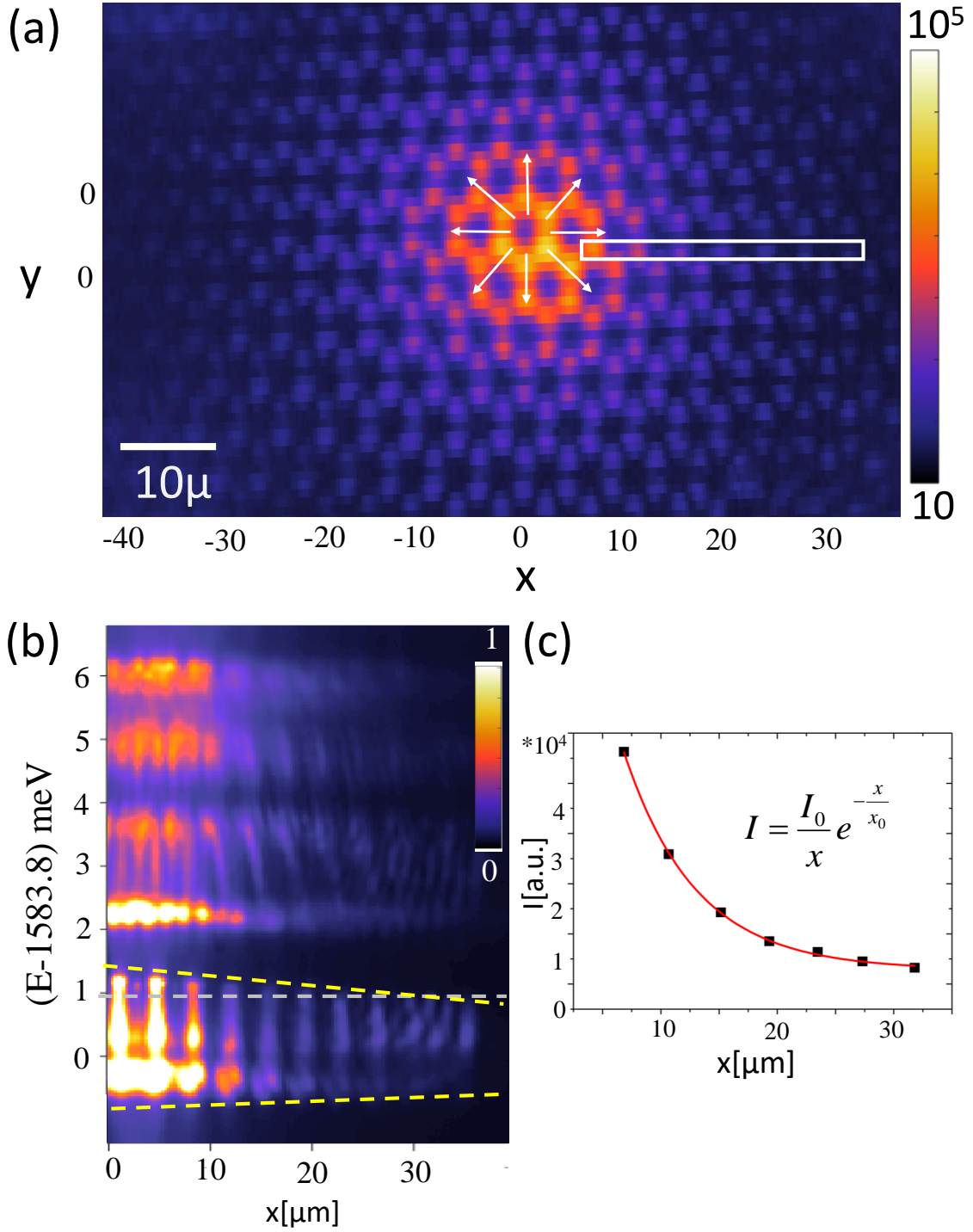
Figure 26: **Propagation in honeycomb lattice** (a)Spatially resolved emission from the lattice at the energy $1584.8 meV$ (white dashed line in (b)), excited below threshold in the center with a $2\mu m$ wide spot. Polaritons are created in the center and propagate radially. (b) Corresponding real space spectrum along direction parallel to the $x-$ axis (white rectangle in (a)). (c) Black points represent maxima of the emission intensity on each pillar on figure (b) for the energy marked with the dashed white line. Red line is exponential fit to this points, from which we obtain propagation length $8\mu m$

$k = 0$, where the polariton group velocity is 0. Indeed, by looking at the spectra along $x-$ direction, fig. 26(b), we can observe that the emission intensity follows this trend and gives the characteristic conical shape to the propagation (yellow dashed lines in fig. 26(b)).
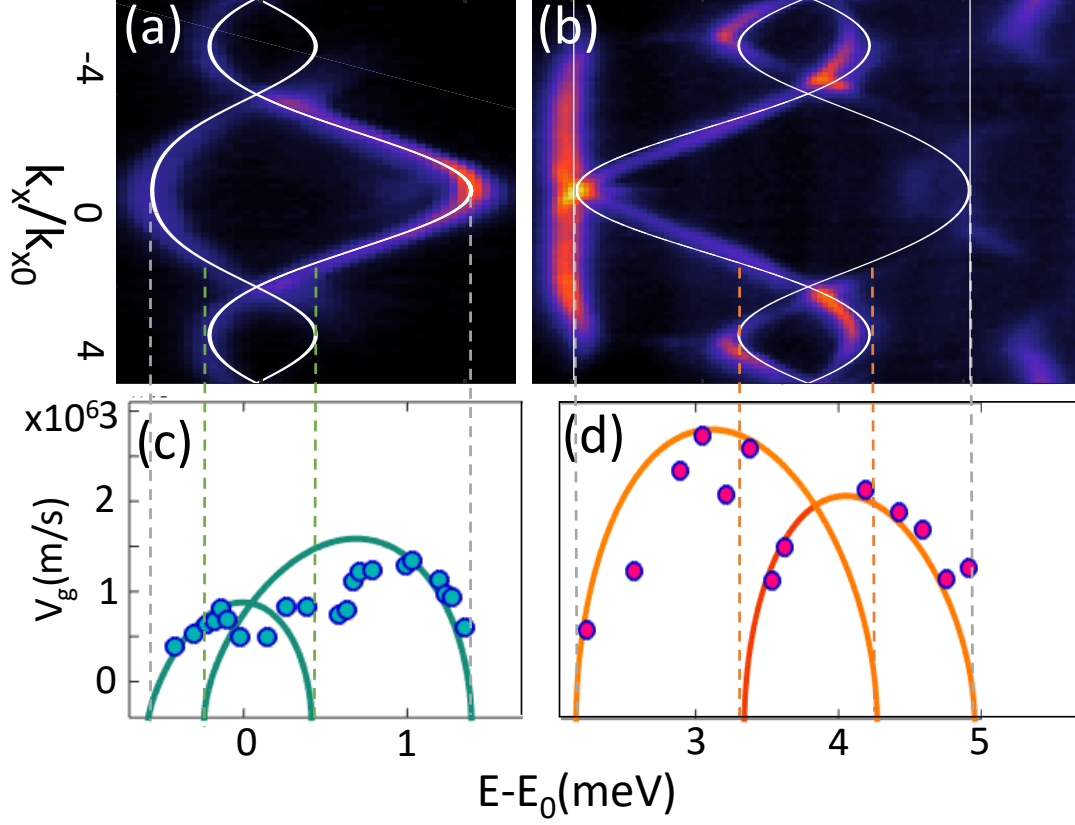
Figure 27: **Group velocity** Points are the experimental values of the group velocity v_g for polaritons in the (a) $s-$ bands (b) $p-$ bands extracted by fitting the decrease of the intensity signal along the propagation. Solid lines represent the group velocities extracted from the fitted tight binding dispersion (polariton lifetimes of $\tau_s = 3.5ps$ and $\tau_p = 4.5ps$ are considered for the $s-$ and $p-$ bands, respectively.

The propagation in the honeycomb lattice is expected to be governed by the graphene dispersion which defines its group velocity. It can be calculated as

$$v_g = \frac{1}{\hbar} \frac{\partial E(k_x, k_y = 0)}{\partial k_x} \tag{78}$$

using for $E(k_x, k_y)$ the expression given in eq. 76, with parameters employed to fit polariton graphene dispersion, fig. 27(a). The analogue analysis is carried out here also for the $p-$ bands. In the chapter 5 we will study in detail the particular dispersion that describes these bands, which contains Dirac cones and flat-bands. For the moment we can observe these features in fig. 27(b) and see how it affects propagation.

The calculated group velocities for $s-$ and $p-$ bands are plotted with green and orange lines respectively in fig. 27 (c,d) We compare them with experimental v_{g-exp} obtained by dividing the extracted propagation lengths by a constant lifetime for each of the two bands, $v_{g-exp} = x_0/\tau$. The values $\tau_s = 3.5ps$ and $\tau_p = 4.5ps$ are chosen such that

the best match between the calculation and the experiment is obtained. The trend of the experimental v_{g-exp} follows well the calculated curves, confirming that polaritons propagate according to their graphene-like nature. Note that in energy regions between the green and orange dashed lines contributions from polaritons with small group velocity around $k_x = 3, -3 * k_{x0}$ and those with large one close to $k_x = 2, -2 * k_{x0}$ are present, such that the speed obtained experimentally is an average of those values.

The presented results confirm that propagation of polaritons in a honeycomb lattice is governed by the engineered dispersion. In that way polaritons represents a great potential to simulate transport in 2D lattices.

However, let us comment on the values of polariton lifetime used to obtain group velocities in fig. 26(c,d). They are an order of magnitude smaller than the one expected from the nominal Q factor of the cavity ($Q = 70000 \rightarrow \tau = 30ps$). Similar results were obtained by examining several honeycomb lattices indicating that the polariton quality factor is reduced by the etching procedure of 2D structures. Influence on both excitonic and photonic component is possible. Most probably it is the exciton that is affected. In fact, when the sample is fabricated, after the etching procedure, it is passivated, in order to prevent oxidation. The efficiency of this process might be significantly reduced in the holes between pillars in the honeycomb lattice, in which case non-radiative absorption is enhanced in the sample. We consider this explanation the most probable as the quality factor in other etched structures, like micropillars and wires is not significantly reduced (it is measured to be 65000 for the 1D wires for example [148]). At the moment, a further study is carried out in our group in order to optimize the etching and passivation procedures and minimize this effect.
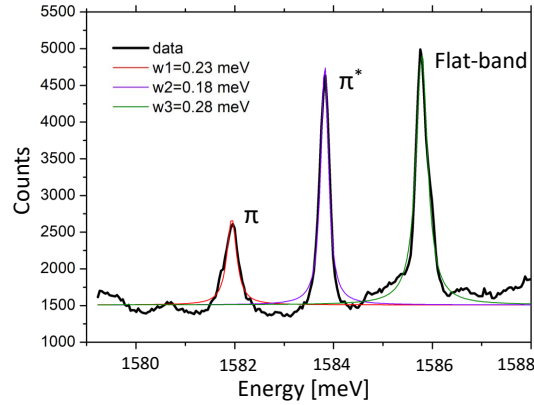
Figure 28: Emission line from a polariton state at $k_x = 0$ measured in the middle of a hexagonal lattice. Three peaks belong to the π and π^* $s-$ bands and flat $p-$ band. Red, violet and green line represent their corresponding Lorentzian fits, respectively. The resulting widths of the emission lines are $230\mu eV$ for the cavity, and $180\mu eV$, $260\mu eV$ and $280\mu eV$.

We will now discuss the linewidth measured in a honeycomb lattice. Figure 28(a) shows energy dependence of the intensity measured in momentum space at $k_x = 0, k_y = k_{y0}$ for the honeycomb lattice excited nonresonantly. Here, we can observe three peaks, two of them belong to the $s-$ (π and π^*) and the third is the flat-band in the $p-$ bands (see

chapter 5). The fitted FWHM for the three peaks is respectively $230\mu eV, 180\mu eV$, and $280\mu eV$.

The obtained line widths are larger than those we expect from the uncertainty principle: $\Delta E = \frac{\gamma}{2} = \frac{\hbar}{2\tau}$. Using the expression $\gamma = \frac{\hbar}{\tau}$ and the lifetime we obtained from the propagation measurement for the $s-$ bands we get the linewidth $\gamma = 160\mu eV$. This difference can be understood taking into account the effect that arises upon non-resonant excitation. In that case rapid changes of the exciton energy lead to the change of polariton energy and result in broadened linewidths, once that acquisition time in the experiment is on the order of seconds.

Again, measured linewidths are larger than those measured upon non-resonant excitation in planar cavities and wires [148], that typically have values $90 - 120\mu eV$.

Increasing polariton lifetime in honeycomb lattices is thus an important technological challenge towards improving the emulator.

3.5.4 *Tuning the lattice geometry and parameters*

One of the crucial advantages of the artificial polariton lattice in general, is the possibility to control its geometry and hopping parameters. Realization of different types of lattice terminations allowed to study edge states, to which chapters 4, 5 are devoted. The fact that photonic coupling in the lattice depends on the pillar size and inter pillar distance, allowed to controllably tune the hopping parameter in the lattice. In that way, it was possible to experimentally simulate strain with magnitudes not reachable in electronic graphene, as it will be discussed in chapter 6.

During my thesis I have designed several honeycomb lattices. For this task it was important to know the dependence of coupling on the interpillar distance. We carried out the study on diatomic molecules, measuring dimers with different sizes and inter-pillar distances. This data is corroborated with the results obtained by solving the 2D Shrödinger equation. The study revealed how the hopping parameter changes with the inter-pillar distance in the $s-$ and the $p-$ bands. This two cases are very different as both confinement and hopping amplitude significantly depend on the shape of the mode.

Let us consider in detail the spectrally resolved real space emission from a diatomic molecule of diameter $D = 4\mu m$ and inter-pillar distance $a = 3\mu m$, figure 29(a).

In the spectrum, we can recognize the $s-$ and the $p-$ modes separated by the gap of $1.5meV$. As we discussed, the two lowest energy states $S1$ and $S2$ correspond to the bonding and anti bonding $s-$ modes of the molecule. The states $P1$ and $P2$ have maxima in the region between the pillars, and thus are bonding modes of the p_x and the p_y states, respectively, while the states $P3$ and $P4$ have minima in between the pillars and represent anti-bonding modes. We can thus deduce the hopping amplitudes for the $s-$ and the $p-$ bands, by measuring the splitting between the modes: $t_s = (E(S2) - E(S1))/2$ and $t_L = (E(P4) - E(P1))/2$. Here, t_L is the coupling in the $p-$ bands along the link between the pillars, or between the p_x states in our case, see the inset on top of the figure 29(a). As expected it is significantly larger than the coupling t_P between p_y orbitals equal to $t_P = (E(P3) - E(P2))/2$.

Before we examine how t_s and t_L depend on the distance in the pillars, let us compare the values we obtained with the ones calculated by numerically solving a 2D Shrödinger

Figure 29: (a) Real space spectrum for a dimer with diameter $D = 4\mu m$ and inter-pillar distance $a = 3\mu m$. The splitting between the modes gives: $t_s = (E(S2) - E(S1))/2 =$ and $t_L = (E(P4) - E(P1))/2 =$. The inset on the top of the figure is a schematic representation of coupling between $p-$ modes of a dimer. (b) Corresponding shape of the eigenfunctions obtained by solving the 2D Shrödinger equation (c) Dependence of coupling in the $s-$ and the $p-$ bands for a dimer with $3\mu m$ pillars. Experimental data is given by dots, calculation by solid line.

equation. The equation takes into account a massive particle inside an infinitely high potential well in 2D, that is:

$$E\psi = H\psi = (-\frac{\hbar\nabla^2}{2m} + V(r))\psi, \tag{79}$$

where ∇ is the Laplace operator in 2D and $V(r)$ is a step function with the geometry of the overlapping circles of diameter D and distance a between their centers. The polariton mass can be considered as equal to the effective polariton mass in a 2D cavity. It can thus be found by measuring and fitting the parabolic dispersion of a planar cavity structure at the same exciton-photon detuning.

In fig. 29(b) the modulus square of eigenfunctions obtained from solving the 2D Shrödinger equation for a dimer with the same R and a as the one examined in fig. 29(a) is depicted together with the corresponding energies. The shape of the states in $x - y$ plane clearly corresponds to those measured experimentally. More importantly, for the given inter-pillar distance the values of tunneling t_s and t_L obtained by the simulation and in the experiment agree within 10% accuracy.

Let us now investigate how changing the distance between the pillars changes the hopping amplitude. The spectra from a series of $d = 3\mu m$ dimers with different inter-pillar distances are analyzed and results are presented by dots fig. 29(c). The values obtained by simulation for the same pillar size are depicted by solid line.

We can see that the experimental data follow well the trend obtained from the simulations. Only when the overlap between the pillars is small, the experimental curve deviates from the prediction. The possible explanation is that during the etching the sharp shape in between the pillars is not fully etched, leading to slightly larger value of the coupling. This explanation is reinforced by the fact that the effect is more significant for the $p - bands$, as coupling t_L is larger than coupling t_s. It was thus important to take into account this effect when designing the honeycomb lattice.

The next information necessary for the lattice design is how the presented trend changes when the pillar size is varied. In figure 30(a) we plot calculated dependence of the coupling on inter-pillar distance, for three different values of pillar diameter $D_1 = 2.5\mu m, D_2 = 2.75\mu m$ and $D_3 = 3.5\mu m$. The slope of the line is significantly different for the three cases. As expected for the pillars with smaller diameter the change of hopping parameter is faster. This fact can be used to suitably choose the lattice parameters depending on the effect that is studied. Most of our lattices are made with the $D = 2.75\mu m$ with the intermediate slope.

Now that the parameters for tuning the hopping parameter in the dimer are known, it is important to have in mind that they cannot be directly transfered to the HCL. There, each pillar overlaps not only with one but with three others. For that reason the confinement in the pillars is different, as well as the hopping parameter between them.

To account for this difference, we have used the value of hopping amplitude obtained from the first polariton graphene sample, C4T44E. As the pillar size in that sample is $D = 2.75\mu m$ and the distance $a = 2.4\mu m$ lead to coupling of $t_s = 0.25meV$ and $t_L = 1.2meV$. The curves in fig.30(a) for the $D = 2.75\mu m$ are linearly "rescaled" such that they include the values of hopping t_s and t_L obtained experimentally in the honeycomb lattice. The results presented in fig.30(b) are used to design lattices in which strain is implemented, as will be presented in chapter 6.
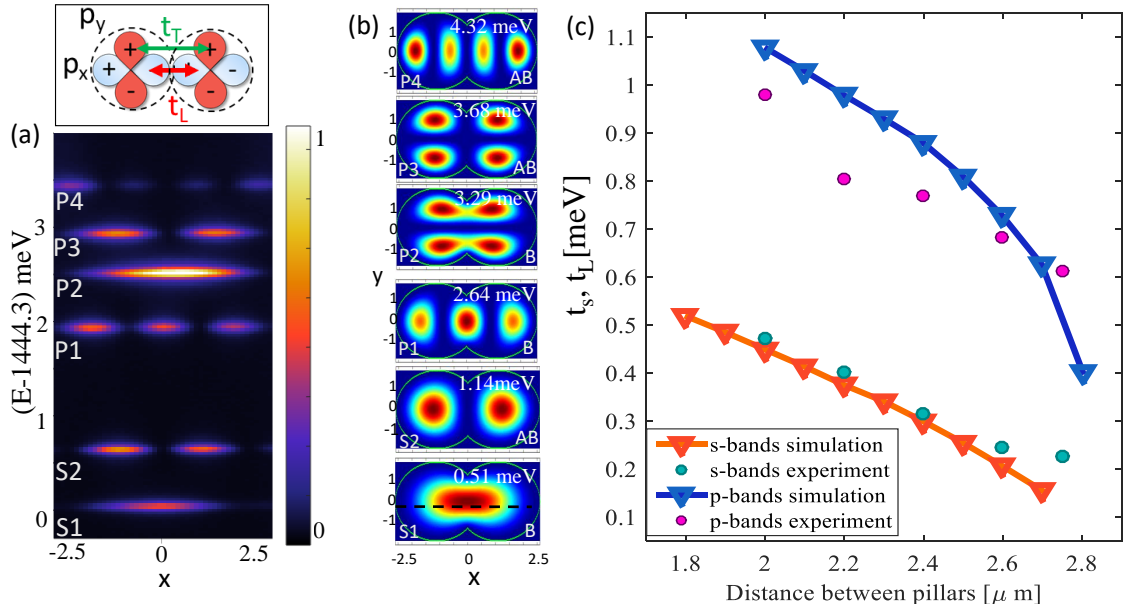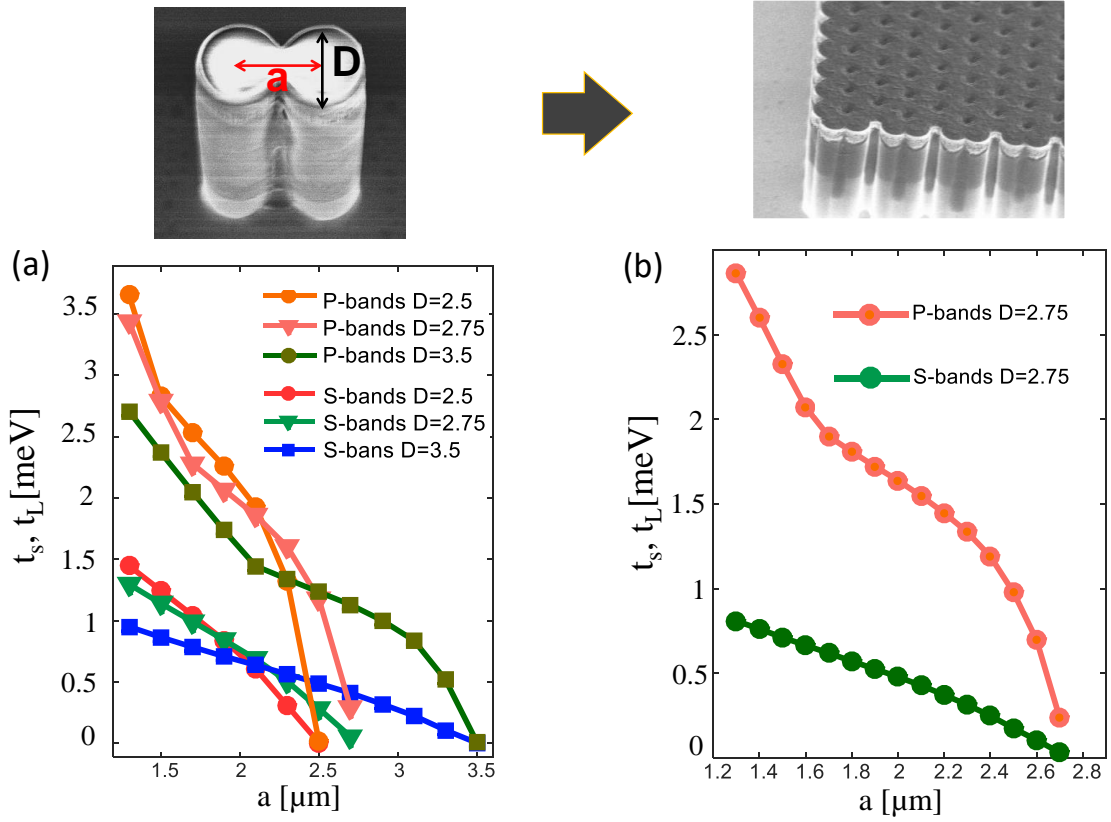
Figure 30: (a) Real space spectrum for a dimer with diameter $D = 4\mu m$ and inter-pillar distance $a = 3\mu m$. The splitting between the modes gives: $t_s = (E(S2) - E(S1))/2 =$ and $t_L = (E(P4) - E(P1))/2 =$. (b) Corresponding shape of the eigenfunctions obtained by solving the 2D Shrödinger equation (c) Dependence of coupling in the $s-$ and the $p-$ bands for a dimer with $3\mu m$ pillars. Experimental data is given by dots, calculation by solid line.

DIRECT IMAGING OF EDGE STATES IN POLARITON GRAPHENE

In the first chapter of this manuscript we recapitulated the main ideas of band theory of solids. We discussed how Bloch states, extended over the whole lattice, arise as a consequence of translational symmetry in an infinite lattice (or the one with periodic boundary conditions). We applied this theory, in tight binding approximation, to the honeycomb lattice in order to calculate the band structure of graphene.

In the second chapter we demonstrated a simulator of graphene Hamiltonian, built using microcavities in which quasi-particles polaritons are subjected to graphene-like potential landscape. Due to particular properties of these half-light half-matter quasi particles bulk properties of a graphene lattice could be directly observed.

The band theory of solids, and our experimental study up to now, however, neglect the fact that real crystals are finite and thus break the translational symmetry at their edges. A fundamental property of such crystals is the possibility to host surface states, additional states that are localized on the surface of the material and can reside in the gap [149].

Surface states can have radically different properties from the ones in the bulk. They can provide conductive channels in materials which would otherwise be insulators. This is the case in the quantum Hall effect and other topological insulators [4], materials that are insulating in the bulk, but conductive at their surface. Such systems became of great interest due to the "topologically protected", unidirectional surface states, present in two-dimensional topological insulators, and can provide electrical transport with low losses, insensitive to defects of the material. Indeed, in the case of 2D systems, surface states are one-dimensional egde states. They are evanescent in the direction normal to the edge, with the wavefunction spreading in the parallel direction Importantly, the appearance of topological edge states can be predicted from the properties of the bulk wavefunctions, through the so called, bulk-edge correspondence.

Surface states, weather they present topological protection or not, play a very important role in a wide range of low dimensional materials. Dirac materials, in particular, as we will see throughout this thesis, often host edge states. They reside close to the Dirac point, and due to lattice symmetries their wave functions have peculiar properties, such as sublattice polarization, spin polarization or even net spin current [150]. Their appearance can be related the bulk properties of the wavefucntion, in particular to the non-zero winding around the Dirac points.

Even though the edge states have raised a tremendous interest both in the case of three dimensional and two dimensional systems they are hard to study experimentally. The need of crystals with chemically unperturbed crystalline surface and the necessity to measure local properties with atomic resolution, as in the case of the 2D materials, hindered the study of fundamental properties of surface states. In graphene, while it is possible to prepare different kinds of terminations and visualize them using scanning tunneling microscopy [151, 152], the existence of electronic edge states has only been evidenced via

the measurement of the local density of states, which provides information on their energy and on the curvature of their dispersion, but misses any information on their microscopic spatial structure and on their momentum distribution [151].

An entirely new way of approaching the problem is introduced with the creation of photonic simulators which allowed visualizing and manipulating edge states like never before. In particular, photonic systems allow realizing any type of lattice termination, even those that are not chemically stable in graphene such as the bearded edge, as will be explained latter.

In this chapter we will first give a short general review on the appearance and main types of the surface states in solids. Then, we will focus on edge states in graphene as they were first discovered, using the numerical tight-biding calculation. The connection between the edge states and the bulk properties of the honeycomb lattice, i.e. the bulk-edge correspondence, will be explained in the following section.

In the section 4.4 the main topic of this chapter will be addressed: direct visualization of graphene edge states both in real and momentum space, using a polariton honeycomb lattice.

4.1   CRITERIA FOR THE EXISTENCE OF THE SURFACE STATES IN 1D LATTICES

The first theoretical study of surface states dates back to the 1930's and was done by Tamm [153]. He considered electrons in a simple one-dimensional periodic square potential (the so called Kronig-Penney model). When thinking about the possible electronic states he applied and mathematically demonstrated a simple argumentation: in order for a state to reside in a gap, and still satisfy the Schroedinger equation with a given potential, it's momentum k has to be complex, i.e. of the form $p + \mathrm{i}q$. This leads to wave functions which are proportional to $e^{\mp qx}$, which however cannot represent a physically possible state for an infinite crystal, as they would be unbounded. For a (semi)finite crystal, with an edge at $x = 0$, however, a wave function proportional to $e^{\mp qx}$ represents a physically possible solution for $x > 0$ (inside the crystal). Such wave function has its maximum on the first atom and decreases exponentially inside the lattice.

Soon after the discovery of the surface states, Fowler [154] and Rijanow [155] showed that these levels occur in pairs when taking into account the lattice finite on the two sides. The formation of the edge states in three dimensional crystals, that is of surface states was discussed first starting from the free electron model by Maue [156] and in more general potentials and in tight-binding approximation by Goodwin [157]. These works clarified the main properties of the gap states that were associated with experimentally decaying wavefunctions in crystals.

The discovery of surface states by Tamm attracted the interest of many researchers. They tried to understand their nature, how they emerge from the bulk bands and to explain their origin from the symmetries of the crystal. These efforts eventually led to the formulation of first bulk-edge correspondence theorems, which connect the Berry phase of the bulk wavefunctions with the existence of surface states, as we will discuss in sub-section 4.2.

A first breakthrough in this direction was the theory of edge states developed by Shockley [149]. He realized that two types of edge states can be distinguished. The first type are
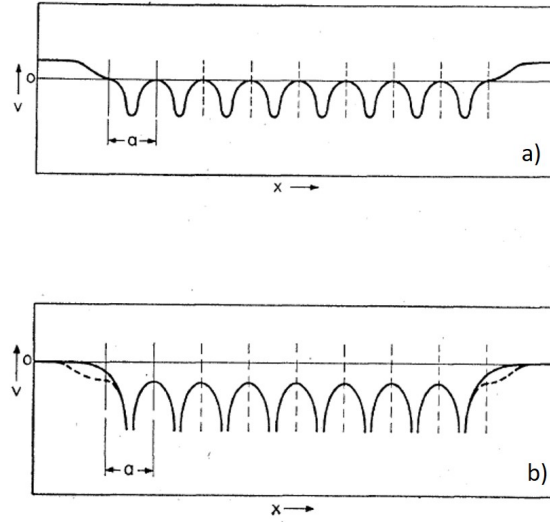
Figure 31: **Potentials in one dimensional lattice** [149] (a) A 1D potential used by Shockley
(b) Potential with the abrupt change of potential at the edges, typically used for calcu-
lation of edge states in tight binding approximation before Shockley (solid line) and its
correction (dashed line).

those which arise due to the asymmetric termination of a periodical potential, as described
by Tamm. They arise when a perturbation at a solid surface is present, resulting in an
abrupt change of the potential at the surface, as the one given by solid lines in the figure
31(b). This situation takes place in presence of lattice defects, as well as in narrow-band
materials with a large inter atomic distance [149].

The second type are those studied by Shockley himself. He explored the formation of
edge states in a finite one dimensional lattice, assuming one electron per atom, and a
potential that ends symmetrically around the last lattice site, resulting in less abrubt
change of potential at the edges, as the one given in fig. 31(a). The goal was to understand
how the surface levels originate from the atomic levels when varying the lattice constant
from infinity to a finite value. He found that as atoms get close enough such that lattice
bands cross, one state can be expelled from those bands to form a surface state. Figure 32
shows the energy spectrum for a one-dimensional lattice with eight atoms as a function
of the lattice constant and formation of the edge states from the crossing bands that lay
in the middle of the gap. This mechanism is contrasted to the one that takes place when
Tamm- or Goodwin- type potential are used. In that case edge states lie near the band
from which they originate, and can appear in the case of both uncrossed and crossed bands.

Shockley was the first to use symmetry arguments to explain the existence of the edge
states. He also provided the necessary condition for the appearance of the edge states in
tight binding approximation: band crossing. This condition is necessary but not sufficient.
This and many other works that followed, didn't offer any criteria which could predict if
edge states are going to appear in the gap of a spectrum of a certain crystal.

Such explanation was attempted by Zak [158] in 1985, who found selection rules for
the appearance of edge states based on the symmetry of the band wavefunction (that
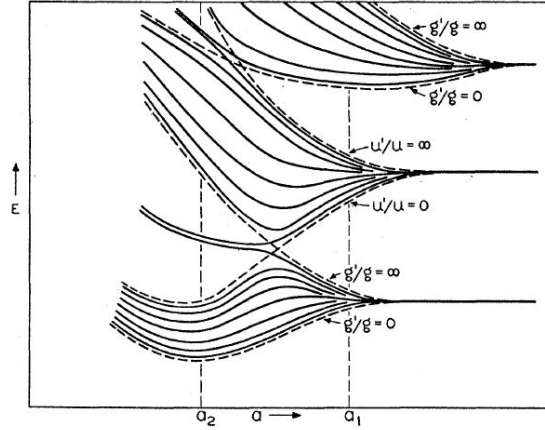
Figure 32: Energy spectrum for a one-dimensional lattice with Shockley potential with eight atoms, as given in [149]

is corresponding Wannier function). Similarly to Shockley, he emphasized the difference between crystals that terminate at a general point in the lattice and those that terminate at a symmetry center. He carried out the demonstration using a one dimensional crystal with inversion symmetry, (fig. 33) which can be ended in two ways. On the one hand, the surface is located at one of the symmetry centers of the system potential (or symmetry plane in three dimensional case), given by the positions $x_{v3} = a/2$ and $x_{v1'} = 0$, for the considered lattice. In this case, the potential is perfectly periodic up to the edge and it may give rise to the Shockley states. On the other hand crystals ending in arbitrary position, such as (x_{v2}) or at the point of lattice defect $x_{v2'}$, both without symmetry, show edge states which are Tamm states.

The first case, a symmetric ending of the crystal, allows defining the criteria that purely rely on the symmetry of the bulk wavefunctions.

His reasoning begins with a general statement: to obtain an edge state it is necessary to ensure the continuous matching between the wavefuntions in the crystal, $\psi_k(x)$, and the ones outside the crystal $\phi(x)$, as well between their derivatives. In the case of one dimensional lattice we have:

$$\frac{(d/dx)\psi_k(x)}{\psi_k(x)}|_{x_v} = \frac{(d/dx)\phi(x)}{\phi(x)}|_{x_v},$$ (80)

where x_v is the coordinate of the lattice edge. Now, the right hand side of the above equation is negative at the edge $x = x_v$: the logarithmic derivative of $\phi(x)$ is negative because for a surface state one requires that $\phi(x)$ falls off exponentially for $x > 0$ (outside the lattice). We can define the quantity:

$$\rho(k, x_v) \frac{(d/dx)\psi_k(x)}{\psi_k(x)}|_{x_v} \equiv \frac{\psi_k(x)'}{\psi_k(x)}|_{x_v},$$ (81)

which then also needs to be negative inside the gap, if we want an edge state to be formed.

At this point symmetry considerations begin to play a role. Zak shows that $\rho(k, x_v)$ keeps its sign inside a gap for all values of k and that it can change sign only when
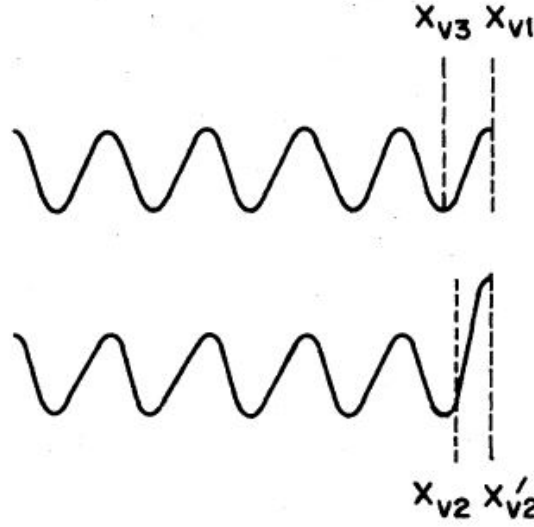
Figure 33: **Potential in one dimensional lattice** (a) A periodic potential used by Shockley (b) Potential which is not periodic on the edges, typically used for calculation of edge states in tight binding approximation before Shockley (solid line) and its correction to periodic potential (dashed line).

traversing a band. Whether the sign of $\rho(k, x_v)$ will change from one gap to the other depends only on the symmetry of the wavefunction between these two gaps.

As we mentioned, the symmetry of the Bloch wavefunctions is determined from the corresponding Wannier functions. These localized functions have a symmetry center which coordinates can take exactly the values of 0 and $a/2$, with respect to the atomic nucleus position. Wannier functions can be even or odd for the inversion I with respect to the their symmetry center.

Now, if the lattice ending at position x_v matches the symmetry center of that specific band, $\rho(k, x_v)$ will change the sign and if it doesn't match it won't. Provided the knowledge of sign of $\rho(k, x_v)$ in one of the gaps, for example below the lowest energy band, one can obtain the information about the change of this sign and the existence of the edge states in all other gaps. The starting information on the sign depends on the specific shape of the potential, but it is calculated to be positive for usually considered cases of one-dimensional potentials (meaning that there is no edge states below the first band). After this discussion provided by Zak the criterion of band crossing used by Shockley is reviewed and considered to be only a way to change the symmetry of the bands and it is not necessary per se.

While the criterion presented above may link the appearance of the edge states with the symmetries of the bulk wave function in one dimensional lattices, generalization of such a method for an arbitrary crystal in two or three dimensions remains a challenge. However, for a special class of materials, called topological insulators, there exists a theory that predicts the existence of edge states from the properties of the bulk and establishes the so called bulk-boundary correspondence [4]. These materials are insulating in their bulk, but contain conductive channels at their surface. In fact, the topological surface states arise at the surface between two materials that belong to the two different topological classes [159].

They are called topological classes simply because it is not possible to transform a Hamiltonian belonging to one class to a Hamiltonian belonging to the another by continuous deformation of its parameters, without closing the gaps. Different classes are characterized by a different values of a topological invariant, a discrete quantity that can be calculated from the bulk wave functions. Then, at the interface between a semiconductor with zero value of the topological invariant and with the nonzero topological invariant, edge states arise, in order to close the gap and allow the non continuous change of the Hamiltonian.

Obtaining a material which is not topologically trivial (with non zero topological invariant) is not a straight forward task. Physically, it requires either to break the time-reversal symmetry (for instance when magnetic field is applied to a 2D electron gas, for Hall effect) or to introduce a strong spin-orbit coupling.

The bands in graphene are not gapped, and therefore the theory of topological insulators cannot be applied to them. However, we can still define a bulk related topological invariant, that will allow us to predict the existence of edge states in certain conditions. As we discussed in the first chapter, topology of graphene is related to the symmetries: time-reversal symmetry(TRS), the particle-hole symmetry (PHS), as well as the "sublattice" or "chiral" symmetry (SLS). The Dirac cones, featuring nonzero winding and Berry phase, represent 2D point degeneracy, which is essential in creating topologically nontrivial phases [159]. As a consequence, edge states in graphene have a topological origin. In order to demonstrate the bulk-edge correspondence in graphene, we will shortly review here a 1D toy model for topological insulators, the so called SSH model, widely used in the literature to introduce the basic concepts of topological invariants and bulk-edge correspondence [160, 73].

4.2 BULK-EDGE CORRESPONDENCE IN SSH MODEL
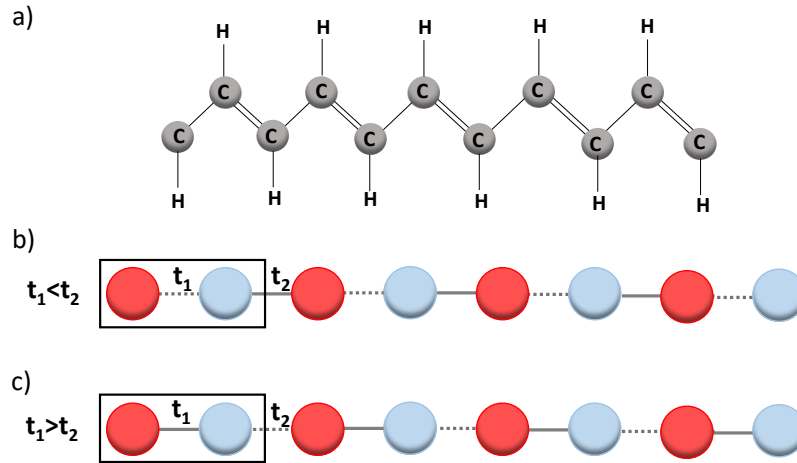
Figure 34: (a) The structure of polyacetylene-a polymer with alternating double and single bonds. This chain can be described using the so called SSH model, a 1D finite lattice with intercell hopping amplitude t_1 different from the intercell hopping amplitude t_2. Two dimerisations are possible (b) $t_1 < t_2$ and (c)$t_1 > t_2$. The dashed lines represent the weaker link between the cites. The unit cell is defined with the black rectangle.

The Su-Schrieffer-Heeger (SSH) model describes a system of spinless, non interacting electrons in a one dimensional chain with the staggered hopping amplitudes [160, 73]. It was originally used to describe the chain of polyacetilene, fig. 34(a), but schematically can be represented by a chain with N unit cells, each of the cells containing two atoms. The hopping amplitude inside the unit cell (t_1) is allowed to be different from the one in between the unit cells (t_2), fig.34(b). Within the tight binding approximation the Hamiltonian of the model reads:

$$H = -\sum_{m=1}^{N} \left(t_1 a_m^\dagger b_m + h.c. \right) - \sum_{m=1}^{N-1} \left(t_2 b_m^\dagger a_{m+1} + h.c. \right),$$

(82)

where $a_m^\dagger$ and $b_m^\dagger$ are the creation operators on the sub-lattice site a_m (b_m) in the m-th unit cell, and N is the total number of unit cells.
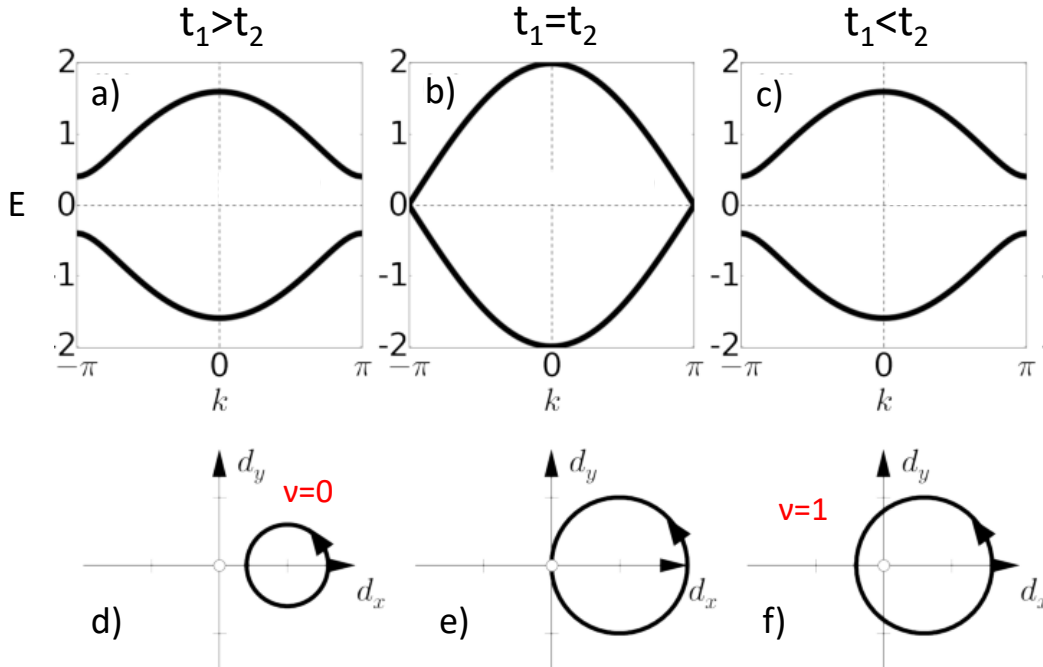
Figure 35: **Topological phases of the SSH model.** (a), (c) The system is a semiconductor for both dimerisations, $t_1 < t_2$ and $t_1 > t_2$. The identical band structure features two bands separated by gap. b) In the case $t_1 = t_2$ the gap is closed and the system is metallic. (d-f) The topology of the system is given by the number of times the vector $\mathbf{d} = (t_1 + t_2 cos(k), t_2 sin(k))$ winds around the origin, when scanning k across the first Brillouin zone. Two semiconducting phases can be differed: d) the one with the winding number $\nu = 0$ for $t_1 > t_2$ and f) the one with $\nu = 1$ for $t_1 < t_2$. Figure taken from [73]

We can first calculate the bulk properties of this lattice by imposing the periodic (Born-von Karman) boundary conditions. We obtain the Hamiltonian in momentum space, $H(k)$ in the basis $(a(k), b(k))$:

$$H(k) = \begin{pmatrix} 0 & t_1 + t_2 e^{-ik} \\ t_1 + t_2 e^{ik} & 0 \end{pmatrix}$$

(83)

For all the values of the parameters $t_1, t_2 > 0$ and $t_1 \neq t_2$ the eigen states form two bands separated by a gap of magnitude $2\,|t_1 - t_2|$, fig. 35(a,c). However, the Hamiltonian $H(k)$ exhibits two topologically distinct phases associated to the two possible dimerizations of the lattice, $t_1 < t_2$ and $t_1 > t_2$. To reveal this feature we can follow the trajectory of the vector consisting of the real and imaginary part of one off-diagonal element of $H(k)$: $\mathbf{d} = (t_1 + t_2 cos(k), t_2 sin(k)) \equiv (d_x, d_y)$, on a closed loop in the Brillouin zone $k = [0, 2\pi]$. As the wavenumber runs through the Brillouin zone, this vector traces out a closed circle of radius t_2 on the $d_x - d_y$ plane, centered at the point $(t_1, 0)$. For the values $t_1 < t_2$ it encloses the origin, 35(f), and for $t_1 > t_2$ it does not, 35(d). The number that counts the number of times the loop winds around the origin is called the winding number ν, fig. 35(f). It is an integer that determines the two topological classes of $H(k)$: we cannot transform one class into another without passing through a topological phase transition for $t_1 = t_2$, fig. 35(b, e), when the system is not semiconducting but metallic. For any Hamiltonian with chiral symmetry, ν can be calculated from [73]:

$$H(k) = \begin{pmatrix} 0 & h(k) \\ h(k)^* & 0 \end{pmatrix}, \qquad h(k) = d_x(k) - d_y(k), \tag{84}$$

using the complex logarithm function $log(|h|e^{i\arg h}) = \log|h| + i\arg h$, the winding number ν is:

$$\nu = \frac{1}{2\pi i} \int_{BZ} \frac{d}{dk} \log h(k) dk = \frac{1}{2\pi} \int_{BZ} = \frac{d(\arg h)}{dk} \tag{85}$$

Interestingly, the ratio t_1/t_2 governs more than just the properties of the bulk Hamiltonian. If we look at the lattice with a finite number of unit cells, and starting from eq. 82 we numerically calculate the eigen states of the finite chain, the results will be different for $t_1 < t_2$ and $t_1 > t_2$. The system with $t_1 < t_2$ will exhibit zero energy states strongly localized at the outermost pillar. More generally, it can be shown for a wider class of gapped one-dimensional chiral Hamiltonians, that the topological winding number calculated from the bulk Hamiltonian is equal to the number of pairs of the zero energy edge states [161].

Note that although the value of ν associated to either dimerization depends on the definition of the unit cell, in finite size chains the choice is unambiguous since it is defined by the hopping amplitude between the first and second sites of the chain. This is however different in the topological insulators in two or three dimensions, where the topological invariant (Chern number for example) does not depend in any way on the edge.

The bulk-edge correspondence in SSH model will be useful for demonstrating the origin of the edge states in graphene in this chapter, and understanding of the new edge states presented in chapter 5.

We would like to point out here that the winding number (in systems with chiral symmetry) is closely related to another quantity in topological physics, the one-dimensional Berry phase, or also called the Zak phase. This quantity is sometimes also used in literature for expressing the bulk-edge correspondence. It is defined as:

$$\zeta \equiv i \int_0^{2\pi} \langle \Psi| \frac{d}{dk} |\Psi\rangle , \tag{86}$$

where $|\Psi\rangle$ is the wavefunction of an eigen state. In chiral systems the two component wavefunction has the form $|\Psi\rangle = \frac{1}{\sqrt{2}}\left(1, e^{i\phi(k)}\right)$, giving the Zak phase:

$$\zeta = -\frac{1}{2}\int_0^{2\pi} \frac{d\phi}{dk} = -\pi\nu \tag{87}$$

This means that there is a simple relation between the Zak phase and the winding number. However, an important difference is that the Zak phase is defined only modulo 2π, and can only tell if there are odd/even number of topological edge states. On the other side, the winding number can take any integer value and thus contain more information.

4.3 EDGE STATES IN GRAPHENE

4.3.1 *Tight binding calculations*

The easiest way to predict edge states in a finite 2D lattice such as graphene is by calculating the eigenvalues and eigenfunctions of a graphene ribbon. A ribbon is a structure that is infinite (or with periodic boundary conditions) in one direction and finite in the direction perpendicular to it. The use of this geometry is convenient because it allows expanding the wave function into plane waves in the direction where the ribbon is considered to be infinite and simplify the problem for solving the Schrödinger equation.

There are three fundamentally different ways to end a honeycomb lattice and to make edges, due to the fact that the lattice is not Bravais (before taking two atoms per unit cell into account). Those are zig zag edge, depicted in fig. 37(a), armchair edge fig. 37(b) and bearded edge, fig. 37(c). In this study the edges are oriented along the $y-$axis in the case of the zig-zag and the bearded edges and along the $x-$axis for the armchair edge.
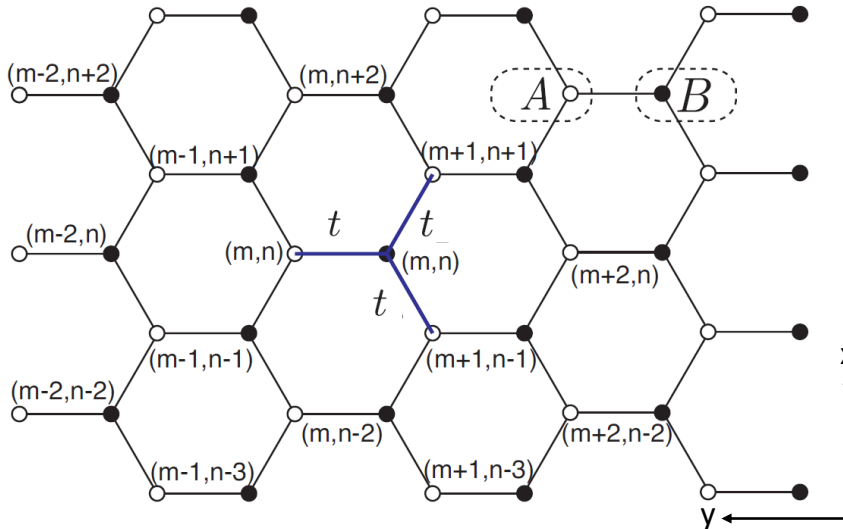
Figure 36: **Graphene nanoribon with bearded edges**

Let us see how we can calculate eigen states of a graphene ribbon. We consider, first a ribbon with bearded edges, like the one in depicted in fig. 36. The real space graphene Hamiltonian reads:

$$H = -t \sum_{\text{m-n is even}} \left(a_{m,n}^\dagger b_{m,n} + a_{m+1,n+1}^\dagger b_{m,n} + a_{m+1,n-2}^\dagger b_{m,n} + h.c. \right) \tag{88}$$

where $a_{m,n}^\dagger$ $(b_{m,n}^\dagger)$ are operators that create a particle at sub-lattice A(B), in the unit cell m, n, that is at positions $\mathbf{r}(A_{m,n})(\ \mathbf{r}(B_{m,n}))$. Equivalent definitions apply for the annihilation operators.

If the periodic boundary conditions are imposed in the direction parallel to the edge (here, $x-$ direction) the creation operator $a_{m,n}^\dagger$ can be expressed as:

$$a_{m,n}^\dagger = \frac{1}{N} \sum_{k_x} e^{-ik_x x_m} a_n^\dagger(k_x) \tag{89}$$

where x_m is the $x-$ coordinate of the position vector $\mathbf{r}_{m,n} \equiv m\mathbf{a_1} + n\mathbf{a_2}$. Similar expressions can be found for operators $b_n^\dagger(k_x), a_n(k_x), b_{n(k_x)}$

By inserting these expressions in 94, summing over m and defining $\theta \equiv (e^{-i\frac{\sqrt{3}}{2}ak_x} + e^{i\frac{\sqrt{3}}{2}ak_x}) = 2\cos(\frac{\sqrt{3}}{2}ak_x)$ we obtain Hamiltonian in basis $(a_n^\dagger(k_x), b_n^\dagger(k_x))$ where n counts the number of unit cells in the direction perpendicular to the edge, $n \in (1, N)$:

$$\mathcal{H}(k_x) = -t \begin{pmatrix} \ddots & & & & & & & \\ & 0 & 1 & 0 & 0 & 0 & 0 & \\ & 1 & 0 & \theta & 0 & 0 & 0 & \\ & 0 & \theta & 0 & 1 & 0 & 0 & \\ & 0 & 0 & 1 & 0 & \theta & 0 & \\ & 0 & 0 & 0 & \theta & 0 & 1 & \\ & 0 & 0 & 0 & 0 & 1 & 0 & \\ & & & & & & & \ddots \end{pmatrix} \tag{90}$$

which has $N \times N$ elements. The spectrum of a graphene nanoribbon can be obtained by diagonalizing this Hamiltonian for each value of k_x.

In the calculation the difference between bearded and zigzag case is that, to calculate the bearded edge, one starts from the A sub-lattice and ends at the B sub-lattice. For the zigzag, one starts from the B sublattice and ends at the A sublattice. In the case of the armchair edge the ribbon is infinitely long along x-direction and similar expressions can be obtained.

In figures 37(d,e,f) the band structure of ribbons with zig-zag, armchair and bearded edges are shown, obtained by numerically solving Schrödinger equation with graphene ribbon Hamiltonian with $N = 50$, and taking into account both the nearest neighbor hopping t and the next nearest neighbor hopping $t' = 0.01t$. In figure 37 we can observe edge bands appear for the zigzag and bearded edges but not for the armchair. They appear as zero energy quasi flat bands, connecting the Dirac cones (they are flat for $t' = 0$). The regions in momentum space supporting the edge states are complementary. The zigzag
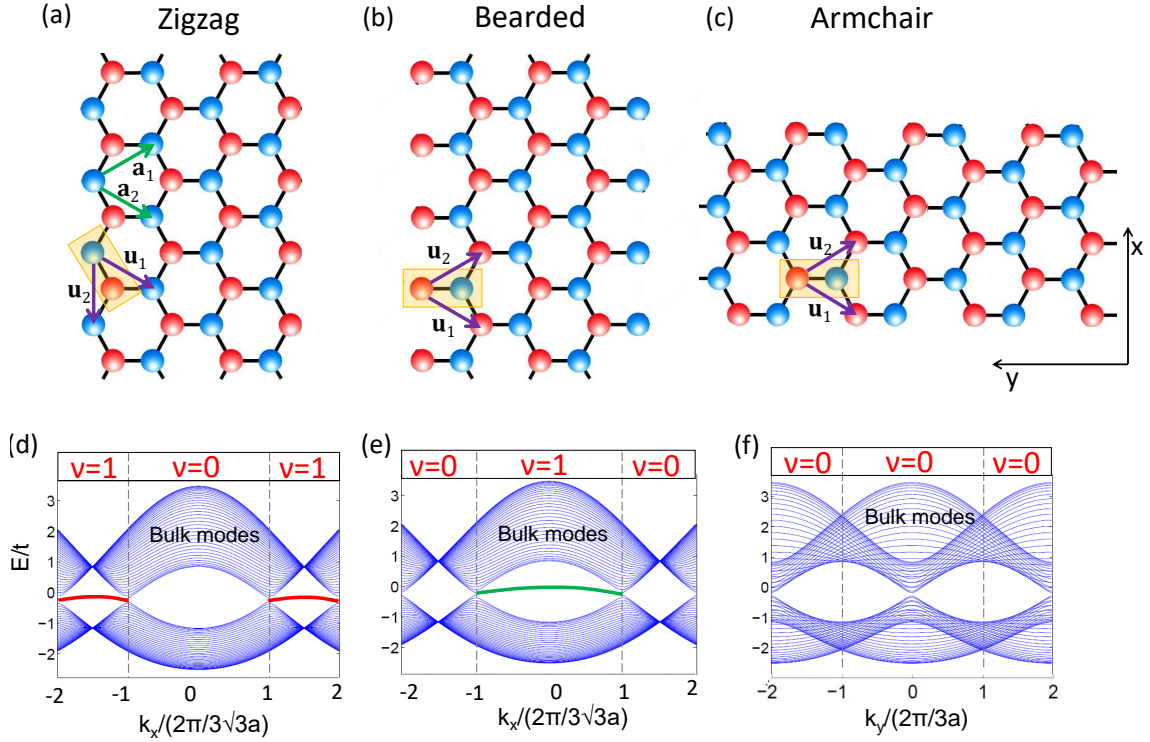
Figure 37: **Edge states in graphene ribbons, the tight-biding calculation.** (a-c) Graphene ribbons with the three different types of edges: zig-zag, armchair and bearded. (d,f) Calculated band-structure for graphene ribbons with bearded (green) and zigzag (red) edges. The different blue lines correspond to the projection on the $k_y - E$ plane of the dispersion of the different transverse modes due to the confinement in the x-direction. The red and green lines show the edge bands corresponding to zigzag and bearded terminations, respectively. (e) The calculation done for the armchair edge (here, parallel to the x-direction) does not feature edge states.

edge band appears for $k_{x(zig-zag)} \in [-2, -1]k_{x0} \cup [1, 2]k_{x0}$, and the bearded edge band for $k_{x(bearded)} \in [-1, 1]k_{x0}$, with $k_{x0} = 2\pi/(3\sqrt{3}a)$ and a being the inter atom distance.

Spatial distributions of the wave functions can be obtained by solving the eigen problem of the tight binding Hamiltonian. They reveal that the edge states are localized on the outermost sites, with an exponentially decaying amplitude into the bulk $\psi_{edge}(x) \sim e^{\frac{-x}{l_e}}$. In the absence of next-nearest-neighbor coupling the penetration length has the following analytic expression: [162]:

$$l_e = \frac{3a}{2 \left\| ln\left(2\cos(k_y\sqrt{3}a/2)\right) \right\|} \tag{91}$$

The finite penetration results in a finite width in momentum space for the edge states. Figure 38(b) shows the $k_x - k_y$ momentum distribution of the zigzag and bearded edge states calculated by Fourier transforming with respect to y the spatial distributions of the edge state for each k_x as obtained from the solution of the tight-binding Hamiltonian. The edge modes are spread around straight lines connecting the Dirac points at the border of the Brillouin zone, as schematically represented in figure 38(a). The edge states with
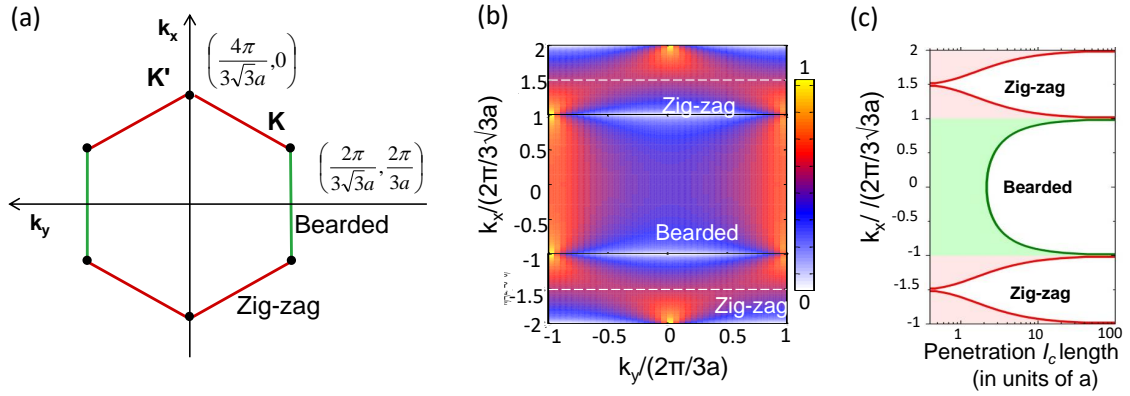
Figure 38: **Penetration length of graphene edge states.** (a) First Brillouin zone showing the regions in k space where the edge states are expected. (b) Simulation of the momentum distribution for zigzag and bearded edge states obtained by Fourier transforming along the x-direction the calculated spatial wavefunction of the edge states corresponding to different k_y values. Dashed lines show fully delocalized edge states along k_x. (c) Penetration length of the amplitude of the edge states wavefunction according to equation 91. As in (a) green color is used to depict bearded edge states, and red zigzag

k_x corresponding to the center of the zigzag band ($k_x = \pm 1.5 k_{x0}$) are fully delocalized in the k_y-direction (see dashed line in figure 38(b)). Correspondingly, these states are spatially fully localized, down to a single site (see figure 38(c)). In the case of the bearded edge state, maximum spatial localization is attained at $k_x = 0$, with a penetration length of $2.2a$, larger than the maximally localized zigzag edge state. At the Dirac points, the penetration length becomes infinite, and the edge states merge into bulk modes.

4.3.2 *Bulk edge correspondence in graphene*

By solving numerically the eigen problem of a ribbon Hamiltonian we can predict the emergence of the edge states for certain type of edges. However, we dont dispose of any criteria for their appearance, nor information about their behavior under lattice deformation.

Such insights can be obtained by analyzing some general properties of graphene Hamiltonian. Indeed, it has already been shown, using various slightly different approaches, that for graphene it is possible to establish a bulk-edge correspondence similar to the one which exist in topological insulators [163, 79]. This correspondence will help us to understand better the edge states which we study experimentally in this chapter, and also to explore the nature of the newly discovered edge states in orbital graphene, presented in the next chapter.

In previous section we applied the periodic boundary conditions in one direction of the graphene lattice, and effectively reduced a two-dimensional problem to an equivalent one-dimensional problem. Let us have a closer look at the general form of the Hamiltonian 90 we obtained.

It is not hard to notice that this Hamiltonian has the same form as the one describing a one dimensional chain with staggered hopping amplitudes, the so-called SSH model. We can rewrite Hamiltonian 90 as:

$$H = -t \sum_{m=1}^{N} \left(a_m^\dagger b_m + h.c. \right) - t \sum_{m=1}^{N-1} \left(\theta(k_{||}) b_m^\dagger a_{m+1} + h.c. \right), \tag{92}$$

where N is the number of unit cells in the direction where the ribbon is finite, t the nearest neighbor hopping, and θ is a function of the momentum $k_{||}$ parallel to the edge that depends on the type of edge. For each value of $k_{||}$ we can easily identify this Hamiltonian with one given in eq. 82 that describes the SSH model. Hopping amplitude within the unit cell dimer, t, is the same as the one in honeycomb lattice and the effective hopping amplitude between adjacent unit cell dimers in the chain is θt.

This means that for each value of $k_{||}$ we can calculate the winding number ν as in eq. 85 to predict the appearance of edge states. The values of ν are indicated on top of the panels in the figures 37(d-f). In case when $t < \theta$ $\nu = 0$, while if $t > \theta$ $\nu = 1$. Non-zero value of the winding number indicates the region of existence of pairs of edge states in graphene ribbon with zig-zag and bearded edges.

Here, we have established the direct connection between graphene ribbons and SSH model in order to understand topological origin of graphene edge states. An alternative (analogue) approach that leads to this same resultshas also been developed. In [79] the authors examined directly topological properties of a graphene Hamiltonian in momentum space:

$$\hat{\mathcal{H}}_s = -t \begin{pmatrix} 0 & f_s^* \\ f_s & 0 \end{pmatrix}, \tag{93}$$

with $t_s > 0$ being the hopping amplitude and the factor $f_s = 1 + e^{i\mathbf{k}\cdot\mathbf{u}_1} + e^{i\mathbf{k}\cdot\mathbf{u}_2}$. Here, the unit cell vectors $\mathbf{u}_{1,2}$ are those who contain the information about the considered edge. They can be taken as follows: $\mathbf{u}_1 = \mathbf{a}_1$, $\mathbf{u}_2 = \mathbf{a}_1 - \mathbf{a}_2$ for zigzag edges, and $\mathbf{u}_1 = \mathbf{a}_1$, $\mathbf{u}_2 = \mathbf{a}_2$ for bearded and armchair, given in terms of the reference vectors $\mathbf{a}_{1,2}$ defined in Fig. 37(a). The corresponding unit cell dimers are also given in the figure.

The number of zero-energy edge states is determined by the winding of the phase of the off-diagonal component ($f_s = |f_s| e^{i\phi(\mathbf{k})}$) for each value of $k_{||}$ [163, 164, 79]:

$$\mathcal{W}(k_{||}) = \frac{1}{2\pi} \int_{BZ} \frac{\partial \phi(\mathbf{k})}{\partial k_\perp} dk_\perp, \tag{94}$$

where integration is performed over momentum $k_{||}$ perpendicular to the edge in the first Bz.

This expression has similar (analogue) form to the one used to calculate winding number in SSH Hamiltonian in momentum space eq. 84.

4.4   IMAGING OF THE EDGE STATES IN POLARITON GRAPHENE

4.4.1   *State of the art*

Creation of artificial systems offers new, advantageous ways to study edge states. Before presenting our results, we would like to mention other works on this topic.

The spatial and momentum distributions of certain edge wavefunctions have been studied using coupled waveguides in 2014 [88] by the group of M. Segev and A. Szameit. The honeycomb lattice was realized by femtosecond-laser writting in fused silica, fig. 39(a). Then the system is excited at the edge with an elliptically shaped HeNe laser spot, under a variety of incident angles related to different values of momentum parallel to the edge. The authors demonstrated that the light emerging from the output facet of the sample is confined to the edge for the values of momenta where the edge states are predicted in a honeycomb lattice, fig. 39(b) and spread into the bulk for other values, fig. 39(c).

Figure 39(d) shows the fraction of optical power that remains confined on the edge of the structure for different values of momenta, edge being defined as the two outer rows of waveguide lattice. When the lattice is excited at the zig-zag edge we can see (green line) that the fraction of optical power is strongly increased for the interval $ka = (-4\pi/3, -2\pi/3) \cup (2\pi/3, 4\pi/3)$ where the edge state is theoretically predicted to exist. The situation is different for the bearded edge (blue line), where the maximum of the optical power is around $ka = 0$, related to the bearded edge state in graphene.

While it allowed the first study of graphene edge states using a simulator, coupled waveguides don't provide the combined information on real, momentum, and energy phase spaces needed to reconstruct the band dispersion of the eigenfunctions, and in particular of the edge states.

Another artificial graphene system in which edge states have been studied is the one of coupled microwave resonators [94]. In that system, a peak in density of states measurements is observed at zero energy when the signal from the edges is analyzed 39(e). The authors also demonstrated how edge states can be manipulated by distorting the lattice. Edge states in armchair type of edge are created in that way, figure 39(f, g).

Coupled waveguides
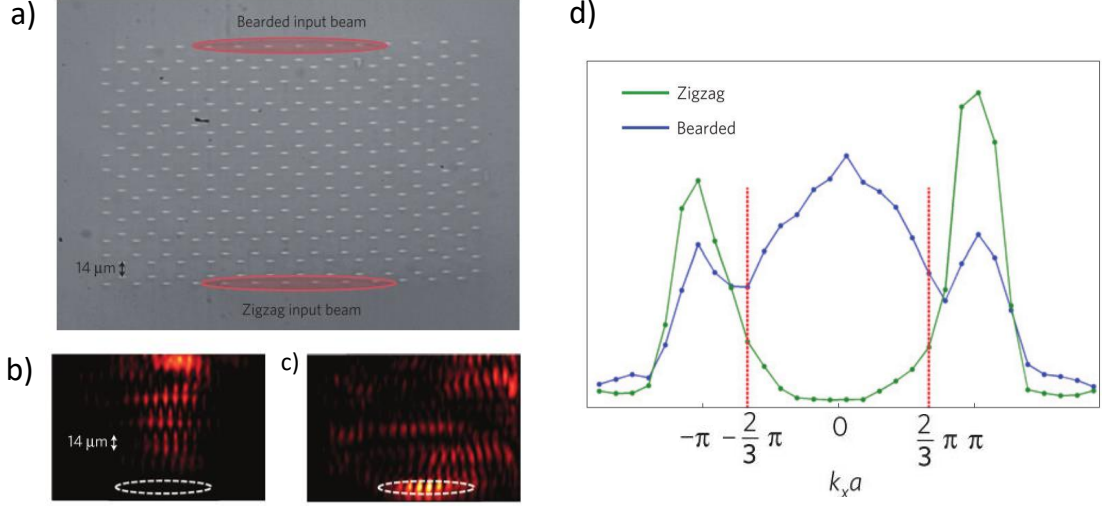
Microwave resonators
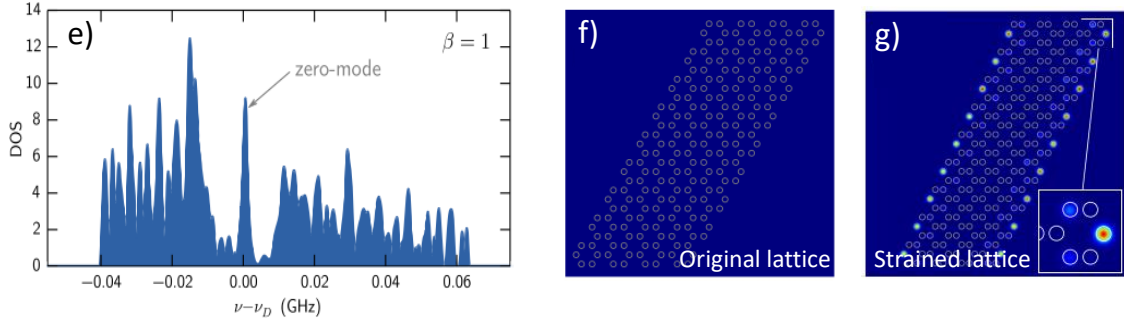
Figure 39: **Momentum-resolved measurements of edge states in a photonic honeycomb lattice.** [88] (a) Microscope image of the input facet of a femtosecond-written honeycomb lattice. Red ellipses mark the input beams for the bearded and zigzag edges. (b,c) Wavefunction emerging from the output facets for: (b) probe beam launched at zigzag edge at $k = 0$, leading to diffraction into the bulk, (c) probe launched at zigzag edge at $k \leq \pi/a$ leading to edge confinement due to the presence of an edge state. Dashed ellipses mark the expected position of the output beam when an edge state is present. (d) Fraction of power confined to the edge for the zigzag (green) and bearded (blue) edges; the peaks indicate strong confinement due to the presence of edge states. Taken from [88](e) zigzag edge state observed trough density of states (f, g) deformation of the lattice leads to creation of armchair edge states. Taken from [94]

4.4.2   *Polariton honeycomb lattice*

In this section we will present the results of the experimental study of edge states in a polariton honeycomb lattice.As discussed in chapter 3 the design of the lithography mask allows controlled creation of the geometry of the edges. Figure 40 shows an optical microscope image of a lattice with the three types of edges: zig zag, bearded and armchair. The diameter of the pillars is $d = 2.75\mu m$ and the inter pillar distance $a = 2.4\mu m$. We perform low temperature photoluminescence experiments after a non-resonant excitation with Ti:Sapph monomode laser at 740 nm, as described in chapter 3, sections 3.3.5 and 3.3.6. The sample is at $-17meV$ exciton-photon detuning (measured at **k**=0), thus corresponding to photonic polaritons. The emission is collected using high NA=0.65 objective and analyzed, in real and momentum space, using a spectrometer coupled to a CCD camera.
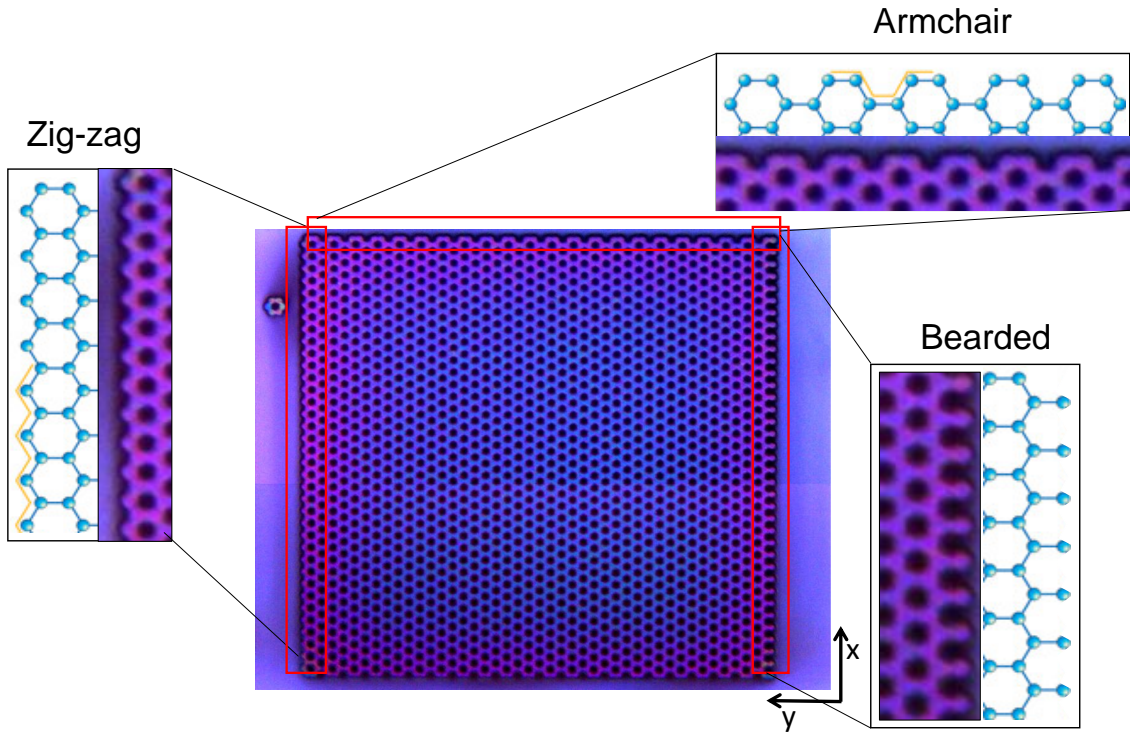
Figure 40: **Optical microscope image of the sample.** The three considered types of edges: zig-zag, armchair end bearded are zoomed and compared to the drawing of the corresponding type of the edge.

In the first configuration of the experiment we use a small Gaussian spot with FWHM of about $3\mu m$, covering approximately one pillar, in order to excite selectively bulk or edge regions of the lattice and compare the results.

Figures 41 (a-c) shows the momentum-space emission from the bulk, that we have analyzed in detail in the previous chapter, section 3.5.2. In (a), the emission at the zero energy is reproduced. We observe again six isolated bright spots at the Dirac points, which identify the first Brillouin zone hexagon. This map of momentum space will allow us to better visualize the directions in momentum space of interest when studying the edge

states. Figure 41 (b) shows the energy-resolved far-field emission along line 1, parallel to k_x at $k_y = 1.7(2\pi/3a)$. As this line doesn't pass through the Dirac points, two bands are gapped. The black curve in figure 41(b) depicts the dispersion expected from the tight-binding approximation with $t = 260\mu eV$ and $t' = -0.1t$ (i.e. $-25\mu eV$).
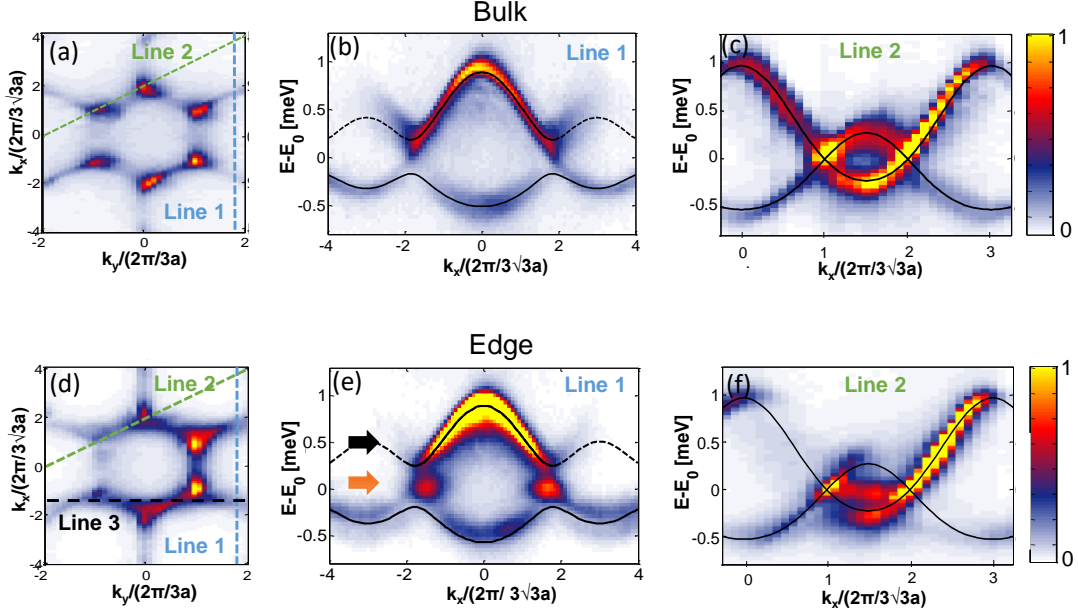
Figure 41: **Zig zag edge, momentum-space emission.** (a), (d) Measured photoluminescence intensity in momentum space at the energy of the Dirac points ($E_0 = 1569.2meV$) under bulk (a) and zigzag edge (d) excitation. (b), (e) Spectrally resolved far-field emission along line 1 in (a) and (d), passing through the second Brillouin zone, for excitation in the bulk (b) and in the zigzag edge (d). (c), (f). Measured dispersion along line 2 in (b) and (d), respectively. The black lines show fits to the tight-binding honeycomb dispersion.

4.4.3 *Zig-zag edge*

We focus now on the situation where the excitation spot is moved to one of the external pillars forming the zigzag edge. When we consider the edge of the lattice, translation symmetry is broken, and momentum perpendicular to the edge is not a good quantum number anymore. However, certain structure in momentum space is retained (as calculation in fig. 38 (b) shows), enabling us to still use the tomography technique (as explained in section 3.3.6) to reveal energy bands in two dimensional momentum space.

Figure 41 (d) shows the luminescence at the energy of the Dirac points for this excitation configuration. The Dirac cones are now continuously connected by a bright line in the $k_{y(zig-zag)}$ region while there is a dark region in the middle at the $k_{y(bearded)}$ region, as expected from figures 38(a), (b). Additionally, along line 3 we observe a spread emission in k_x, indicating an edge mode fully localized in real space. This feature matches the state marked by a dashed line in the simulation shown in figure 38(b). The overall emitted

intensity in momentum space in fig 41 (d), is asymmetric with respect to $k_y = 0$, since polaritons can only flow toward the inner part of the lattice.

When analyzing the energy-resolved emission along line 1, fig. 41(e), two additional lobes are clearly observed in the gap between the upper and lower bands. Their location in momentum space corresponds to that expected for the edge states shown in figure 38(a) (red lines). The measured full-width-at half- maximum of the lobes along the k_x-direction in figure   41 (e) is $0.75k_{x0}$, in agreement with the theoretical prediction for the edge states along the same line in momentum space extracted from the simulation shown in figure 38(b), within a 20% error (figure to add eventually).

Note that in the presented data, emission from the bulk states is also present when we excite the lattice at the outermost pillar. This should not be surprising taking into account the finite density of states of bulk bands near the edge and the Gaussian excitation spot.

The quasi-dispersionless character of the band associated to the edge states can be evidenced by selecting a cut in momentum space along line 2 in figure 41(d), which contains the $k_{x(zig-zag)}$ region. Figure 41(f) shows a flat band linking the two Dirac cones. No such state is present in the bulk (figure 41(c)), where only the corresponding bulk dispersion is detected. In figure 41(f) only the states with group velocities propagating towards the bulk(positive slope) emit light, explaining the asymmetry in the emission.

Although bulk bands are asymmetric around $E = 0$ in our system, the edge states band stays flat. The origin of this asymmetry can be twofold. One possibility is the presence of the next nearest neighbor hopping (NNN) t'. It is well known [47] that nonzero t' breaks particle-hole symmetry in graphene such that bulk bands become asymmetric. NNN also affect the edge states, they loose their perfectly flat character and become slightly dispersive, a feature we don't see in our experiment. However, the magnitude of this effect obtained from the tight binding calculation for $t = 0.26 meV$ and $t' = 0.01t$ is $50\mu eV$, significantly smaller then the measured linewidth, $\approx 200\mu eV$. Presence of NNN hopping remains thus possible and we continue using the NNN and the simple tight binding calculation to achieve a good fitting of the bulk bands.

Another probable explanation is the non orthogonality of the wavefuctions on the two adjacent overlapping pillars. In fact, the tight binding approximation assumes the use of a basis of orthogonal wavefunctions on each lattice which are coupled through a certain hopping amplitude. Physically, the coupling between lattice sites arises exactly due to overlapping of their wavefunctions. This means wave functions are not orthogonal any more. While such deviation from the tight binding approximation is also present in the electronic lattices, it is more pronounced in our photonic system. Calculations that include this effect [article in preparation] show that it influences the bulk bands but does not deform the edge state bands.

In addition to momentum-space imaging, our system allows evidencing the localization of the edge states by looking at the real-space emission. For this purpose, we use a slightly different experimental configuration, with a large Gaussian laser spot, $20\mu m$ in diameter, covering around 30 pillars. In this way, we are able to excite edge modes on several pillars. Figure 42(a) shows the emitted intensity at the energy of the middle of the upper bulk band, 0.5 meV above the Dirac points (black arrow in figure 41(e)). They present the expected honeycomb pattern, with an intensity distribution following the pump spot. Figure 42(c) shows the real-space emission at the energy of the edge state (orange arrow in figure 41(e)).

In this case, the outermost line of pillars shows a much stronger emission, present only on one site in each unit cell (one sublattice). Such shape definitely confirms that the observed modes correspond to edge states in the system.

The fact that the zero energy edge state wavefunction only exist in one of the two sub-lattices is a noticeable feature of graphene lattice. It is a consequence of chiral symmetry (SLS). This symmetry, as we discussed in chapter 2, makes the whole spectrum of a lattice symmetric with respect to $E = 0$. In the bulk, pairs of states have the energies E and $-E$, and are present on both sub-lattices.

A different situation happens at the edges. Chiral symmetry, which is also called sub-lattice symmetry, given by the symmetry operator $\hat{\Gamma}$, allows to can define orthogonal sub-lattice projectors $\hat{P}_A$ and $\hat{P}_B$:

$$\hat{P}_A = \frac{1}{2}(\mathbb{1} + \hat{\Gamma}), \quad \hat{P}_B = \frac{1}{2}(\mathbb{1} - \hat{\Gamma}), \tag{95}$$

where $\mathbb{1}$ represents the unity operator on the Hilbert space of the system. Note that for projectors: $\hat{P}_A + \hat{P}_B = \mathbb{1}$ and $\hat{P}_A \hat{P}_B = 0$. For the zero energy edge state we can then write:

$$\hat{H}\left|\psi_n\right\rangle = 0 \qquad \hat{H}\hat{P}_{A/B}\left|\psi_n\right\rangle = \hat{H}(\left|\psi_n\right\rangle + \hat{\Gamma}\left|\psi_n\right\rangle) = 0, \tag{96}$$

meaning that the edge states can have support only at the one sub-lattice, as we observe experimentally.

Experimental observation of edge states real space patterns can be further supported by simulating the polariton honeycomb lattice using a driven-dissipative model. This model describes more accurately our simulator than the simple tight-binding calculation. To implement it, we added to the tight-binding Hamiltonian a monochromatic resonant pump and cavity losses of $\gamma = 0.1t$ for all lattice sites. The Schröedinger equation in that case reads:

$$i\hbar\frac{\partial}{\partial t}\psi = \left(H - i\frac{\gamma}{2}\right)\psi + F_p e^{i\omega t}, \tag{97}$$

where H is the tight-binding Hamiltonian. We calculate the steady state with a pumping beam F_p at $\hbar\omega = E_0$, with the Gaussian envelope that covers the whole sample with an incident momentum $k = (1/(2\sqrt{(3)}), 3/2)k_{y0}$, corresponding to the center of the segment connecting the Dirac points where the zigzag edge state is expected. In that way simulation describes the transmission through the sample when exciting the lattice on resonance with a CW laser of frequency ω. It is, however expected to also describe well the spatial profile of a steady state under non-resonant excitation in a reflection geometry, which we measure experimentally.

The result is shown in figure 42(d), revealing the edge state fully localized on the outer-most pillars, as expected from equation 91. The same simulation at the energy of the bulk bands shows emission from the whole lattice, as depicted in figure 42(b).

Bulk band energy
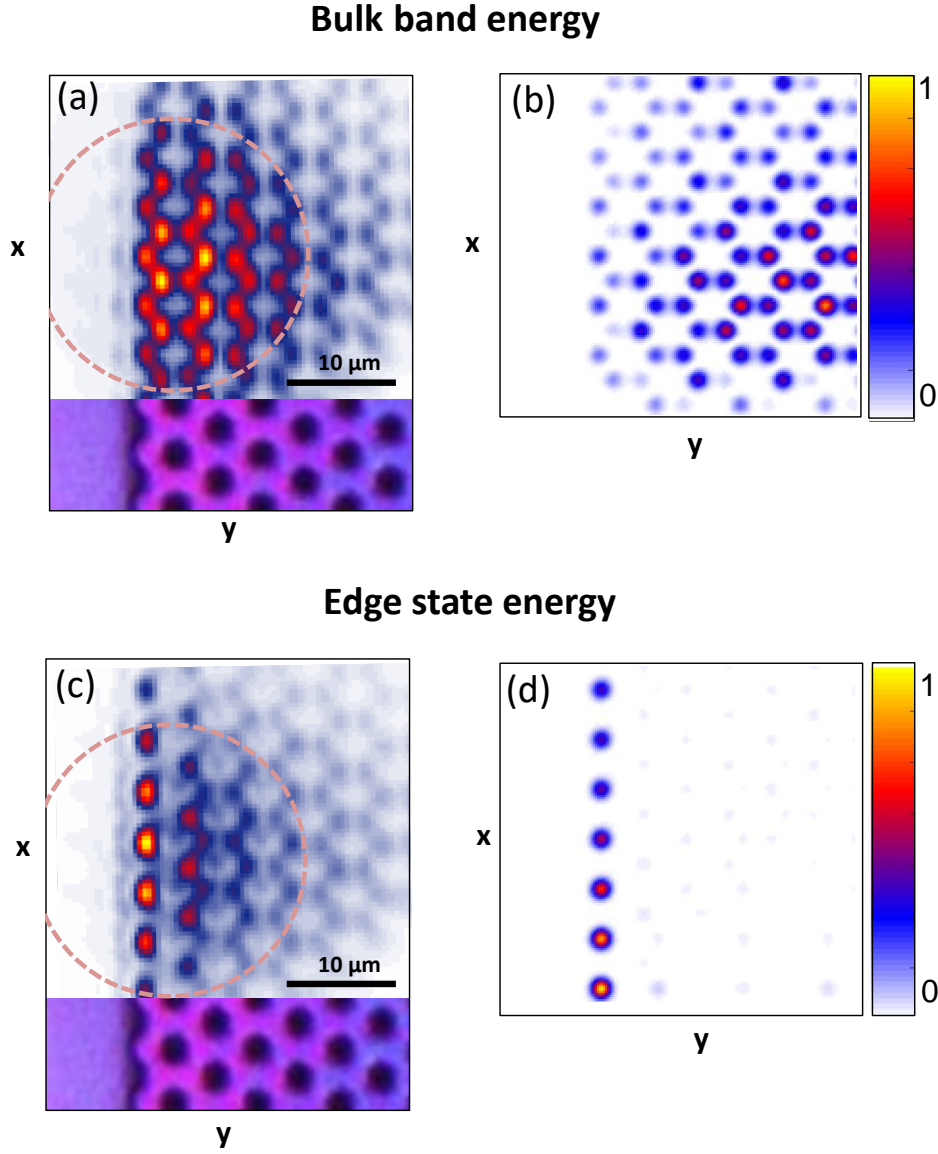
Edge state energy

Figure 42: **Zig zag edge, real-space emission.** (a), (c) Measured real-space emission at the energy of the bulk band (a) (energy marked with a black arrow in figure 41)(e)), and at the energy of the edge state (c) (red arrow in figure 41(e)). Dashed lines show the half maximum intensity of the excitation laser spot. The lower part of the panels shows an optical microscope image of the edge. (b), (d). Simulations of emission of a driven-dissipative polaritonic honeycomb lattice coherently pumped at an energy corresponding to bulk states (b), and at the energy and momentum of a zigzag edge state (d).

4.4.4 *Bearded edge*

Bearded terminations have also been predicted to exhibit edge states[162]. The experimental investigation of this type of edge band is not straightforward in carbon graphene where dangling bonds specific to this kind of termination are chemically unstable. Thus, it has been studied mostly theoretically and using graphene analogues [94, 88]. To study

the energy-momentum dispersion of this kind of edge state, we have fabricated a lattice containing bearded edges, with pillar diameter of $d = 2.5\mu m$, and interpillar distance $a = 1.76\mu m$, giving the same tight-binding tunneling amplitudes as in the lattice with the zigzag edges. However, the smaller pillar diameter results in non-radiative losses that give rise to a larger linewidth ($\sim 350\mu eV$). Experiments are performed under the same conditions as described previously, in both real and reciprocal space configurations.

Figure 43(a) shows the momentum space at the energy of the Dirac points when exciting the bulk of the lattice using a small excitation spot, ($3\mu m$). Again, we are able to identify the six Dirac points of the first Brillouin zone with gaps between them. They are less pronounced than in fig. 41 due to the broader linewidth. The bulk dispersion along line 1 defined in figure 43(a), containing the $k_{y(bearded)}$ region, is shown in figure 43(b). The expected shape of the bands is observed, with crossings at two Dirac points. When the probe is placed on the edge of the sample, different patterns are observed. The momentum-space map at the Dirac point energy shows an enhanced emission in the $k_{y(bearded)}$ region in fig. 43(e)), revealing the edge states band. Its full-width-at-half-maximum along the k_x-direction at $k_y = 0$ is $0.50k_{x0}$, with $k_{x0} = 2\pi/(3a)$, in excellent agreement with the prediction in figure 38(b), where this value is $0.45k_{x0}$. The dispersion along line 1 (fig. 43(f)) shows now a flatband connecting the two Dirac points in the momentum-space region corresponding to $k_{y(bearded)}$.

To study the spatial location of the state we perform measurements and simulations of the real-space emission under excitation with a large pump spot ($20\mu m$). Figure 43(h) shows a simulation of the emitted intensity when exciting the edge state at $k_y = 0$. The observed bearded edge state resides on the sub-lattice corresponding to the bearded ending, and it penetrates several lattice sites into the bulk, as expected from equation 91. In the experiment (figure 43(g)), we observe bright spots on the outermost pillars of the lattice. This emission is absent at the energy of the bulk modes (figure 43(c)), and thus it corresponds to the edge state. The penetration depth is, however, difficult to estimate experimentally due to the emission from the bulk modes from the crystal at the same energy.
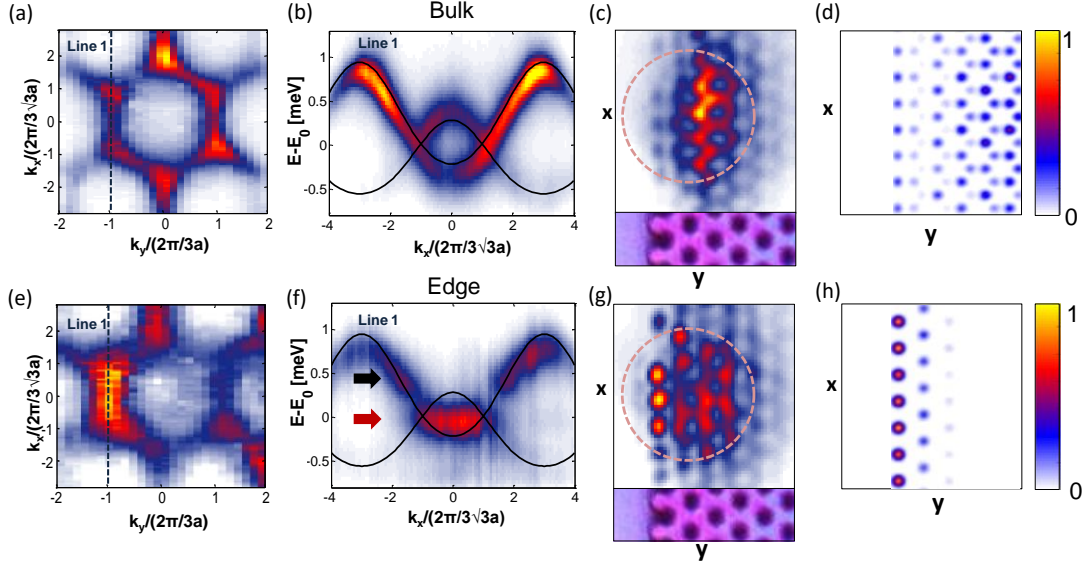
Figure 43: **Bearded edge.** (a), (e) Measured photoluminescence intensity in momentum space at the energy of the Dirac points, in the bulk (a) and on the bearded edge (e). (b), (f) Spectrally resolved far-field emission along line 1 in (a), passing through the region where edge states are expected, in the bulk (b) and on the bearded edge (f). (c), (g) Measured real-space emission at the energy of the bulk band (black arrow in (f)), and at the energy of the edge state (red arrow in (f)). $E_0 = 1578.1meV$. Dashed lines show the half-maximum intensity of the excitation laser spot. The polarization of detection is parallel to the edge (vertical). (d), (h) Simulations corresponding to resonant excitation of bulk and edge modes respectively.

In the case when the excitation spot is placed in the armchair edge, no edge states have been observed. This is consistent with the predictions based on the winding number 35.

4.4.5 *Polarization effects*

One of the specific characteristics of polaritons, different from other photonic simulators like coupled waveguides or microwave resonators, is their significant polarization-dependent properties. The polarization-dependent penetration of the electromagnetic field in the Bragg mirrors forming the cavity results in a TE-TM splitting between linearly polarized modes, whose magnitude increases quadratically with the in-plane momentum [165]. This splitton is responsible for the so-called optical spin-Hall effect [166, 167, 168]. Additionally, the polarization-dependent hopping between coupled micropillars [169] has been shown to give rise to a spin-orbit coupling effects. In hexagonal photonic molecules this gives rise to a fine structure which could be revealed in polariton condensation regime [140].

It is thus to examine polarization effects in polariton HCL. Figure 44(a) reproduces figure 41(b) showing the energy-resolved far-field emission upon small spot excitation located at the center of the lattice. Here, we select the emission linearly polarized parallel to the direction of the edge (y), as in all the results we have presented so far. When selecting the opposite linear polarization direction, fig. 44(b) we do not observe significant effects. The reason is that the period of the lattice is big enough to restrict the first Brillouin zone

to small values of in-plane momenta where the TE-TM splitting is expected to be smaller than the measured linewidth.

Nevertheless, we do observe significant polarization effects when analyzing the emission from the edge states. When selecting linear polarization perpendicular to the edge, figure 44(d), we observe that the edge state is located at a lower energy $\Delta E = 160 \mu eV$, with respect to the polarization parallel to the edge as given in the figure 41(b) and reproduced here in fig. 44(c). Similar polarization splittings have been reported in 1D polariton microwires [23, 170]. The splitting may arise from the interplay between two effects. First, the asymmetric photonic confinement along and perpendicular to the edge could induce a linear polarization splitting of the confined photonic modes. Second, the finite-size etched structure may give rise to strain crystal fields resulting in the splitting of the excitonic modes with polarization directions along and perpendicular to the strain field. In the considered structure, a strain mismatch between the x- and y-directions could take place close to the edge of the honeycomb lattice. Given the significant value of ΔE, the excitonic origin of the splitting seems the most likely. Indeed, photonic confinement effects are expected to result in polarization splittings of $5 - 10 \mu eV$ in this kind of structures [22], much smaller than the linewidth. Note that the strain field might penetrate a few sites into the lattice, thus affecting the energy of the bulk bands close to the edge.
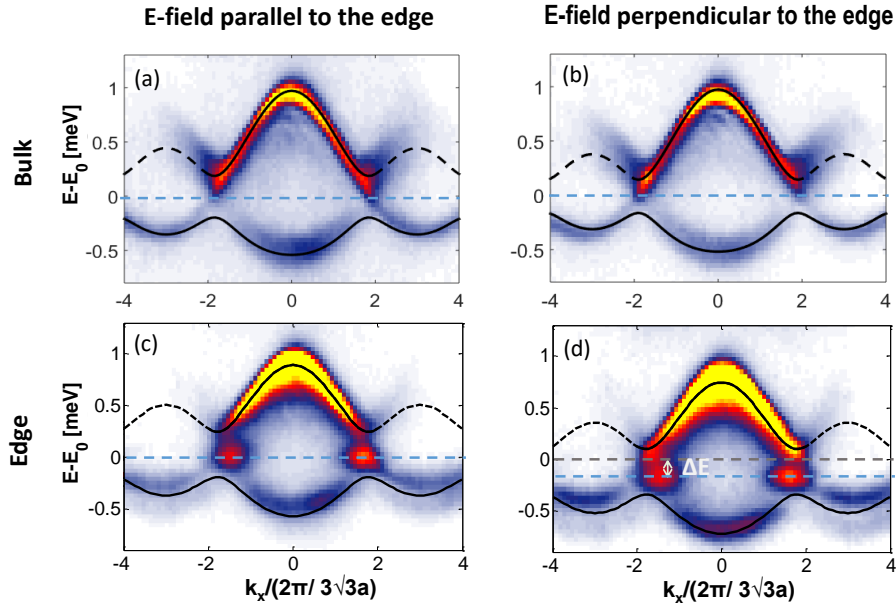
Figure 44: **Polarization effects.** Measured dispersion along line 1 in fig.41, when the excitation is performed on the middle of the lattice (a,b) and on the zigzag edge (c,d). Linear polarization of detection is parallel (a,c) and perpendicular (b,d) to the edge. ΔE indicates the energy splitting between the modes with opposite linear polarizations, detected when the excitation is performed on the edge (c,d). No such splitting is present when the lattice is excited in the middle.

4.5 CONCLUSION

In low dimensional systems such as graphene, the samples often have small size, and their electric and magnetic properties can importantly change with the appearance of the edge states.

In order to understand the nature of edge states in graphene, a short review of the theory of the edge states in the finite size crystals was given in the beginning of this chapter.

As a system characterized by symmetries such as particle-hole, time reversal and chiral symmetry, graphene features edge states with particular properties. They are different from the Tamm states, associated with the lattice defects, and can be classified as the Shockley states [171]. Thanks to the symmetries of the crystal, graphene ribbons can be mapped to the one dimensional topological insulator (the SSH model), which allows to predict appearance of the graphene edge states, that is, to establish a bulk edge correspondence. This bulk edge correspondence is however, different from the one in Chern insulators, as it depends on the type of the edge.

We have used a polariton graphene simulator to directly observe the localized states associated with graphene edges. Clear identification of the different kinds of edge states was possible thanks to the realization of the zig zag and bearded type of the edges in the simulator lattice. Unique visualization of such modes, combining the information on energy and momenta of their wavefunctions, as well as on their spatial form, is obtained trough real-space and far-field imaging of polaritons. Zig zag and bearded edges show zero energy states, connecting the graphene Dirac cones are occupying complementary ranges of momenta parallel to the edge. In real space the eigen functions take nonzero values only one of the two sub-lattices, as imposed by the chiral symmetry of the crystal.

The theoretical and experimental techniques presented in this chapter will be employed to study newly discovered, orbital edge states in polariton honeycomb lattice, which are the topic of the next chapter.

ORBITAL EDGE STATES

The physics of graphene is remarkable in its simplicity. Only two electronic bands, isotropic and cylindrically symmetric, provide the richness of its properties. However, in most other lattices, in both 2D and 3D, unconventional properties originate from higher energy, orbital bands, characterized by a more elaborate geometry. For example, non-trivial topological phases of matter, are in most cases the consequence of band inversion. Transport properties of superconductors, 2D materials or strongly correlated systems also depend strongly on their orbital configuration. Many of these systems are hardly understood, and very difficult to study due to the complicated band structure. Creation of emulators bring not only new prospects in the efforts to study these systems, but also the possibility to use the orbital degree of freedom to construct states with new properties [172].

In this chapter we will employ polariton HCL to study the orbital version of graphene. This structure was proposed theoretically for the first time in 2007 by Wu and co-workers, who considered a honeycomb lattice with $p_{x,y}$ orbitals in each lattice site [173, 174]. Experimentally, it was first reported in the polariton-based graphene simulator created in our group [28].

In the first part we will review both the theoretical proposal and the first experimental observation of orbital graphene. The central part will be devoted to the discovery and detailed study of edge states in this system.

First, we will explore experimentally the emission from the zig zag edge and demonstrate the existence of two types of edge states, flat and dispersive ones. Then, we will analyse theoretically the Hamiltonians describing the orbital graphene ribbons with different edge types in order to explore weather the discovered edge states have topological origin and are (weakly) topologically protected as in the case of graphene.

Finally, experimental observation of dispersive (i.e propagating), edge states in the armchair type of edge will be presented.

5.1 SHORT INTRODUCTION TO ORBITAL DEGREE OF FREEDOM

In addition to charge and spin, electrons in the lattice present an orbital degree of freedom. This degree of freedom reflects the fact that for any atom, the probability of finding an electron in a specific point of the region around it, depends on the electron's energy and angular momentum, given by the discreet quantum numbers $n \in \mathbb{N}_0$ and $l \in [0, n]$, respectively. The corresponding wavefunctions have very different geometry 45 are called orbitals, labeled with letters $s, p, d, f, ..$, corresponding to the angular momentum quantum number $l = 0, 1, 2, 3, 4...$.

When atoms are coupled in a lattice electrons keep some properties originating from their orbital nature. As we have seen in previous chapters, in the case of deep lattices, the tight binding approximation can be employed and electronic states can be described as superposition of atomic states. Two formalisms can be used for that purpose. Usually, a
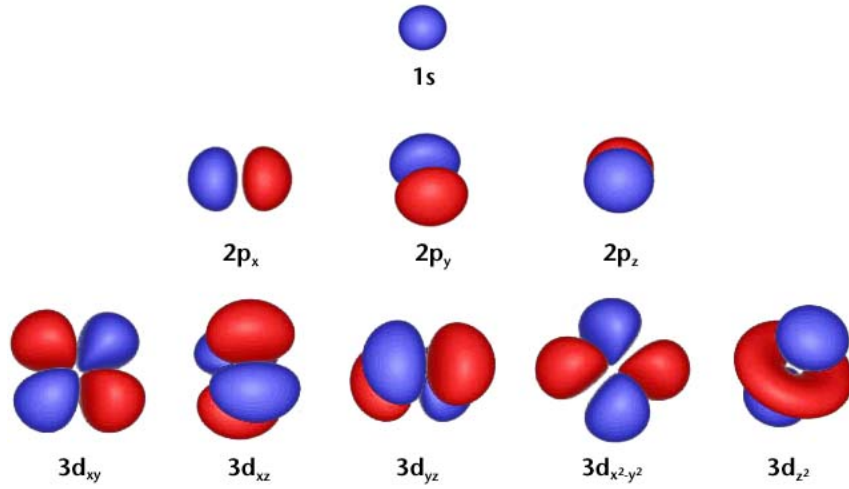
Figure 45: Atomic orbitals

system is described in terms delocalized one-particle Bloch orbitals $\psi_{n,k}(r)$, labeled by a crystal momentum k lying inside the Brillouin zone, and a band index n. Another type of description, in terms of the set of localized orbitals called Wannier functions is also possible. These functions, labeled by a cell index $\mathbf{R}$ and band-like index n can be obtained from Bloch bands by unitary transformations. They allow to better capture some of the physical properties that emerge as the consequence of various spatial forms of electron clouds [175].

Understanding the orbital degree of freedom, and how it combines with those of spin and charge, has helped obtaining models that capture the essence of many complicated materials. A few examples are transition metal oxides, super-conducting cuprates and ferromagnets [176, 177]. More recently, the interest in orbital degree of freedom has taken a new thrust due to the rapid emergence of two-dimensional materials [178], such as black phosphorus [179, 180, 181], and two-dimensional transition metal dichalcogenides [29], whose bands originate from spatially anisotropic atomic orbitals.

Significant efforts have been made toward understanding edge states in these materials. They have been observed in MoS_2 flakes [182], and recent works aim at quantifying their impact in the transport properties [183]. They have been shown to play an important role in lateral hetero-structures of 2D materials, which represent potential building blocks for device applications [184]. In that work, the interface states were studied using scanning tunneling microscopy, facing considerable challenges in creating atomically sharp and straight interfaces. Edge states in orbital modes have also been studied theoretically in connection to $d-$wave superconductivity [163, 185], and spin-orbit coupling in superlattices of nanocrystals [186], systems very hard to realize experimentally with tunable parameters.

A photonic simulator of orbital bands would represent, in that sense, a new way of approaching these topics, and studying the microscopic properties of orbital edge states [187]. In a more general framework, it would provide a platform to simulate some aspects of orbital bands which are essential in various topological insulators with band inversion [30].

5.2 ORBITAL GRAPHENE

We have seen that in graphene, only the p_z orbitals contribute to its properties, as $s-$ and $p_{x,y}$ orbitals hybridize and form the in plane covalent bonds, responsible for the material mechanical properties.

However, in 2007 a structure was proposed in which the particular geometry of the honeycomb lattice is combined with the strong spatial anisotropy of the p orbitals. It is obtained by taking into account p_x and p_y orbitals in each lattice site. These two orbitals are degenerate, have two lobes in orthogonal spatial directions, (see fig. 45) and anisotropic phase distribution (fig. 46(a)). As a result, a band structure with new distinct features is obtained.
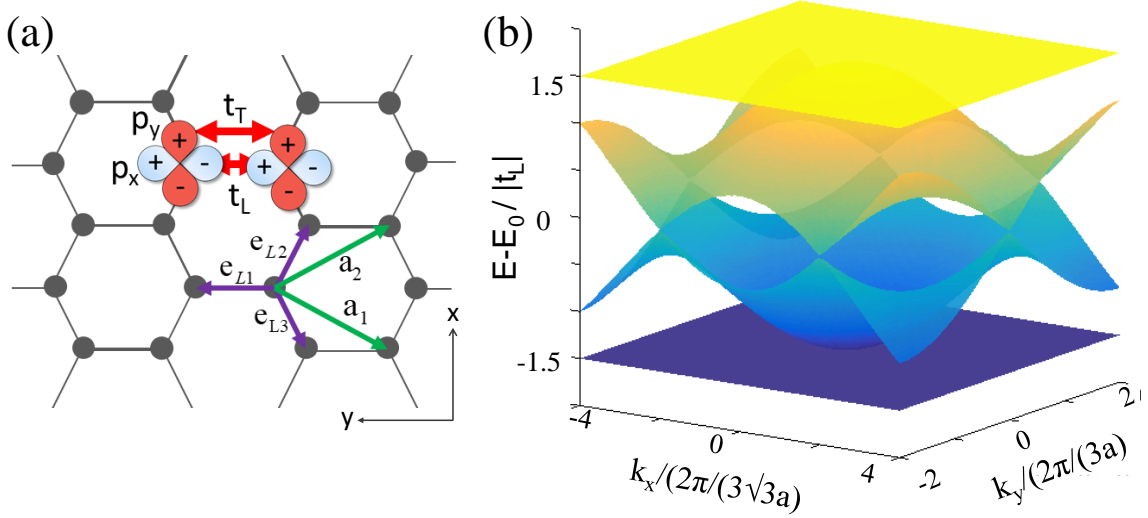
Figure 46: (a) Sketch of orbital graphene: p_x and py orbitals (blue and red, respectively) are present at each site of a hexagonal lattice. They are coupled along the link (t_L) and perpendicular to it (t_T). For both orbitals, there is a π phase difference between the lobes, marked here with $+$ and $-$. (b) Corresponding dispersion, obtained in tight-binding approximation, reveals four bands: two of them are flat, and the other two are dispersive featuring linear intersections.

To reveal it, we construct the eigen problem for the one-particle spinless tight-binding Hamiltonian. In this case, we can distinguish the hopping via orbitals projected to directions parallel and perpendicular to the links connecting the lattice sites, t_L and t_T, respectively (see Fig. 46(a)). The Hamiltonian reads:

$$H_P = - \sum_{(m,n)} \{ t_L (\hat{a}^\dagger_{(m,n)} \cdot \mathbf{e}_{L1})(\mathbf{e}_{L1} \cdot \hat{b}_{(m,n)}) + (t_L \hat{a}^\dagger_{(m+1,n)} \cdot \mathbf{e}_{L2})(\mathbf{e}_{L2} \cdot \hat{b}_{(m,n)}) \qquad (98)$$

$$+ (t_L \hat{a}^\dagger_{(m,n+1)} \cdot \mathbf{e}_{L3})(\mathbf{e}_{L3} \cdot \hat{b}_{(m,n)}) + t_T (\hat{a}^\dagger_{(m,n)} \cdot \mathbf{e}_{T1})(\mathbf{e}_{T1} \cdot \hat{b}_{(m,n)})$$

$$+ (t_T \hat{a}^\dagger_{(m+1,n)} \cdot \mathbf{e}_{T2})(\mathbf{e}_{T2} \cdot \hat{b}_{(m,n)}) + (t_T \hat{a}^\dagger_{(m,n+1)} \cdot \mathbf{e}_{T3})(\mathbf{e}_{T3} \cdot \hat{b}_{(m,n)}) \} + h.c.$$

where

$$\mathbf{e}_{L1}^{\dagger} \equiv (0, -1)a \equiv \mathbf{e}_y \quad \mathbf{e}_{L2}^{\dagger} \equiv \left(\frac{\sqrt{3}}{2}, \frac{1}{2}\right)a \quad \mathbf{e}_{L3}^{\dagger} \equiv \left(\frac{-\sqrt{3}}{2}, \frac{1}{2}\right)a$$

$$\mathbf{e}_{T1}^{\dagger} \equiv (1, 0)a \equiv \mathbf{e}_y \quad \mathbf{e}_{T2}^{\dagger} \equiv \left(\frac{1}{2}, -\frac{\sqrt{3}}{2}\right)a \quad \mathbf{e}_{T3}^{\dagger} \equiv \left(\frac{1}{2}, \frac{\sqrt{3}}{2}\right)a$$

and

$$\hat{a}_{m,n} \equiv \begin{pmatrix} \hat{a}_{(m,n),x} \\ \hat{a}_{(m,n),y} \end{pmatrix} \quad \mathbf{b}_{m,n} \equiv \begin{pmatrix} \hat{b}_{(m,n),x} \\ \hat{b}_{(m,n),y} \end{pmatrix},$$

where, $a_{(m,n),x}$ is the annihilation operator of an electron in p_x orbital in the unit cell given by the position vector $\mathbf{r}_{m,n} \equiv m\mathbf{a}_1 + n\mathbf{a}_2$ on the A sub-lattice, and m, n are numbers of unit cells in $x-$ and $y-$ direction, respectively. Other operators $a_{(m,n),y}$, $b_{(m,n),x}$ and $b_{(m,n),y}$ are defined in a similar way. For each of the three nearest neighbor links (purple lines in fig. 46(a)) the unit vectors $\mathbf{e}_{Li}$ and $\mathbf{e}_{Ti}$, $i = (1, 2, 3)$ are directed respectively along and orthogonally to the link direction. In the Hamiltonian, they serve to extract the projections of the P state respectively along and orthogonal to the link.

To express the Hamiltonian in momentum space, an infinite lattice is assumed (or periodic boundary conditions are imposed in $x-$ and $y-$ direction) and the corresponding operators in momentum space are found by means of the Fourier transform of Hamiltonian 98. We also assume, for the moment, that only t_L is significant, while the effect of a nonzero t_T will be discussed in a later section. In the basis of operators $(a_x(\mathbf{k}), a_y(\mathbf{k}), b_x(\mathbf{k}), b_y(\mathbf{k}))$ we can write the following 4×4 Hamiltonian:

$$\mathcal{H}(\mathbf{k}) = -t_L \begin{pmatrix} 0_{2\times 2} & Q(\mathbf{k})^{\dagger} \\ Q(\mathbf{k}) & 0_{2\times 2} \end{pmatrix}, \tag{99}$$

with

$$Q(\mathbf{k})) = \begin{pmatrix} f_1 & g \\ g & f_2 \end{pmatrix}, \tag{100}$$

where $f_1 = \frac{3}{4}(e^{i\mathbf{k}\cdot\mathbf{u}_1} + e^{i\mathbf{k}\cdot\mathbf{u}_2})$, $f_2 = 1 + \frac{1}{4}(e^{i\mathbf{k}\cdot\mathbf{u}_1} + e^{i\mathbf{k}\cdot\mathbf{u}_2})$, and $g = \frac{\sqrt{3}}{4}(e^{i\mathbf{k}\cdot\mathbf{u}_1} - e^{i\mathbf{k}\cdot\mathbf{u}_2})$, $\mathbf{u}_{1,2}$ are primitive vectors, and $t_L < 0$, to account for the antisymmetric phase distribution of the p-orbitals. To later describe finite size samples, we make a choice of unit cell dimer and primitive vectors such that it allows the full reconstruction of the lattice including its edges. As in the case of $s-$ bands, (see previous chapter, end of section 4.3.2) we take the primitive vectors as follows: $\mathbf{u}_1 = \mathbf{a}_1$, $\mathbf{u}_2 = \mathbf{a}_1 - \mathbf{a}_2$ for zigzag edges, and $\mathbf{u}_1 = \mathbf{a}_1$, $\mathbf{u}_2 = \mathbf{a}_2$ for bearded and armchair, given in terms of the reference vectors $\mathbf{a}_{1,2}$ defined in Fig. 46(a).

The diagonalization of Hamiltonian(99) gives rise to four bands with interesting features, plotted in figure 46(b). Two of them are dispersive and intersect linearly around K and K' points, giving rise to Dirac cones, similarly to the $s-$ bands. The other two have a flat character, they lay above and below the dispersive ones, and touch them at one point,

making the whole dispersion gapless. Analytical expressions for the energy of the dispersive and the flat bands, E_d and E_f, respectively read [173]:

$$E_d = \pm\frac{2}{3}t_L|\det Q(\mathbf{k})| \equiv \pm\frac{2}{3}t_L|f_p| \tag{101}$$

$$E_f = \pm\frac{3}{2}t_L \tag{102}$$

$p-$ bands, thus keep the main feature of graphene dispersion, the Dirac cones, but offer even richer physics. For example, the touching between the flat- and dispersive band was theoretically studied in [188, 189] and was shown to support creation of nematic and quantum anomalous Hall phases in the case of nonzero interactions between the electrons.

As discussed in the first chapter 2, in micropillars $p_{x,y}$ orbitals are well separated from the $s-$ bands giving the unique opportunity to study orbital physics, inset left in fig 47. In polariton honeycomb lattice the coupling of these orbitals results in four bands separated by a $0.7meV$ gap from the lowest energy $s-$ bands, that represent exactly the orbital graphene 24. Experimentally, orbital graphene dispersion was observed for the first time during the first study of polariton HCL in our group, and reported in [28].

In figure 47(a) we present the experimentally obtained momentum space spectrum of $p-$ bands in polariton HCL, taken along the direction passing through the Γ point of the second Bz, $(k_y = 2\pi/3\sqrt{3}a)$. We can observe that the lowest observed band indeed shows a flat character, while the two intermediate dispersive bands form Dirac cones in K and K' points. The bands are well reproduced by the tight binding calculation ($t_L = 1.2meV$ and $t_T = 0$, 102), given in the figure 47(c).

Some differences between the calculation and the experiment are observed. The higher band is not flat as it is expected. A possible explanation was already discussed [28]. By taking into account a weak hopping also for the $p-$ states orthogonal to the link t_T, the flat band gets deformed (while still touching the dispersive band in a single point). In 47(d) we plot the tight-binding dispersion obtained by taking $t_L = 1.2meV, t_T = 0.2$ to demonstrate this effect. The assumption of increased hopping for the upper bands is reasonable for our system as the tunneling probability varies exponentially with the barrier height relative to the state, and thus increases strongly for higher energy states.

The dispersions presented in figures 47(c,d) are obtained by Fourier transforming the spatial wavefunctions calculated in the tight binding approximation. They account for the interference effects which are at the origin of the brightness variations we observe discussed and which were discussed in chapter 3, section 3.5.2. For this particular cut, the emission is found to be the strongest below the energy of the Dirac cones, both theoretically and experimentally. For these reasons, when analyzing this type of dispersions, we will always focus on the energy region below the Dirac points.

The spatial properties of lattice eigenfunctions are also different in the $p-$ bands with respect to the $s-$ bands. Due to the spatial anisotropy and particular phase properties of the $p-$ orbitals, the form of the wavefunction can be very different from the honeycomb geometry. Figure 47(b) shows the real space emission under non-resonant excitation ($30\mu m$ FWHM spot), at the energy of the flat band for which intensity maxima sit between the pillars, and are arranged in a geometry of the so called Kagome lattice.

Using our simulator we are able to go beyond bulk physics of orbital graphene and explore $p-$ bands edge states.
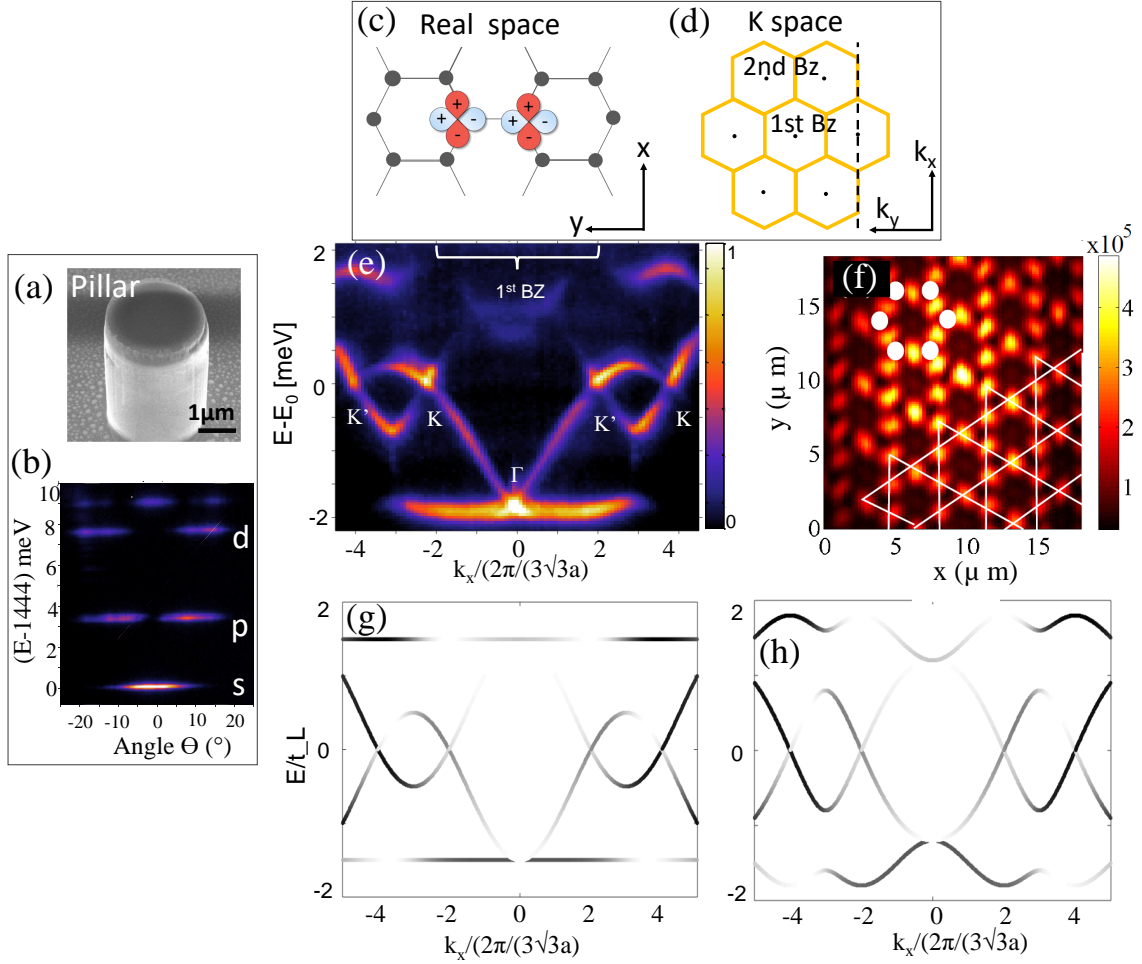
Figure 47: **A polariton orbital graphene** (a) a SEM image of a micropillar. (b) The corresponding far field emission. Sates s, p, d are well separated (c) A scheme of HCL with p_x, p_y orbitals at each lattice site. (d) A scheme of the corresponding reciprocal lattice. (e) Momentum space luminescence from the bulk of polariton HCL for $k_y = 4\pi/(3a)$ (black dashed line in (d)). K and K' mark the positions of the Dirac cones. Flat band is visible in the lower part of the spectrum. (g, h) Dispersion for the same cut in momentum space obtained by the tight binding calculation taking (g) $t_L = 1.2 meV$ and $t_T = 0$, and (h) $t_L = 1.2 meV$ and $t_T = 0.2$. (f) Real space image at the energy of the flat-band, $E - E_0 = -1.5 meV$ (see spectrum (e)). The centers of six pillars are shown in white disks. The Kagome geometry of the emission lobes is underlined with white lines (the panel (f) is taken from [28])

5.3 EXPERIMENTAL OBSERVATION OF ZIG-ZAG EDGE STATES

We are first going to examine the zig-zag type of edge. We perform the same type of experiments as in the case of $s-$ bands edge states. Dispersion is imaged in a luminescence experiment upon non-resonant excitation. Under the exact same conditions, we excite, using $2\mu m$ FWHM spot, first the bulk (to obtain the result presented in fig. 47(a)), and then the outermost pillar on the edge. The measured dispersion is shown in fig. 48(a).

In addition to the bulk modes, new bands are evidenced, marked with yellow and white dashed lines in the figure. Those marked in yellow are flat and show up at the center of both the first and adjacent Brillouin zones, at the energy of the Dirac crossings. Those in white dashed lines lie between the bulk dispersive and flat bands and have a marked dispersive character. All new states are delocalized in momentum space, in the direction perpendicular to the edge, appearing at the very same energy for any value of k_y (not shown here) suggesting they are spatially localized in this direction. This is different from the bulk bands in fig. 47(a), which change energy when probing different values of k_y and are extended in real space.
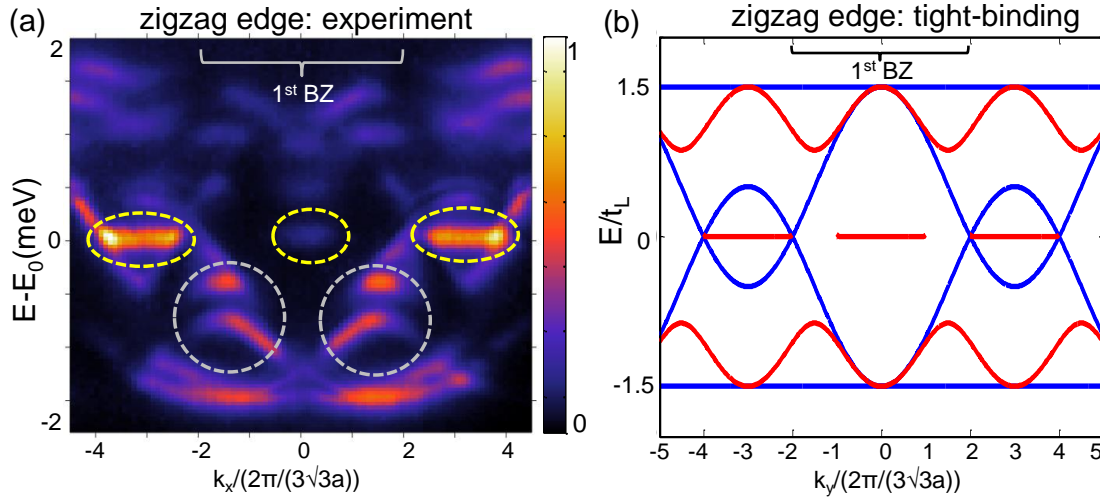
Figure 48: (a) Momentum space luminescence upon excitation on the zigzag edge for $k_y = 4\pi/(3a)$. Yellow and black dashed lines surround photoluminescence from edge states. $E_0 = 1573$ meV and $t_L = -1.2$meV. (b) Tight-binding calculation of the band structure. Blue lines: bulk energy bands at $k_x = 4\pi/(3a)$; red lines: edge states obtained for a nanoribbon with zigzag edges. All calculations are for $t_T = 0$.

We note that a splitting is observed in the lowest flat band and in the edge states at around $k_x = 1.8 \cdot (2\pi/3\sqrt{(3)})$ in fig. 48(a). It may be due to a polarization dependent confinement of the outermost micropillars, discussed in the previous chapter, and the transverse electric-transverse magnetic (TE-TM) splitting characteristic of semiconductor microcavities [190] .

The final confirmation of the localized nature of the newly discovered states is given by resolving spatially the emission at their corresponding energies. Again, this is done using an excitation spot of $\approx 20\mu m$ FWHM in order to excite the edge and partly the bulk

of the lattice, allowing us to visualize the geometry of wavefunctions along the edge and inside the bulk.

Figure 49(a) depicts the real space emission intensity at the energy of the Dirac cones, where the new dispersionless state is found. The emission is strongly localized on the outermost edge row and as in the case for the $s-$ bands edge states, present only on one sub-lattice, reflecting the chiral symmetry of the system. Differently from the case of the $s-$ bands, the maximum of emission is away from the center of the pillars, and originate only from p_x orbitals.
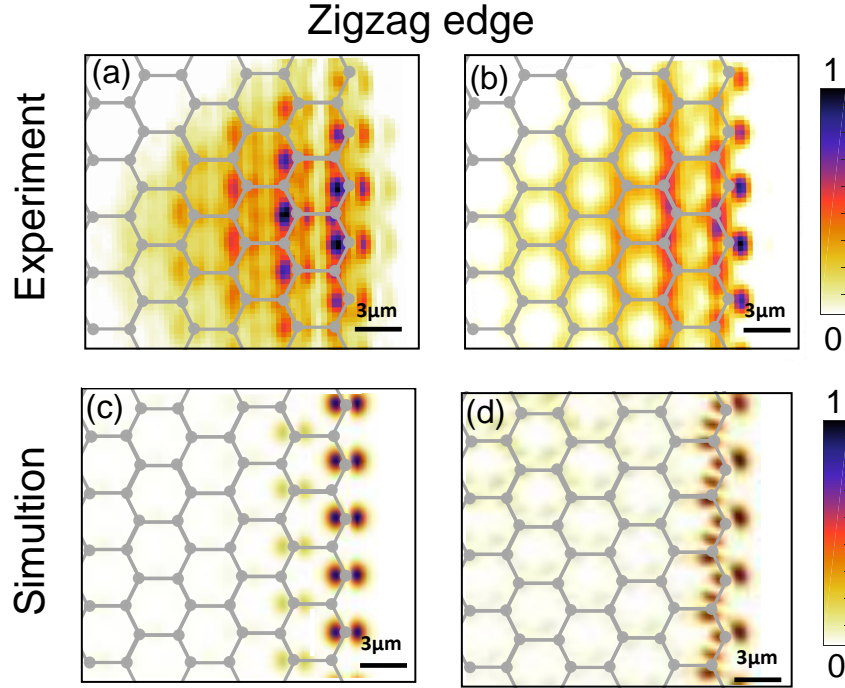
Zigzag edge

Figure 49: Real space emission upon excitation on the zigzag edge. Edge state at the energy of Dirac cones has nonzero amplitude on only one sub-lattice as observed from (a) experiment, (c) simulation. Dispersive edge, probed at the highest energy ($k_x = 1.8 \cdot 2\pi/s\sqrt{3}a$, see fig 48) has nonzero amplitudes A_x and B_y. A hexagonal lattice is sketched on top of the data to mark the position of the center of the micropillars.

The situation is different for the real space emission at the energy, $0.6 \cdot *(E - E_0)/t_L$ (center of the gray dashed circle), where the new dispersive state is present,(see (fig. 48(a)). The real space emission, given in fig. 49(b) is clearly localized at the edge, but this time both sub-lattices contribute to its shape. More precisely, the emission from the outermost, A pillars, has the shape of the p_x orbitals, while emission from the B pillars that of the p_y orbital, resulting in the particular shape of the edge state.

The interpretation of the experimental data can be supported with tight binding calculations. In fig. 48(b), we plot in blue lines the bulk modes, which are the analytic result given by eq. 99 for the value ($k_x = 2 \cdot 2\pi/3a$) and are fully delocalized. Edge states can be calculated by considering a nanoribbon with zigzag terminations on both edges and periodic boundary conditions along the direction parallel to the edge, following the method analogous to that described for ribbons in section 4.3. The solutions for exponentially de-

caying eigenfunctions are given with red lines in fig. 48(b). We can see that the spread in momentum and the position in energy match quantitatively the experimental observations, particularly for the modes at and below the Dirac cones.

Spatial form of the calculated wavefunctions at energies corresponding to those of the figures 49(a,b) is given in fig. 49(c,d), respectively. It reveals the shape of the edge states that matches well the experimental data. The calculated wavefunction shows nonzero coefficients only for p_x component on A sub-lattice in 49(c), and for p_x component on A sub-lattice and p_y on B sub-lattice in fig. 49(d).

We have thus evidenced new edge states in zig-zag edge in orbital graphene. Numerical calculations can reveal the edge states that are expected to appear in other types of edges. Results for nanoribbons with zigzag, bearded, and armchair edges are summarized in fig. 50. Two kinds of edge modes are visible: (i) bands of zero-energy modes in the central gap, present in zigzag and bearded edges, and (ii) dispersive modes in the upper and lower gaps in all three types of edges, and in the middle gap of the armchair termination.
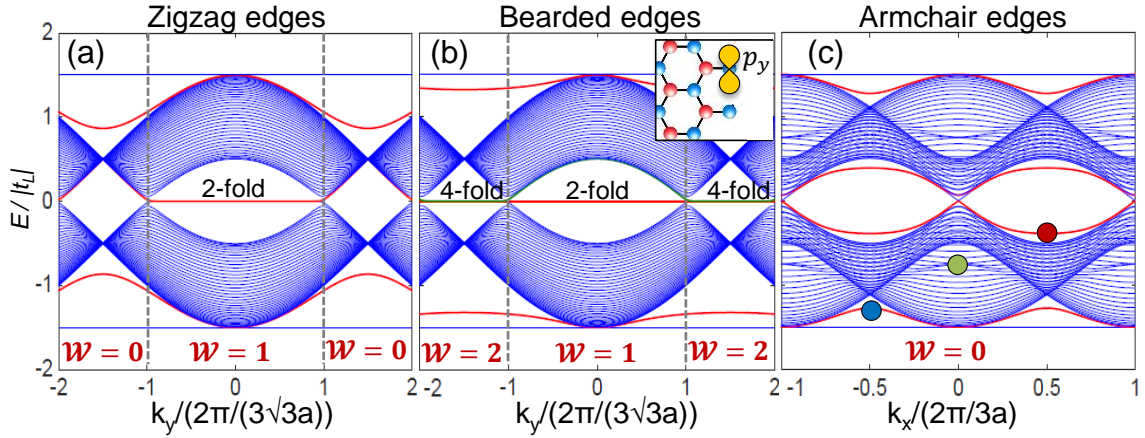
Figure 50: Calculated eigenmodes in the first Brillouin zone for a nanoribbon as a function of the wave vector $k_\parallel$ parallel to the edges, with (a) zigzag ($k_\parallel = k_x$), (b) bearded ($k_\parallel = k_x$) and (c) armchair ($k_\parallel = k_y$) terminations. Blue curves: bulk spectra for different values of the transverse momentum $k_\perp$. Red and green curves: edge states. For bearded edges, the inset shows the uncoupled p_y orbitals that give rise to a pair of edge states spreading over all $k_\parallel$.

How can we understand the origin and the nature of these states? Are they connected to the properties of bulk states wavefunction, that is, does there exist a bulk-edge correspondence for these states?

5.4   BULK-EDGE CORRESPONDENCE FOR ZERO ENERGY EDGE STATES

To answer these questions, in the framework of this study a theoretical investigation was carried out by T. Ozawa, from BEC-CNR center in Trento, Italy and G. Montambaux from LPS in Orsay.

The zero-energy edge modes which recall strongly the edge modes in the π and π^* $s-$bands of regular graphene, whose existence can be related to the winding number of the

wave functions in momentum space. For $s-$ sates the winding number was calculated following:

$$\mathcal{W}(k_\parallel) = \frac{1}{2\pi} \int_{BZ} \frac{\partial \phi(\mathbf{k})}{\partial k_\perp} dk_\perp, \tag{103}$$

where $\phi(\mathbf{k})$ is the phase of the off-diagonal component of the Hamiltonian $f_s = |f_s| e^{i\phi(k)}$, and the one-dimensional integration over $k_\perp$ is performed along a loop around the Brillouin zone in a direction perpendicular to the considered edge [79].

This analysis can be extended to more general situations, by analyzing the symmetries of the Hamiltonian. Schnyder and co-authors developed a ten-fold way classification of topological insulators for which bulk-edge correspondence can be established [65]. The topological insulators are classifed according to three symmetries: time-reversal, particle-hole, and chiral symmetries, that we already defined in the first chapter of the thesis.

By fixing a value of $k_\parallel$, the dependence of Hamiltonian 99 on $k_\perp$ can be regarded as a one-dimensional model in the, so called, BDI (chiral orthogonal) class which contains time-reversal, chiral and particle-hole symmetry. Indeed, let us examine the symmetries of our $\mathcal{H}(\mathbf{k})$. First, we can notice that it is invariant under the simultaneous operation of complex conjugation and $\mathbf{k} \to -\mathbf{k}$. Denoting the complex conjugation as $\mathcal{K}$, this means we have:

$$\mathcal{K}\mathcal{H}(\mathbf{k})\mathcal{K}^{-1} = \mathcal{H}(-\mathbf{k}), \tag{104}$$

which means we can take the time-reversal symmetry operator as $\mathcal{T} = \mathcal{K}$. (As discussed, the "time-reversal symmetry" here does not need to correspond to the physical one).

As for the chiral symmetry, we can note that the matrix $\sigma_z \otimes I_{2\times2} = diag(1, 1, -1, -1)$ anti-commutes with the Hamiltonian:

$$\sigma_z \otimes I_{2\times2}\mathcal{H}(\mathbf{k})(\sigma_z \otimes I_{2\times2})^{-1} = -\mathcal{H}(\mathbf{k}), \tag{105}$$

This means that we have the chiral symmetry $\mathcal{C} = \sigma_z \otimes I_{2\times2}$, but also the particle hole symmetry, $\mathcal{P} = \sigma_z \otimes I_{2\times2} \cdot \mathcal{K}$, which satisfies $\mathcal{P}\mathcal{H}(\mathbf{k})\mathcal{P}^{-1} = -\mathcal{H}(-\mathbf{k})$.

It is also important that our time-reversal symmetry and the particle-hole symmetry have the property $\mathcal{T}^2 = \mathcal{P}^2 = +1$ which puts our model in the class BDI of the ten-fold classification of topological insulators, as that of the SSH model.

For this class, the number of pairs of zero energy edge modes is given by the winding of the phase ϕ obtained from $f_p \equiv \det Q = |\det Q| e^{i\phi(\mathbf{k})}$ as discussed in [191]. In our case Q is given with the expressions 99, 100.

We calculate the winding using $\phi(\mathbf{k})$ and expression 103. In figure 51(d,e,f) we show the value $\nu\left(k_\parallel\right)$, for the $p-$bands as a function of momenta parallel to the edge $k_\parallel$ for the three type of edges considered here. In the figures, colored regions represent the rectangular first Bz., in red areas the calculated winding number is even, while it is odd in green ones.

To illustrate the calculation of winding number in a more intuitive way, we plot in each of the panel of fig. 51(d,e,f) the arrows corresponding to calculated angles $\phi(\mathbf{k})$. Now we can trace the directions these arrows point to, along a line in the first Bz (that is starting from one edge of Bz and going to the other) in direction parallel the edge (k_y for zigzag and bearded edges in our case). If we choose, for example a line in the red region of

fig. 51(d), we can see that all along k_y arrows point in the same direction, to the left. In this case winding $\nu = 0$. If, however we pick a direction inside the green colored area, arrows change their direction along the path. They rotate for $360°$ between the edges of the first Bz, making one full loop and giving winding $\nu = 1$.

The winding number $\mathcal{W}\left(k_\parallel\right)$ matches with the number of the zero-energy modes calculated by diagonalization of the Hamiltonian, fig. 50(a,b,c).
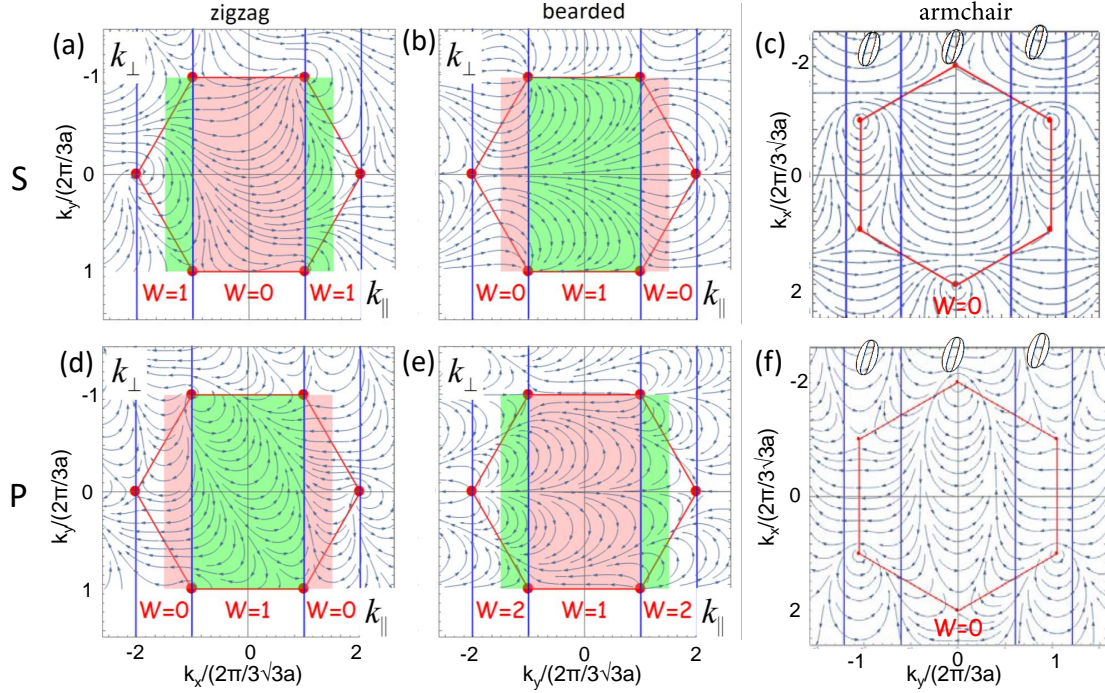
Figure 51: Winding of the phase $\phi(\mathbf{k})$ for p-band graphene (top row) and orbital s-band graphene (bottom rows). The winding number $\mathcal{W}(k_\parallel)$ is indicated, $k_\parallel$ being the direction of the wave vector along the edge. The colored region is a rectangular Brillouin zone. In the pink regions, the winding number $\mathcal{W}$ is even while it is odd in the green regions. Both in s- and p-bands, the regions in momentum of existence of edge states are complementary between the zigzag and bearded edges. Additionally, they are complementary between s- and p-bands for the same kind of edge. There is an additional p-edge state at the bearded edge for all values of $k_\parallel$, resulting in an additional winding of the phase. For armchair edge winding has value zero for both s- and p-bands for all values of $k_\parallel$ indicating the absence of zero energy edge states.

An interesting feature of fig. 51 is that the regions in momentum space where the zero-energy modes are present in the zigzag edge ($k_\parallel \in [-2\pi/(3\sqrt{3}a), 2\pi/(3\sqrt{3}a)]$) are *complementary* to the regions in which they are present in s-band graphene for the same kind of edge ($k_\parallel \notin [-2\pi/(3\sqrt{3}a), 2\pi/(3\sqrt{3}a)]$). A similar situation takes place for the bearded edges: in the p-bands, pairs of edge modes appear in the region in k-space complementary to the regions where they appear in the s-bands.

The complementarity in the position in momentum space of zero-energy edge modes between s-bands, and p-bands, can be understood by analyzing the symmetry of Hamilto-

nians given by eq. 99 for the p- and eq. 93 for s-bands. The expressions f_p and f_s, whose winding determines the existence of zero-energy edge modes, can be related analytically:

$$f_p\left(zigzag\right) = \frac{3}{4}e^{i\mathbf{k}\cdot(\mathbf{a}_1-\mathbf{a}_2)}f_s\left(bearded\right) \tag{106}$$

$$f_p\left(bearded\right) = \tfrac{3}{4}e^{i\mathbf{k}\cdot\mathbf{a}_2}f_s\left(zigzag\right) \tag{107}$$

where $f_s/f_p\left(zigzag/bearded\right)$ are written using the choice of unit cell that corresponds to the zigzag/bearded edge [79]. A consequence of eq. (106) is that the winding of the phase of $f_p\left(zigzag\right)$ is the same as of $f_s\left(bearded\right)$ (the vector $\mathbf{a}_1 - \mathbf{a}_2$ is parallel to the edge, so the prefactor of the right hand part of eq. (107) gives no winding in the orthogonal direction).

A similar situation takes place for eq. (107): in addition to the exchange of the position between zigzag and bearded edge states, of respectively, s- and p-bands, the phase factor $e^{i\mathbf{k}\cdot\mathbf{a}_2}$ provides an extra winding over the whole Brillouin zone, and gives rise to an extra pair of edge state for all values of k_x, in the bearded edges of the p-bands. Physically, this edge states arises from dangling p_y orbitals fully localized in the outermost pillars, uncoupled to the bulk, as sketched in the inset of fig. 50(b), and adds to the pair of edge states discussed above.

The armchair edge does not have any zero-energy edge mode and is characterized by the winding zero along the whole $k_\parallel$.

5.5   DISPERSIVE EDGE STATES

5.5.1   *Analytical calculation of dispersive edge states*

One of the most distinctive features of fig. 48 and 50 is the observation of additional dispersive edge modes between the dispersive and the flat bands of the bulk. These modes are present for all values of $k_\parallel$ and for all the investigated types of edges.

We can obtain analytical expression of the dispersive edge modes by looking for solutions of finite size Hamiltonian with an exponential decay into the bulk ($\psi(x) \sim e^{-x/\xi}$, ξ being the penetration length). The calculation procedure is analogous to the one used to calculate analytically edge states in graphene which can be found in Refs. [162, 94] and was done by T. Ozawa and G. Montambaux. The treatment relies on consideration of a real space graphene ribbon Hamiltonian for each type of the edge. By imposing solutions with exponential decay, the Shrodinger equation is reduced to only few independent equations and the same number of unknowns. We have summarized this procedure for the case of the $s-$ bands and generalized it for the $p-$ bands in the supplementary of the paper [192]. We reproduce it in this manuscript as an appendix, 7.1.

By applying this method to zigzag and bearded edges, we find the following eigen energies for the $p-$ bands edge modes:

$$E_{disp.edge}^{zigzag}(k_\parallel) = \pm t_L \frac{\sqrt{3}}{2}\sqrt{2 + \cos\left(\sqrt{3}k_\parallel a\right)} \tag{108}$$

$$E_{disp.edge}^{bearded}(k_\parallel) = \pm t_L \frac{\sqrt{3}}{2}\frac{\sqrt{5 - 2\cos\left(\sqrt{3}k_\parallel a\right)}}{\sqrt{2 - \cos\left(\sqrt{3}k_\parallel a\right)}}. \tag{109}$$

The penetration length of the edge states can also be extracted from these calculations. They are found to be:

$$\xi_{disp.edge}^{zig}(k_\parallel) = (\ln \cos{(\frac{\sqrt{3}}{2}k_\parallel)})^{-1} \tag{110}$$

$$\xi_{disp.edge}^{beard}(k_\parallel) = (\ln \frac{\cos{(\frac{\sqrt{3}}{2}k_\parallel)}}{2 - \cos{(\sqrt{3}k_\parallel)}})^{-1}. \tag{111}$$

As evidenced in fig. 50, dispersive edge states exist also for armchair terminations, which do not contain any edge modes in the case of regular electronic graphene. The analytic calculation for the armchair edges requires the use of two different penetration lengths [147]. We thus take the advantage of our photonic simulator to explore these novel edge modes.

5.5.2 *Experimental observation of armchair edge states*

Chiral symmetry of the bipartite honeycomb lattice does not allow the formation of flat zero-energy edge states in the armchair edge, following eq. 96 and calculation of the winding number. This is however not true for the dispersive edge states, predicted to appear in all the gapped regions between the flat- and dispersive- band..

Fig. 52(a,b) shows the measured dispersion along the direction parallel to the armchair edge (for $k_x = -2 \cdot 2\pi/2\sqrt{3}a$, black dashed line in fig. 52(e)) when the lattice is excited in the bulk and at the armchair edge, respectively. In both figures black dashed lines represent the tight-binding calculation of the bulk modes for this particular cut in momentum space. In figure 52, for excitation at the edge, we observe the two main groups of edge modes: one is close to the zero energy (red dot), in between the dispersive bulk bands, and the other is in between the flat- and dispersive- bulk bands (green and blue dots). Both groups are more clearly visible below zero-energy.

We will compare the obtained experimental results with the driven dissipative simulation of polariton lattice. We search the steady states of the equation:

$$i\hbar\frac{\partial}{\partial t}\psi = \left(H_p - i\frac{\gamma}{2}\right)\psi + F_p e^{i\omega t}, \tag{112}$$

similar to eq. 97, in which H_p is now the real space Hamiltonian of $p-$ band graphene.

We assume losses at a rate $\gamma = 0.2t_L$ for all lattice sites. To simulate the bulk luminescence we place the coherent pump F_p, with a certain frequency ω, at the central site of the ribbon, far from the edges. The time-independent amplitudes for the A and B sub-lattice sites are then obtained for steady states of eq. 112.

To reconstruct the dispersion, the distribution obtained from the above equations is Fourier transformed and the procedure is repeated for different frequencies ω of the pump. Figure 52(c) shows the Fourier transformed intensity as a function of k_y for $k_x = -2 \cdot 2\pi/2\sqrt{3}a$ for different resonant pump frequencies.

As we can see, the main features of the experiment are well reproduced by the simulation, including the destructive interference in the upper dispersive band around $k_y = 0$. This point crosses a high symmetry direction along which odd real-space eigenfunctions interfere destructively in the far field. We perform a similar calculation with the excitation spot placed at the edge with the armchair boundary instead of the central site of the lattice.
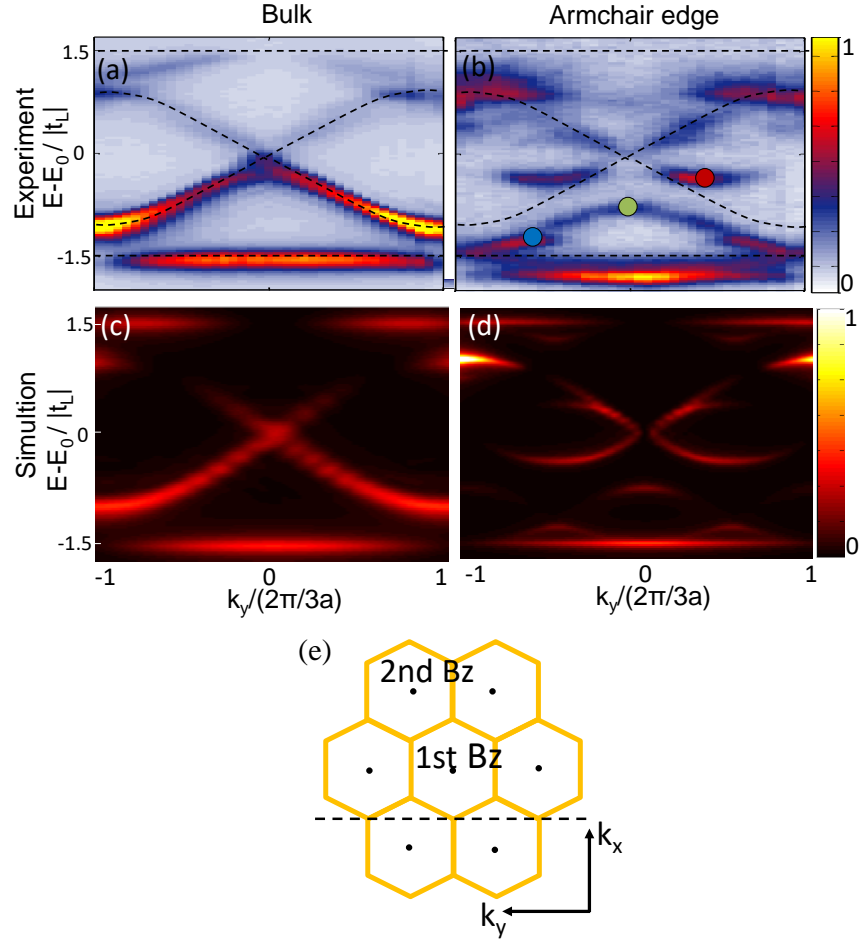
Figure 52: (a-b)Measured momentum-space luminescence along the k_y direction for $k_x = -4\pi/(3\sqrt{(3)}a)$ (black dashed line in (e)) when exciting the bulk (a) or the edge (b) of a ribbon with armchair terminations. (c-d) Momentum space distribution for the same value of k_y obtained from a driven-dissipative tight-binding simulation for excitation in the bulk (c) and at the edge (b).

The computed intensity pattern is plotted in fig. 52(d), and reproduces well the edge states observed experimentally in fig. 52(b).

Interestingly, both experiment and the tight-binding calculations in fig. 50(c) suggest an additional edge mode within the bulk energy band (green dot), figures 52(c) and 53(b). Despite the fact that it is at the energy of the bulk modes, simulations shows that it is fully delocalized in momentum space, along the k_x direction, perpendicular to the edge.

We use our photonic simulator to explore the spatial distribution of these novel edge modes. Figure 53(a-c) shows the real space emission from the photonic simulator excited close to the armchair edge for three emission energies, corresponding to the three different dispersive edge states indicated in fig. 52(b). Again, we employ a pump spot of 20 μm in diameter, allowing the measurement of the wavefunctions of the edge modes, which penetrate several microns into the bulk. For the lowest-energy dispersive edge state (fig. 53(a)),
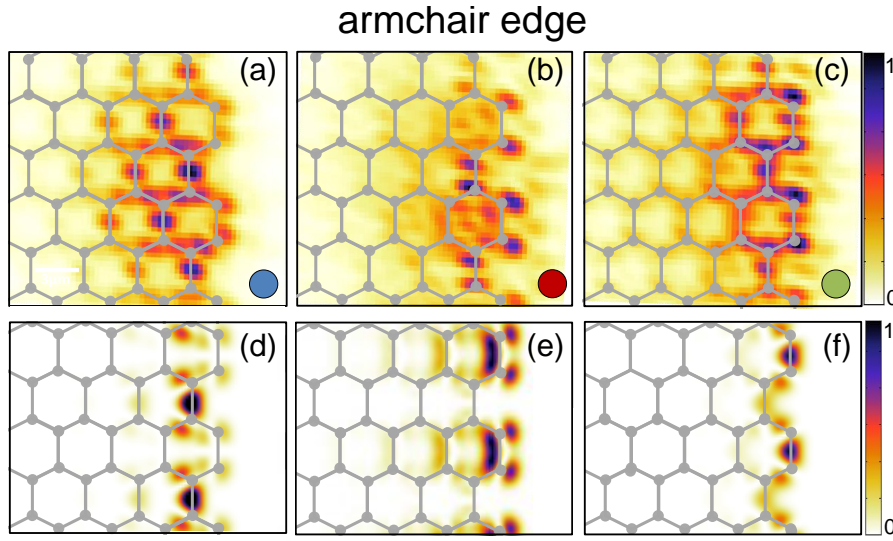
Figure 53: Real space emission from dispersive edge states in an armchair termination. (a-c) Measured photoluminescence when selecting the energies indicated with circles in Fig. 52(b). (d-f) Corresponding tight-binding eigenfunctions. A hexagonal lattice is sketched on top of the data to mark the position of the center of the micropillars.

the emission is localized in the second to the last row of micropillars, with a gradual decrease towards the bulk. These features along with the lobe structure are well reproduced by the plot of the tight-binding solution for the edge state at the corresponding energy $[k_x = \pi/(3a)$; fig. 53(d)]. Figure 53(b) shows the emission pattern for the lowest-energy edge mode in the central gap. In this case, the outermost pillars show the highest intensity, in a pattern significantly different from the modes shown in figs. 53(a) and (d). It is worth noting that in the experiment, the energy of the emission is filtered with the use of a spectrometer, but no particular in-plane momentum is selected. Therefore, bulk modes contribute to the emission at the energies studied in figs. 53(a)-(c), explaining the differences with the calculated individual eigenfunctions depicted in figs. 53(d)-(f).

Finally, when selecting the emission at the highest energy of the mode within the bulk bands, (green dot), the experiment and tight-binding calculations shown in fig. 53(c),(f) attest the significant localization of these modes in the edge region.

In conclusion, in this chapter we provided a detailed experimental characterization of the zero-energy and dispersive orbital edge states in excited bands of a photonic honeycomb lattice. The zero-energy modes are well described using topological arguments based on the symmetries of the bulk Hamiltonian. Whether any topological argument can be applied to the dispersive edge modes is an intriguing question which is not clarified yet.

Our experiments and theoretical analysis could offer insights into multimode lattice systems such as transition metal dichalcogenides [29] or mechanical lattices of springs and masses, which have been predicted to show similar dispersive edge modes [191, 58]. Taking advantage of the intrinsic nonlinearities of polaritons, honeycomb lattices of coupled micropillars appear as excellent candidates to explore nonlinear bulk and edge states with orbital structure [172].

Another important aspect of orbital physics is the behavior of the bands upon lattice deformations. The change of lattice geometry can affect both bulk and edge states. It can cause the change of the topology of the bands, significantly modifying the properties of the material. The idea to use pressure on bulk materials, or strain in 2D lattices in order to induce superconducting or topological phase transitions has been already tested [193, 194, 77]. However, achieving the desired level of control and magnitude of pressure or strain proved to be very challenging in electronic lattices.

In the next chapter we will examine how new types of quasi-particles with anisotropic transport properties can be obtained in a polariton honeycomb lattice by controllably tuning the tunneling probability between the lattice sites.

UNCONVENTIONAL DIRAC CONES IN STRAINED HONEYCOMB LATTICE

6.1 INTRODUCTION

In the work presented in the previous two chapters we have used a polariton simulator to explore edge states of the honeycomb lattice. We discovered new edge states in the orbital graphene and established the connection between their existence and the lattice bulk properties.

In this chapter we will focus on bulk properties and show how we can modify the bulk dispersion. In this way we will be able to create new types of Dirac dispersions and foster unconventional transport regimes for polaritons.

In the first section 6.2, we will follow the recent development in both electronic and artificial Dirac systems which led to discovery of new type of Dirac dispersions. Quasi-particles corresponding to these dispersions are characterized by exotic transport and magnetic properties. They attracted significant attention due to their potential for creation of future photonic and electronic devices on one side, and the possibility to simulate gravitational effects on the other. Then, in section 6.3 we will review in more details a well known result, the study of manipulation and merging of Dirac cones in graphene.

More precisely, when a uniform strain is applied to the lattice, the distance between Dirac points with opposite topological charges in the Brillouin zone is reduced and eventually they can be annihilated to open a gap. A particular point of interest for our study will be the fact that at the critical point of this transition, from the Dirac to a gapped phase, a so called semi-Dirac dispersion arises: linear in one direction, and parabolic in the other.

By engineering of hopping parameters in the polariton honeycomb lattice we will be able to implement the uni-directional strain and directly observe, for the first time in a photonic system, a semi-Dirac dispersion, section 6.4.2.

In the sections 6.5 and 6.6, we will extend the study to orbital polariton graphene and explore the modification of the $p-$ bands degeneracies under strain. We will demonstrate realization of the second possible type of topological phase transition in two dimensions: the one in which Dirac cones with equal topological charges are created. Most interestingly, the tuning of Dirac dispersion trough this phase transition will allow us to create new type of critically tilted Dirac cone.

In this way it will be shown that the polariton honeycomb lattice is a convenient platform to engineer and combine different types of Dirac photons.

6.2 UNCONVENTIONAL DIRAC CONES

In the first chapter, *Introduction to Dirac physics*, we have seen how the symmetries of the honeycomb lattice shape the form of the Hamiltonian allowing the conduction and the

valence band to cross linearly around Dirac points. The quest for other materials featuring Dirac cones advanced slowly due to the necessity of the particular form of Hamiltonian to prevent avoided crossings. Once these conditions are fulfilled, however, Dirac points appear as robust objects. Manipulation of the honeycomb lattice and its band structure has engendered numerous efforts both for fundamental reasons and potential applications in devices.

Discovery of new materials and development of artificial lattices in the last few years, allowed important advancement in this direction resulting in better understanding, and creation of new gapless topological phases. It was shown that Dirac points and the dispersion in their vicinity can be modified and manipulated.

The emergence, modification, or annihilation of Dirac cones represents a Lifshitz transition. Originally, this term was used to describe a discontinuity of the chemical potential μ at $T = 0$ in metals that would lead to an abrupt change of Fermi surface, giving rise to anomalies in the electron properties of metals [195]. Now, it is used to label a transition in electronic crystals in which the topology of the Fermi surface is changed. Lifshitz transitions have been extensively studied, for a broader class of materials by Volovik [196, 195]. His work has attracted significant attention recently because it describes the emergence of new materials exhibiting Dirac cones, namely, topological semi-metals [197, 76].

For example, the so called Weyl semi-metals display a linear dispersion in all three directions of momentum space around the point of intersection of the bands. They are obtained by breaking inversion or time reversal symmetry in the system which lifts the degeneracy of the three dimensional Dirac cone. They are symmetry protected and as a consequence they hold non trivial topological properties that lead to variety of novel phenomena including surface Fermi arcs [198], chiral anomaly, negative magnetoresistance [199], nonlocal transport [200], anomalous quantum Hall effect [75].

It was also shown recently that all Dirac/Weyl cones in both 2D and 3D can be divided in two distinct groups and that the topology of the Fermi surface is what defines each category.

Dirac cones in graphene, for example, belong to the Type I or "classical" Dirac cones. They have a Fermi surface which is a point (as a geometrical object, a point is topologically equivalent to a closed line). The density of states at the energy of Fermi level in this case is zero.

This is, nevertheless not the only possible case and a different type of Dirac cones exists. Let us write the effective Hamiltonian of a Weyl or a Dirac cone in general form, which includes σ_i Pauli matrices and also the identity σ_0 matrix:

$$H(\mathbf{k}) = \sum_{i,j} k_i v_{ij} \sigma_j \tag{113}$$

Here $i \in (x, y, z)$ and $j \in (0, x, y, z)$, k_i's are wave vectors and σ_j's are the identity and the Pauli matrices. The coefficients v_{ij} $(j \neq 0)$ are proportional to the velocity of the quasi-particle in each momentum or spin direction. As we will see below v_{i0} will result in "tilt" of the cone. This Hamiltonian can be applied also in two dimensions, which is the case we will concentrate on. Then we have $i \in (x, y)$ and $j \in (0, x, y)$. In both 2D and 3D cases the energy dispersion relation corresponding to the above Hamiltonian can be found

by solving its eigen problem, that is by solving the time independent Shrödinger equation. It reads [201]:

$$\epsilon = \sum_i (k_i v_{i0} \pm \sqrt{\sum_{j \neq 0} (k_i v_{ij})^2}) = T(\mathbf{k}) \pm U(\mathbf{k}) \tag{114}$$

If all the v_{i0} are equal to zero we obtain an anisotropic Type I cone as the one depicted in fig. 54(a).

Type I Dirac cones
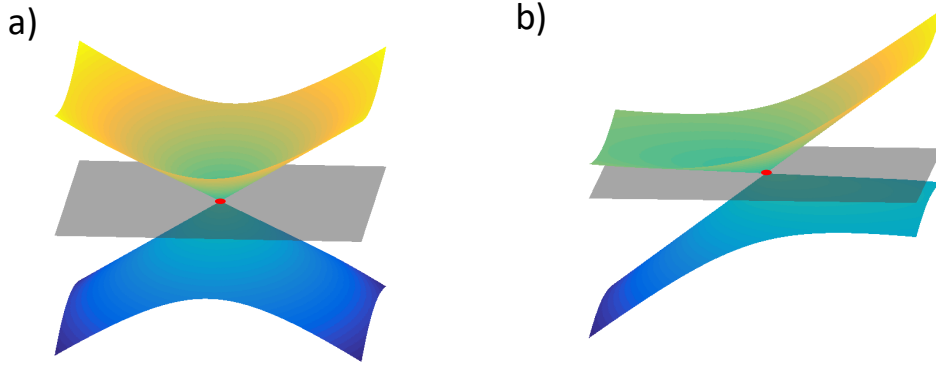
Figure 54: **Type I Dirac cones.** Fermi surface is a point. a) Isotropic Dirac cone b) Tilted Dirac cone

In the case when one of the coefficients v_{i0} is non-equal to zero the Dirac cone is tilted, fig. 54(b). This energy dispersion which exhibits Weyl fermions with several different velocities, is predicted to appear in the quasi-two-dimensional organic semiconductor $\alpha - (BEDT - TTF)_2 I_3$ [202, 203], as well as in hydrogenized graphene [204]. Tilted Dirac cones have been proposed for their non isotropic transport properties to be used for valley filtering in $p - n$ junctions [205] and generation of photo current [206] otherwise forbidden in the ideal two-dimensional Dirac spectrum by symmetry.

A particular situation occurs when one of the terms v_{i0} is large enough such that $|T(\mathbf{k})| > |U(\mathbf{k})|$. This happens precisely when $\left(\frac{v_{x0}}{v_{xi}}\right)^2 + \left(\frac{v_{y0}}{v_{iy}}\right)^2 > 1$. In that case, a strongly tilted or Type II Dirac cone is produced. Its corresponding Fermi surface is then not a point, but a cone, that is an open line (see red line in fig. 55(a)).

As Fermi surface separates occupied from empty states in crystals, its shape directly influences their density of states, electronic and magnetic properties. The density of states at the Fermi level in the case of type II Dirac points for example, is necessarily different from zero.

The new type of Dirac points is interesting for another reason. If we consider that the Dirac cones represent analogues of the relativistic Dirac particles, the above condition, $|T(\mathbf{k})| > |U(\mathbf{k})|$, indicates a Lorentz boost with a speed larger than the speed of light. As Lorentz invariance is violated in that case, creation of Type II Dirac cone would be

the realization of a particle inconsistent with the standard model. In the context of general relativity Type II Dirac cone spectrum is predicted to emerge behind a black hole horizon [207].
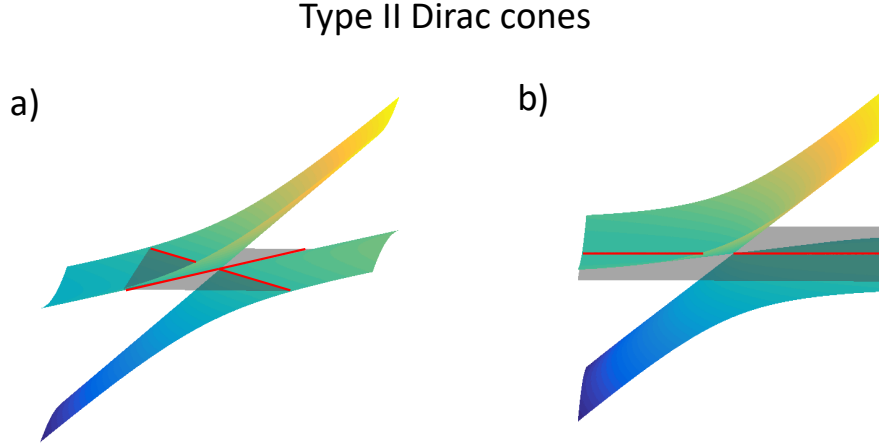
Type II Dirac cones

Figure 55: **Type II Dirac cones.** Once the tilt in a certain direction is strong enough, bands cross zero energy at more than one point. a) Fermi surface is a Dirac cone. b) In the critical point of the transition Fermi surface is a line.

Still, it is possible to attain this regime in solid state systems, where the Fermi velocity is orders of magnitude smaller than the speed of light. Type II Weyl points have been realized between electron and hole pockets in semi-metals with strong spin-orbit-like coupling. For example, in bulk transition metal dichalcogenides $MoTe_2$ [208], $PtSe_2$ [209], or in the superconductor $PdTe_2$ [210]. Equally, it is possible to engineer them in photonic lattices as recently achieved in works [211, 10].

Very recently, a particular attention was given to the situation that is predicted to appear at the point of the critical tilt between Type I and Type II cones. This happens precisely when $\left(\frac{v_{0x}}{v_{ix}}\right)^2 + \left(\frac{v_{0y}}{v_{iy}}\right)^2 = 1$. In that case a Dirac cone with particular properties is created. It is characterized by a Fermi surface in the form of a straight line, as depicted with red line in fig. 55(b). Zero and infinite effective masses of a corresponding quasi-particle are combined along one direction of momentum space.

Because of its distinct properties this kind of dispersion is also named Type III Dirac cone. It has been argued recently, for example, that it represents an interesting candidate for simulating gravitational effects in the laboratory . Specifically, due to its particular anisotropic dispersion Type III Weyl points have been proposed for solid-state realization of the black-hole-horizon analogue in inhomogeneous $Zn_2In_2S_5$, to simulate black hole evaporation with high Hawking temperature [212].

While the study of strongly tilted (Type II and Type II) linear dispersion was up to now mostly concentrated on 3D systems, a question arise weather these unusual quasi particles, can be realized in two dimensional systems? This would allow to attain strong modification of Klein tunneling, magnetic properties, collapse of Landau levels and modified particle-particle interactions.

6.2.1 *Merging of Dirac cones*

Tilting of Dirac cones is not the only way they can be manipulated. They can also merged during a Lifshitz transition. In graphene, it has been shown that by changing the relative strength of the three nearest neighbor hopping parameters, Dirac points can move in momentum space and eventually annihilate.

A general theoretical framework for merging of Dirac cones in 2 dimensions is provided in seminal works of G. Montambaux and co-workers [213]. Two universal scenarios of merging have been provided depending on topological charge attributed to each Dirac point.

As discussed in chapter 2 Dirac cones are characterized by a winding number (topological charge) ω. This quantity describes the winding of the phase of the wavefunction around the cone. It can be found directly from the Hamiltonian in the vicinity of Dirac point:

$$H(\mathbf{q}) = \hbar v_F \mathbf{h} \cdot \boldsymbol{\sigma} \equiv h_x(\mathbf{q})\sigma_x + h_y(\mathbf{q})\sigma_y \tag{115}$$

as:

$$\omega = \frac{1}{2\pi} \int \nabla \phi(\mathbf{q}) d\mathbf{q}, \tag{116}$$

where ϕ is defined through components of the vector $\mathbf{h} = (h_x, h_y)$:

$$\tan \phi = \frac{h_x}{h_x}. \tag{117}$$

Dirac cones with opposite topological charges can neutralize and open a gap, characterized by zero winding. Exactly at the merging transition a particular semi-Dirac dispersion is created. Linear along one direction of momentum space, and quadratic in the orthogonal one, this dispersion corresponds to quasi-particles with interesting anisotropic properties. They are massless in one spatial direction, but possess a finite effective mass in the orthogonal one. Unusual consequences have been predicted this of semi-Dirac dispersion, such as square root dependence of density of states on the energy, or modification in the spacing of Landau levels [214]. Recently, signatures of such dispersion have been evidenced in doped black phosphorus using ARPES measurements [215].

On the contrary, if Dirac points with equal charges merge, it will not be possible to open a gap, but only to modify the Dirac cones. This is the type of transition that occurs in bilayer graphene, for example. In that case a quadratic band touching, characteristic for low energy bilayer graphene, can be transformed into two Dirac cones with equal charge. This type of transition will be discussed theoretically and experimentally in more details in section 6.5.3.

Lifshitz transitions are thus a route towards creation of new types of Dirac dispersions. But how can they be triggered? In the case of 2D lattices an important change in geometry, and thus significant modification of their transport properties can be achieved by application of strain. Under strain, the distance between atoms is altered, and so is the hopping amplitude strength between the atoms leading to a reshaping of graphene dispersion and even a Lifshitz transition. The fact that strong in-plane carbon bonds in graphene allow reversible tensile elastic strain up to 20%, encouraged research on the possible effects of this

modification. In the next section we will analyze few significant results from the literature on the effects of strain on graphene.

6.3   STRAIN AND GRAPHENE

Depending on the form and the magnitude of strain, various effects on the dispersion of graphene are possible [216]. Anisotropic strain inevitably alters the lattice isotropy, thus changing qualitatively the lattice dispersion.

One striking effect, for example is the possibility to create artificial gauge fields. A non-uniform strain, with a gradient in magnitude, effectively introduces a term in the Hamiltonian equivalent to a vector potential. The result is the formation of a pseudo-magnetic field in the vicinity of the two inequivalent Dirac points [217]. The sign of the field is opposite for each of them such that the net magnetic field is zero. In spite of this, Landau levels are formed, as confirmed in graphene by the STM measurements [218, 219].

Introduction of artificial gauge fields is a particularly important task in the area of photonics, where the use of real magnetic field is not viable. It represents a milestone towards the achievement of topologically non trivial phases. By implementing strain in honeycomb lattice Landau levels for photons have been observed in coupled waveguides by M. Rechtsman [90] and co-workers, and a proposal has been made for the observation of the helically propagating edge states by G.Salerno et al. [220, 221].

6.3.1   *Uniaxial strain*

A different modification of graphene band structure takes place under uniform strain. This transformation corresponds to a relative change of the hopping parameters t_1, t_2 and t_3 inside the lattice unit cell. In the first theoretical consideration of such deformation by Pereira [222], it was shown that the position of the Dirac points can be changed, that is, they can be pushed away from the $\mathbf{K}$ and $\mathbf{K}'$ point. If the magnitude and the angle of deformation are in a certain range, Dirac points can also merge, giving rise to a gapped dispersion. This situation represents a phase transition: a semi-metalic phase is replaced with a semiconductor phase.

For the orientation of the lattice shown in fig. 56(a) strain applied along $y-$axis will cause $t_1 \neq t_2 = t_3$. Labeling $t' \equiv t_3$ and $t \equiv t_1 = t_2$ we can introduce a parameter $\beta = t'/t$ and generalize the form of the graphene Hamiltonian given in chapter 2:

$$H_s = t_s \begin{pmatrix} 0 & f_s \\ f_s^* & 0 \end{pmatrix} \quad , \quad f_s(\mathbf{k}) = t(\beta + e^{i\mathbf{k}\mathbf{a}_1} + e^{i\mathbf{k}\mathbf{a}_2}) \tag{118}$$

where:

$$\mathbf{k}\mathbf{a}_1 = \frac{3}{2}k_y a + \frac{\sqrt{3}}{2}k_x a \quad , \quad and \quad \mathbf{k}\mathbf{a}_2 = \frac{3}{2}k_y a - \frac{\sqrt{3}}{2}k_x a. \tag{119}$$

We can define:

$$K_y = \frac{3}{2}k_y a \quad , \quad K_x = \frac{\sqrt{3}}{2}k_x a \tag{120}$$
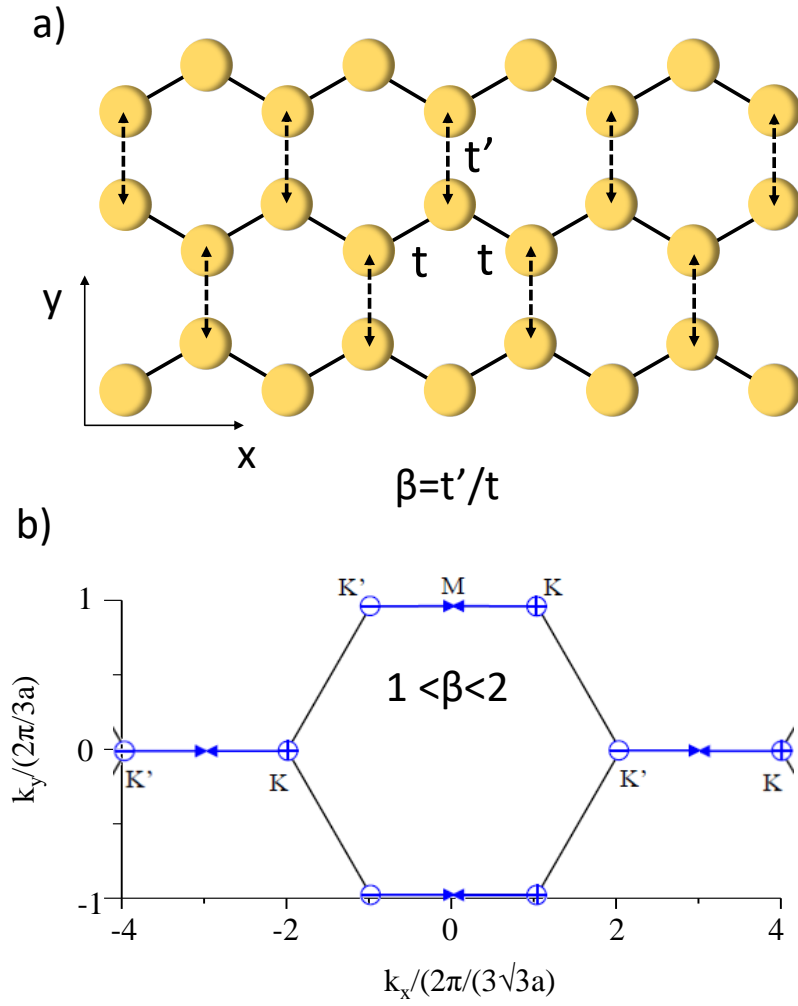
Figure 56: **Uni-axial strain in honeycomb lattice.** a) Scheme of the lattice under the strain along $y-$direction, parallel to the one of the bonds. Hopping parameter along that bond, t', is changed with respect to the hopping parameter along the other two NN links, t. b) Evolution of Dirac points. For $t'/t > 1$ they move away from **K** and **K**$'$ points, along the direction perpendicular to the strain, and finally merge in **M** point for $t'/t = 2$.

and write f_s in a convenient form:

$$f_s = \beta + 2\cos K_x e^{iK_y} \tag{121}$$

The spectrum of the $s - bands$ graphene then becomes:

$$\epsilon_s = \pm t_s |f_s| = \pm t_s \left| \beta + 2cosK_x e^{iK_y} \right| \tag{122}$$

The position of Dirac points can be easily found from the previous expression by making $\epsilon_s = 0$:

$$K_y = 0 \quad , \quad cosK_x = \beta/2. \tag{123}$$

From the equations, we can see that, as the parameter β increases, the two inequivalent Dirac cones in graphene are displaced from $\mathbf{K}$ and $\mathbf{K}'$. They get closer together, and eventually they merge when $\beta = 1$ ($t' = 2t$) at the $\mathbf{M}$ point of momentum space fig. 56(b).

This phase transition can be understood in terms of the topological charge (winding) attributed to each Dirac point. Opening of the gap, characterized by the zero winding, is the result of merging of Dirac cones with winding $+1$ and -1.

6.3.2   *The Universal Hamiltonian I*

The merging scenario has been described by G. Montambaux and coworkers [213]. They have introduced the so called universal Hamiltonian, which governs the fusion of Dirac cones with opposite topological charges in two dimensions independently of the atomic or microscopic parameters of the particular system they appear in.

In the vicinity of the transition, the Hamiltonian describing the transition can be written in the general form [61]:

$$H_{+-}(\mathbf{q}) = \begin{pmatrix} 0 & \Delta_{+-} + \frac{q_x^2}{2m^*} - ic_y q_y \\ \Delta_{+-} + \frac{q_x^2}{2m^*} + ic_y q_y & 0 \end{pmatrix}, \tag{124}$$

where

$$\Delta_{+-} = \frac{1}{2} - \frac{1}{\beta}$$

and c_y and the effective mass m^* depend on the macroscopic parameters of the lattice, that is of the form of f_s. The spectrum corresponding to this Hamiltonian reads:

$$\epsilon = \pm \sqrt{\left(\Delta_{+-} + \frac{q_x^2}{2m^*} \right)^2 + q_y^2 c_y^2}. \tag{125}$$

The transformation of the dispersion with the change of parameter $\Delta_{+-} < 0$ is given in figure 57. The phase featuring two Dirac points, is obtained for $\Delta_{+-} < 0$ (when choosing $m^* > 0$ without loss of generality). Increasing the gap parameter reduces the distance between Dirac points $2q_{\mathbf{K}} = 2\sqrt{-2m^*\Delta_{+-}}$, and shifts the energy of the saddle point between them. As Δ_{+-} increases from negative to positive values, the energy of the saddle point increases and transforms into the hybrid semi-Dirac point at $\Delta_{+-} = 0$. For $\Delta_{+-} > 0$ a gap with the magnitude $2\Delta_{+-}$ finally opens.
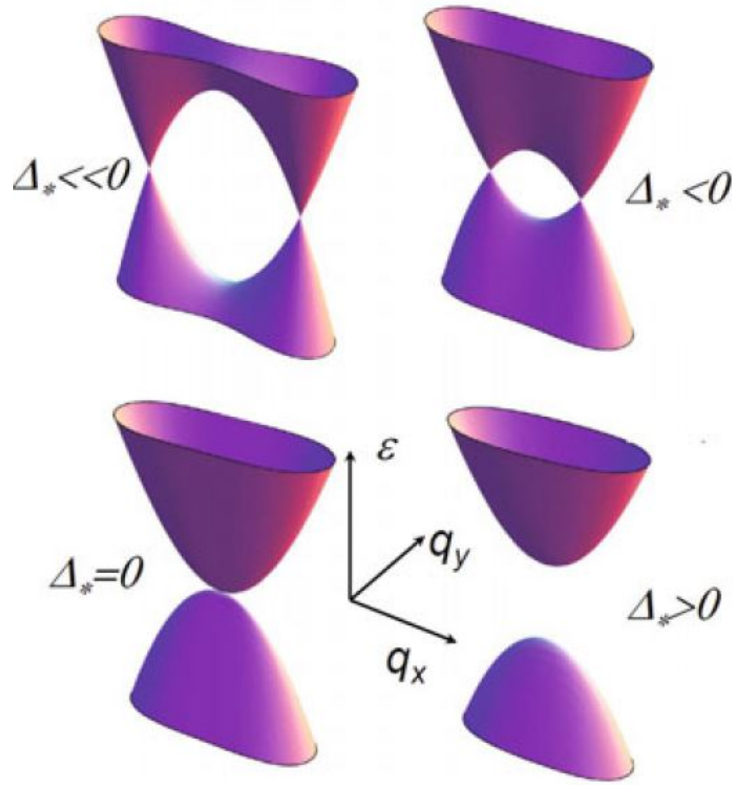
Figure 57: **Merging of Dirac cones with opposite charge.** Evolution of the spectrum when the quantity Δ_{+-} is varied and changes in sign at the topological transition. The low-energy spectrum stays linear in the q_y direction. Taken from [213].

While the geometry of the proposed uniaxial deformation is simple enough to imagine its implementation in graphene, the strain magnitude needed to reach the transition is estimated to be around 20%, which is slightly beyond the limit of breaking the bonds between atoms in graphene. This is why this transition has been observed for the first time in artificial systems, namely, in a hexagonal optical lattice in cold atoms [Tarruell et al.] and in an array of coupled microwave resonators. In the latter experiment, shown in fig. 58, the merging of Dirac cones was revealed from the measurement of the density of states [93].
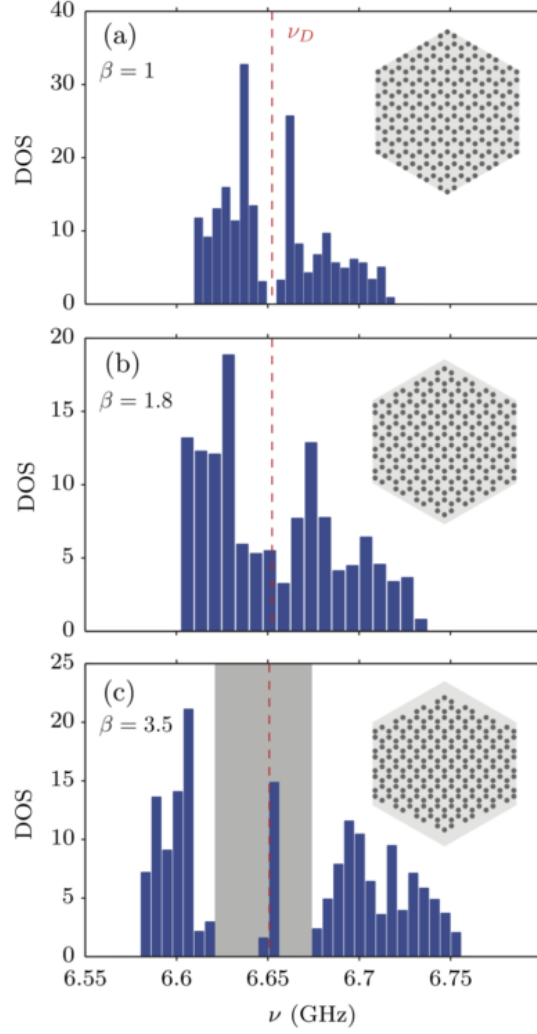
Figure 58: **Topological Transition of Dirac Points in a Microwave Experiment** Experimental DOS for (a) the regular graphene ($\beta = 1$), (b) and (c) anisotropic structures with $\beta = 1$ and $\beta = 1$, respectively. The dashed red lines indicate the Dirac frequency ν_D. The gray zone shows the band gap with edge states at ν_D. Taken from [93].

6.4 TOPOLOGICAL TRANSITION IN POLARITON GRAPHENE

As we already demonstrated a polariton HCL allows to observe Dirac dispersions in a direct manner. This will give us the opportunity to directly observe deformation of the dispersions during the topological phase transition in graphene. Even more importantly, it will allow us to study the modification of orbital bands, as will be presented in the last sections.

6.4.1 *Engineering of hopping parameters*

Engineering hopping parameters in a honeycomb lattice consisting of micropillars is a relatively straightforward task. The coupling between pillars is given by their size and distance (chapter 3), both of which can be controlled by designing the e-beam lithography mask.

We have modified the hopping parameters of the honeycomb lattice in order to implement the uni-axial strain described in the previous section. A mask with different sets of lattices is designed. In each set, the size of the pillars is fixed, as well as the length d of two out of three links each pillar shares with other pillars (see inset of fig. 59(a)). Then, the length d', of the third link is changed from lattice to lattice, leading to different values of the anisotropic coupling $t' \neq t$.

In fig. 59(b) we see a scanning electron microscopy image of a sample containing two sets of lattices mimicking strain i.e $\beta < 1$ ($t' < t$, columns of lattices a and b), and two set of lattices mimicking compression i.e. $\beta > 1$ ($t' > t$, columns c and d). Each set begins with an isotropic lattice with pillar size $D = 2.75\mu m$ and interpillar distances $d' = d$. The values of D, d and d' are given in the table in fig. 59(c).

To image the dispersions, standard luminescence experiments with non resonant excitation, using a $3\mu m$ excitation spot, are performed at 10K. The lattices have an exciton-photon detuning, measured at the lowest band at the Γ point, between $-17meV$ for all the lattices in column a, and -14 for all the lattices in column d (the columns are placed perpendicularly to the direction of the gradient of cavity energy).

(c)	a D=2.75µm d=2.40µm (strain)			b D=2.75µm d=2.2µm (strain)	c D=2.75µm d=2.40µm (compression)	d D=2.75µm d=2.30µm (compression)		
	[µm]	[meV]		[µm]	[µm]	[µm]	[meV]	
1	d'=2.40	t_L=-0.90	β_P=1.0	d'=2.20	d'=2.40	d'=2.30	t_S=0.17	β_S=1.0
2	d'=2.60	t_L=-0.85	β_P=0.75	d'=2.40	d'=2.20	d'=2.10	t_S=0.17	β_S=2
3	d'=2.65	t_L=-0.85	β_P=0.55	d'=2.60	d'=2.10	d'=2.00	t_S=0.18	β_S=2.6
4	d'=2.70	t_L=-0.85	β_P=0.50	d'=2.70	d'=2.00	d'=1.70	t_S=0.18	β_S=3.4
5	d'=2.72	t_L=-0.85	β_P=0.45	d'=2.72	d'=1.7	d'=1.6	t_S=0.19	β_S=3.8
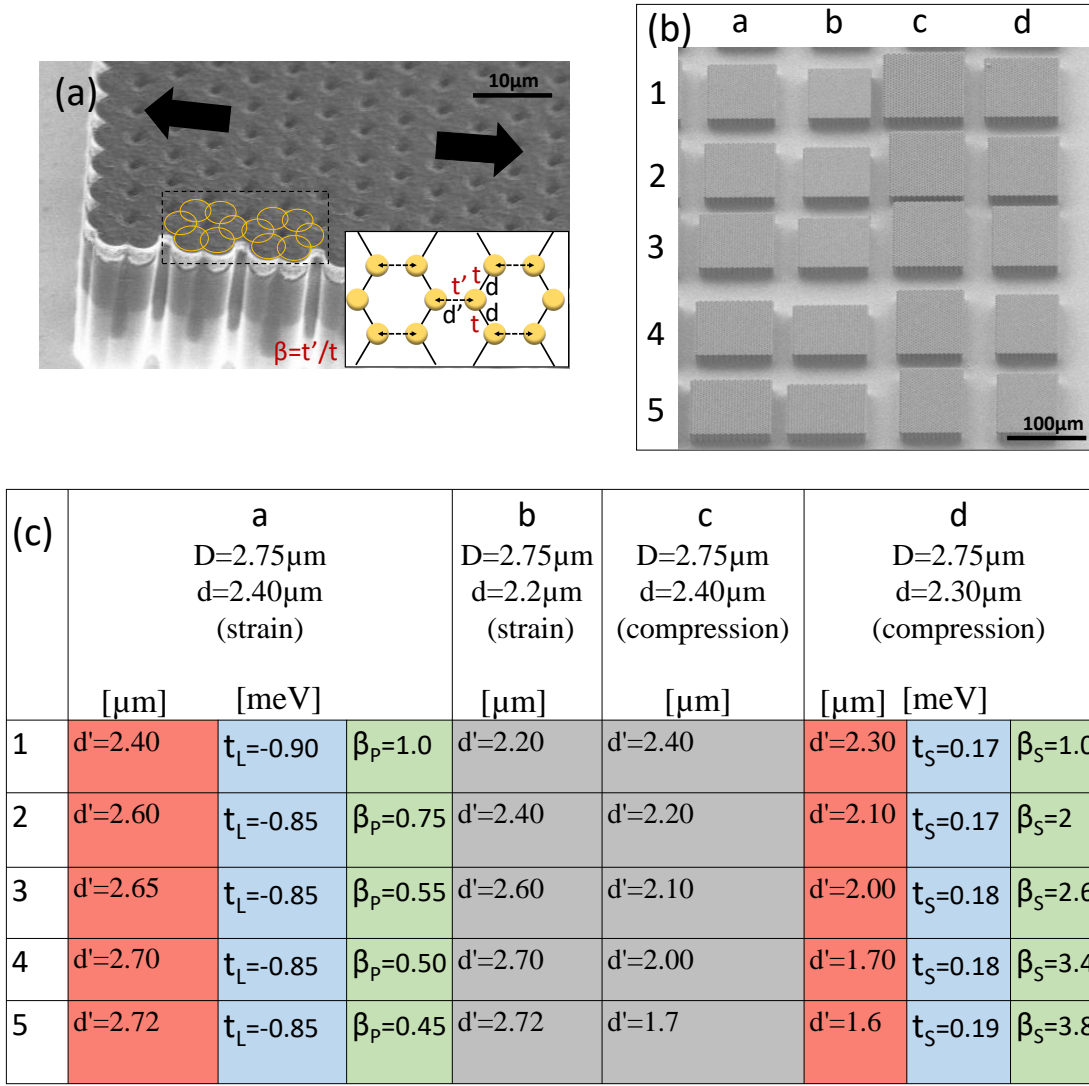
Figure 59: **Engineering of hopping parameters in polariton honeycomb lattices** Scanning electron microscope image of the sample. a) Hopping is changed by varying the distance between the pillars d' with respect to the distances d (defined in inset) b) Sets of lattices designed to simulate strain (a,b columns) or compression (c,d columns) in the lattice. (c) Corresponding lattice parameters. The values of t and β were obtained from fits to the experimental dispersions.

6.4.2 *Realization of semi-Dirac dispersion*

In order to study topological phase transition that occurs in graphene, we select a set of compressed lattices. We start from the isotropic lattice 1-d in fig. 59(b), with inter pillar distances $d' = d = 2.3\mu m$.

Figure 60(a) shows its dispersion along the k_x direction (for $k_y = 4\pi/3a$), (line 1 in fig. 60(f)). As expected, two Dirac cones are located at **K** and **K**$'$ points. The corresponding tight binding fit is shown with white lines. In the fit, the nearest and the next nearest

neighbor hopping parameters take the values $t = 0.17 meV$ and $t_{NNN} = 0.015 meV$, respectively.

A very different situation is found on fig. 60(c) showing the dispersion of the lattice 2-d, with the reduced distance $d' = 2.1 \mu m$, along the same direction. Along the k_x direction upper and lower bands show a quadratic touching around the **M** point ($k_x = 0$).

The hybrid nature of this dispersion is evidenced when imaging the dispersion along the perpendicular k_y direction in fig 60(d). In order to avoid the dark regions in the first Brillouin zone, we image the dispersion along line 2 (orange line in fig. 60(f)). Clearly, we observe linear band intersections around $k_y = (-3, 0, 3)k_{x0}$, all corresponding to the **M** point. We evidence thus, the dispersion of the semi-Dirac phase, reached when the value of the strain parameter in the fit is $\beta = 2$.

Further modification of the band structure with the reduction of distance d' is shown in fig. 60(e), for the lattice 4-d with $d' = 1.7 \mu m$. It leads to the opening of a gap of magnitude $0.65 meV$, and fitted strain parameter $\beta = 3.4$.

We note that, when fitting the data we obtained not only increased t', but also slightly increased values of the couplings t and t_{NNN} (see the table in fig. 59(b)). This isotropic increase of couplings is reasonable taking into account that approaching the pillars decreases the confinement in them.

We also notice that there is a small mismatch between the theory and the experiment in figs. 60(c,e). The most probable reason for that is the increase of non orthogonality of the wave functions in the pillars (see chapter 2) in the compressed lattices. The more the pillars overlap, the less the lattice can be described using wave functions of isolated atoms, as it is done in the tight binding approximation. Still, for the presented bands the deviation is not large, and there is no qualitative change of the shape of the bands.

The results discussed in this section represent the first direct observation of a phase transition between semi-metallic and insulating phases in two dimensions. We demonstrated that our system is very suitable for designing the dispersions in two dimensions. The relatively rapid increase of coupling with the pillar to pillar distance allows to explore a wide range of regimes. Tuning of strain parameter $1 < \beta < 4$ is achieved by changing the distance between the pillars by 30%. The critical point $\beta = 2$ is reached with a change by only 10%. Additionally this rate can be adjusted by modifying the size of the pillars (see section 3.5.4, fig. 30). The platform is thus very promising for implementing more complicated forms of deformation such as the nonuniform strain, which leads to formation of an artificial gauge field in the lattice.

Yet, even without going into more complicated geometries than the uni-axial strain, we can observe new kinds of transitions in polariton HCL. This is possible by making use of the orbital degree of freedom which is the subject of the next section.
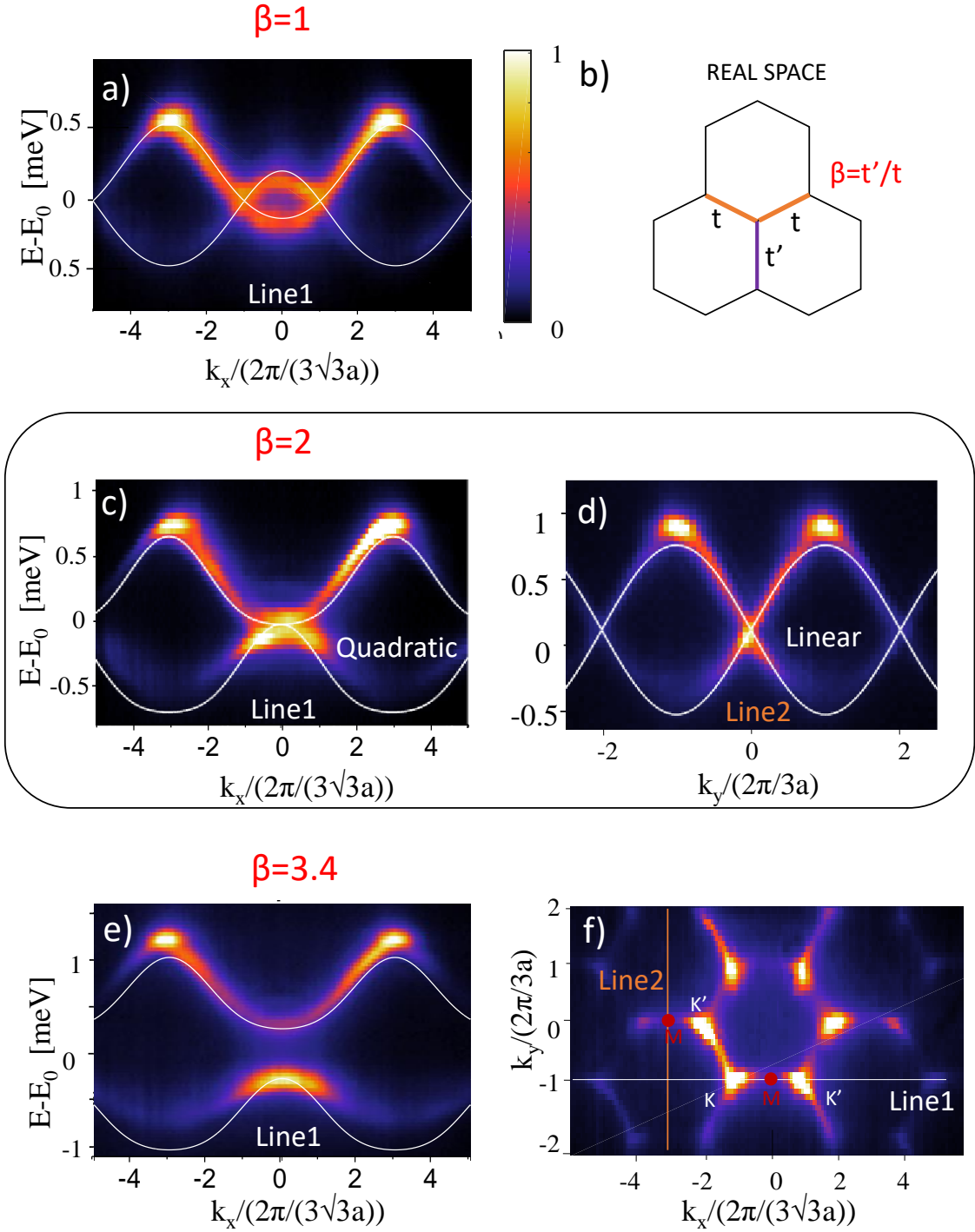
Figure 60: **Topological transition in polariton graphene** Intensity in the far field for the lattices with varied ratio $\beta = t'/t$ (as defined in b)). a) Isotropic lattice ($\beta = 1$) featuring two Dirac cones. c,d) $\beta = 2$. Semi-Dirac dispersion is observed , quadratic along k_x and linear along k_y direction. e) $\beta = 3.4$ The gapped phase. f) Map of momentum space at zero energy is used to mark the position of the high symmetry points.

6.5 STRAIN IN ORBITAL GRAPHENE

Different approaches, such as nanomanipulation, use of spin-orbit like coupling or pressure (i.e strain) have already been used on solid state matter in order to tune orbital band structure and evidence new kind of topological phase transitions.

In particular, with the discovery of new types of linear dispersions in solid state systems, these efforts opened new frontiers in the search of of quasi-particles whose propagation can be related to that of relativistic particles [201, 223]. Type-I and Type-II Weyl semi metals have been found or proposed in three dimensional transition metal dichalcogenide crystals with spin-orbit like coupling $TaAs$, WTe and $MoTe_2$. These features occur between electron and hole pockets, that is between the N-th and (N+1)th bands, where N is the total number of valence electrons per unit cell [224, 225, 208].

The ability to tune higher orbital bands in a simulator increases the chances of discovering and understanding new topological phase transitions and quasi particles. Transposing of new types of Dirac dispersions to bosons and particularly to photons allows studying them in new regimes, without the necessity to match the Fermi level with a point in the dispersion.

The rich yet simple band structure of orbital graphene provides a new playground for Dirac manipulation. It holds Dirac points, as well as band touching between a dispersive and a flat-band (see chapter 5). In this section we explore how these band degeneracies can be modified. Again, we will study uni-axial strain in the lattice, that is the case when $d' \neq d$, as depicted in the beginning of this chapter, fig. 59). In $p-$ bands this will lead to a change of the hopping parameter t_L along that link, and we can define $\beta_p = t'_L/t_L$.

In particular, $p-$bands Hamiltonian can also be written in the off diagonal form:

$$H_p = t_L \begin{pmatrix} 0 & Q \\ Q^* & 0 \end{pmatrix}, \quad Q = \begin{pmatrix} f_1 & g \\ g^* & f_2 \end{pmatrix}, \tag{126}$$

where f_1, f_2 and g, already introduced in chapter 5, can now be rewritten as:

$$f_1 = \frac{3}{4}s \quad , \quad f_2 = \beta + \frac{s}{4} \quad , \quad g = \frac{\sqrt{3}}{4}d \tag{127}$$

with:

$$s = e^{i\mathbf{k}\mathbf{a}_1} + e^{i\mathbf{k}\mathbf{a}_2} \quad , \quad d = e^{i\mathbf{k}\mathbf{a}_1} - e^{i\mathbf{k}\mathbf{a}_2}. \tag{128}$$

The spectrum consists of four bands, $\pm\epsilon_f$ and $\pm\epsilon_d$. In the case of $\beta_p = 1$, f and d denote the flat and the dispersive bands, respectively. When $\beta_p \neq 1$ there is no flatband but an important relation holds:

$$\epsilon_f \epsilon_d = |detQ| \tag{129}$$

With

$$\begin{aligned} detQ &= f_1 f_2 - g^2 \\ &= \frac{3}{4}e^{iK_y}\left(2\beta_p \cos K_x + e^{iK_y}\right). \end{aligned} \tag{130}$$

Finally, the position of the zero energy Dirac points in the $p-$band is given by $\epsilon_d = 0 \Rightarrow detQ = 0 \Rightarrow f_1 f_2 = g^2$. Therefore, we obtain from 130:

$$1 + 2\beta_p \cos K_x e^{-iK_y} = 0 \tag{131}$$

that is

$$K_y = 0 \quad , \quad cos(K_x) = -1/(2\beta_p). \tag{132}$$

It is also possible to find the winding number that describes Dirac cones in $p-$ bands, as well as the dispersive-flat band touching, for each value of parameter β_p. The procedure to calculate it was developed by Gilles Montambaux, from Laboratoire de Physique des Solids in Orsay during the collaboration initiated with this work. We provide details on this calculation in appendix .1. It consists of finding the effective 2×2 Hamiltonian $H_{eff}(\mathbf{k})$ in the vicinity of the desired point in momentum and energy. It is shown that H_{eff} can be written in terms of two Pauli matrices, and that it is thus possible to calculate the winding corresponding to it. We display the obtained values of ω for each band degeneracy in panels 1,2 shown on the left and right sides of figures 61.

Fig. 61(a-e) shows the deformation of the dispersion in the set of 5 lattices, column (1-5)a in fig 59(b), for which the parameter $\beta_p = t'_L/t_L$ is gradually decreased. All the figures show momentum space luminescence along the k_x direction passing through the Γ point in the second Bz., that is, for $k_y = 4\pi/3a$.

We start with the dispersion of an isotropic, non deformed honeycomb lattice, with a pillar size of $2.75\mu m$ and pillar to pillar distances $d = d' = 2.4\mu m$. In fig. 61(a) we can recognize Dirac cones around $(E - E_0)/t_L = 0$ and the dispersive-flat band touching at $E = (E - E_0)/t_L = -1.5$ (yellow and red dashed rectangles, respectively).

The white lines are obtained by tight binding simulation in which parameters t_L and β_p are fitted to experimental data. For the isotropic lattice we obtain $t_L = 0.90meV$ and $\beta_p = 1$. In panels 1 and 2, next to the figures, we show calculated dispersions in the two dimensional momentum space for the regions inside the rectangles, where we want to follow the dispersion deformation.

6.5.1   The zero energy region

We will first concentrate on the region around zero energy. Figure 61(b) displays dispersion measured on first deformed lattice, in which $d' = 2.6\mu m$. We can see that Dirac cones in $\mathbf{K}$ and $\mathbf{K}'$ points changed their position in momentum space and that they are closer to each other. The dispersion is well fitted using the parameter $\beta_p = 0.75$.

When reducing β_p Dirac cones move close to each other (see fig. 61(c) for $d' = 2.65\mu m$ and $\beta_p = 0.55$). In the next lattice, $d' = 2.7\mu m$, Dirac cones completely merge, revealing the quadratic band touching, fig. 61(d), similarly to the case of the $s-$band, discussed in the previous section.

The analogy is further confirmed if the distance d' is set to $2.72\mu m$: quadratic bands start to separate opening a gap, fig. 61(e). The opened gap proves to be small compared to the polariton linewidth $(200meV)$ to be clearly observed. However, the experimental data is well fitted using $\beta_p = 0.45$, which displays two quadratic bands separated by the gap around zero energy.
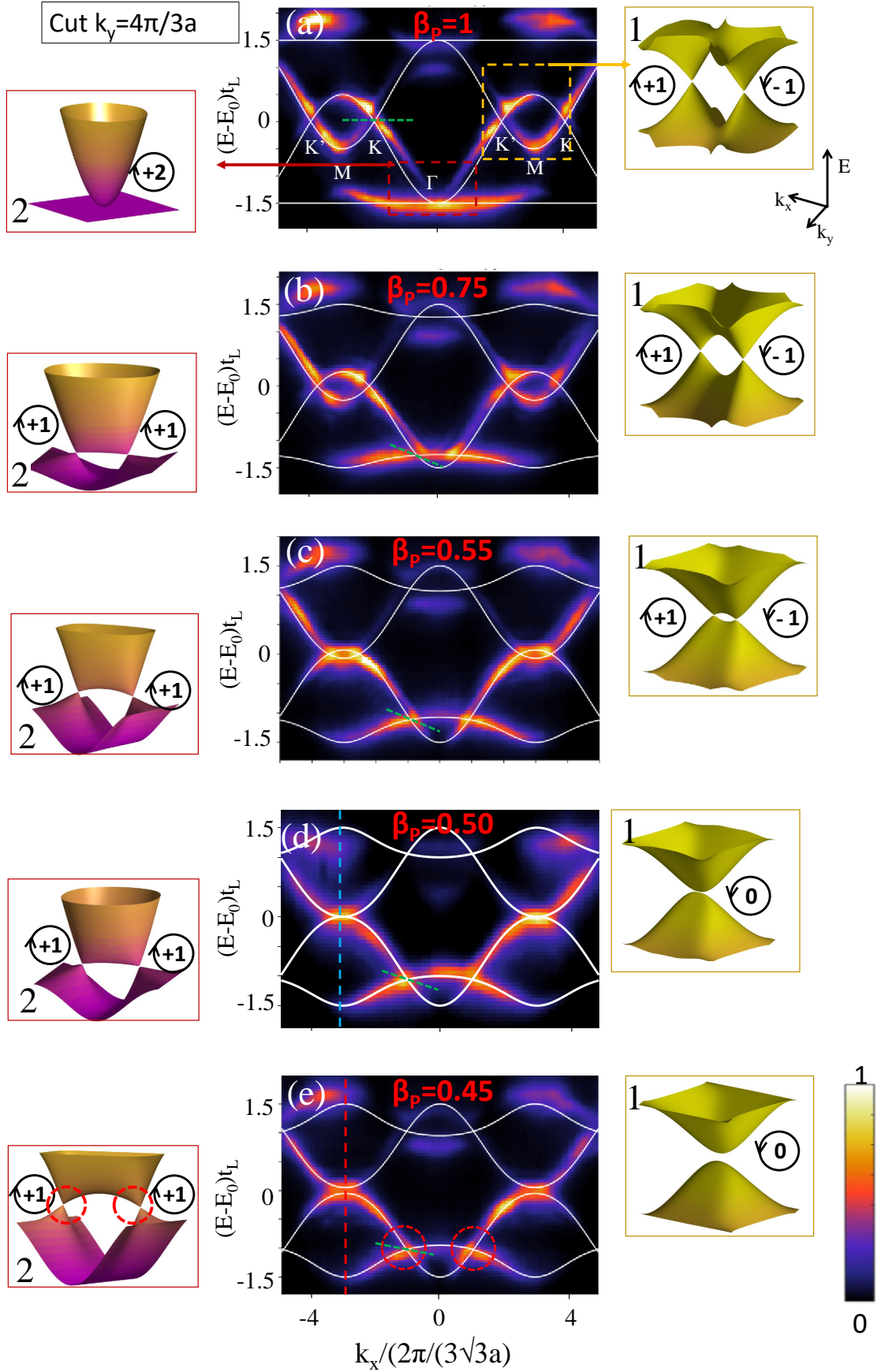
Figure 61: **Modification of band structure in orbital graphene** a) Intensity of far field emission for lattices in column (1-5)a in fig 59(b) at the energy of $p-bands$. $E_0 = 1570meV$, $k_y = 4\pi/3a$. Tight binding fit to the data is represented with the white lines in central panels, and in the insets 1 and 2, for the two regions of interest defined by red and yellow dashed rectangles in (a). Values of $\beta_p < 1$ obtained from the fit are given in each panel.

To confirm that the gap opening takes place in the most deformed lattice, we will compare the intensity of the spectra around the **M** points ($k_x = 3 \cdot 2\pi/(3\sqrt{3}a)$) where the cones merge (blue and red lines in figures 61(d) and (e) respectively). In fig.62(a) we display the intensity measured along the blue dashed line: we see only one peak present at the $E = 0$. The situation is different in fig.(b), which reveals the intensity along the red dashed line, where we resolve two peaks, confirming the opening of the gap.

The scenario evidenced here represents a topological phase transition due to the merging of Dirac cones with opposite winding, described in details in the previous section. The moving of Dirac cones in momentum space we detect here is exactly the same as the one presented in fig.56(b). Indeed, in collaboration with Gilles Montambaux we have shown that the universal Hamiltonian I (eq. 124) is a good approximation for $p-bands$ graphene under the effect of uni-axial strain around zero energy, see the appendix .1.
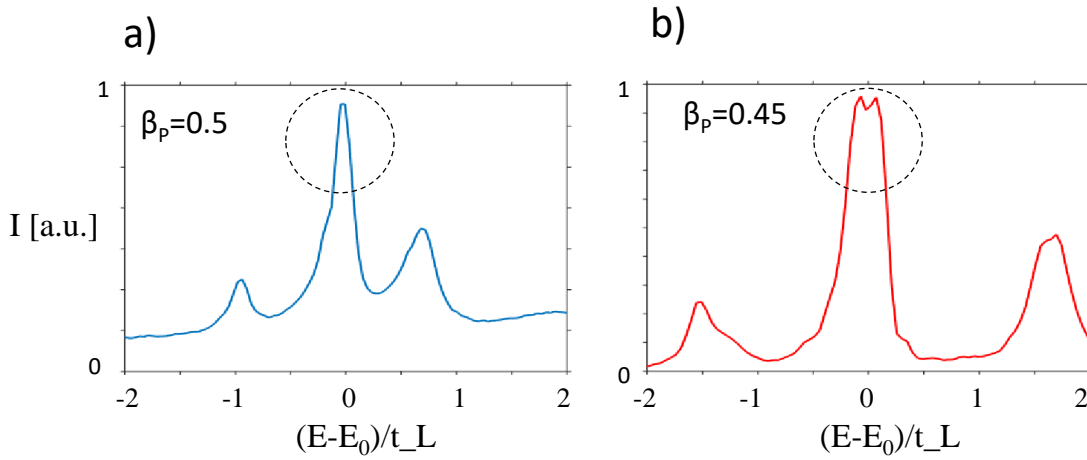
Figure 62: **Gap opening** a) The intensity of emission along the blue dashed line in fig. 61(d). Only one peak is visible at zero energy. b) The intensity along the red dashed line in fig. 61(e). Two peaks around zero energy prove the gapped phase is achieved for $\beta_p = 0.45$.

There is, however, an important difference between the phase transition transformation in the $s-$bands and in the $p-$bands: the direction of transformation necessary to achieve the modification. For $s-$ bands the lattice was "compressed" in order to increase the parameter β_p. For $p-$ band on the contrary, the necessary deformation corresponds to stretching the lattice, that is to the decrease of the coupling t'_L with respect to the coupling t_L.

To understand this difference we can analyze the two Hamiltonians, for $s-$ and $p-$ bands and in particular the equations defining the position of Dirac cones eq. 123 and eq. 132, respectively. The comparison between the two equations shows that the motion of the Dirac points under the uni-axial strain in the $p-$ bands is exactly the opposite to the motion in the $s-$bands. In the $s-$bans, Dirac points move and merge when $\beta_p = 2$. In the $p-$bands, they move and merge when β_p decreases to the value $\beta_p = 1/2$.

6.5.2 *Creation of tilted Dirac points with equal charge*

We will now go back to fig. 61 and concentrate on the low energy region, indicated by the red dashed lines in fig. 61(a). There, we will monitor the reshaping of the touching between the dispersive and the flat band.

As soon as the modification of the hopping $t'_L \neq t_L$ is introduced, the dispersion is significantly modified. The two lower energy bands now intersect linearly around two points, one on each side of the Γ point. A pair of new Dirac cones is created. In the ensemble of figures 61(b-e) we can explore the evolution of this new Dirac points with the change of parameter β_p. As the deformation is increased both the position and the energy of the Dirac points change. They move away from the Γ point while their energy rises. Tight binding calculations reported in white lines and the panels next to the each figure, help us following this evolution.

Looking more carefully at the measured and calculated dispersions, we can observe that the new Dirac cones are different from the ones we find at zero energy. They are tilted along the k_y direction (see green dashed lines in figs. 61(b-e), which traces the bisection of the crossing bands at the Dirac cone). When they appear, for $\beta_p = 0.75$, the tilt is very strong, and it is reduced as the lattice deformation is more important.

To further explore the properties of these new Dirac cones, we report their dispersions in two orthogonal directions, k_y and k_x, for the fixed value of the parameter $\beta_p = 0.5$. Figure 63(a) reproduces figure 61(d) and shows the dispersion in k_x along Line 1. Fig. 63(c) shows the dispersion in k_y measured along Line 2. In figure 63(b) we observe the linear crossing of the bands in the vicinity of $k_y = 1$ (red dashed square). A linear dispersion is present both along k_x and k_y directions, thus confirming the observation of tilted Dirac cones as the one depicted in fig. 63(d).

6.5.3 *The Description with the Universal Hamiltonian II*

How can we explain the transformation of the dipersive-flat band touching into a pair of Dirac points? Is such a transition controlled by conservation of some topological quantities? These questions are answered in collaboration with G. Montambaux. He developed a procedure for determining the winding properties of the Hamiltonian close to the band degeneracies in a multi-band system, in a similar manner as described in the previous section, to understand the merging of the Dirac cones. In that case, an effective 2×2 Hamiltonian was deduced to describe the region of around $p-$ bands Dirac points at zero energy.

Now, we will deduce the effective Hamiltonian around the Γ point, that is around the energy region $(E - E_0)/t_L = -3/2$. As explained in appendix .1, we start by the diagonalization of 4×4 $p-$ bands Hamiltonian of the non deformed lattice at the Γ point, where
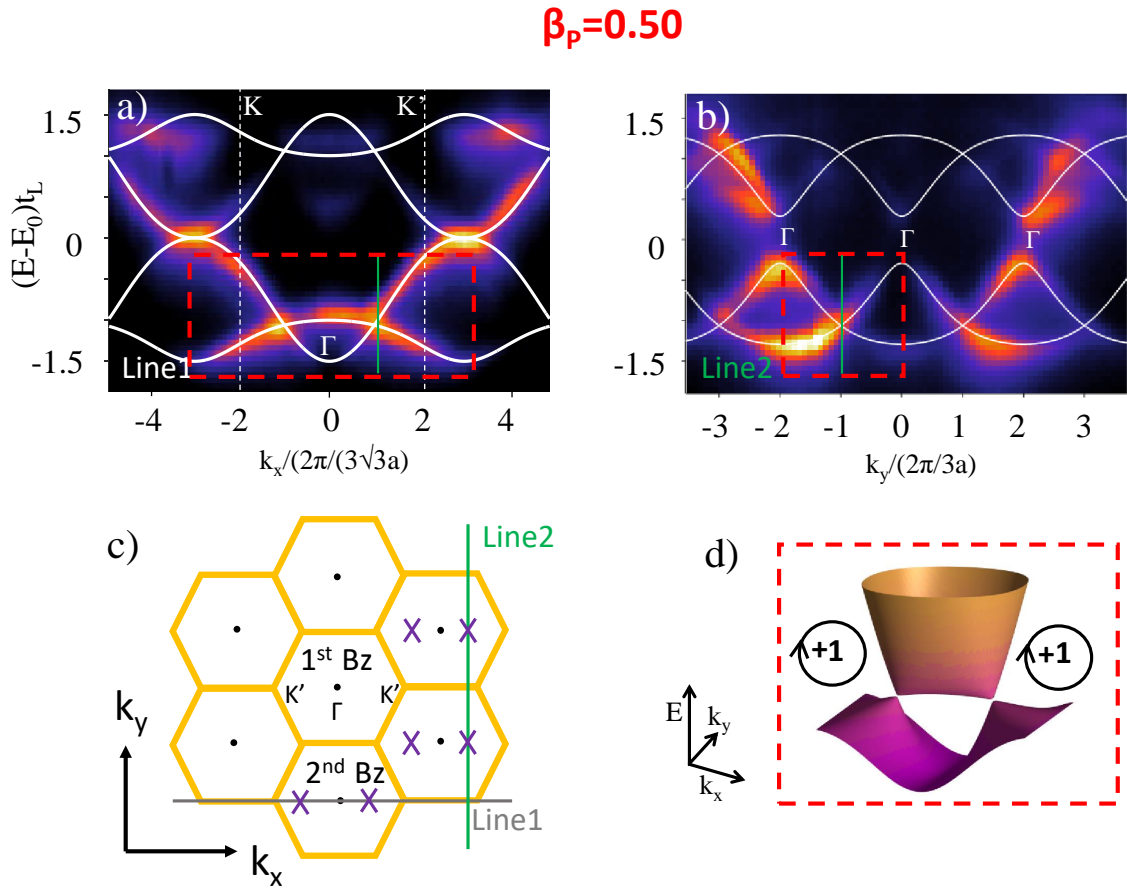
Figure 63: **Tilted Dirac cones**. $\beta_p = 0.5$ a) Dispersion along k_x direction. A pair of tilted Dirac cones is created in low energy region of $p-$bands when the lattice is strained (red dashed rectangle). b) Dispersion in perpendicular direction, trough one of the Dirac points (line 2 in c)). Linear intersection is observed. c) A scheme of lattice momentum space d) Visualization of the new Dirac cones in two dimensional momentum space (tight-binding calculation)

$f_1 = 3/2$ and $f_2 = 3/2$ and $g = 0$. We obtain the following eigen functions of the 4 eigen values $(f_1, f_2, -f_1, -f_2)$:

$$\frac{1}{\sqrt{2}}\begin{pmatrix} 1 \\ 0 \\ 1 \\ 0 \end{pmatrix}, \frac{1}{\sqrt{2}}\begin{pmatrix} 0 \\ 1 \\ 0 \\ 1 \end{pmatrix}, \frac{1}{\sqrt{2}}\begin{pmatrix} 1 \\ 0 \\ -1 \\ 0 \end{pmatrix}, \frac{1}{\sqrt{2}}\begin{pmatrix} 0 \\ 1 \\ 0 \\ -1 \end{pmatrix} \tag{133}$$

We can then rewrite the full Hamiltonian using this basis, but separating the subspaces of energies $3/2$ and $-3/2$. The Hamiltonian reads:

$$\mathcal{H}_\Gamma(\mathbf{k}) = \begin{pmatrix} \mathcal{R}f_1(\mathbf{k}) & \mathcal{R}g(\mathbf{k}) & -i\mathcal{I}f_1(\mathbf{k}) & -i\mathcal{I}g(\mathbf{k}) \\ \mathcal{R}g(\mathbf{k}) & \mathcal{R}f_2(\mathbf{k}) & -i\mathcal{I}g(\mathbf{k}) & -i\mathcal{I}f_2 \\ i\mathcal{I}f_1(\mathbf{k}) & i\mathcal{I}g(\mathbf{k}) & -\mathcal{R}f_1(\mathbf{k}) & -\mathcal{R}g(\mathbf{k}) \\ i\mathcal{I}g(\mathbf{k}) & i\mathcal{I}f_2(\mathbf{k}) & -\mathcal{R}g(\mathbf{k}) & -\mathcal{R}f_2(\mathbf{k}) \end{pmatrix} \equiv \begin{pmatrix} \mathcal{H}_+ & \mathcal{C} \\ \mathcal{C}^\dagger & \mathcal{H}_- \end{pmatrix}, \tag{134}$$

where $\mathcal{I}$ and $\mathcal{R}$ represent imaginary and real parts of functions f_2, f_2 and g. We can thus introduce an effective 2×2 Hamiltonian associated to the subspace of energy $-3/2$. Following the procedure described in the appendix .1 one can find the effective Hamiltonian at the second order:

$$\mathcal{H}_{eff}(\mathbf{k}) = \mathcal{H}_- + \frac{1}{3}\mathcal{C} \cdot C^\dagger \tag{135}$$

After expanding the terms f_1, f_2 and g around the Γ point up to the second order term in $\mathbf{k}$, we obtain:

$$\mathcal{H}_{eff} = H_0\sigma_0 - \frac{3}{16}\begin{pmatrix} k_x^2 - k_y^2 & 2k_xk_y \\ 2k_xk_y & k_y^2 - k_x^2 \end{pmatrix} \tag{136}$$

with $H_0 = \frac{3}{2} - \frac{3}{16}(k_x^2 + k_y^2)$, and σ_0 is a 2×2 unit matrix. Now, we can examine the properties of this Hamiltonian. The presence of the σ_0 term is related to the tilt of the Dirac cones observed in figs. 61 and 63. However this term doesn't affect the topological winding of the cone. This is why we will neglect it for the moment and rewrite second term of the above Hamiltonian in a more convenient form, using σ matrices:

$$\mathcal{H} = h_x(\mathbf{k})\sigma_x + h_z(\mathbf{k})\sigma_z \tag{137}$$

As we can see it contains terms proportional to two sigma matrices. But in contrast to the case of zero energy Dirac cones in both $s-$ and $p-$ bands these are not σ_x and σ_y but σ_x and σ_y. This means that the vector $\mathbf{h} = (h_x, h_z)$ winds in $x - z$ plane when $\mathbf{k}$ makes a circle around the Γ point. If we write $k_x = |k|sin\theta$, $k_z = |k|cos\theta$, and $|k| \equiv k$, components (h_x, h_z) become: $h_x = k^2\cos\theta\sin\theta = k^2\sin 2\theta$ and $h_z = k^2(\cos\theta^2 - \sin\theta^2) = k^2\cos(2\theta)$. The winding of $\mathbf{h}(\mathbf{k})$ when $\mathbf{k}$ makes a full turn around the origin can be found from $\tan\phi = h_z/h_x = \tan 2\theta$, section 2.3.3:

$$\omega = \frac{1}{2\pi}\int_0^{2\pi} 2d\theta \quad = 2 \tag{138}$$

Now that we have found the topological charge around the undeformed band touching we are interested in discovering what happens in the case when $\beta_p \neq 1$. We thus include $f_2 = \beta_p + 1/2$ into the calculation and the effective Hamiltonian becomes:

$$\mathcal{H}_{eff} = H_0 \sigma_0 - \frac{3}{16} \begin{pmatrix} k_x^2 - k_y^2 + \delta & 2k_x k_y \\ 2k_x k_y & k_y^2 - k_x^2 - \delta \end{pmatrix} \tag{139}$$

Here we have $H_0 = 1 + \frac{\beta_p}{2} - \frac{3}{16}(k_y^2 + k_x^2)$ and the merging parameter is defined as $\delta = \frac{8}{3}(\beta_p - 1)$.

The Hamiltonian we obtained to describe the deformation in the $p-$ bands has exactly the form of the universal Hamiltonian describing the splitting of a quadratic point with charge $+2$ into two Dirac points of charge $+1$ [226]. It has already been applied to explain the transition in bilayer graphene when the quadratic touching is transformed into a pair of Dirac points without opening of the gap. It can be written in the general form:

$$H_{++} = \left(\Delta_{++} + \frac{q_x^2 - q_y^2}{2m^*} \sigma_a + \frac{q_x q_y}{m^*} \sigma_b \right) \tag{140}$$

We can see that Hamiltonian 139 can be obtained by taking $a = z$, $b = x$, $m^* = \frac{8}{3}$ and $\Delta_{++} = \delta/2m^*$.

The modification of bands around the Γ point in orbital graphene represents thus the realization of second the possible scenario for merging (or emergence) of Dirac point in two dimensions.

6.6   ENGINEERING THE CRITICAL TYPE II DIRAC POINTS

6.6.1   *Compression in orbital bands*

In the previous sections we have evidenced two scenarios for the creation and annihilation of Dirac points in two dimensions. The classification of transitions is performed in terms of winding of Dirac cones. Hybrid dispersions with the direction dependent properties were generated through these transitions. We have experimentally observed the creation of Dirac cones whose tilt depends on the strength of the deformation by changing the ratio between hopping parameters in orbital graphene, $\beta_p < 1$. However, the critical point necessary for the creation of type II Dirac points, for which the corresponding Fermi level would be an open line and not a point, was not reached. We will see now that this is possible by compressing the orbital graphene, that is for $\beta_p > 1$.

Figure 64(a) shows dispersion of a non deformed lattice, this time along the k_y direction, at $k_x = -3k_{x0}$ (across the line 1 depicted in fig. 64(b)). The pillar size is $2.75\mu m$ and pillar to pillar distances $d' = d = 2.6\mu m$. We can observe also the dispersive-flat band touching at $(E - E_0)/t_L = \pm\frac{3}{2}$. It is well described by the tight binding calculation (white lines), particularly in the low energy region which we are going to examine (the upper part is modified due to the nonzero t_T, see 5.2)

Figure 64(c) shows the intensity of emission along the same direction in a deformed lattice, $d' = 2.4\mu m$. A very particular situation takes place: around two points in momentum space a flat-linear intersection is created.

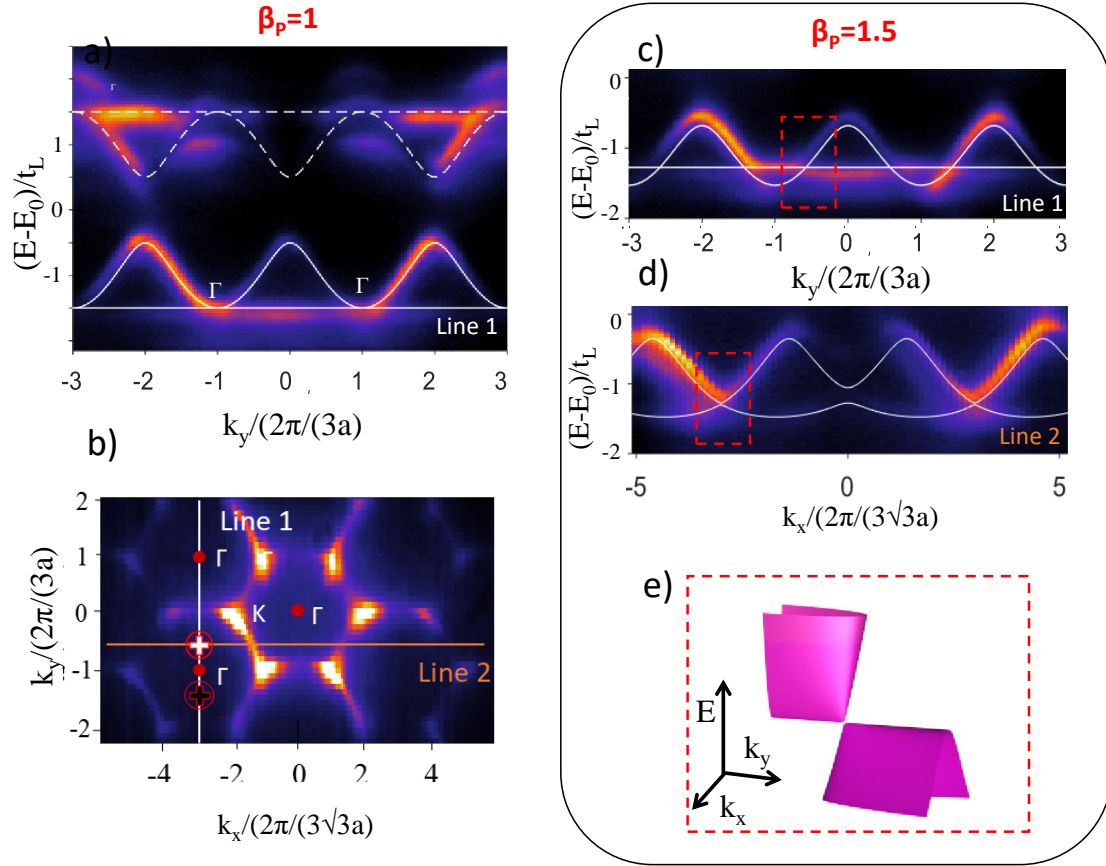Figure 64: **Critical type II Dirac points** a) Measured dispersion of an isotropic lattice along k_y direction (line 1 in b)). c),d) Dispersion of critical Type II Dirac point for $\beta_p = 1.5$, along the two perpendicular directions k_y and k_x, respectively. Along k_y a particular flat-linear dispersion of critically tilted Dirac cone is obtained. e) 2D visualization of obtained Dirac cone.

Let's look closer to the dispersion of one of such intersections, for example the one inside the red dashed rectangle in fig. 64(c). We can see that along the k_y direction zero and constant velocities are combined. It means that the quasi particle described by this dispersion has combined zero and infinite massed in the k_y direction, and it can move only in one sens along the y axis. This is exactly the situation predicted to happen in critically tilted Dirac cones expected to appear in the transition between Type I and Type II cones, as we introduced in the beginning of this chapter.

To explore the direction dependent properties of these observed Dirac cones, we plot the emission intensity along the k_x direction, (along the Line 2 in fig. 64(b)). The red dashed rectangle, fig. 64, marks the region around the Dirac cone we have analyzed above. We observe a linear crossing of the bands, meaning that we have indeed realized a critical Type II Dirac dispersion as the one visualized from tight binding calculation in fig. 64(e).

The results we obtained represent the first observation of this kind of dispersion. They can also be interpreted as the first observation of critical Type II Dirac quasi-particles. Still, certain precaution has to be taken when dealing with the analogy between quasi particles in solid state, or photonic systems and a free elementary particles, such as Dirac or Weyl particles, predicted by the standard model. While in the limited region of momentum space the two might have equivalent dispersions the analogy is not absolute. For example, in lattices Dirac cones appear in pairs. This is the case in graphene, for example, where two inequivalent Dirac points are labeled with the valley index. The analogy holds as long as no scattering between valley occurs. In the case of Type I Dirac cones, this is achieved by staying in the vicinity of zero energy (at least if an additional valley mixing mechanism is not introduced).

While in electronic lattices probing electrons with particular wave-vector, and avoiding valley mixing mechanisms can be very challenging, it is facilitated in polariton systems. Both energy and momentum of polaritons can be directly controlled in resonant pumping configuration. Scattering rates are low in state of the art samples with small density of defects allowing to potentially probe only one cone.

6.6.2 *The strong compression limit*

The specific simulator we used in the experiment, however doesn't allow us to successfully implement compression stronger then $\beta_p = 1.6$. When pillars are approached to reach $\beta_p = 2$, coupling of the $p - bands$ with the lower $s-$ and higher $d-$ bands becomes significant. The energy difference between bands is reduced, leading to deformation of the $p-$ bands dispersion. With the pillar size we used $2.75\mu m$ the separation between the bands in an non deformed lattice equals $1.5meV$, and for compressed lattices it reduces to $0.3meV$.

A way to overcome this problem could be the use of pillars with smaller diameter. In this way the energy distance between s, p, and d bands is increased, and mixing of the bands, which becomes important when pillars are strongly approached in compressed lattices, is minimized.

To complete the study of the behavior of orbital graphene bands upon compression, we provide results obtained by numerical simulation, in tight-binding approximation. Full deformation of the semi-flat Dirac dispersion under the uni-axial compression, that is for

the range of deformation parameter $1 \geq \beta_p \geq 2.5$ is given in figures 65(a-d). The figures display dispersions obtained along k_y direction, passing through the Γ point in the first Brillouin zone.

They reveal that the critical Type II Dirac cones are created by the moving of the dispersive bands away from the zero energy, while the energy of the flat band stays fixed at $E - E_0/t_L = \pm\frac{3}{2}$. Under this transformation, a pair of flat-Dirac cones is created around the Γ point, as we demonstrated experimentally. Then, as the deformation increases, Dirac cones from the adjacent Brillouin zones become closer together to each other, until they finally merge, fig. 65(c). The value of the deformation parameter when the merging occurs is $\beta_p = 2$. Dispersive and flat-band then touch again in a single point, this time at the **M** point. When the anisotropy of hopping parameters is increased above this point a gap opens and the system is described by four separate bands, fig. 65(d).

Following this evolution we can notice that the critical Type II Dirac cones are created for $\beta_p > 1$ according to the second type of topological phase transition, without opening of the gap, but annihilated at $\beta_p = 2$ according to the first one. The full transition from these two situations has been described in detail from a theoretical point of view in a recent work [227].

6.7 CONCLUSION

In conclusion, by engineering the hopping parameters in a honeycomb lattice we have directly evidenced two types of topological phase transitions in 2 dimensions.

The first one describes transition from the semi-metalic phase with two Dirac cones of opposite topological charge, into a gapped semiconductor phase. At the critical point of this phase transition a semi-Dirac dispersion for photons is created.

In the second scenario Dirac cones with equal charge emerge from the dispersive-flat band touching without opening of the gap. Dirac dispersions with tunable tilt are created in this case, including the critically tilted Type II cone. While we have not been able to observe pure Type II Dirac cones, recent theoretical works point out lattice geometries where they could be experimentally implemented in photonics [211].

Our system represents, thus, an extraordinary platform to tailor the properties of photonic dispersion. Taking into account the ability of photons, or polaritons, to propagate in the lattice, the doors are opened for studying, [212, 205] their exotic transport properties.

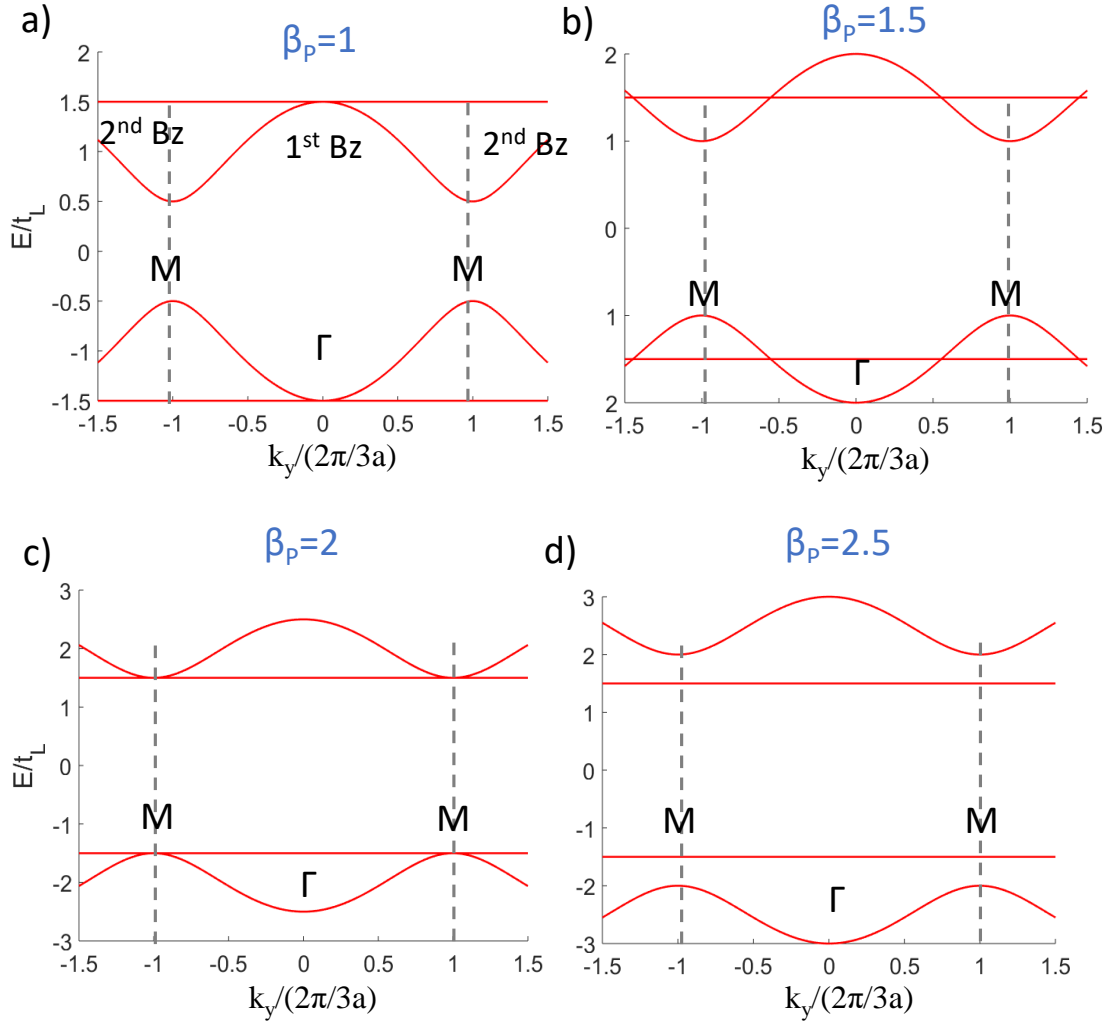Figure 65: **Creation and merging of critical type II Dirac points** a-d) $p-$bands graphene dispersions obtained with tight binding calculation reveal full evolution of critical type II Dirac points for $\beta_p > 1$. a,b) They are created in pairs around Γ point in each Brillouin zone. By increasing β_p, they approach and finally merge in **M** point. c) Four separated bands are obtained for $\beta > 2$.

7

In this thesis, we have studied the physical properties of cavity-polaritons in two-dimensional honeycomb lattices. The etching technique of microcavity structures developed in C2N allowed to create a lattice potential deep enough to access both $s-$ and $p-$ bands. The structure is well described by the tight-binding approximation: effective dispersion of the lowest $s-$ bands mimics the one of electrons in graphene. Additionally, higher energy $p-$ modes allow exploring dispersion featuring both Dirac cones and dispersive-flat band touchings, unavailable in graphene.

The out of equilibrium nature of the system provides direct experimental access to the system global band structure in low temperature luminescence experiments.

In the first experiment presented in this thesis, we explored the states at the edge of the lattice. Edge states predicted for graphene could be studied without the influence of edge impurities and instabilities that appear in the electronic lattice. We have evidenced their flat dispersion in zigzag and bearded edges as well as the geometry of their wavefunctions. Their location in momentum space corresponds well to the predictions obtained in the literature using topological arguments (i.e. by applying bulk-edge correspondence) and their wavefunction shape to the predictions attained by consideration of lattice symmetries.

In orbital graphene, we have evidenced for the first time different types of edge states. Non dispersive zero energy states connecting the Dirac points are found in regions of momentum space complementary to those of the edge states in the $s-$ bands. Their origin and position in momentum space are explained in terms of topological arguments, a result obtained in collaboration with theoreticians G. Montambaux and T. Ozawa.

Additionally, dispersive, i.e conducting, edge states appear in the gaps between the flat- and dispersive- bulk bands. Analytical expressions for their dispersion is found for the zigzag and bearded types of edges. Moreover, in contrast to the zero-energy states, dispersive ones have been experimentally found also in armchair edge. Weather topological arguments can be applied to these edge states is an open question and the topic of an ongoing study.

In the last chapter of the thesis we have focused on the bulk properties of the lattice. We demonstrated a way to tune Dirac cones and thus tailor the transport properties of the corresponding quasi particles.

Uni-axial strain was implemented in polariton honeycomb lattices by changing the distance between pillars along the lattice armchair direction. In this way, topological phase transitions are triggered. In s- bands, Dirac cones characterized by opposite topological windings merge, giving rise to a semi-Dirac dispersion, linear in one direction, and parabolic in the orthogonal one.

Under the effect strain, the band structure of orbital graphene represents a sandpit for creation of new Dirac cones, with different topological and transport properties from those in graphene. We have been able to observe tilted Type I, as well as critically tilted Type II Dirac dispersions.
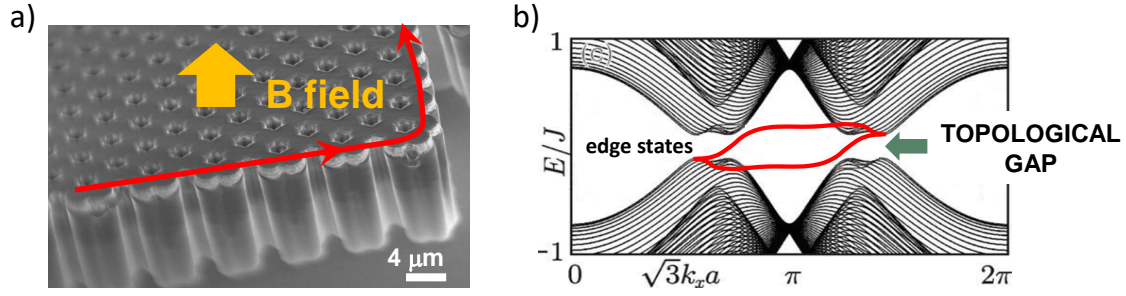
Figure 66: **Creation of polariton topological insulator** (a) SEM image of the polariton graphene simulator with the schematic representation of application of magnetic field and unidirectional edge state. (b) Spectrum of polariton topological insulator, red lines represent unidirectional edge state [228, 229]

The results obtained in this PhD work illustrate the power of polariton emulators for addressing a variety of physical phenomena at the frontier between photonics, Dirac matter physics and topological physics. Several research perspectives can be envisaged along three main directions.

The possibility to observe edge states is very important in the perspective of creating a Chern insulator in polariton graphene, as detailed in two theoretical proposals [228, 229]. By applying a magnetic field on polaritons, a polariton Zeeman splitting can be induced and time reversal symmetry can be broken. In presence of a Zeeman splitting and TE-TM splitting-present in the micro-cavities, Dirac cones in the honeycomb lattice have been predicted to open a topologically non trivial gap. Unidirectional edge states, protected from back scattering on defects and impurities, are predicted to emerge. Creation of such states at optical frequencies is a long sought goal in the very active field of topological photonics [159]. The practical difficulty lies in the necessity to create effective magnetic field for photons, a problem that has been successfully solved for microwave and telecom frequencies in gyromagnetic crystals [230, 231].

Implementation of this proposal in the optical frequency range would allow realization of compact optical isolators as well as other photonic devices immune to disorder. Polaritons represent a system with which a topological insulator could be realized. In addition their excitonic content offers the exciting possibility of exploring nonlinear effects [16]. Possibly unfeasible in natural graphene, phenomena such as soliton solutions of the nonlinear Dirac equation expected for instance in the armchair edge [232] could be experimentally addressed. With the creation of a polariton topological insulator another great perspective is the exploration of **topological phases of interacting photons**, a very interesting topic of both photonics and solid state physics [233, 234].

The second topic is the **study of exotic transport properties imposed by anisotropic Dirac cones**. For example, it has been predicted that the Klein tunneling is modified in tilted Dirac cones, fig.67. For particles around cones with opposite chirality, perfect transmission is achieved in two separated directions. The feature could be used to perform valley filtering and beam splitting, as explained in [205].
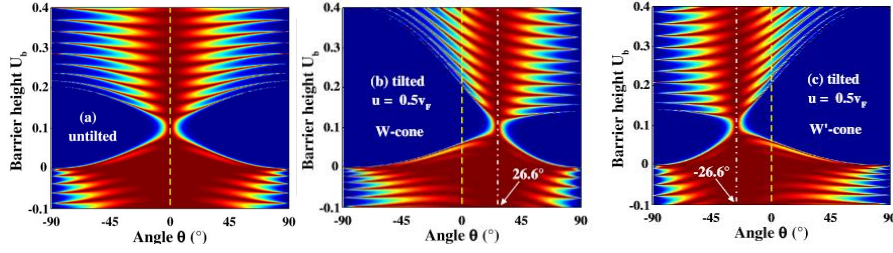
Figure 67: **Klein tunneling of tilted Dirac-Weyl fermions** Barrier versus angle maps of transmission probability without a) and with b,c) the effects of tilted energy dispersion.

Additionally, our results open new perspectives for the engineering of interfaces with different types of Dirac dispersions. This route has been recently proposed for simulating gravitational effects in the laboratory. Achieving critically tilted Type II dispersion (in the reference called Type III) is at the heart of the proposal for creation of solid-state analogue of a black hole horizon [235].
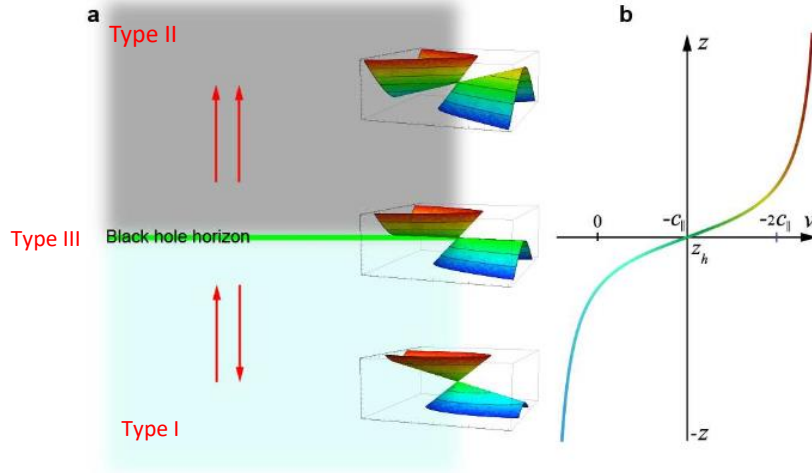
Figure 68: **Black Hole Horizon with a Type-III Dirac Semimetal** a) Schematic illustration of the solid-state analogue of black hole horizon in an inhomogeneous $Zn_2In_2S_5$ with controllable structural distortion. The red arrows indicate quasi particle propagating directions in each region. b) The dependence of the dragging velocity v on the z coordinate.

The third perspective would be to superimpose honeycomb lattice- with the **optically induced- potentials** for polaritons. Creation of localized potentials for polaritons trough their interaction with the optically induced exciton reservoir has been widely implemented in microcavity systems [23, 26]. This would allow for example, to engineer fully localized states in graphene [236], or to study symmetry breaking predicted to appear for charged and massless Dirac fermion in an attractive $1/r$ Coulomb potential [237].

Part I

APPENDIX A

7.1 ANALYTICAL EXPRESSIONS FOR THE ENERGY OF THE DISPERSIVE EDGE STATES

To obtain the analytical expressions for the energy of the dispersive, non-zero energy edge states in zigzag and bearded edges we look for the exponentially decaying solutions of the tight-binding Hamiltonian of a nanoribbon. To illustrate the procedure we apply it first to the simpler case of s-bands graphene [94]. The first step is to reduce the two-dimensional problem of a nanoribbon to an equivalent one-dimensional problem, that is, to reduce our s-band honeycomb problem to the SSH problem. This is done in section 4.3, where we obtained Hamiltonian 90.

Now, we search for eigenvalues of this Hamiltonian corresponding to eigenfunctions which are exponentially decaying into the bulk: $|A_M| = |A_0|e^{\frac{-3a}{2\xi}M} \equiv |A_0||\Omega|^M$. Here A_0 is the amplitude of the wavefunction on the first site of the chain, M counts the number of unit cells from the edge and ξ is the penetration length. In order to have a decaying wavefunction, we need to have $|\Omega| < 1$. Analogue expressions can be written for the B sites. Figure 69 shows bearded and zigzag ribbons and the equivalent 1D chains, with corresponding hopping and wavefunction amplitudes for the edge states.

After imposing the exponentially decaying solution to the problem, the Schrödinger equation for bearded edges has the form:

$$
-t_s \begin{pmatrix} 0 & 1 & 0 & 0 & 0 & 0 & \\ 1 & 0 & \alpha & 0 & 0 & 0 & \\ 0 & \alpha & 0 & 1 & 0 & 0 & \\ 0 & 0 & 1 & 0 & \alpha & 0 & \\ 0 & 0 & 0 & \alpha & 0 & 1 & \\ 0 & 0 & 0 & 0 & 1 & 0 & \\ & & & & & & \ddots \end{pmatrix} \begin{pmatrix} A_0 \\ B_0 \\ A_0\Omega \\ B_0\Omega \\ A_0\Omega^2 \\ B_0\Omega^2 \\ \vdots \end{pmatrix} = E \begin{pmatrix} A_0 \\ B_0 \\ A_0\Omega \\ B_0\Omega \\ A_0\Omega^2 \\ B_0\Omega^2 \\ \vdots \end{pmatrix} \tag{141}
$$

This system of equations has four unknowns: A_0, B_0, Ω and E. However, we can normalize the wavefunction to the amplitude A_0 of the outermost site. Therefore we have only three unknowns left. They can be found by taking the first three equations from the set of equations (141):

$$
\epsilon A_0 = t_s B_0
$$
$$
\epsilon B_0 = t_s A_0(1 + \alpha\Omega)
$$
$$
\epsilon A_0\Omega = t_s B_0(\alpha + \Omega) \tag{142}
$$

All the other equations contained in Eq.(141) are equivalent to the set (142). Using the condition $|\Omega| < 1$ we obtain the regions in momentum space where the zero energy edge states exist, Ref. [94]. For the bearded edge we have $B_0 = 0$ and:

$$
\Omega = \frac{-1}{\alpha} = \frac{-1}{2\cos(\frac{\sqrt{3}}{2}ak_y)}
$$
$$
2|\cos\frac{\sqrt{3}}{2}ak_y| > 1
$$

$$
\tag{143}
$$
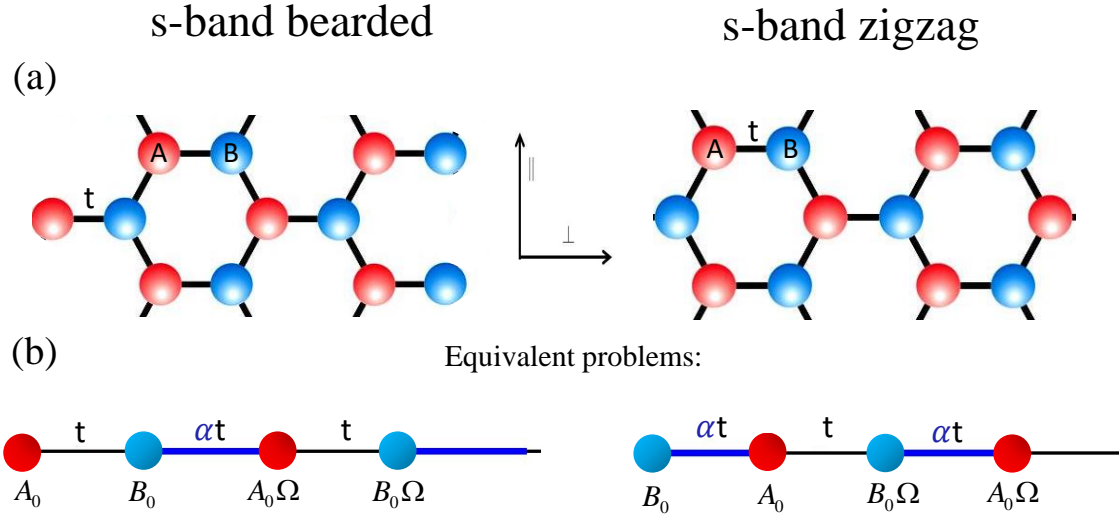
Figure 69: (a) *s*-bands honeycomb lattice nanoribbons with bearded and zigzag edges (b) Equivalent dimer chains. Hopping amplitudes are given on the links between the chain sites, and amplitudes of the edge states wave functions below the chain sites.

corresponding to the region marked in green in the upper-right panel of Fig. 51 in the chapter5, where the winding number has value 1.

To obtain expressions for the energies of the dispersive edge states in the *p*-bands we follow the same procedure. In this case, due to the existence of two modes per site, the reduction to the 1D problem involves two coupled chains corresponding to the p_x and p_y orbitals on each lattice site. Figure 70 shows the hopping amplitudes corresponding to a ribbon with zigzag edges.

We search again for exponentially decreasing solutions of the form $|A_{Mx}| = |A_{0x}||\Omega|^M$ with $|\Omega| < 1$ (equivalently for $|A_{My}|$, $|B_{Mx}|$, $|B_{My}|$). Now we have six unknown variables $A_{0x}, A_{0y}, B_{0x}, B_{0y}, \Omega, E$ or five after we normalize them to B_{0y}. By taking the first five linear equations of the the Schrödinger problem, we get the set of coupled equations:

$$
\begin{aligned}
\epsilon B_{0y} &= t_L(\gamma A_{0x} + \alpha A_{0y}) \\
\epsilon B_{0x} &= t_L(3\alpha A_{0x} + \gamma A_{0y}) \\
\epsilon A_{0x} &= t_L(3\alpha B_{0x} + \gamma^* B_{0y}) \\
\epsilon A_{0y} &= t_L(\alpha B_{0y} + \gamma^* B_{0x} + \Omega B_{0y}) \\
\epsilon B_{0y}\Omega &= t_L(A_{0y} + \alpha A_{0y}\Omega + \gamma A_{0x}\Omega)
\end{aligned}
\tag{144}
$$

The energy of the dispersive edge state in the zigzag edge is obtained by solving Eqs. (144) and is given by:

$$
E^{zig}_{disp.edge}(k_\parallel) = \pm t_L \frac{\sqrt{3}}{2}\sqrt{2 + \cos\left(\sqrt{3}k_\parallel a\right)}.
\tag{145}
$$
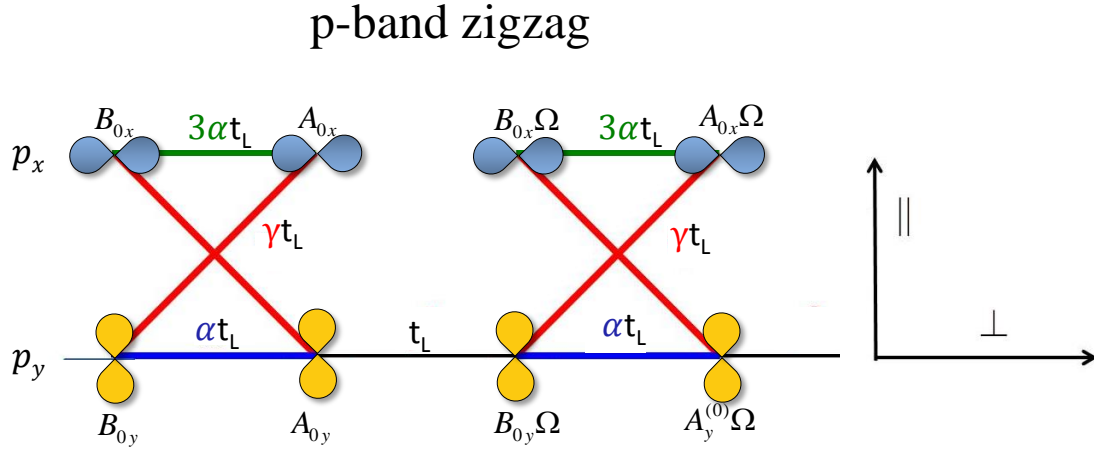
p-band zigzag

Figure 70: Amplitudes of the wave function for zigzag nanoribbon in the p-band: the problem is reduced to two coupled dimer chains.The hopping amplitudes are given on the links between the chain sites.

The penetration length ξ can be easily obtained:

$$\Omega = \cos(\frac{\sqrt{3}}{2}k_\parallel a) \tag{146}$$

$$\xi = -\frac{3a}{2\ln\left[\cos(\frac{\sqrt{3}}{2}k_\parallel a)\right]}.$$

The amplitudes of the dispersive edge states eigenfunctions on the unit cell located at the edge are:

$$A_{0x} = \mp\frac{i}{\sin(\frac{\sqrt{3}}{2}k_\parallel a)}\sqrt{\cos(\frac{\sqrt{3}}{2}k_\parallel a) + 2} \quad , \quad A_{0y} = 0$$

$$B_{0x} = -i\sqrt{3}\cot(\frac{\sqrt{3}}{2}k_\parallel a) \quad , \quad B_{0y} = 1 \tag{147}$$

where $\mp$ for the A_{0x} coefficient applies, respectively, to the positive/negative energy dispersive states.

Similar expressions describing the energy of the dispersive edge state in bearded edges (109 in the chapter 5, can be found in the same way.

Part II

APPENDIX B

.1 TOPOLOGICAL DESCRIPTION OF MERGING OF ZERO ENERGY DIRAC CONES IN ORBITAL GRAPHENE

In this appendix, we are going to demonstrate a theoretical method for determining topological properties of band degeneracies in $p-$bands graphene. The method is applicable to both undeformed and deformed lattice. It has been developed by G. Montambaux form LPS Orsay, and it consists of deducing an effective Hamiltonian around a certain point in momentum space. The procedure is similar to the one developed in [82] for bilayer graphene.

We are going to use this method here here in the appendix to show that the Lifshitz transition at zero energy in $p-$bands graphene, for $\beta < 1$, can be understood as merging of Dirac points with opposite topological charge. In the main text we will use it to understand the emergence of Dirac point from the dispersive-flat touching.

The procedure starts by taking the original Hamiltonian of the problem exactly in a certain point ($\Gamma, \mathbf{M}$ or $\mathbf{D}$ for example). This Hamiltonian can be easily diagonalized and written in a block diagonal form:

$$\mathcal{H}^{(0)} = \begin{pmatrix} H_+^{(0)} & 0 \\ 0 & H_-^{(0)} \end{pmatrix} \tag{148}$$

where $H^{(0)}$ and $H_-^{(0)}$ are also diagonal. Using the obtained basis we can rewrite the original Hamiltonian, which will now have the form:

$$\mathcal{H} = \begin{pmatrix} H_+ & \mathcal{C} \\ \mathcal{C}^\dagger & H_- \end{pmatrix} \tag{149}$$

where $\mathcal{C}, H_+ - H_+^{(0)}, H_- - H_-^{(0)}$ are small. By introducing the 4×4 Green function:

$$G(\mathcal{H}) = \begin{pmatrix} G_{11}(\mathcal{H}) & G_{12}(\mathcal{H}) \\ G_{21}(\mathcal{H}) & G_{22}(\mathcal{H}) \end{pmatrix} \tag{150}$$

Defined through its inverse:

$$G^{-1}(\mathcal{H}) = E - \mathcal{H} \tag{151}$$

we can obtain for the 2×2 Green function:

$$\begin{aligned} G_{11}(\mathcal{H}) &= (E - H_+ - \mathcal{C} \cdot (E - H_-)^{-1} \cdot \mathcal{C}^\dagger)^{-1} \\ &\equiv (E - \mathcal{H}_{eff})^{-1} \end{aligned} \tag{152}$$

defining the effective 2×2 Hamiltonian $\mathcal{H}_{eff}$. At lowest order, we then have:

$$\mathcal{H}_{eff} = H_+ + \mathcal{C} \cdot (E - H_-^0) \cdot \mathcal{C}^\dagger \tag{153}$$

.0.1   *Vicinity of Dirac points in $p-$ bands graphene*

To apply the procedure on the zero energy Dirac cones we start from the Hamiltonian of $p-$bands graphene given in the main text by the expressions 126-128. First, we concentrate

on the vicinity of the Dirac points when $\beta = 1$. The coordinates of one of the **K**point are $(K_y = 0, K_x = -2\pi/3)$ Hamiltonian at this point can be written as:

$$
\mathcal{H}_K = \frac{3}{4}\begin{pmatrix} 0 & 0 & -1 & i \\ 0 & 0 & i & 1 \\ -1 & -i & 0 & 0 \\ -i & 1 & 0 & 0 \end{pmatrix} \tag{154}
$$

Its eigen functions, associated respectively with the energies 0,0,3/2,-3/2 are found to be:

$$
\frac{1}{\sqrt{2}}\begin{pmatrix} 0 \\ 0 \\ i \\ i \end{pmatrix}, \frac{1}{\sqrt{2}}\begin{pmatrix} -i \\ 1 \\ 0 \\ 0 \end{pmatrix}, \frac{1}{2}\begin{pmatrix} i \\ 1 \\ -i \\ 1 \end{pmatrix}, \frac{1}{2}\begin{pmatrix} -i \\ -1 \\ -i \\ 1 \end{pmatrix} \tag{155}
$$

It this new basis Hamiltonian can be rewritten in the diagonal form. In the vicinity of the **K** point, where $\mathbf{q} = \mathbf{k} - \mathbf{K}$ it takes the form:

$$
\mathcal{K}(\mathbf{q}) = H_s = t_s \begin{pmatrix} \mathcal{H}_0 & \mathcal{C} \\ \mathcal{C}^\dagger & \mathcal{H}_e \end{pmatrix}, \tag{156}
$$

T blocks $\mathcal{H}_0$ and $\mathcal{H}_e$ correspond respectively to the low energy (around E=0) and high energy (around $E = \pm\frac{3}{2}$) regions. Explicitly they take the form:

$$
\mathcal{H}_0 = \frac{1}{2}\begin{pmatrix} 0 & f_2 - f_1 + 2ig \\ f_2^* - f_1^* - 2ig^* & 0 \end{pmatrix} \tag{157}
$$

and

$$
\mathcal{H}_e = \frac{1}{2}\begin{pmatrix} \mathcal{R}(f_2 - f_1) + 2\mathcal{I}(g) & i\mathcal{I}(f_1 - f_2) + i\mathcal{R}(g) \\ -i\mathcal{I}(f_1 - f_2) - i\mathcal{R}(g) & \mathcal{R}(f_1 - f_2) - 2\mathcal{I}(g) \end{pmatrix} \tag{158}
$$

They are coupled by the off-diagonal block $\mathcal{C}$:

$$
\mathcal{C} = \frac{1}{2\sqrt{2}}\begin{pmatrix} f_1^* + f_2^* & f_1 + f_2 \\ -(f_1^* + f_2^*) & f_1 + f_2 \end{pmatrix} \tag{159}
$$

Finally, at low energy, near the **K** points and to the lowest order of vector **q** the vicinity od the Dirac points is well described y the low energy 2x2 Hamiltonian:

$$
\mathcal{H}_e ff = \frac{3}{4}\begin{pmatrix} 0 & q_x - iq_y \\ q_x - iq_y & 0 \end{pmatrix} \tag{160}
$$

From the above expression we can conclude that the linear spectrum at low energy corresponds to two usual Dirac points. We already know that they are characterized with opposite charge, as guaranteed by the property of Hamiltonian: $\mathcal{H}_{\mathbf{K}'} = \mathcal{H}_{\mathbf{K}^*}$.

.0.2   *Merging of zero energy Dirac points in p−bands*

Now we are interested to describe the merging of Dirac points we have evidenced experimentally. It happens when

$$K_y = 0 \quad , \quad \cos(K_x) = -1 \tag{161}$$

, that is for $k_x = 2\pi/\sqrt{3}$,(**M** point). We can diagonalize $\mathcal{H}_M$, taken exactly in this point, then find the eigen values and the eigen functions, and write the Hamiltonian in its vicinity in the form:

$$\mathcal{H}_M(\mathbf{k}) \equiv \begin{pmatrix} \mathcal{H}_0 & \mathcal{C} \\ \mathcal{C} & \mathcal{H}_e \end{pmatrix} \tag{162}$$

After taking into account the necessary terms at lowest order in perturbation, we obtain Hamiltonian which is linear in q_y and quadratic in q_x:

$$\mathcal{H}_{eff} = \begin{pmatrix} \beta - \frac{1}{2} - \frac{3}{16}q_x^2 & -\frac{3}{4}iq_y \\ \frac{3}{4}iq_y & \frac{1}{2} - \beta + \frac{3}{16}q_x^2 \end{pmatrix} \tag{163}$$

As announced the obtained Hamiltonian has exactly the form 124 of the Universal Hamiltonian $\mathcal{H}_\pm$ with $\Delta = 1/2 - \beta$, $m* = 8/3$ and $c = 3/4$.

PUBLICATIONS AND CONFERENCES

List of publications

1. <u>Marijana Milićević</u>, O. Bleu, D. D. Solnyshkov, I. Sagnes, A. Lemaitre, L. Le Gratiet, J. Bloch, G. Malpuech and A. Amo, *Lasing in optically induced gap states in photonic graphene,* to be submitted

2. <u>Marijana Milićević</u>, T. Ozawa, G. Montambaux, I. Carusotto, E. Galopin, A. Lemaître, L. Le Gratiet, I. Sagnes, J. Bloch, and A. Amo, *Orbital Edge States in a Photonic Honeycomb Lattice*, [Physical Review letters, 118, 107403 (2017](#))

3. <u>M. Milićević</u>, T. Ozawa, P. Andreakou, I. Carusotto, T. Jacqmin, E. Galopin, A. Lemaître, L. Le Gratiet, I. Sagnes, J. Bloch, and A. Amo, *Edge states in polariton honeycomb lattices,* [2D Materials 2, 034012 (2015).](#)

Conferences

1. <u>Invited</u> - *Creation of Semi-Dirac Photons Through Topological Phase Transitions in Photonic Honeycomb Lattices,* GDR PHYSIQUE QUANTIQUE MESOSCOPIQUE-SESSION PLANIERE, Aussois, France, December 4-7, 2017

2. <u>Invited</u> – Polartion graphene emulator, CONDENSED MATTER DIVISION OF EUROPEAN PHYSICAL SOCIETY- CMD26, Groningen, The Netherlands, September 49, 2016

3. *Orbital edge states in polariton honeycomb lattices, COST JOINT SCHOOL OF QUANTUM SIMULATION AND MANY-BODY PHYSICS WITH LIGHT, Chania, Greece, 4-9 June 2016*

4. *Edge states in polariton honeycomb lattices,* INTERNATIONAL CONFERENCE ON OPTICS OF EXCITONS IN CONFINED SYTEMS, OECS15, Jerusalem, Israel, October 11-16, 2015

5. *Edge states in polariton honeycomb lattices,* CONGRES GENERAL DE LA SOCITE FRANCAISE DE PHYSIQUE, Strasbourg, France, August 24-28, 2015

2D Materials

CrossMark

PAPER

Edge states in polariton honeycomb lattices

M Milićević[1], T Ozawa[2], P Andreakou[1], I Carusotto[2], T Jacqmin[1,3], E Galopin[1], A Lemaître[1], L Le Gratiet[1], I Sagnes[1], J Bloch[1] and A Amo[1]

1   Laboratoire de Photonique et Nanostructures, LPN/CNRS, Route de Nozay, 91460 Marcoussis, France
2   INO-CNR BEC Center and Dipartimento di Fisica, Università di Trento, I-38123, Povo, Italy
3   Present address: Laboratoire Kastler Brossel, UPMC-Sorbonne Universités, CNRS, ENS-PSL Research University, Collège de France, 4 place Jussieu, Case 74, F75252 Paris Cedex 05, France.

E-mail: alberto.amo@lpn.cnrs.fr

Keywords: polariton, photonic graphene, edge states, optics

Abstract

The experimental study of edge states in atomically thin layered materials remains a challenge due to the difficult control of the geometry of the sample terminations, the stability of dangling bonds, and the need to measure local properties. In the case of graphene, localized edge modes have been predicted in zigzag and bearded edges, characterized by flat dispersions connecting the Dirac points. Polaritons in semiconductor microcavities have recently emerged as an extraordinary photonic platform to emulate 1D and 2D Hamiltonians, allowing the direct visualization of the wavefunctions in both real- and momentum-space as well as of the energy dispersion of eigenstates via photoluminescence experiments. Here we report on the observation of edge states in a honeycomb lattice of coupled micropillars. The lowest two bands of this structure arise from the coupling of the lowest energy modes of the micropillars, and emulate the π and $\pi^\star$ bands of graphene. We show the momentum-space dispersion of the edge states associated with the zigzag and bearded edges, holding unidimensional quasi-flat bands. Additionally, we evaluate polarization effects characteristic of polaritons on the properties of these states.

Introduction

Graphene is a 2D material with extraordinary transport properties. Many of them arise from its non-trivial geometry with two identical atoms per unit cell, resulting in linear bands crossing at two non-equivalent Dirac points. The spinor character of the wavefunctions gives rise to a Berry phase of $\pm\pi$ when circumventing each of these points in momentum space. This feature is at the origin of its non-conventional transport properties like ballistic Klein propagation [1, 2], antilocalization in the presence of disorder [3], or Veselago lensing effects when traversing a potential step [4]. The non-zero Berry phase around the Dirac points has an interesting consequence: the existence of edge states in finite-size samples. Indeed, it has been recently shown that the existence of such states can be related to the non-zero Berry phase along a straight trajectory in momentum space defined by the geometry of the considered edge [5–7]. Because

the Berry phase depends on the trajectory, not all possible edge geometries present localized states [8].

The most commonly considered graphene terminations are the so-called armchair, zigzag, and bearded. Among them, only the last two present localized states, characterized by a flat dispersion linking the K and K' Dirac points [8–11]. Although these edge states may play an important role in the localization and transport in small-size graphene nanoribbons, experimental studies on the spatial distributions of the wavefunctions and their dispersion are not straightforward. While different kinds of terminations can be prepared in graphene and visualized using scanning tunneling microscopy [12, 13], the existence of electronic edge states has only been evidenced via the measurement of the local density of states, which provides information on their energy and on the curvature of their dispersion, but misses any information on their microscopic spatial structure and on their momentum distribution [12].

Photonic graphene analogues are an ideal platform to experimentally address the single particle physics of 2D lattices [14]. Optically induced honeycomb lattices in photorefractive crystals have been employed to study conical diffraction effects [15, 16] and the spinor character of the wavefunctions on the honeycomb lattice [17]. Arrays of photonic coupled waveguides can be engineered with single site precision, and they have been recently used to engineer artificial gauge fields in strained honeycomb lattices [18] and to fabricate a photonic analogue of a Floquet–Chern insulator [19]. Lattices of microwave resonators have also been shown to mimic several properties of electronic graphene [20, 21]. The possibility to control both the local geometry and the coupling has been used in both systems [7, 22], as well as in experiments with ultracold atoms [23], to study exciting phenomena like the topological transition associated to the merging of Dirac cones, as first suggested by Montambaux *et al* [24, 25], and edge states. Moreover, photonic systems allow realizing any type of lattice termination, even those that are not stable in graphene such as the bearded edge. The spatial and momentum distributions of certain edge wavefunctions have been studied using microwave resonators [26] and coupled waveguides [7, 27]. However, neither of these two systems provides the combined information on real, momentum, and energy spaces needed to reconstruct the band dispersion of the eigenfunctions, and in particular of the edge states.

In this sense, arrays of coupled micropillars in semiconductor microcavities provide a versatile platform to study 1D and 2D photonic lattices. In a single micropillar, photons are confined in the three spatial dimensions, and they are strongly coupled to quantum well excitons placed at the maxima of the electromagnetic field. The new eigenstates of the micropillars are polaritons, with a mixed exciton–photon nature that provides them with significant interactions [28]. By partially overlapping two micropillars, we can engineer the hopping of photons, and thus polaritons, between different pillars [29, 30]. By extending this coupling to 2D arrays, a polariton honeycomb lattice has been recently realized [31]. Other techniques to engineer polariton lattices have been recently reported [32–37].

The coupled micropillar system is well described by a tight-binding Hamiltonian giving rise to polariton dispersions analogue to the electronic π and $\pi^\star$ bands of graphene. One of its main assets is that the escape of photons out of the microcavity provides all the information regarding the amplitude, phase, momentum, and energy of the polariton eigenstates: angularly resolved spectroscopy reveals the energy bands of the system, evidencing the characteristic linear dispersion around the Dirac cones, as shown in [31]. In the present work, we report on the observation of localized edge states along zigzag and bearded edges in such a honeycomb lattice of coupled micropillars. We observe a flat band dispersion for these edge states, connecting K and K' points at complementary regions in momentum space, as expected from tight-binding calculations [8]. Despite the non-zero next-to-nearest neighbor coupling in our lattices, the observed edge states remain flat up to the resolution given by the polariton linewidth. Our results are promising in view of observing topologically protected edge states when combining polariton polarization effects and external magnetic fields to realize a photonic topological insulator [38–40].

The polariton honeycomb lattice

In our experiments we use a $Ga_{0.05}Al_{0.95}As$ $\lambda/2$ cavity embedded in two $Ga_{0.05}Al_{0.95}As/Ga_{0.8}Al_{0.2}As$ Bragg mirrors with 28 (40) top (bottom) pairs, the same as in the original realization of the polariton honeycomb lattice [31]. The cavity contains three sets of four 70 Å GaAs quantum wells located at the three central maxima of the confined electromagnetic field, resulting in a Rabi splitting of 15 meV. The planar microcavity, grown by molecular beam epitaxy, is etched down to the substrate in the form of a series of honeycomb lattices of coupled micropillars, as shown in figure 1 of [31]. The zero dimensionality of the micropillars imposes quantized energy levels for polaritons. Therefore, they behave like artificial photonic atoms. The lowest energy polariton eigenstate of an individual micropillar presents cylindrical symmetry, like the p_z orbitals of graphene. To introduce the coupling between the micropillars, we etch them so that they partially overlap (the interpillar distance is set to be smaller than their diameter). The narrow region between the pillars represents a potential barrier for photons and thus, for polaritons, through which they can evanescently tunnel. The coupling strength can be tuned by choosing the size of the pillars and the distance between them [29]. To enhance the tunneling we consider lattices with predominantly photonic polaritons, at −17 meV exciton–photon detuning.

By properly designing the lithographic mask used to etch the planar cavity into a honeycomb lattice, we engineer different types of edges in our samples. Figure 1(a) shows a lattice containing the most commonly considered edge types: zigzag, armchair, and bearded. The lattice consists of nearly 30 unit cells along the crystallographic axes. This size is large enough for the properties of the bulk to be dominant when probing lattice sites located near the center, while simultaneously showing edge physics when probing the properties in the edges.

Before reporting on the experimental results, we first consider the graphene dispersion relation for the bulk and edge bands using a tight-binding model including next-nearest-neighbor hopping $t' = -0.08\,t$, where t is the nearest neighbor coupling. This is the

Figure 1. Honeycomb lattice edges. (a) Optical microscope image of the sample containing the three considered types of edges. (b) Calculated band-structure of an infinite honeycomb lattice in the tight-binding approximation with nearest- and next-nearest-neighbor coupling. (c) Calculated band-structure for graphene nanoribbons with bearded (green) and zigzag (red) edges. The different blue lines correspond to the projection on the k_y-E plane of the dispersion of the different transverse modes due to the confinement in the x-direction. The red and green lines show the edge bands corresponding to zigzag and bearded terminations, respectively. (d) First and adjacent Brillouin zones showing the regions in k space where the edge states are expected. (e) Simulation of the momentum distribution for zigzag and bearded edge states obtained by Fourier transforming along x the calculated spatial wavefunction of the edge states corresponding to different k_y values. Dashed lines show fully delocalized edge states along k_x. (f) Penetration length of the amplitude of the edge states wavefunction according to equation (1).
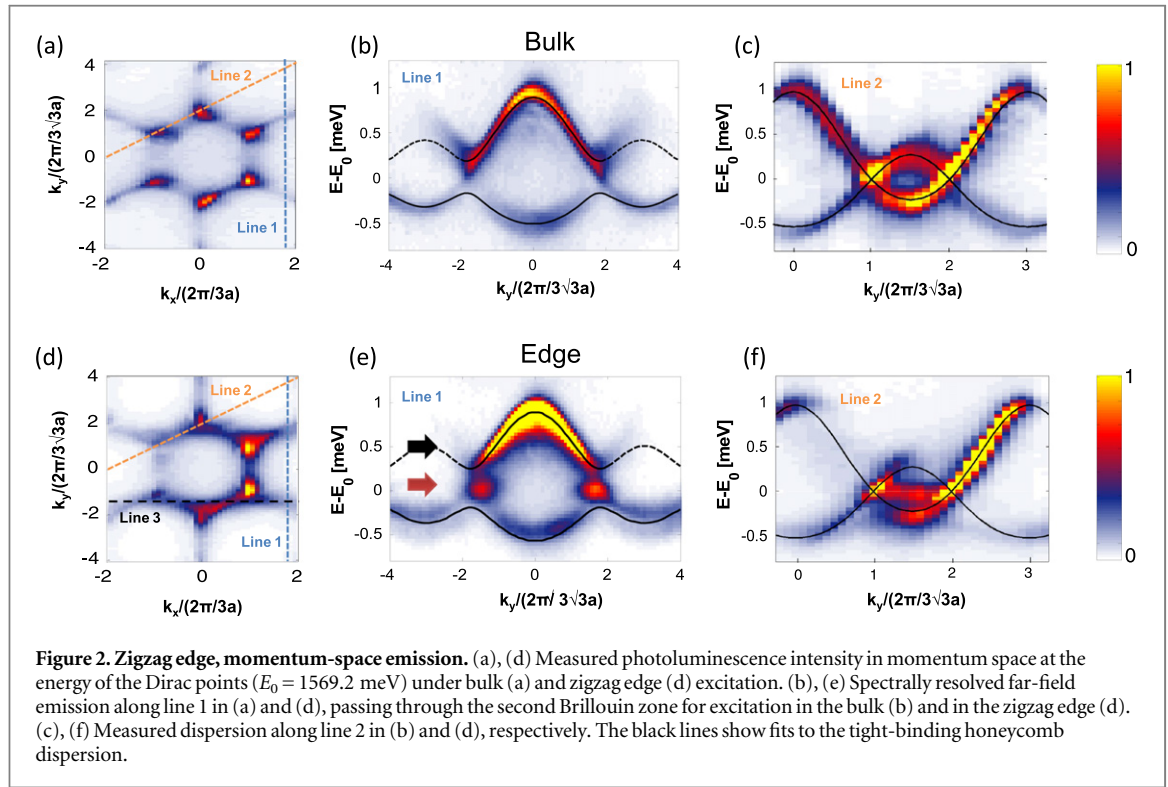
value used in [31] to describe our lattices. Figure 1(b) shows the calculated momentum-energy relation for an infinite honeycomb lattice without edges. It features positive and negative energy bands intersecting at two inequivalent Dirac points in the first Brillouin zone. To calculate the dispersion of the edge states we consider a nanoribbon geometry: an infinite lattice in the y-direction and of finite width in the x-direction, ending with the same type of boundary on both sides. Therefore, the calculated dispersions are continuous along k_y, with several transverse modes corresponding to the confinement in the x-direction. The result is shown in figure 1(c) for ribbons with either zigzag or bearded edges. Each of the different transverse modes corresponds to each individual line in the figures. Edge bands appear for the zigzag and bearded edges in complementary regions of k_y connecting the Dirac cones [8, 9] as indicated in red and green, respectively, in figure 1(d). The zigzag edge band appears for $k_{y(zigzag)} \in [-2, -1]k_{y0} \cup [1, 2]k_{y0}$, and the bearded edge band for $k_{y(bearded)} \in [-1, 1]k_{y0}$, with $k_{y0} = 2\pi/(3\sqrt{3}a)$ and a being the interpillar distance. The dispersion of the edge states deviates from a perfect flatband as a consequence of the next-nearest-neighbor hopping parameter included in the calculation. However this deviation is rather small: 50 μeV in total for a value of $t = 250\,\mu$eV.

Spatially, the edge states are localized on the outermost sites, with an exponentially decaying amplitude into the bulk $\left(\psi_{edge}(x) \sim e^{-x/l_e}\right)$. In the absence of next-nearest-neighbor coupling the penetration length follows [8]:

$$l_e = \frac{3a}{2\left|ln\left(2\cos\left(k_y\sqrt{3}a/2\right)\right)\right|} \tag{1}$$

The finite penetration results in a finite width in momentum space for the edge states. Figure 1(e) shows the k_x–k_y momentum distribution of the zigzag and bearded edge states calculated by Fourier transforming with respect to x the spatial distributions of the edge state for each k_y as obtained from the solution of the tight-binding Hamiltonian. The edge modes are spread around straight lines connecting the Dirac points at the border of the Brillouin zone, as schematically represented in figure 1(d). The edge states with k_y corresponding to the center of the zigzag band ($k_y = \pm 1.5\,k_{y0}$) are fully delocalized in the k_y-direction (see dashed line in figure 1(e)). Correspondingly, these states are spatially fully localized, down to a single site (see figure 1(f)). In the case of the bearded edge state, maximum spatial localization is attained at $k_y = 0$, with a penetration length of 2.2a, larger than the maximally localized zigzag edge state. At the Dirac

Figure 2. Zigzag edge, momentum-space emission. (a), (d) Measured photoluminescence intensity in momentum space at the energy of the Dirac points ($E_0 = 1569.2$ meV) under bulk (a) and zigzag edge (d) excitation. (b), (e) Spectrally resolved far-field emission along line 1 in (a) and (d), passing through the second Brillouin zone for excitation in the bulk (b) and in the zigzag edge (d). (c), (f) Measured dispersion along line 2 in (b) and (d), respectively. The black lines show fits to the tight-binding honeycomb dispersion.
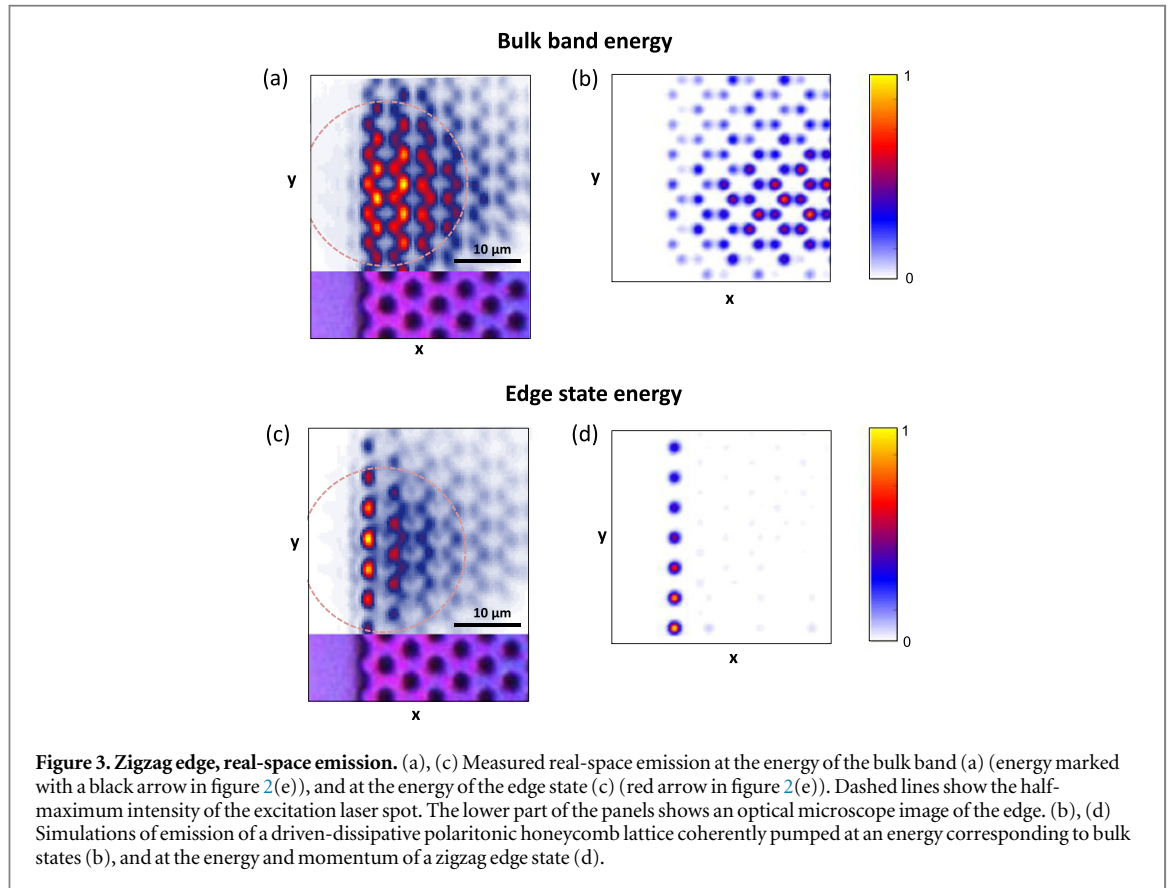
points, the penetration length becomes infinite, and the edge states merge into bulk modes. Note that no edge state is formed for armchair edges.

To experimentally access the polariton wavefunctions and dispersions we perform low temperature (10 K) photoluminescence experiments, analogous to the procedure carried out in [31]. We excite the sample non-resonantly using a Ti:Sapph monomode laser at 740 nm, about 100 meV above the lowest band of the honeycomb lattice. The excitation creates electron–hole pairs in the quantum wells, which relax incoherently and, under low power excitation, populate all polaritonic energy bands. We analyze the far-field emission arising from photons escaping out of the cavity. Owing to momentum-conservation laws, each photon is emitted with in-plane momentum equal to the in-plane momentum of the polariton in which it originated. Thus, there is a direct correspondence between the angle of emission and the in-plane momentum of polaritons up to a reciprocal lattice vector. Each angle of emission corresponds to a point in the Fourier plane of the collecting lens, a high numerical aperture microscope objective (NA = 0.65), which is also used for the excitation. By imaging the Fourier plane on the entrance slit of a spectrometer, we resolve in energy and in-plane momentum the far-field emission along the line given by the slit (parallel to k_y), for a given value of k_x, which we record on a CCD camera. By varying the position of the image of the Fourier plane on the slit, we collect the dispersion for different values of k_x. We are thus able to reconstruct a 3D matrix whose axis are k_x, k_y and the emission energy [41]. The described tomography process is also carried

out for the real-space emission to reconstruct the spatial distribution of the emitted light at a given energy, and study the localization of the edge state. We select the linear polarization of the emission using a set of half-waveplates and linear polarizers.

We study a graphene simulator similar to the one shown in figure 1(a), containing zigzag edges. The diameter of the pillars ($d = 3\,\mu$m) and the interpillar distance ($a = 2.4\,\mu$m) result in a significant tunneling strength, $t = 250\,\mu$eV, in combination with a relatively narrow linewidth $\sim 150\,\mu$eV. For the excitation, we focus the laser in a Gaussian spot with a diameter of $3\,\mu$m, covering around one pillar. We select the emission linearly polarized along the y axis, parallel to the edge. Since the emission arises mainly from the excited area, we are able to selectively image the dispersion from the bulk or the edge. Figure 2(a) shows the momentum-space emission at the energy of the Dirac point (zero energy) when exciting the lattice in the bulk. We observe six isolated bright spots at the Dirac points, which identify the first Brillouin zone hexagon. These are the points in which upper and lower bands meet (figure 1(b)). The triangular shape of the points is due to the trigonal warping known to be present in the honeycomb lattice spectrum for non-zero energies [42], visible here because of the finite linewidth. Figure 2(b) shows the energy-resolved far-field emission along line 1, parallel to k_y at $k_x = 1.7 \cdot (2\pi/3a)$. We select a line passing through the second Brillouin zone in order to evidence the upper band, whose emission is strongly reduced in the first Brillouin zone due to destructive interference effects [31]. In figure 2(b), we can identify the upper and lower energy bands

Figure 3. Zigzag edge, real-space emission. (a), (c) Measured real-space emission at the energy of the bulk band (a) (energy marked with a black arrow in figure 2(e)), and at the energy of the edge state (c) (red arrow in figure 2(e)). Dashed lines show the half-maximum intensity of the excitation laser spot. The lower part of the panels shows an optical microscope image of the edge. (b), (d) Simulations of emission of a driven-dissipative polaritonic honeycomb lattice coherently pumped at an energy corresponding to bulk states (b), and at the energy and momentum of a zigzag edge state (d).

separated by a gap as expected for the graphene dispersion for this value of k_x (figure 1(b)). The black curve in figure 2(b) depicts the dispersion expected from the tight-binding approximation with $t = 250\,\mu\text{eV}$ and $t' = -0.08$ t (i.e., $-20\,\mu\text{eV}$). Note that the next-nearest neighbor coupling is evidenced via the asymmetry of the bands above and below E_0.
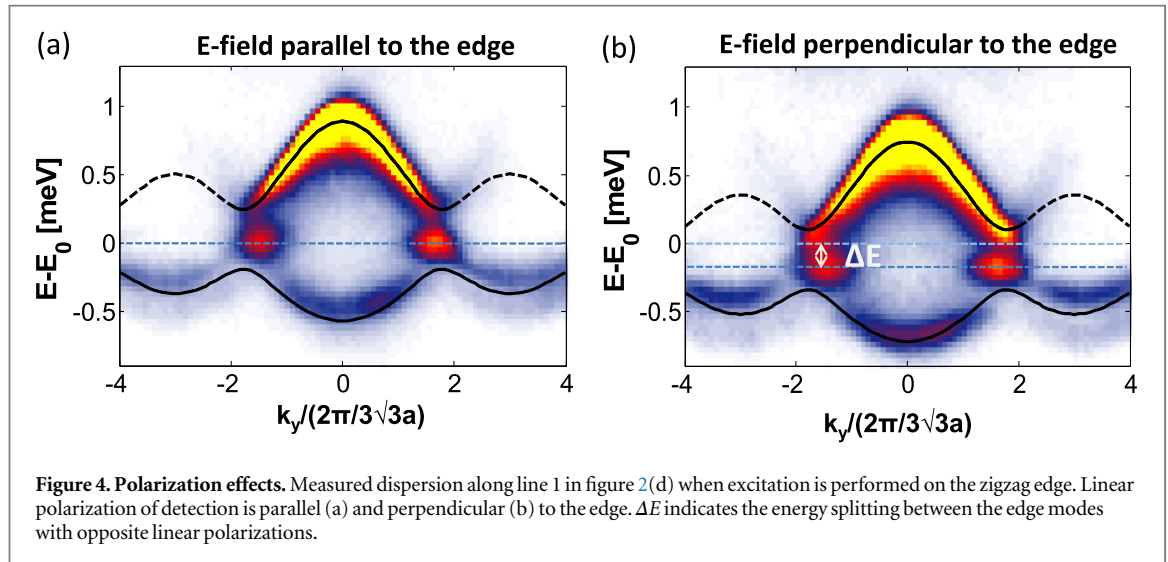
Zigzag edge

We now address the situation when the excitation spot is moved to one of the external pillars forming the zigzag edge. Figure 2(d) shows the luminescence at the energy of the Dirac points for this excitation configuration. The Dirac cones are now continuously connected by a bright line in the $k_{y(zigzag)}$ region while there is a dark region in the middle at the $k_{y(bearded)}$ region, as expected from figures 1(d), (e). Additionally, along line 3 we observe a spread emission in k_x, indicating a fully localized edge mode. This feature matches the state marked by a dashed line in the simulation shown in figure 1(e). The overall emitted intensity in momentum space is asymmetric since light is collected at the edge and translational symmetry is broken. When analyzing the energy-resolved emission along line 1 (figure 2(e)), two additional lobes are clearly observed in the gap between the upper and lower bands. Their location in momentum space corresponds to that expected for the edge states shown in figure 1(d) (red lines). The measured full-width-at-

half-maximum of the lobes along the k_y-direction in figure 2(e) is 0.75 k_{y0}, in agreement with the theoretical prediction for the edge states along the same line in momentum space extracted from the simulation shown in figure 1(e), within a 20% error.

The quasi-dispersionless character of the band associated to the edge states can be evidenced by selecting a spectral cut along line 2 in figure 2(d), which contains the $k_{y(zigzag)}$ region. Figure 2(f) shows a flat band linking the two Dirac cones. No such state is present in the bulk (figure 2(c)), where only the corresponding bulk dispersion is detected. Only the states with group velocities propagating towards the bulk (positive slope) emit light, explaining the asymmetry of figure 2(f). For a clearer comparison with the edge states band, a fit of the bulk bands is presented in figures 2(e) and (f) by a black curve. Although our system exhibits effects of next-nearest-neighbor tunneling for the bulk bands, the edge states band stays flat within the linewidth. Indeed the magnitude of the curvature obtained in the tight-binding calculations (50 μeV) is small compared to the emission linewidth (150 μeV). Note that emission from bulk states is also present in figures 2(e) and (f).

In addition to momentum-space imaging, our system allows evidencing the localization of the edge states by looking at the real-space emission. For this purpose, we use a large Gaussian laser spot, 20 μm in diameter, covering around 30 pillars. In this way, we are able to excite edge modes on several pillars, and to

Figure 4. Polarization effects. Measured dispersion along line 1 in figure 2(d) when excitation is performed on the zigzag edge. Linear polarization of detection is parallel (a) and perpendicular (b) to the edge. ΔE indicates the energy splitting between the edge modes with opposite linear polarizations.

compare the emission of the edge and bulk states from a single set of measurements. Figure 3(a) shows the emitted intensity at the energy of the middle of the upper bulk band, 0.5 meV above the Dirac points (black arrow in figure 2(e)). The bulk modes present the expected honeycomb pattern, with an intensity distribution following the pump spot. Figure 3(c) shows the real-space emission at the energy of the edge state (E_0, red arrow in figure 2(e)). In this case, the outermost line of pillars shows a stronger emission, corresponding to the localized edge state.

This interpretation is supported by simulations of a driven-dissipative model of the honeycomb lattice. In the simulations, we added to the tight-binding Hamiltonian a monochromatic resonant pump and cavity losses of $\gamma = 0.1\,t$ for all lattice sites. We calculate the steady state with a pumping beam at E_0 that covers the whole sample with an incident momentum $\mathbf{k} = \left(1/\left(2\sqrt{3}\right),\, 3/2\right)k_{y0}$, corresponding to the center of the segment connecting the Dirac points where the zigzag edge state is expected. The result is shown in figure 3(d), revealing the edge state fully localized on the outermost pillars, as expected from equation (1). The same simulation at the energy of the bulk bands shows emission from the whole lattice, as depicted in figure 3(b).

One of the specific characteristics of polaritons, different from other photonic simulators like coupled waveguides or microwave resonators, is their significant polarization-dependent properties. The polarization-dependent penetration of the electromagnetic field in the Bragg mirrors forming the cavity results in a linearly polarized TE-TM splitting whose magnitude increases quadratically with the in-plane momentum [43], resulting in the so-called optical spin-Hall effect [44–46]. Additionally, the polarization-dependent hopping between coupled micropillars [47] has been shown to give rise to spin–orbit coupling effects in hexagonal photonic molecules in

the polariton condensation regime [48]. When analyzing the spontaneous emission from the bulk of the honeycomb lattice presented here we observe negligible effects. The reason is that the period of the lattice is big enough to restrict the first Brillouin zone to small values of in-plane momenta where the TE-TM splitting is expected to be smaller than the measured linewidth.

Nevertheless, we do observe significant polarization effects when analyzing the emission from the edge states. Figure 4(a) reproduces figure 2(e) showing the energy-resolved far-field emission upon small spot excitation located at one of the outermost pillars of the zigzag edge. Here, we select the emission linearly polarized parallel to the direction of the edge (y), as in all the results we have presented so far. When selecting the opposite linear polarization direction, perpendicular the edge, we observe that the edge state is located at a lower energy $\Delta E = 160\,\mu$eV. Similar polarization splittings have been reported in 1D polariton microwires [49, 50]. The splitting may arise from the interplay between two effects. First, the asymmetric photonic confinement along and perpendicular to the edge could induce a linear polarization splitting of the confined photonic modes. Second, the finite-size etched structure may give rise to strain crystal fields resulting in the splitting of the excitonic modes with polarization directions along and perpendicular to the strain field. In the considered structure, a strain mismatch between the x- and y-directions could take place close to the edge of the honeycomb lattice. Given the significant value of ΔE, the excitonic origin of the splitting seems the most likely. Indeed, photonic confinement effects are expected to result in polarization splittings of 5–10 μeV in this kind of structures [48], much smaller than the linewidth. Note that the strain field might penetrate a few sites into the lattice, thus affecting the energy of the bulk bands close to the edge.
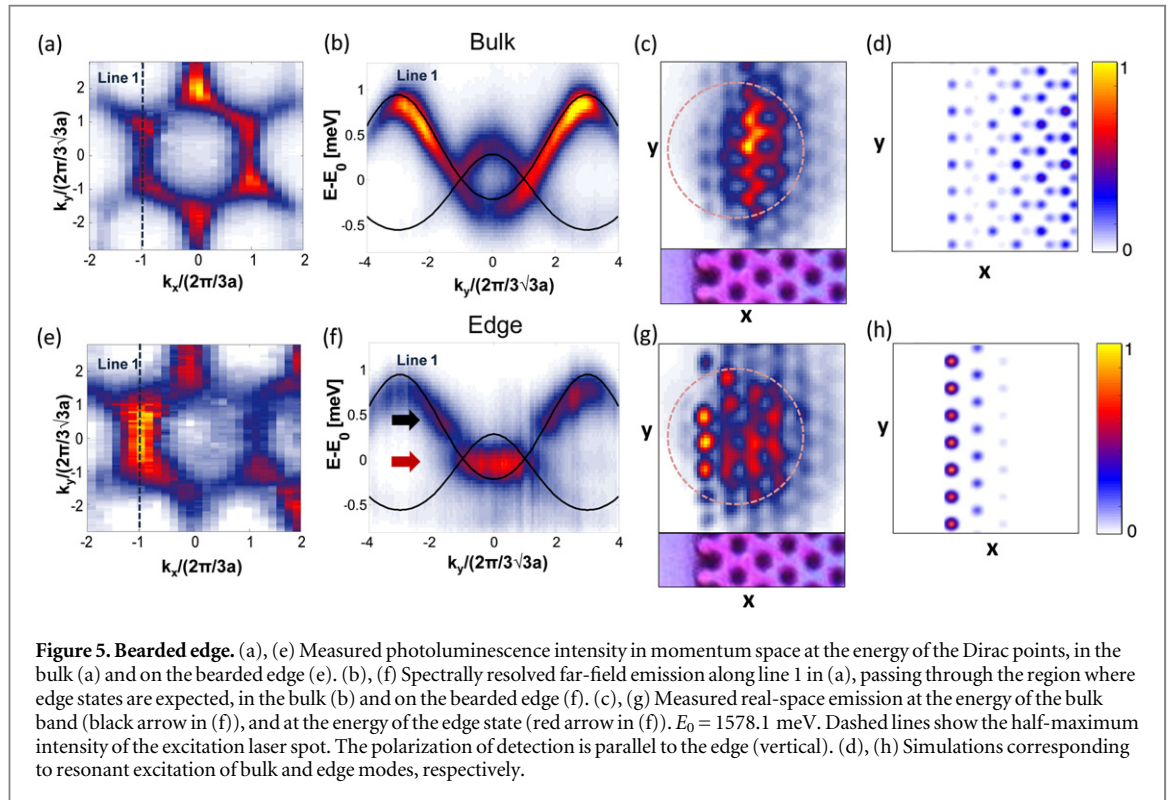
Figure 5. Bearded edge. (a), (e) Measured photoluminescence intensity in momentum space at the energy of the Dirac points, in the bulk (a) and on the bearded edge (e). (b), (f) Spectrally resolved far-field emission along line 1 in (a), passing through the region where edge states are expected, in the bulk (b) and on the bearded edge (f). (c), (g) Measured real-space emission at the energy of the bulk band (black arrow in (f)), and at the energy of the edge state (red arrow in (f)). $E_0 = 1578.1$ meV. Dashed lines show the half-maximum intensity of the excitation laser spot. The polarization of detection is parallel to the edge (vertical). (d), (h) Simulations corresponding to resonant excitation of bulk and edge modes, respectively.

This is the origin of the observed redshift of the bulk bands in figure 4(b) with respect to figure 4(a).

Bearded edge

Bearded terminations have also been predicted to exhibit edge states [11]. Experimental investigation of this type of edge band is not feasible in carbon graphene where dangling bonds specific to this kind of termination are chemically unstable. Thus, it has been studied mostly theoretically and using graphene analogues [8, 26, 27]. To study the energy-momentum dispersion of this kind of edge state, we have fabricated a lattice containing bearded edges, with pillar diameter of $d = 2.5\,\mu m$, and interpillar distance $a = 1.76\,\mu m$, giving the same tight-binding tunneling amplitudes as in the lattice with the zigzag edges. However, the smaller pillar diameter results in non-radiative losses that give rise to a larger linewidth ($\sim 350\,\mu eV$). Experiments are performed under the same conditions as described previously, in both real and reciprocal space configurations. Figure 5(a) shows the momentum space at the energy of the Dirac points when exciting the bulk of the lattice. Again, we are able to identify the six Dirac points of the first Brillouin zone with gaps between them. They are less pronounced than in figure 2 due to the broader linewidth. The bulk dispersion along line 1 defined in figure 5(a), containing the $k_{y(bearded)}$ region, is shown in figure 5(b). The expected shape of the bands is observed, with crossings at two Dirac points. When the probe is placed on the edge of the sample, different patterns are observed. The momentum-space map at the Dirac point energy shows an enhanced emission in the $k_{y(bearded)}$ and equivalent regions (figure 5(e)), revealing the edge states band. Its full-width-at-half-maximum along the k_x-direction at $k_y = 0$ is 0.50 k_{x0}, with $k_{x0} = 2\pi/(3a)$, in excellent agreement with the prediction in figure 1(e), where this value is 0.45 k_{x0}. The dispersion along line 1 (figure 5(f)) shows now a flatband connecting the two Dirac points in the momentum-space region corresponding to $k_{y(bearded)}$. As previously described for the zigzag edges, the linewidth detain us from observing non-flatness of the edge band.

To study the spatial location of the state we perform measurements and simulations of the real-space emission under excitation with a large pump spot. Figure 5(h) shows a simulation of the emitted intensity when exciting the edge state at $k_y = 0$. The observed bearded edge state resides on the sublattice corresponding to the bearded ending, and it penetrates several lattice sites into the bulk, as expected from equation (1). In the experiment (figure 5(g)), we observe bright spots on the outermost pillars of the lattice. This emission is absent at the energy of the bulk modes (figure 5(c)), and thus it corresponds to the edge state. The penetration depth is, however, difficult to estimate experimentally due to the emission from the bulk modes at the same energy.

Conclusion

We have used a photonic graphene simulator to directly visualize the localized states associated with

the bearded and zigzag types of graphene edges. Clear identification of the different kinds of edge states is possible thanks to real-space and far-field imaging. Although we mainly used the photonic nature of polaritons in the present experiments in a honeycomb lattice, their excitonic content offers the exciting possibility of exploring nonlinear effects [28]. Virtually unfeasible in natural graphene, phenomena such as soliton solutions to the non-linear Dirac equation expected for instance in the armchair edge [51] can be experimentally addressed.

Acknowledgments

References

[1] Katsnelson M I, Novoselov K S and Geim A K 2006 *Nat. Phys.* **2** 620
[2] Allain P and Fuchs J N 2011 *EPJ B* **83** 301
[3] McCann E, Kechedzhi K, Fal'ko V I, Suzuura H, Ando T and Altshuler B L 2006 *Phys. Rev. Lett.* **97** 146805
[4] Cheianov V V, Fal'ko V I and Altshuler B L 2007 *Science* **315** 1252
[5] Ryu S and Hatsugai Y 2002 *Phys. Rev. Lett.* **89** 077002
[6] Delplace P, Ullmo D and Montambaux G 2011 *Phys. Rev. B* **84** 195452
[7] Rechtsman M C, Plotnik Y, Zeuner J M, Song D, Chen Z, Szameit A and Segev M 2013 *Phys. Rev. Lett.* **111** 103901
[8] Kohmoto M and Hasegawa Y 2007 *Phys. Rev. B* **76** 205402
[9] Fujita M, Wakabayashi K, Nakada K and Kusakabe K 1996 *J. Phys. Soc. Japan* **65** 1920
[10] Nakada K, Fujita M, Dresselhaus G and Dresselhaus M 1996 *Phys. Rev. B* **54** 17954
[11] Klein D J 1994 *Chem. Phys. Lett.* **217** 261
[12] Kobayashi Y, Fukui K, Enoki T, Kusakabe K and Kaburagi Y 2005 *Phys. Rev. B* **71** 193406
[13] Tao C *et al* 2011 *Nat. Phys.* **7** 616
[14] Polini M, Guinea F, Lewenstein M, Manoharan H C and Pellegrini V 2013 *Nat. Nanotechnol.* **8** 625
[15] Peleg O, Bartal G, Freedman B, Manela O, Segev M and Christodoulides D N 2007 *Phys. Rev. Lett.* **98** 103901
[16] Bahat-Treidel O, Peleg O, Segev M and Buljan H 2010 *Phys. Rev. A* **82** 13830
[17] Song D, Paltoglou V, Liu S, Zhu Y, Gallardo D, Tang L, Xu J, Ablowitz M, Efremidis N K and Chen Z 2015 *Nat. Commun.* **6** 6272
[18] Rechtsman M C, Zeuner J M, Tunnermann A, Nolte S, Segev M and Szameit A 2013 *Nat. Phot.* **7** 153
[19] Rechtsman M C, Zeuner J M, Plotnik Y, Lumer Y, Podolsky D, Dreisow F, Nolte S, Segev M and Szameit A 2013 *Nature* **496** 196
[20] Bittner S, Dietz B, Miski-Oglu M, Oria Iriarte P, Richter A and Schäfer F 2010 *Phys. Rev. B* **82** 014301
[21] Bellec M, Kuhl U, Montambaux G and Mortessagne F 2013 *Phys. Rev. B* **88** 115437
[22] Bellec M, Kuhl U, Montambaux G and Mortessagne F 2013 *Phys. Rev. Lett.* **110** 033902
[23] Tarruell L, Greif D, Uehlinger T, Jotzu G and Esslinger T 2012 *Nature* **483** 302
[24] Montambaux G, Piéchon F, Fuchs J N and Goerbig M 2009 *Phys. Rev. B* **80** 153412
[25] Lim L K, Fuchs J N and Montambaux G 2012 *Phys. Rev. Lett.* **108** 175303
[26] Bellec M, Kuhl U, Montambaux G and Mortessagne F 2014 *New J. Phys.* **16** 113023
[27] Plotnik Y *et al* 2014 *Nat. Mater.* **13** 57
[28] Carusotto I and Ciuti C 2013 *Rev. Mod. Phys.* **85** 299
[29] Galbiati M *et al* 2012 *Phys. Rev. Lett.* **108** 126403
[30] Abbarchi M *et al* 2013 *Nat. Phys.* **9** 275
[31] Jacqmin T, Carusotto I, Sagnes I, Abbarchi M, Solnyshkov D, Malpuech G, Galopin E, Lemaître A, Bloch J and Amo A 2014 *Phys. Rev. Lett.* **112** 116402
[32] Lai C W *et al* 2007 *Nature* **450** 529
[33] Kim N Y, Kusudo K, Wu C, Masumoto N, Loffler A, Hofling S, Kumada N, Worschech L, Forchel A and Yamamoto Y 2011 *Nat. Phys.* **7** 681
[34] Cerda-Méndez E A, Krizhanovskii D N, Wouters M, Bradley R, Biermann K, Guda K, Hey R, Santos P V, Sarkar D and Skolnick M S 2010 *Phys. Rev. Lett.* **105** 116402
[35] Cerda-Méndez E A, Krizhanovskii D N, Biermann K, Hey R, Skolnick M S and Santos P V 2012 *Phys. Rev. B* **86** 100301
[36] Tanese D *et al* 2013 *Nat. Commun.* **4** 1749
[37] Tanese D, Gurevich E, Baboux F, Jacqmin T, Lemaître A, Galopin E, Sagnes I, Amo A, Bloch J and Akkermans E 2014 *Phys. Rev. Lett.* **112** 146404
[38] Karzig T, Bardyn C E, Lindner N and Refael G 2015 *Phys. Rev. X* **5** 031001
[39] Nalitov A V, Solnyshkov D D and Malpuech G 2015 *Phys. Rev. Lett.* **114** 116401
[40] Bardyn C E, Karzig T, Refael G and Liew T C H 2015 *Phys. Rev. B* **91** 161413(R)
[41] Nardin G, Paraïso T K, Cerna R, Pietka B, Léger Y, El Daif O, Morier-Genoud F and Deveaud-Plédran B 2009 *Appl. Phys. Lett.* **94** 181103
[42] Castro N A H, Guinea F, Peres N M R, Novoselov K S and Geim A K 2009 *Rev. Mod. Phys.* **81** 109
[43] Panzarini G, Andreani L C, Armitage A, Baxter D, Skolnick M S, Astratov V N, Roberts J S, Kavokin A V, Vladimirova M R and Kaliteevski M A 1999 *Phys. Rev. B* **59** 5082
[44] Kavokin A, Malpuech G and Glazov M 2005 *Phys. Rev. Lett.* **95** 136601
[45] Leyder C, Romanelli M, Karr J P, Giacobino E, Liew T C H, Glazov M M, Kavokin A V, Malpuech G and Bramati A 2007 *Nat. Phys.* **3** 628
[46] Maragkou M, Richards C E, Ostatnicky T, Grundy A J D, Zajac J, Hugues M, Langbein W and Lagoudakis P G 2011 *Opt. Lett.* **36** 1095
[47] de Vasconcellos S, Calvar A, Dousse A, Suffczynski J, Dupuis N, Lemaître A, Sagnes I, Bloch J, Voisin P and Senellart P 2011 *Appl. Phys. Lett.* **99** 101103
[48] Sala V G *et al* 2015 *Phys. Rev. X* **5** 011034
[49] Wertz E *et al* 2010 *Nat. Phys.* **6** 860
[50] Sturm C *et al* 2014 *Nat. Commun.* **5** 3278
[51] Haddad L H, Weaver C M and Carr L D 2015 *New J. Phys.* **17** 063033

Orbital Edge States in a Photonic Honeycomb Lattice

M. Milićević,[1] T. Ozawa,[2] G. Montambaux,[3] I. Carusotto,[2] E. Galopin,[1] A. Lemaître,[1]
L. Le Gratiet,[1] I. Sagnes,[1] J. Bloch,[1] and A. Amo[1]

[1]*Centre de Nanosciences et de Nanotechnologies, CNRS, Univ. Paris-Sud, Université Paris-Saclay,
C2N-Marcoussis, 91460 Marcoussis, France*
[2]*INO-CNR BEC Center and Dipartimento di Fisica, Università di Trento, I-38123 Povo, Italy*
[3]*Laboratoire de Physique des Solides, CNRS, Univ. Paris-Sud, Université Paris-Saclay, 91405 Orsay Cedex, France*
(Received 21 September 2016; published 8 March 2017)

We experimentally reveal the emergence of edge states in a photonic lattice with orbital bands. We use a two-dimensional honeycomb lattice of coupled micropillars whose bulk spectrum shows four gapless bands arising from the coupling of p-like photonic orbitals. We observe zero-energy edge states whose topological origin is similar to that of conventional edge states in graphene. Additionally, we report novel dispersive edge states in zigzag and armchair edges. The observations are reproduced by tight-binding and analytical calculations, which we extend to bearded edges. Our work shows the potentiality of coupled micropillars in elucidating some of the electronic properties of emergent two-dimensional materials with orbital bands.

Boundary modes are a fundamental property of finite-size crystals. They play an important role in the electronic transport and in the magnetic properties of low-dimensional materials [1–4]. Their existence has long been related to the microscopic details of the edge of the crystal [5–7]. Recent advances in the study of topological physics have revealed that, for topologically nontrivial materials, the existence of surface states is directly related to the properties of the bulk [8–10]. This is the case of conduction electrons in graphene [11–13], in which the nearest neighbor coupling of the cylindrically symmetric p_z orbitals of the carbon atoms gives rise to two bands (here labeled s bands) crossing in an ungapped spectrum (Dirac cones). The localized edge modes in this system exist for any type of termination except for armchair [14,15]. They are topologically protected by the chiral symmetry of the honeycomb lattice, and their existence can be predicted by calculating the winding number of the bulk wave functions [11–13].

In 2007, Wu and coworkers proposed an orbital version of graphene by considering a honeycomb lattice with $p_{x,y}$ orbitals in each lattice site [16,17]. The strong spatial anisotropy of the orbitals results in four ungapped bands with distinct features: two bands showing Dirac crossings and two flat bands, which were first reported experimentally in a polariton-based photonic simulator [18]. The interest in this kind of orbital Hamiltonian has taken a new thrust due to the rapid emergence of two-dimensional materials [19], such as black phosphorus [20–22] and two-dimensional transition metal dichalcogenides [23], whose bands originate from spatially anisotropic atomic orbitals. Edge states in MoS_2 flakes have been observed [24], and recent works aim at quantifying their impact in the transport properties [25]. Edge states in orbital modes have also been studied theoretically in connection to d-wave superconductivity

[11,26] and spin-orbit coupling in superlattices of nano-crystals [27], systems very hard to realize experimentally with tuneable parameters. A photonic simulator of orbital bands would open the door to the study of the microscopic properties of orbital edge states [28] and the connection to the topological properties of orbital bulk bands. In a more general framework, it would provide a platform to simulate some aspects of orbital bands which are essential in various topological insulators with band inversion [29].

In this Letter we report the experimental observation of edge states in the $p_{x,y}$ orbital bands of a honeycomb lattice made out of coupled micropillars etched in a planar microcavity. The advantage of this system over other photonic simulators, such as coupled waveguides [30,31] or microwave resonators [32], is that the radiative emission of light from the micropillars provides direct optical access to both the spatial distribution of the wave functions and to the energy-momentum dispersions [33]. We find two kinds of edge states: (i) zero-energy states in the zigzag and bearded edges, with a topological origin similar to that of edge states in conventional graphene; and (ii) a novel kind of dispersive edge state that emerges not only in zigzag and bearded terminations, but also in armchair edges. We support experimental data with numerical tight-binding calculations and provide analytical expressions for the energy of the dispersive edge states.

To experimentally study orbital edge states in $p_{x,y}$ bands we employ the polaritonic honeycomb lattice reported in [18,34] and shown in Fig. 1(c). The sample is a two-dimensional heterostructure made out of a $Ga_{0.05}Al_{0.95}As$ $\lambda/2$ cavity embedded in two $Ga_{0.05}Al_{0.95}As/Ga_{0.8}Al_{0.2}As$ Bragg mirrors with 28 (40) top (bottom) pairs with twelve GaAs quantum wells grown at the three central maxima of the electromagnetic field
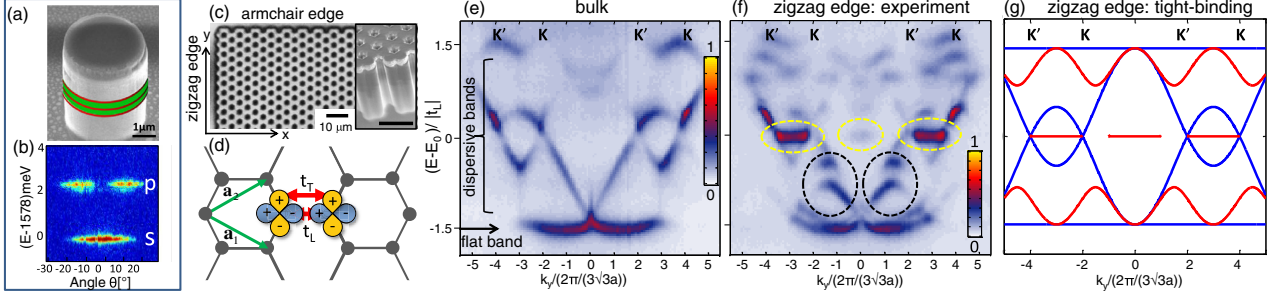
FIG. 1. (a) Scanning electron microscope image of a single micropillar. The red lines sketch the position of the quantum wells embedded in the cavity (depicted in green). (b) Corresponding momentum space spectra showing confined s and p-modes. (c) Optical microscope photograph of the honeycomb lattice under study showing two types of edges. The inset shows a scanning electron microscope image. (d) Sketch of the $p_{x,y}$ orbital (blue and yellow, respectively) and their couplings along the link (t_L) and perpendicular to it (t_T). [(e) and (f)] Momentum space luminescence from the bulk (e) and the zigzag edge (f) for $k_x = 4\pi/(3a)$. K and K' mark the positions of the Dirac cones. Yellow and black dashed lines surround photoluminescence from edge states. $E_0 = 1573$ meV and $t_L = -1.2$ meV. (g) Tight-binding calculation of the band structure. Blue lines, bulk energy bands at $k_x = 4\pi/(3a)$; red lines, edge states obtained for a nanoribbon with zigzag edges. All calculations are for $t_T = 0$.

confined in the heterostructure. The exciton resonance is 17 meV above the cavity mode at $k = 0$, and the exciton photon coupling results in a 15 meV Rabi splitting. After the molecular beam epitaxy growth, the cavity is processed by electron beam lithography and dry etching into a honeycomb lattice of overlapping micropillars (diameter 3 μm, center-to-center distance $a = 2.4$ μm). As shown in Fig. 1(c), both zigzag and armchair terminations were fabricated. The lowest energy level of each micropillar [Figs. 1(a) and 1(b)] is cylindrically symmetric, similarly to the p_z orbitals in graphene. The hopping of photons in these modes [35] gives rise to the π and π^* bands of graphene, whose edge states have been experimentally reported in the same structure [34]. The first excited state is made of two antisymmetric modes, $p_{x,y}$, oriented in orthogonal directions in the horizontal plane, as sketched in Fig. 1(d).

The characterization of the bulk band structure is performed at 10 K in the linear regime by exciting the center of the lattice with a low power (5 mW) nonresonant laser (740 nm), focused on a 4 μm diameter excitation spot. This provides incoherent excitation of all modes with a nonvanishing spatial overlap with the pump. The same microscope objective is used both to excite and to collect the emission [36]. Figure 1(e) displays the photoluminescence spectrum as a function of momentum parallel to the vertical edge, k_y, for $k_x = 4\pi/(3a)$; we select the emission linearly polarized along the same direction. The dispersion shows four bulk bands corresponding to the coupling of the $p_{x,y}$ orbitals (the s bands, lying at lower energy, are not shown) [18]. The lowest band is almost flat, while the two middle ones are strongly dispersive with two band crossings similar to those at the K and K' Dirac points in graphene s bands. The highest energy band corresponds to a deformed flat band [18]. The inhomogeneity in the emitted intensity is the consequence of (i) the energy relaxation efficiency and lifetime of photons in different

modes, and (ii) destructive interference in the far-field emission along certain high-symmetry directions [18,38,39]. Such a destructive interference effect is the reason why we select the value of $k_x = 4\pi/(3a)$ instead of the equivalent $k_x = 0$, where the emission intensity is strongly reduced. Tight-binding simulations, including coupling of the photons out of the cavity, nicely reproduce the observed emission pattern [36].

To access the edge states we place the spot on the outermost pillar of the zigzag edge. The measured dispersion is shown in Fig. 1(f). In addition to the bulk modes, new bands are evidenced, marked with yellow and black dashed lines in the figure. Those marked in yellow are flat and show up at the center of both the first and adjacent Brillouin zones, at the energy of the Dirac crossings. Those in black dashed lines lie between the bulk dispersive and flat bands and have a marked dispersive character. These states are delocalized in momentum space in the direction perpendicular to the edge, appearing at the very same energy for any value of k_x (not shown here) and, as we see below, they are localized in real space at the edges. This is different from the bulk bands in Fig. 1(e), which change energy when probing different values of k_x and are delocalized in real space. Note that the polarization dependent confinement of the outermost micropillars [34] and the transverse electric-transverse magnetic (TE-TM) splitting characteristic of semiconductor microcavities [40] may account for the observed splitting in the lowest flat band and in the edge states at around $k_y = \pm 1.5[2\pi/(3\sqrt{3}a)]$, black dashed lines in Fig. 1(f).

The $p_{x,y}$ orbital bands can be described by a tight-binding Hamiltonian [17,18]. If we assume that only the hopping via orbitals projected along the links connecting the micropillars is significant $|t_L| \gg |t_T|$, see Fig. 1(d), the Hamiltonian in the a_x, a_y, b_x, b_y basis, corresponding to the $p_{x,y}$ orbitals of the A and B sublattices, can be written in momentum space in the following 4×4 form:

$$\hat{\mathcal{H}}_p = -t_L \begin{pmatrix} 0_{2\times 2} & Q^\dagger \\ Q & 0_{2\times 2} \end{pmatrix}, \quad \text{with}$$

$$Q = \begin{pmatrix} f_1 & g \\ g & f_2 \end{pmatrix}, \qquad (1)$$

where $f_1 = \frac{3}{4}(e^{i\mathbf{k}\cdot\mathbf{u}_1} + e^{i\mathbf{k}\cdot\mathbf{u}_2})$, $f_2 = 1 + \frac{1}{4}(e^{i\mathbf{k}\cdot\mathbf{u}_1} + e^{i\mathbf{k}\cdot\mathbf{u}_2})$, and $g = (\sqrt{3}/4)(e^{i\mathbf{k}\cdot\mathbf{u}_1} - e^{i\mathbf{k}\cdot\mathbf{u}_2})$; $\mathbf{u}_{1,2}$ are primitive vectors and $t_L < 0$, to account for the antisymmetric phase distribution of the p orbitals. To later describe finite-size samples, we make a choice of unit cell dimer and primitive vectors such that it allows the full reconstruction of the lattice including its specific edges. We take the primitive vectors as follows: $\mathbf{u}_1 = \mathbf{a}_1$, $\mathbf{u}_2 = \mathbf{a}_1 - \mathbf{a}_2$ for zigzag edges, and $\mathbf{u}_1 = \mathbf{a}_1$, $\mathbf{u}_2 = \mathbf{a}_2$ for bearded and armchair, given in terms of the reference vectors $\mathbf{a}_{1,2}$ defined in Fig. 1(d); the corresponding unit cell dimers are detailed in Ref. [36].

The diagonalization of Hamiltonian (1) gives rise to two flat bands with energies $\pm\frac{3}{2}t_L$, and two dispersive bands with energies $\pm\frac{2}{3}t_L|\det Q|$, that is [16]

$$\pm\frac{t_L}{2}\sqrt{3 + 2\cos(\sqrt{3}k_y a) + 4\cos(3k_x a/2)\cos(\sqrt{3}k_y a/2)}.$$
$$(2)$$

Figures 1(e) and 1(f) are well described by a value of $t_L = -1.2$ meV, significantly larger than the measured linewidth ($\approx 150\ \mu$eV) and on-site energy disorder ($\approx 30\ \mu$eV, as measured in a similar one-dimensional structure [41]). To account for the edge bands experimentally reported in Fig. 1(f) we compute the eigenmodes of Hamiltonian (1) in a finite-size sample. We consider a nanoribbon with zigzag terminations on both edges and periodic boundary conditions along the direction parallel to the edge. The bulk modes, blue lines in Fig. 1(g), are the analytic result [Eq. (2)] and are delocalized all over the ribbon, while the red lines in Fig. 1(g) are edge states, calculated on a finite-size system, whose wave function exponentially decays. The spread in momentum and the position in energy match quantitatively the experimental observations, particularly for the modes at and below the Dirac cones. In the experiment, the high energy part of the spectrum is deformed due to the coupling to higher modes, and to the nonzero value of t_T, whose strength increases with energy [18].

Tight-binding calculations for nanoribbons with zigzag, bearded, and armchair edges are shown in Fig. 2. Two kinds of edge modes are visible: (i) bands of zero-energy modes in the central gap, present in zigzag and bearded edges, and (ii) dispersive modes in the upper and lower gaps in all three types of edges, and in the middle gap of the armchair termination.

We first analyze the zero-energy edge modes. They recall strongly the edge modes in the π and π^* bands of regular graphene, whose existence can be related to the winding
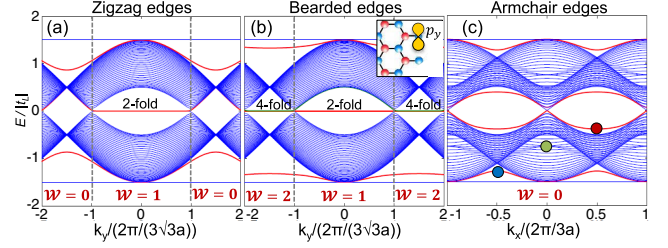

FIG. 2.   Calculated eigenmodes in the first Brillouin zone for a nanoribbon as a function of the wave vector $k_\parallel$ parallel to the edges, with (a) zigzag ($k_\parallel = k_y$), (b) bearded ($k_\parallel = k_y$), and (c) armchair ($k_\parallel = k_x$) terminations. Blue curves: bulk spectra for different values of the transverse momentum $k_\perp$. Red and green curves: edge states. For bearded edges, the inset shows the uncoupled p_y orbitals that give rise to a pair of edge states spreading over all $k_\parallel$.

number of the wave functions in momentum space [11–13]. The Hamiltonian describing graphene (s bands) is a chiral 2×2 Hamiltonian,

$$\hat{\mathcal{H}}_s = -t_s \begin{pmatrix} 0 & f_s^* \\ f_s & 0 \end{pmatrix}, \qquad (3)$$

with $t_s > 0$ being the hopping amplitude for the s orbitals and the factor $f_s = 1 + e^{i\mathbf{k}\cdot\mathbf{u}_1} + e^{i\mathbf{k}\cdot\mathbf{u}_2}$. The unit cell vectors $\mathbf{u}_{1,2}$ contain the information about the considered edge, as discussed above. The number of zero-energy edge states is determined by the winding of the phase of the off-diagonal component [$f_s = |f_s|e^{i\phi(\mathbf{k})}$] [11–13],

$$\mathcal{W}(k_\parallel) = \frac{1}{2\pi}\int_{BZ}\frac{\partial\phi(\mathbf{k})}{\partial k_\perp}dk_\perp, \qquad (4)$$

where the one-dimensional integration over $k_\perp$ is performed along a loop around the Brillouin zone in a direction perpendicular to the considered edge.

This analysis can be extended to more general situations: the existence of zero-energy modes can be related to the winding properties of the Hamiltonian in the following way. By fixing a value of $k_\parallel$, the dependence of Hamiltonian (1) on $k_\perp$ can be regarded as a one-dimensional model in the BDI (chiral orthogonal) class of the classification of topological insulators introduced by Schnyder et al. [10]. For this class, the number of pairs of zero-energy edge modes is given by the winding of the phase ϕ obtained from $f_p \equiv \det Q = |\det Q|e^{i\phi(\mathbf{k})}$ [42]. Figure 2 shows the value of $\mathcal{W}(k_\parallel)$ for the p bands as a function of momenta parallel to the edge $k_\parallel$ for the three types of edge considered here [36]. The winding number $\mathcal{W}(k_\parallel)$ matches with the number of the zero-energy modes calculated by diagonalization of the Hamiltonian.

An interesting feature of Fig. 2 is that the regions in momentum space where the zero-energy modes are present in the zigzag edge ($k_\parallel \in [-2\pi/(3\sqrt{3}a),\ 2\pi/(3\sqrt{3}a)]$) are complementary to the regions in which they are

present in *s*-band graphene for the same kind of edge $(k_\parallel \notin [-2\pi/(3\sqrt{3}a), 2\pi/(3\sqrt{3}a)])$. A similar situation takes place for the bearded edges: in the *p* bands, pairs of edge modes appear in the region in *k* space complementary to the regions where they appear in the *s* bands. Additionally, for bearded terminations, the *p* bands show an extra pair of zero-energy edge modes spread all over $k_\parallel$. It arises from dangling p_y orbitals fully localized in the outermost pillars, uncoupled to the bulk, as sketched in the inset of Fig. 2(b), and adds to the pair of edge states discussed above. The armchair edge does not have any zero-energy edge mode.

The complementarity in the position in momentum space of zero-energy edge modes between *s* and *p* bands can be understood by analyzing the symmetry of Hamiltonians (1) and (3), for the *p* and the *s* bands, respectively. The expressions f_p and f_s, whose winding determines the existence of zero-energy edge modes, can be related analytically,

$$f_p(\text{zigzag}) = \frac{3}{4} e^{i\mathbf{k} \cdot (\mathbf{a}_1 - \mathbf{a}_2)} f_s(\text{bearded}) \tag{5}$$

$$f_p(\text{bearded}) = \frac{3}{4} e^{i\mathbf{k} \cdot \mathbf{a}_2} f_s(\text{zigzag}), \tag{6}$$

where $f_s(\text{zigzag})[f_p(\text{bearded})]$ is written using the choice of unit cell that corresponds to the zigzag (bearded) edge [13]. A consequence of Eq. (5) is that the winding of the phase of $f_p(\text{zigzag})$ is the same as of $f_s(\text{bearded})$ [the vector $\mathbf{a}_1 - \mathbf{a}_2$ is parallel to the edge, so the prefactor of the right-hand part of Eq. (5) gives no winding in the orthogonal direction]. A similar situation takes place for Eq. (6): in addition to the exchange of the position between zigzag and bearded edge states, of respectively, *s* and *p* bands, the phase factor $e^{i\mathbf{k}\mathbf{a}_2}$ provides an extra winding over the whole Brillouin zone, and gives rise to an extra pair of edge state for all values of k_x, in the bearded edges of the *p* bands.

One of the most distinctive features of Figs. 1 and 2 is the observation of additional dispersive edge modes between the dispersive and the flat bands of the bulk. These modes are present for all values of $k_\parallel$ and for all the investigated types of edges. We can obtain analytical expression of the dispersive edge modes by searching for solutions of the Hamiltonian with an exponential decay into the bulk [$\psi(x) \sim e^{-x/\xi}$, ξ being the penetration length], using the treatment described in Refs. [2,32]. Applying this method to zigzag and bearded edges, we find the following eigenenergies for the edge modes [36]:

$$E_{\text{disp edge}}^{\text{zigzag}}(k_\parallel) = \pm t_L \frac{\sqrt{3}}{2} \sqrt{2 + \cos(\sqrt{3}k_\parallel a)} \tag{7}$$

$$E_{\text{disp edge}}^{\text{bearded}}(k_\parallel) = \pm t_L \frac{\sqrt{3}}{2} \frac{\sqrt{5 - 2\cos(\sqrt{3}k_\parallel a)}}{\sqrt{2 - \cos(\sqrt{3}k_\parallel a)}}. \tag{8}$$

As evidenced in Fig. 2(c), dispersive edge states exist also for armchair terminations, which do not contain any edge modes in the case of regular electronic graphene. The analytic calculation for the armchair edges is more elaborate [43]: the decay of the wave function is not a simple exponential but it involves two different penetration lengths.

We take advantage of our photonic simulator to explore the spatial distribution of these novel edge modes. Figure 3 shows the real space emission from the photonic simulator excited close to the armchair edge for three emission energies, corresponding to three different dispersive edge states indicated in Fig. 2(c) (see Ref. [36] for the experimental dispersion of the armchair edge modes). We employ a pump spot of 20 μm in diameter, allowing the measurement of the wave functions of the edge modes, which penetrate several microns into the bulk.

For the lowest-energy dispersive edge state [Fig. 3(a)], the emission is localized in the second to the last row of micropillars, with a gradual decrease towards the bulk. These features along with the lobe structure are well reproduced by the plot of the tight-binding solution for the edge state at the corresponding energy [$k_x = \pi/(3a)$; Fig. 3(d)]. Figure 3(b) shows the emission pattern for the lowest-energy edge mode in the central gap. In this case, the outermost pillars show the highest intensity, in a pattern significantly different from the modes shown in Figs. 3(a) and 3(d). It is worth noting that in the experiment, the energy of the emission is filtered with the use of a spectrometer, but no particular in-plane momentum is selected. Therefore, bulk modes contribute to the emission at the energies studied in Figs. 3(a)–3(c), explaining the
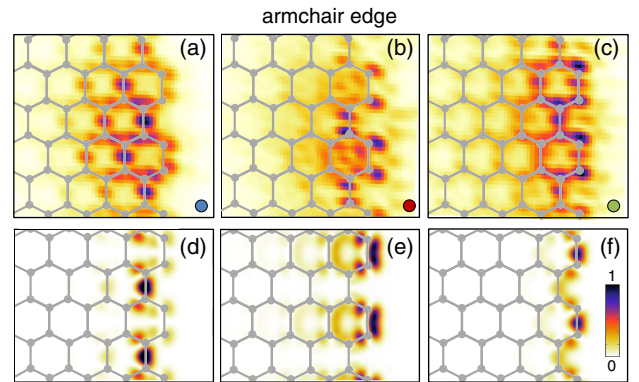

FIG. 3. Real space emission from dispersive edge states in an armchair termination. [(a)–(c)] Measured photoluminescence when selecting the energies indicated with circles in Fig. 2(c). [(d)–(f)] Corresponding tight-binding eigenfunctions. A hexagonal lattice is sketched on top of the data to mark the position of the center of the micropillars.

differences with the calculated individual eigenfunctions depicted in Figs. 3(d)–3(f).

Interestingly, the tight-binding calculations in Fig. 2(c) reveal an additional edge mode within the bulk energy band (green dot). Despite being immersed in the bulk band, when selecting the emission at the highest energy of this mode, the experiment and tight-binding calculations shown in Figs. 3(c) and 3(f) attest to the significant localization of these modes in the edge region.

In summary, our results provide a detailed characterization of the zero-energy and dispersive orbital edge states in excited bands of a photonic honeycomb lattice. The zero-energy modes are well described using topological arguments based on the symmetries of the bulk Hamiltonian. Whether any topological argument can be applied to the dispersive edge modes is an intriguing question. Our experiments and theoretical analysis provide insights into multimode lattice systems such as transition metal dichalcogenides [23] or mechanical lattices of springs and masses, which have been predicted to show similar dispersive edge modes [42,44]. Taking advantage of the intrinsic nonlinearities of polaritons, honeycomb lattices of coupled micropillars appear as excellent candidates to explore nonlinear bulk and edge states with orbital structure [45].

[1] K. Nakada, M. Fujita, G. Dresselhaus, and M. S. Dresselhaus, Phys. Rev. B **54**, 17954 (1996).
[2] M. Kohmoto and Y. Hasegawa, Phys. Rev. B **76**, 205402 (2007).
[3] Y. Li, Z. Zhou, S. Zhang, and Z. Chen, J. Am. Chem. Soc. **130**, 16739 (2008).
[4] Y. Li, W. Zhang, M. Morgenstern, and R. Mazzarello, Phys. Rev. Lett. **110**, 216804 (2013).
[5] W. Shockley, Phys. Rev. **56**, 317 (1939).
[6] I. Tamm, Zeitschrift für Physik **76**, 849 (1932).
[7] J. Zak, Phys. Rev. B **32**, 2218 (1985).
[8] M. Z. Hasan and C. L. Kane, Rev. Mod. Phys. **82**, 3045 (2010).
[9] X.-L. Qi and S.-C. Zhang, Rev. Mod. Phys. **83**, 1057 (2011).
[10] A. P. Schnyder, S. Ryu, A. Furusaki, and A. W. W. Ludwig, Phys. Rev. B **78**, 195125 (2008).
[11] S. Ryu and Y. Hatsugai, Phys. Rev. Lett. **89**, 077002 (2002).
[12] R. S. K. Mong and V. Shivamoggi, Phys. Rev. B **83**, 125109 (2011).
[13] P. Delplace, D. Ullmo, and G. Montambaux, Phys. Rev. B **84**, 195452 (2011).
[14] Y. Kobayashi, K.-i. Fukui, T. Enoki, K. Kusakabe, and Y. Kaburagi, Phys. Rev. B **71**, 193406 (2005).
[15] J. Lado, N. García-Martínez, and J. Fernández-Rossier, Synth. Met. **210**, 56 (2015).
[16] C. Wu, D. Bergman, L. Balents, and S. Das Sarma, Phys. Rev. Lett. **99**, 070401 (2007).
[17] C. Wu and S. Das Sarma, Phys. Rev. B **77**, 235107 (2008).
[18] T. Jacqmin, I. Carusotto, I. Sagnes, M. Abbarchi, D. D. Solnyshkov, G. Malpuech, E. Galopin, A. Lemaître, J. Bloch, and A. Amo, Phys. Rev. Lett. **112**, 116402 (2014).
[19] S. Z. Butler, S. M. Hollen, L. Cao, Y. Cui, J. A. Gupta, H. R. Gutiérrez, T. F. Heinz, S. S. Hong, J. Huang, A. F. Ismach, E. Johnston-Halperin, M. Kuno, V. V. Plashnitsa, R. D. Robinson, R. S. Ruoff, S. Salahuddin, J. Shan, L. Shi, M. G. Spencer, M. Terrones, W. Windl, and J. E. Goldberger, ACS Nano **7**, 2898 (2013).
[20] J.-H. P. Churchill and O. H. Hugh, Nat. Nanotechnol. **9**, 330 (2014).
[21] L. Li, Y. Yu, G. J. Ye, Q. Ge, X. Ou, H. Wu, D. Feng, X. H. Chen, and Y. Zhang, Nat. Nanotechnol. **9**, 372 (2014).
[22] X. Ling, H. Wang, S. Huang, F. Xia, and M. S. Dresselhaus, Proc. Natl. Acad. Sci. U.S.A. **112**, 4523 (2015).
[23] K. S. Novoselov, A. Mishchenko, A. Carvalho, and A. H. Castro Neto, Science **353** (2016).
[24] M. V. Bollinger, J. V. Lauritsen, K. W. Jacobsen, J. K. Nørskov, S. Helveg, and F. Besenbacher, Phys. Rev. Lett. **87**, 196803 (2001).
[25] M. Trushin, E. J. R. Kelleher, and T. Hasan, Phys. Rev. B **94**, 155301 (2016).
[26] S. Ryu and Y. Hatsugai, Physica (Amsterdam) **388C**, 90 (2003).
[27] E. Kalesaki, C. Delerue, C. Morais Smith, W. Beugeling, G. Allan, and D. Vanmaekelbergh, Phys. Rev. X **4**, 011010 (2014).
[28] C. Segarra, J. Planelles, and S. E. Ulloa, Phys. Rev. B **93**, 085312 (2016).
[29] B. A. Bernevig, T. L. Hughes, and S.-C. Zhang, Science **314**, 1757 (2006).
[30] Y. Plotnik, M. C. Rechtsman, D. Song, M. Heinrich, J. M. Zeuner, S. Nolte, Y. Lumer, N. Malkova, J. Xu, A. Szameit, Z. Chen, and M. Segev, Nat. Mater. **13**, 57 (2014).
[31] M. Hafezi, S. Mittal, J. Fan, A. Migdall, and J. M. Taylor, Nat. Photonics **7**, 1001 (2013).
[32] M. Bellec, U. Kuhl, G. Montambaux, and F. Mortessagne, New J. Phys. **16**, 113023 (2014).
[33] I. Carusotto and C. Ciuti, Rev. Mod. Phys. **85**, 299 (2013).
[34] M. Milićević, T. Ozawa, P. Andreakou, I. Carusotto, T. Jacqmin, E. Galopin, A. Lemaître, L. Le Gratiet, I. Sagnes, J. Bloch, and A. Amo, 2D Mater. **2**, 034012 (2015).
[35] M. Galbiati, L. Ferrier, D. D. Solnyshkov, D. Tanese, E. Wertz, A. Amo, M. Abbarchi, P. Senellart, I. Sagnes, A. Lemaitre, E. Galopin, G. Malpuech, and J. Bloch, Phys. Rev. Lett. **108**, 126403 (2012).
[36] See Supplemental Material at http://link.aps.org/supplemental/10.1103/PhysRevLett.118.107403, which includes Ref. [37], for a description of the experimental setup, measured dispersions for the armchair edge, driven-dissipative simulations, and analytical results on the dispersion of zigzag and bearded edge states.

[37] T. Ozawa and I. Carusotto, Phys. Rev. Lett. **112,** 133902 (2014).

[38] E. L. Shirley, L. J. Terminello, A. Santoni, and F. J. Himpsel, Phys. Rev. B **51,** 13614 (1995).

[39] A. Bostwick, T. Ohta, T. Seyller, K. Horn, and E. Rotenberg, Nat. Phys. **3,** 36 (2007).

[40] G. Panzarini, L. C. Andreani, A. Armitage, D. Baxter, M. S. Skolnick, V. N. Astratov, J. S. Roberts, A. V. Kavokin, M. R. Vladimirova, and M. A. Kaliteevski, Phys. Rev. B **59,** 5082 (1999).

[41] F. Baboux, L. Ge, T. Jacqmin, M. Biondi, E. Galopin, A. Lemaître, L. Le Gratiet, I. Sagnes, S. Schmidt, H. E. Türeci, A. Amo, and J. Bloch, Phys. Rev. Lett. **116,** 066402 (2016).

[42] C. L. Kane and T. C. Lubensky, Nat. Phys. **10,** 39 (2013).

[43] T. Ozawa *et al.* (to be published).

[44] Y.-T. Wang, P.-G. Luan, and S. Zhang, New J. Phys. **17,** 073031 (2015).

[45] M. Di Liberto, A. Hemmerich, and C. Morais Smith, Phys. Rev. Lett. **117,** 163001 (2016).

Part III

BIBLIOGRAPHY

BIBLIOGRAPHY

[1] John D. Joannopoulos, Robert D. Meade, and Joshua N. Winn. *Photonic Crystals: Molding the Flow of Light.* Princeton University Press, 1995. (Cited on pages 1 and 24.)

[2] Tomoki Ozawa, Hannah M. Price, Alberto Amo, Nathan Goldman, Mohammad Hafezi, Ling Lu, Mikael Rechtsman, David Schuster, Jonathan Simon, Oded Zilberberg, and Iacopo Carusotto. Topological photonics, 2018. (Cited on pages 1 and 24.)

[3] Alexander B. Khanikaev and Gennady Shvets. Two-dimensional topological photonics. *Nat. Photonics*, 11(12):763–773, dec 2017. (Cited on pages 1 and 24.)

[4] M. Z. Hasan and C. L. Kane. Colloquium: Topological insulators. *Rev. Mod. Phys.*, 82(4):3045–3067, nov 2010. (Cited on pages 1, 67, and 71.)

[5] Xin Zhou, You Wang, Daniel Leykam, and Y D Chong. Optical isolation with nonlinear topological photonics. *New Journal of Physics*, 19(9):095002, 2017. (Cited on page 1.)

[6] Mohammad Hafezi, Eugene A Demler, Mikhail D Lukin, and Jacob M Taylor. Robust optical delay lines with topological protection. *Nature Phys.*, 7(11):907–912, 2011. (Cited on page 1.)

[7] Sunil Mittal and Mohammad Hafezi. Topologically robust generation of correlated photon pairs, 2017. (Cited on page 1.)

[8] Mikael C Rechtsman, Julia M Zeuner, Yonatan Plotnik, Yaakov Lumer, Daniel Podolsky, Felix Dreisow, Stefan Nolte, Mordechai Segev, and Alexander Szameit. Photonic Floquet topological insulators. *Nature*, 496(7444):196–200, 2013. (Cited on page 1.)

[9] Oded Zilberberg, Sheng Huang, Jonathan Guglielmon, Mohan Wang, Kevin P. Chen, Yaacov E. Kraus, and Mikael C. Rechtsman. Photonic topological boundary pumping as a probe of 4d quantum hall physics. *Nature*, 553(7686):59–62, jan 2018. (Cited on page 1.)

[10] Jiho Noh, Sheng Huang, Daniel Leykam, Y.D. Chong, Kevin P. Chen, and Mikael Rechtsman. Experimental observation of optical weyl points and fermi arc-like surface states. *Nature Physics*, 13:611 EP –, Mar 2017. Article. (Cited on pages 1 and 110.)

[11] E. M. Purcell, H. C. Torrey, and R. V. Pound. Resonance absorption by nuclear magnetic moments in a solid. *Phys. Rev.*, 69:37–38, Jan 1946. (Cited on pages 2 and 37.)

[12] R. J. Thompson, G. Rempe, and H. J. Kimble. Observation of normal-mode splitting for an atom in an optical cavity. *Phys. Rev. Lett.*, 68:1132–1135, Feb 1992. (Cited on pages 2 and 28.)

[13] Sergio M. Dutra. *Cavity Quantum Electrodynamics: The Strange Theory of Light in a Box.* Wiley-Interscience, 2004. (Cited on page 2.)

[14] Alexey V. Kavokin, Jeremy J. Baumberg, Guillaume Malpuech, and Fabrice P. Laussy. *Microcavities (Series on Semiconductor Science and Technology).* Oxford University Press, 2017. (Cited on pages 2 and 29.)

[15] Vincenzo Savona. Fifteen years of microcavity polaritons. In *The Physics of Semiconductor Microcavities*, pages 1–29. Wiley-VCH Verlag GmbH & Co. KGaA. (Cited on page 2.)

[16] Iacopo Carusotto and Cristiano Ciuti. Quantum fluids of light. *Rev. Mod. Phys.*, 85(1):299–366, 2013. (Cited on pages 2, 29, and 134.)

[17] A Amo, D Sanvitto, F P Laussy, D Ballarini, E del Valle, M D Martin, A Lemaître, J Bloch, D N Krizhanovskii, M S Skolnick, C Tejedor, and L Viña. Collective fluid dynamics of a polariton condensate in a semiconductor microcavity. *Nature*, 457(7227):291–5, jan 2009. (Cited on page 2.)

[18] R. Hivet, H. Flayac, D. D. Solnyshkov, D. Tanese, T. Boulier, D. Andreoli, E. Giacobino, J. Bloch, A. Bramati, G. Malpuech, and A. Amo. Half-solitons in a polariton quantum fluid behave like magnetic monopoles, 2012. (Cited on page 2.)

[19] M Sich, D N Krizhanovskii, M S Skolnick, A V Gorbach, R Hartley, D V Skryabin, E A Cerda-Mendez, K Biermann, R Hey, and P V Santos. Observation of bright polariton solitons in a semiconductor microcavity. *Nature Phot.*, 6(1):50–55, 2012. (Cited on page 2.)

[20] E Kammann, T C H Liew, H Ohadi, P Cilibrizzi, P Tsotsis, Z Hatzopoulos, P G Savvidis, A V Kavokin, and P G Lagoudakis. Nonlinear Optical Spin Hall Effect and Long-Range Spin Transport in Polariton Lasers. *Phys. Rev. Lett.*, 109(3):36404, 2012. (Cited on pages 2 and 59.)

[21] D Bajoni, E Peter, P Senellart, J L Smirr, I Sagnes, A Lemaître, and J Bloch. Polariton parametric luminescence in a single micropillar. *Appl. Phys. Lett.*, 90:51107, 2007. (Cited on page 2.)

[22] V. G. Sala, D. D. Solnyshkov, I. Carusotto, T. Jacqmin, A. Lemaître, H. Terças, A. Nalitov, M. Abbarchi, E. Galopin, I. Sagnes, J. Bloch, G. Malpuech, and A. Amo. Spin-orbit coupling for photons and polaritons in microstructures. *Phys. Rev. X*, 5:011034, Mar 2015. (Cited on pages 2 and 89.)

[23] E Wertz, L Ferrier, D D Solnyshkov, R Johne, D Sanvitto, A Lemaitre, I Sagnes, R Grousson, A V Kavokin, P Senellart, G Malpuech, and J Bloch. Spontaneous formation and optical manipulation of extended polariton condensates. *Nature Phys.*, 6(11):860–864, 2010. (Cited on pages 2, 46, 59, 89, and 135.)

[24] E Wertz, A Amo, D D Solnyshkov, L Ferrier, T C H Liew, D Sanvitto, P Senellart, I Sagnes, A Lemaître, A V Kavokin, G Malpuech, and J Bloch. Propagation and Amplification Dynamics of 1D Polariton Condensates. *Phys. Rev. Lett.*, 109(21):216404, 2012. (Cited on pages 2 and 59.)

[25] D Tanese, H Flayac, D Solnyshkov, A Amo, A Lemaître, E Galopin, R Braive, P Senellart, I Sagnes, G Malpuech, and J Bloch. Polariton condensation in solitonic gap states in a one-dimensional periodic potential. *Nat. Commun.*, 4:1749, 2013. (Cited on pages 2 and 59.)

[26] D. Tanese, E. Gurevich, F. Baboux, T. Jacqmin, A. Lemaître, E. Galopin, I. Sagnes, A. Amo, J. Bloch, and E. Akkermans. Fractal Energy Spectrum of a Polariton Gas in a Fibonacci Quasiperiodic Potential. *Physical Review Letters*, 112(14):146404, apr 2014. (Cited on pages 2 and 135.)

[27] P. St-Jean, V. Goblot, E. Galopin, A. Lemaître, T. Ozawa, L. Le Gratiet, I. Sagnes, J. Bloch, and A. Amo. Lasing in topological edge states of a one-dimensional lattice. *Nature Photonics*, 11(10):651–656, sep 2017. (Cited on pages 2, 50, and 51.)

[28] Thibaut Jacqmin, Iacopo Carusotto, Isabelle Sagnes, Marco Abbarchi, Dmitry D. Solnyshkov, Guillaume Malpuech, Elisabeth Galopin, Aristide Lemaître, Jacqueline Bloch, and Alberto Amo. Direct Observation of Dirac Cones and a Flatband in a Honeycomb Lattice for Polaritons. *Phys. Rev. Lett.*, 112(11):116402, 2014. (Cited on pages 2, 52, 57, 58, 91, 95, and 96.)

[29] K S Novoselov, A Mishchenko, A Carvalho, and A H Castro Neto. 2D materials and van der Waals heterostructures. *Science*, 353(6298), jul 2016. (Cited on pages 2, 92, and 106.)

[30] B. Andrei Bernevig, Taylor L. Hughes, and Shou-Cheng Zhang. Quantum Spin Hall Effect and Topological Phase Transition in HgTe Quantum Wells. *Science*, 314:1757, 2006. (Cited on pages 2 and 92.)

[31] S Dufferwiel, Feng Li, E Cancellieri, L Giriunas, A A P Trichet, D M Whittaker, P M Walker, F Fras, E Clarke, J M Smith, M S Skolnick, and D N Krizhanovskii. Spin Textures of Exciton-Polaritons in a Tunable Microcavity with Large TE-TM Splitting. *Physical review letters*, 115(24):246401, dec 2015. (Cited on page 2.)

[32] S. Klembt, T. H. Harder, O. A. Egorov, K. Winkler, H. Suchomel, J. Beierlein, M. Emmerling, C. Schneider, and S. Höfling. Polariton condensation in s- and p-flatbands in a two-dimensional lieb lattice. *Applied Physics Letters*, 111(23):231102, dec 2017. (Cited on pages 2 and 48.)

[33] C. E. Whittaker, E. Cancellieri, P. M. Walker, D. R. Gulevich, H. Schomerus, D. Vaitiekus, B. Royall, D. M. Whittaker, E. Clarke, I. V. Iorsh, I. A. Shelykh, M. S. Skolnick, and D. N. Krizhanovskii. Exciton polaritons in a two-dimensional lieb lattice with spin-orbit coupling. *Phys. Rev. Lett.*, 120:097401, Mar 2018. (Cited on pages 2 and 48.)

[34] H. Suchomel, S. Klembt, T. H. Harder, M. Klaas, O. A. Egorov, K. Winkler, M. Emmerling, S. Hoefling, and C. Schneider. An electrically pumped polaritonic lattice simulator, 2018. (Cited on page 2.)

[35] Jerome Cayssol. Introduction to dirac materials and topological insulators. *Comptes Rendus Physique*, 14(9):760 – 778, 2013. Topological insulators / Isolants topologiques. (Cited on page 5.)

[36] Eli Rotenberg. The dirt on topology. *Nature Physics*, 7:8 EP –, Dec 2010. (Cited on page 5.)

[37] Ananda Roy and David P. DiVincenzo. Topological quantum computing, 2017. (Cited on page 5.)

[38] P.A.M Dirac. The quantum theory of the electron. *Proceedings of the Royal Society of London A: Mathematical, Physical and Engineering Sciences*, 117(778):610–624, 1928. (Cited on page 5.)

[39] James D. Bjorken and Sidney D. Drell. *Relativistic Quantum Fields*. McGraw-Hill College, 1965. (Cited on pages 5 and 7.)

[40] P.A.M Dirac. (Cited on page 7.)

[41] Palash B. Pal. Dirac, majorana and weyl fermions. 2010. (Cited on page 9.)

[42] Neil W Ashcroft and N David Mermin. *Solid State Physics*. Harcourt College Publishers, 1976. (Cited on pages 10, 12, and 13.)

[43] Richard D. Mattuck and Physics. *A Guide to Feynman Diagrams in the Many-Body Problem: Second Edition (Dover Books on Physics)*. Dover Publications, 1992. (Cited on page 10.)

[44] K. S. Novoselov, A. K. Geim, S. V. Morozov, D. Jiang, Y. Zhang, S. V. Dubonos, I. V. Grigorieva, and A. A. Firsov. Electric field effect in atomically thin carbon films. *Science*, 306(5696):666–669, 2004. (Cited on page 11.)

[45] A. Fasolino, J. H. Los, and M. I. Katsnelson. Intrinsic ripples in graphene. *Nature Materials*, 6:858 EP –, Sep 2007. (Cited on page 11.)

[46] K. S. Novoselov, A. K. Geim, S. V. Morozov, D. Jiang, M. I. Katsnelson, I. V. Grigorieva, S. V. Dubonos, and A. A. Firsov. Two-dimensional gas of massless dirac fermions in graphene. *Nature*, 438:197 EP –, Nov 2005. (Cited on page 11.)

[47] A H Castro Neto, F Guinea, N M R Peres, K S Novoselov, and A K Geim. The electronic properties of graphene. *Rev. Mod. Phys.*, 81(1):109–162, 2009. (Cited on pages 11, 12, 13, 57, and 84.)

[48] Franz Schwabl. *Advanced Quantum Mechanics*. Springer, 2008. (Cited on page 12.)

[49] A K Geim and K S Novoselov. The rise of graphene. *Nature materials*, 6(3):183–191, 2007. (Cited on page 14.)

[50] M I Katsnelson, K S Novoselov, and A K Geim. Chiral tunnelling and the Klein paradox in graphene. *Nature Phys.*, 2(9):620–625, 2006. (Cited on page 14.)

[51] N. Stander, B. Huard, and D. Goldhaber-Gordon. Evidence for klein tunneling in graphene $p-n$ junctions. *Phys. Rev. Lett.*, 102:026807, Jan 2009. (Cited on page 14.)

[52] Yuanbo Zhang, Yan-Wen Tan, Horst L Stormer, and Philip Kim. Experimental observation of the quantum Hall effect and Berry's phase in graphene. *Nature*, 438(7065):201–4, nov 2005. (Cited on page 14.)

[53] M. O. Goerbig. The quantum hall effect in graphene - a theoretical perspective. 2011. (Cited on page 14.)

[54] Jong-Hyun Ahn and Byung Hee Hong. Graphene for displays that bend. *Nature Nanotechnology*, 9(10):737–738, oct 2014. (Cited on page 14.)

[55] Things you could do with graphene. *Nature Nanotechnology*, 9(10):737–737, oct 2014. (Cited on page 14.)

[56] Amaia Zurutuza and Claudio Marinelli. Challenges and opportunities in graphene commercialization. *Nature Nanotechnology*, 9(10):730–734, oct 2014. (Cited on page 14.)

[57] Graphene opens up to new applications. *Nature Nanotechnology*, 10(5):381–381, may 2015. (Cited on page 14.)

[58] Jinying Wang, Shibin Deng, Zhongfan Liu, and Zhirong Liu. The rare two-dimensional materials with dirac cones. *National Science Review*, 2(1):22–39, 2015. (Cited on pages 15 and 106.)

[59] Jing-Min Hou and Wei Chen. Hidden symmetry and protection of dirac points on the honeycomb lattice. *Scientific Reports*, 5:17571 EP –, Dec 2015. Article. (Cited on page 15.)

[60] Guido van Miert and Cristiane Morais Smith. Dirac cones beyond the honeycomb lattice: A symmetry-based approach. *Phys. Rev. B*, 93:035401, Jan 2016. (Cited on page 15.)

[61] Bertrand Duplantier, Vincent Rivasseau, and Jean-Nöel Fuchs. *Dirac Matter (Progress in Mathematical Physics)*. Birkhäuser, 2017. (Cited on pages 15, 18, and 114.)

[62] Y Hatsugai. Topological aspect of graphene physics. *Journal of Physics: Conference Series*, 334(1):012004, 2011. (Cited on pages 16 and 18.)

[63] H.B. Nielsen and Masao Ninomiya. The adler-bell-jackiw anomaly and weyl fermions in a crystal. *Physics Letters B*, 130(6):389–396, nov 1983. (Cited on page 16.)

[64] Edward Witten. Three lectures on topological phases of matter. 2015. (Cited on page 16.)

[65] Andreas P. Schnyder, Shinsei Ryu, Akira Furusaki, and Andreas W. W. Ludwig. Classification of topological insulators and superconductors in three spatial dimensions. *Phys. Rev.B*, 78(19):195125, nov 2008. (Cited on pages 16 and 100.)

[66] Tristan Needham. *Visual Complex Analysis*. Clarendon Press, 1999. (Cited on page 16.)

[67] Davide Castelvecchi. The strange topology that is reshaping physics. *Nature*, 547(7663):272–274, jul 2017. (Cited on pages 16 and 17.)

[68] Manuel Asorey. Space, matter and topology. *Nature Physics*, 12(7):616–618, jul 2016. (Cited on page 16.)

[69] D. J. Thouless, M. Kohmoto, M. P. Nightingale, and M. den Nijs. Quantized hall conductance in a two-dimensional periodic potential. *Phys. Rev. Lett.*, 49:405–408, Aug 1982. (Cited on page 17.)

[70] J M Kosterlitz and D J Thouless. Ordering, metastability and phase transitions in two-dimensional systems. *Journal of Physics C: Solid State Physics*, 6(7):1181, 1973. (Cited on page 17.)

[71] Carlo Beenakker and Leo Kouwenhoven. A road to reality with topological superconductors. *Nature Physics*, 12(7):618–621, jul 2016. (Cited on page 17.)

[72] Albert Fert, Nicolas Reyren, and Vincent Cros. Magnetic skyrmions: advances in physics and potential applications. *Nature Reviews Materials*, 2(7):17031, jun 2017. (Cited on page 17.)

[73] Pályi A Asboth J. K., Oroszlány L. *A Short Course on Topological Insulators*. Springer, 2016. (Cited on pages 18, 72, 73, and 74.)

[74] Yasuhiro Hatsugai. Chern number and edge states in the integer quantum hall effect. *Phys. Rev. Lett.*, 71:3697–3700, Nov 1993. (Cited on page 18.)

[75] Su-Yangand Hasan M. Zahid Jia, Shuangand Xu. Weyl semimetals, fermi arcs and chiral anomalies. *Nature Materials*, 15:1140 EP –, Oct 2016. (Cited on pages 18 and 108.)

[76] A. A. Burkov. Topological semimetals. *Nature Materials*, 15:1145 EP –, Oct 2016. (Cited on pages 18 and 108.)

[77] Jimin Kim, Seung Su Baik, Sung Won Jung, Yeongsup Sohn, Sae Hee Ryu, Hyoung Joon Choi, Bohm-Jung Yang, and Keun Su Kim. Two-dimensional dirac fermions protected by space-time inversion symmetry in black phosphorus. *Phys. Rev. Lett.*, 119:226801, Nov 2017. (Cited on pages 18 and 106.)

[78] Cheol-Hwan Park and Nicola Marzari. Berry phase and pseudospin winding number in bilayer graphene. *Phys. Rev. B*, 84:205440, Nov 2011. (Cited on pages 18, 19, 20, and 21.)

[79] P. Delplace, D. Ullmo, and G. Montambaux. Zak phase and the existence of edge states in graphene. *Phys. Rev. B*, 84(19):195452, nov 2011. (Cited on pages 20, 78, 79, 100, and 102.)

[80] F. Guinea, M. I. Katsnelson, and A. K. Geim. Energy gaps and a zero-field quantum hall effect in graphene by strain engineering. *Nature Physics*, 6(1):30–33, sep 2009. (Cited on page 20.)

[81] Edward McCann and Mikito Koshino. The electronic properties of bilayer graphene. *Reports on Progress in Physics*, 76(5):056503, 2013. (Cited on page 21.)

[82] Edward McCann and Vladimir I. Fal'ko. Landau-level degeneracy and quantum hall effect in a graphite bilayer. *Phys. Rev. Lett.*, 96:086805, Mar 2006. (Cited on pages 21 and 146.)

[83] K. S. Novoselov, E. McCann, S. V. Morozov, V. I. Falko, M. I. Katsnelson, U. Zeitler, D. Jiang, F. Schedin, and A. K. Geim. Unconventional quantum hall effect and berry's phase of 2pi in bilayer graphene. *Nature Physics*, 2(3):177–180, feb 2006. (Cited on page 21.)

[84] J. Ignacio Cirac and Peter Zoller. Goals and opportunities in quantum simulation. *Nature Physics*, 8(4):264–266. (Cited on page 23.)

[85] I. M. Georgescu, S. Ashhab, and Franco Nori. Quantum simulation. *Rev. Mod. Phys.*, 86:153–185, 2014. (Cited on page 23.)

[86] Alán Aspuru-Guzik and Philip Walther. Photonic quantum simulators. *Nature Physics*, 8(4):285–291, 2012. (Cited on page 24.)

[87] M. Bayer, T. Gutbrod, A. Forchel, T. L. Reinecke, P. A. Knipp, R. Werner, and J. P. Reithmaier. Optical Demonstration of a Crystal Band Structure Formation. *Physical Review Letters*, 83(25):5374–5377, dec 1999. (Cited on pages 24 and 47.)

[88] Yonatan Plotnik, Mikael C Rechtsman, Daohong Song, Matthias Heinrich, Julia M Zeuner, Stefan Nolte, Yaakov Lumer, Natalia Malkova, Jingjun Xu, Alexander Szameit, Zhigang Chen, and Mordechai Segev. Observation of unconventional edge states in 'photonic graphene'. *Nat. Mater.*, 13(1):57–62, jan 2014. (Cited on pages 25, 80, 81, and 86.)

[89] Mikael C. Rechtsman, Yonatan Plotnik, Julia M. Zeuner, Daohong Song, Zhigang Chen, Alexander Szameit, and Mordechai Segev. Topological Creation and Destruction of Edge States in Photonic Graphene. *Physical Review Letters*, 111(10):103901, sep 2013. (Cited on page 25.)

[90] Mikael C Rechtsman, Julia M Zeuner, Andreas Tunnermann, Stefan Nolte, Mordechai Segev, and Alexander Szameit. Strain-induced pseudomagnetic field and photonic Landau levels in dielectric structures. *Nature Phot.*, 7(2):153–158, 2013. (Cited on pages 25 and 112.)

[91] Daohong Song, Vassilis Paltoglou, Sheng Liu, Yi Zhu, Daniel Gallardo, Liqin Tang, Jingjun Xu, Mark Ablowitz, Nikolaos K Efremidis, and Zhigang Chen. Unveiling pseudospin and angular momentum in photonic graphene. *Nat. Commun.*, 6:6272, jan 2015. (Cited on page 26.)

[92] Matthieu Bellec, Ulrich Kuhl, Gilles Montambaux, and Fabrice Mortessagne. Tight-binding couplings in microwave artificial graphene. *Phys. Rev. B*, 88(11):115437, 2013. (Cited on page 26.)

[93] Matthieu Bellec, Ulrich Kuhl, Gilles Montambaux, and Fabrice Mortessagne. Topological Transition of Dirac Points in a Microwave Experiment. *Physical Review Letters*, 110(3):033902, jan 2013. (Cited on pages 26, 115, and 116.)

[94] Matthieu Bellec, Ulrich Kuhl, Gilles Montambaux, and Fabrice Mortessagne. Manipulation of edge states in microwave artificial graphene. *New J. Phys.*, 16(11):113023, nov 2014. (Cited on pages 26, 80, 81, 86, 102, and 140.)

[95] Leticia Tarruell, Daniel Greif, Thomas Uehlinger, Gregor Jotzu, and Tilman Esslinger. Creating, moving and merging Dirac points with a Fermi gas in a tunable honeycomb lattice. *Nature*, 483(7389):302–305, 2012. (Cited on page 26.)

[96] A. Singha, M. Gibertini, B. Karmakar, S. Yuan, M. Polini, G. Vignale, M. I. Katsnelson, A. Pinczuk, L. N. Pfeiffer, K. W. West, and V. Pellegrini. Two-dimensional mott-hubbard electrons in an artificial honeycomb lattice. *Science*, 332(6034):1176–1179, 2011. (Cited on page 26.)

[97] Kenjiro K. Gomes, Warren Mar, Wonhee Ko, Francisco Guinea, and Hari C. Manoharan. Designer dirac fermions and topological phases in molecular graphene. *Nature*, 483(7389):306–310, mar 2012. (Cited on page 26.)

[98] Joshua E S Socolar, Tom C Lubensky, and Charles L Kane. Mechanical graphene. *New Journal of Physics*, 19(2):025003, 2017. (Cited on page 26.)

[99] Marco Polini, Francisco Guinea, Maciej Lewenstein, Hari C Manoharan, and Vittorio Pellegrini. Artificial honeycomb lattices for electrons, atoms and photons. *Nature nanotechnology*, 8(9):625–33, sep 2013. (Cited on page 26.)

[100] Christian Gross and Immanuel Bloch. Quantum simulations with ultracold atoms in optical lattices. *Science*, 357(6355):995–1001, 2017. (Cited on page 26.)

[101] D. Jaksch, C. Bruder, J. I. Cirac, C. W. Gardiner, and P. Zoller. Cold bosonic atoms in optical lattices. *Phys. Rev. Lett.*, 81:3108–3111, Oct 1998. (Cited on page 26.)

[102] P. Soltan-Panahi, J. Struck, P. Hauke, A. Bick, W. Plenkers, G. Meineke, C. Becker, P. Windpassinger, M. Lewenstein, and K. Sengstock. Multi-component quantum gases in spin-dependent hexagonal lattices. *Nature Physics*, 7:434 EP –, Feb 2011. Article. (Cited on page 26.)

[103] L. Duca, T. Li, M. Reitter, I. Bloch, M. Schleier-Smith, and U. Schneider. An aharonov-bohm interferometer for determining bloch band topology. *Science*, 347(6219):288–292, 2015. (Cited on page 27.)

[104] Gregor Jotzu, Michael Messer, Rémi Desbuquois, Martin Lebrat, Thomas Uehlinger, Daniel Greif, and Tilman Esslinger. Experimental realization of the topological haldane model with ultracold fermions. *Nature*, 515:237 EP –, Nov 2014. (Cited on page 27.)

[105] R.W. Boyd. *Nonlinear Optics 3e.* Elsevier India, 2013. (Cited on page 28.)

[106] Claude Cohen-Tannoudji, Bernard Diu, and Frank Laloï¿œ. *Quantum Mechanics, vols. II.* Hermann, Paris, France, 1977. (Cited on page 28.)

[107] Rainer G. Ulbrich and Claude Weisbuch. Resonant brillouin scattering of excitonic polaritons in gallium arsenide. *Phys. Rev. Lett.*, 38:865–868, Apr 1977. (Cited on page 28.)

[108] C. Weisbuch and Ulbrich R.G. *Light Scattering in Solids III: Recent Results (Topics in Applied Physics).* Springer, 1982. (Cited on page 28.)

[109] C. Weisbuch, M. Nishioka, A. Ishikawa, and Y. Arakawa. Observation of the coupled exciton-photon mode splitting in a semiconductor quantum microcavity. *Phys. Rev. Lett.*, 69:3314–3317, Dec 1992. (Cited on page 28.)

[110] Hyang-Tag Lim, Emre Togan, Martin Kroner, Javier Miguel-Sanchez, and Atac Imamoğlu. Electrically tunable artificial gauge potential for polaritons. *Nature Communications*, 8:14540, feb 2017. (Cited on page 29.)

[111] Vera Giulia Sala. *PhD Thesis: Coherence, dynamics and polarization properties of polariton condensates in single and coupled micropillars.* 2013. (Cited on pages 33, 36, 38, and 41.)

[112] R. Houdré, J. L. Gibernon, P. Pellandini, R. P. Stanley, U. Oesterle, C. Weisbuch, J. O'Gorman, B. Roycroft, and M. Ilegems. Saturation of the strong-coupling regime in a semiconductor microcavity: Free-carrier bleaching of cavity polaritons. *Phys. Rev. B*, 52(11):7810–7813, sep 1995. (Cited on page 35.)

[113] R Butté, G Delalleau, A I Tartakovskii, M S Skolnick, V N Astratov, J J Baumberg, G Malpuech, A Di Carlo, A V Kavokin, and J S Roberts. Transition from strong to weak coupling and the onset of lasing in semiconductor microcavities. *Phys. Rev. B*, 65(20):205310, 2002. (Cited on page 35.)

[114] Jacques Dupont-Roc and Claude Grynberg, Gilbert ad Cohen-Tannoudji. *Processus d'interactions entre photons et atomes.* n/a, 1996. (Cited on page 37.)

[115] Y. Yamamoto, F. Tassone, and H. Cao. *Semiconductor Cavity Quantum Electrodynamics (Springer Tracts in Modern Physics).* Springer, 2010. (Cited on page 37.)

[116] P. Goy, J. M. Raimond, M. Gross, and S. Haroche. Observation of cavity-enhanced single-atom spontaneous emission. *Phys. Rev. Lett.*, 50:1903–1906, Jun 1983. (Cited on page 37.)

[117] J.M Gérard and B Gayral. InAs quantum dots: artificial atoms for solid-state cavity-quantum electrodynamics. *Physica E: Low-dimensional Systems and Nanostructures*, 9(1):131–139, jan 2001. (Cited on page 37.)

[118] J J Hopfield. Theory of the Contribution of Excitons to the Complex Dielectric Constant of Crystals. *Phys. Rev.*, 112(5):1555–1567, 1958. (Cited on page 37.)

[119] E. T. Jaynes and F. W. Cummings. Comparison of quantum and semiclassical radiation theories with application to the beam maser. *Proceedings of the IEEE*, 51(1):89–109, Jan 1963. (Cited on page 37.)

[120] Vincenzo Savona, Carlo Piermarocchi, Antonio Quattropani, Paolo Schwendimann, and Francesco Tassone. Optical properties of microcavity polaritons. *Phase Transitions*, 68(1):169–279, 1999. (Cited on page 39.)

[121] A Amo, J Lefrère, S Pigeon, C Adrados, C Ciuti, I Carusotto, R Houdré, E Giacobino, and A Bramati. Superfluidity of Polaritons in Semiconductor Microcavities. *Nature Phys.*, 5:805–810, 2009. (Cited on page 42.)

[122] C Schneider, K Winkler, M D Fraser, M Kamp, Y Yamamoto, E A Ostrovskaya, and S Höfling. Exciton-polariton trapping and potential landscape engineering. *Reports on Progress in Physics*, 80(1):016503, 2017. (Cited on page 46.)

[123] H. Ohadi, Y. del Valle-Inclan Redondo, A. J. Ramsay, Z. Hatzopoulos, T. C. H. Liew, P. R. Eastham, P. G. Savvidis, and J. J. Baumberg. Synchronization crossover of polariton condensates in weakly disordered lattices, 2018. (Cited on page 47.)

[124] E A Cerda-Méndez, D N Krizhanovskii, M S Skolnick, and P V Santos. Quantum fluids of light in acoustic lattices. *Journal of Physics D: Applied Physics*, 51(3):033001, 2018. (Cited on pages 46 and 47.)

[125] C W Lai, N Y Kim, S Utsunomiya, G Roumpos, H Deng, M D Fraser, T Byrnes, P Recher, N Kumada, T Fujisawa, and Y Yamamoto. Coherent zero-state and p-state in an exciton-polariton condensate array. *Nature*, 450:529, 2007. (Cited on page 47.)

[126] Naoyuki Masumoto, Na Young Kim, Tim Byrnes, Kenichiro Kusudo, Andreas Lï¿œffler, Sven Hï¿œfling, Alfred Forchel, and Yoshihisa Yamamoto. Exciton-polariton condensates with flat bands in a two-dimensional kagome lattice. *New J. Phys.*, 14(6):65002, 2012. (Cited on page 47.)

[127] E A Cerda-Méndez, D N Krizhanovskii, M Wouters, R Bradley, K Biermann, K Guda, R Hey, P V Santos, D Sarkar, and M S Skolnick. Polariton Condensation in Dynamic Acoustic Lattices. *Phys. Rev. Lett.*, 105:116402, 2010. (Cited on page 46.)

[128] Edgar A Cerda-Méndez, Dmitry N Krizhanovskii, Klaus Biermann, Rudolf Hey, Maurice S Skolnick, and Paulo V Santos. Dynamic exciton-polariton macroscopic coherent phases in a tunable dot lattice. *Phys. Rev. B*, 86(10):100301, 2012. (Cited on page 46.)

[129] A. Amo, S. Pigeon, C. Adrados, R. Houdré, E. Giacobino, C. Ciuti, and A. Bramati. Light engineering of the polariton landscape in semiconductor microcavities. *Physical Review B - Condensed Matter and Materials Physics*, 82(8), 2010. (Cited on page 46.)

[130] G Tosi, G Christmann, N G Berloff, P Tsotsis, T Gao, Z Hatzopoulos, P G Savvidis, and J J Baumberg. Sculpting oscillators with light within a nonlinear quantum fluid. *Nature Phys.*, 8:190ï¿œ194, 2012. (Cited on pages 46 and 59.)

[131] Natalia G. Berloff, Matteo Silva, Kirill Kalinin, Alexis Askitopoulos, Julian D. Töpfer, Pasquale Cilibrizzi, Wolfgang Langbein, and Pavlos G. Lagoudakis. Realizing the classical XY hamiltonian in polariton simulators. *Nature Materials*, 16(11):1120–1126, sep 2017. (Cited on page 47.)

[132] Na Young Kim, Kenichiro Kusudo, Congjun Wu, Naoyuki Masumoto, Andreas Loffler, Sven Hofling, Norio Kumada, Lukas Worschech, Alfred Forchel, and Yoshihisa Yamamoto. Dynamical d-wave condensation of exciton-polaritons in a two-dimensional square-lattice potential. *Nature Phys.*, 7(9):681–686, 2011. (Cited on page 47.)

[133] N Y Kim, K Kusudo, A Löffler, S Höfling, A Forchel, and Y Yamamoto. Exciton-polariton condensates near the Dirac point in a triangular lattice. *New J. Phys.*, 15(3):35032, 2013. (Cited on page 47.)

[134] R Idrissi Kaitouni, O El Daïf, A Baas, M Richard, T Paraïso, P Lugan, T Guillet, F Morier-Genoud, J D Ganiï¿œœre, J L Staehli, V Savona, and B Deveaud. Engineering the spatial confinement of exciton polaritons in semiconductors. *Phys. Rev. B*, 74(15):155311, 2006. (Cited on pages 47 and 48.)

[135] O El Daïf, A Baas, T Guillet, J.-P. Brantut, R Idrissi Kaitouni, J L Staehli, F Morier-Genoud, and B Deveaud. Polariton quantum boxes in semiconductor microcavities. *Appl. Phys. Lett.*, 88(6):61105, 2006. (Cited on page 47.)

[136] R Cerna, D Sarchi, T K Paraïso, G Nardin, Y Léger, M Richard, B Pietka, O El Daif, F Morier-Genoud, V Savona, M T Portella-Oberli, and B Deveaud-Plédran. Coherent optical control of the wave function of zero-dimensional exciton polaritons. *Phys. Rev. B*, 80(12):121309, 2009. (Cited on page 47.)

[137] Karol Winkler, Julian Fischer, Anne Schade, Matthias Amthor, Robert Dall, Jonas Geßler, Monika Emmerling, Elena A Ostrovskaya, Martin Kamp, Christian Schneider, and Sven Höfling. A polariton condensate in a photonic crystal potential landscape. *New Journal of Physics*, 17(2):023001, jan 2015. (Cited on pages 47 and 48.)

[138] Gregor Dasbach, Manfred Bayer, Matthias Schwab, and Alfred Forchel. Spatial photon trapping: tailoring the optical properties of semiconductor microcavities. *Semicond. Sci. Technol.*, 18(10):S339–S350, 2003. (Cited on page 47.)

[139] Marta Galbiati, Lydie Ferrier, Dmitry D Solnyshkov, Dimitrii Tanese, Esther Wertz, Alberto Amo, Marco Abbarchi, Pascale Senellart, Isabelle Sagnes, Aristide Lemaitre,

Elisabeth Galopin, Guillaume Malpuech, and Jacqueline Bloch. Polariton Condensation in Photonic Molecules. *Phys. Rev. Lett.*, 108(12):126403, 2012. (Cited on page 51.)

[140] V. G. Sala, D. D. Solnyshkov, I. Carusotto, T. Jacqmin, A. Lemaître, H. Terças, A. Nalitov, M. Abbarchi, E. Galopin, I. Sagnes, J. Bloch, G. Malpuech, and A. Amo. Spin-Orbit Coupling for Photons and Polaritons in Microstructures. *Physical Review X*, 5(1):011034, mar 2015. (Cited on pages 50, 51, and 88.)

[141] F. Baboux, L. Ge, T. Jacqmin, M. Biondi, E. Galopin, A. Lemaître, L. Le Gratiet, I. Sagnes, S. Schmidt, H. E. Türeci, A. Amo, and J. Bloch. Bosonic Condensation and Disorder-Induced Localization in a Flat Band. *Physical Review Letters*, 116(6):066402, feb 2016. (Cited on pages 50 and 51.)

[142] Eric L Shirley, L J Terminello, A Santoni, and F J Himpsel. Brillouin-zone-selection effects in graphite photoelectron angular distributions. *Phys. Rev. B*, 51(19):13614–13622, 1995. (Cited on page 57.)

[143] Aaron Bostwick, Taisuke Ohta, Thomas Seyller, Karsten Horn, and Eli Rotenberg. Quasiparticle dynamics in graphene. *Nat. Phys.*, 3, 2007. (Cited on page 57.)

[144] T Freixanet, B Sermage, A Tiberj, and R Planel. In-plane propagation of excitonic cavity polaritons. *Phys. Rev. B*, 61(11):7233–7236, 2000. (Cited on page 59.)

[145] W Langbein, I Shelykh, D Solnyshkov, G Malpuech, Yu. Rubo, and A Kavokin. Polarization beats in ballistic propagation of exciton-polaritons in microcavities. *Phys. Rev. B*, 75(7):75323, 2007. (Cited on page 59.)

[146] V. Goblot, H. S. Nguyen, I. Carusotto, E. Galopin, A. Lemaître, I. Sagnes, A. Amo, and J. Bloch. Phase-controlled bistability of a dark soliton train in a polariton fluid. *Phys. Rev. Lett.*, 117:217401, Nov 2016. (Cited on page 59.)

[147] Tomoki Ozawa. *et al., in preparation.* (Cited on pages 59 and 103.)

[148] Dimitrii Tanese. *PhD Thesis: Non-linear dynamics of one-dimensional polariton gasses in semiconductor microcavities.* 2013. (Cited on pages 62 and 63.)

[149] William Shockley. On the Surface States Associated with a Periodic Potential. *Physical Review*, 56(4):317–323, aug 1939. (Cited on pages 67, 68, 69, and 70.)

[150] J.L. Lado, N. García-Martínez, and J. Fernández-Rossier. Edge states in graphene-like systems. *Synth. Met.*, 210, Part A:56 – 67, 2015. (Cited on page 67.)

[151] Yousuke Kobayashi, Ken-ichi Fukui, Toshiaki Enoki, Koichi Kusakabe, and Yutaka Kaburagi. Observation of zigzag and armchair edges of graphite using scanning tunneling microscopy and spectroscopy. *Phys. Rev. B*, 71(19):193406, may 2005. (Cited on pages 67 and 68.)

[152] Chenggang Tao, Liying Jiao, Oleg V. Yazyev, Yen-Chia Chen, Juanjuan Feng, Xiaowei Zhang, Rodrigo B. Capaz, James M. Tour, Alex Zettl, Steven G. Louie, Hongjie

Dai, and Michael F. Crommie. Spatially resolving edge states of chiral graphene nanoribbons. *Nature Physics*, 7(8):616–620, may 2011. (Cited on page 67.)

[153] Ig. Tamm. Über eine mögliche Art der Elektronenbindung an Kristalloberflächen. *Zeitschrift für Physik*, 76(11-12):849–850, nov 1932. (Cited on page 68.)

[154] H Fowler. *Proc. R. Soc. London*, 56(141), 1933. (Cited on page 68.)

[155] S Rijanow. *Z. Phys.*, 89:806, 1934. (Cited on page 68.)

[156] A. W. Maue. *Z. Phys.*, 94:717, 1935. (Cited on page 68.)

[157] E. T. Goodwin. *Proc. Cambridge Philos. Soc.*, pages 205, volume = 35, year = 1939. (Cited on page 68.)

[158] J. Zak. Symmetry criterion for surface states in solids. *Phys. Rev. B*, 32(4):2218–2226, aug 1985. (Cited on page 69.)

[159] Ling Lu, John D. Joannopoulos, and Marin Soljačić. Topological photonics. *Nature Photonics*, 8(11):821–829, oct 2014. (Cited on pages 71, 72, and 134.)

[160] W. P. Su, J. R. Schrieffer, and A. J. Heeger. Solitons in polyacetylene. *Phys. Rev. Lett.*, 42:1698–1701, Jun 1979. (Cited on pages 72 and 73.)

[161] Tomoki Ozawa. Bulk-Edge correspondence of one-dimensional chiral Hamiltonians. 2016. (Cited on page 74.)

[162] Mahito Kohmoto and Yasumasa Hasegawa. Zero modes and edge states of the honeycomb lattice. *Phys. Rev. B*, 76(20):205402, nov 2007. (Cited on pages 77, 86, and 102.)

[163] Shinsei Ryu and Yasuhiro Hatsugai. Topological origin of zero-energy edge states in particle-hole symmetric systems. *Phys. Rev. Lett.*, 89(7):077002, 2002. (Cited on pages 78, 79, and 92.)

[164] Roger S. K. Mong and Vasudha Shivamoggi. Edge states and the bulk-boundary correspondence in dirac hamiltonians. *Phys. Rev. B*, 83:125109, Mar 2011. (Cited on page 79.)

[165] Giovanna Panzarini, Lucio Claudio Andreani, A Armitage, D Baxter, M S Skolnick, V N Astratov, J S Roberts, Alexey V Kavokin, Maria R Vladimirova, and M A Kaliteevski. Exciton-light coupling in single and coupled semiconductor microcavities: Polariton dispersion and polarization splitting. *Phys. Rev. B*, 59(7):5082–5089, 1999. (Cited on page 88.)

[166] Alexey Kavokin, Guillaume Malpuech, and Mikhail Glazov. Optical Spin Hall Effect. *Phys. Rev. Lett.*, 95(13):136601, 2005. (Cited on page 88.)

[167] C Leyder, M Romanelli, J Ph. Karr, E Giacobino, T C H Liew, M M Glazov, A V Kavokin, G Malpuech, and A Bramati. Observation of the optical spin Hall effect. *Nature Phys.*, 3(9):628–631, 2007. (Cited on page 88.)

[168] Maria Maragkou, Caryl E Richards, Tomas Ostatnicky, Alastair J D Grundy, Joanna Zajac, Maxime Hugues, Wolfgang Langbein, and Pavlos G Lagoudakis. Optical analogue of the spin Hall effect in a photonic cavity. *Opt. Lett.*, 36(7):1095–1097, 2011. (Cited on page 88.)

[169] S.; de Vasconcellos, A.; Calvar, A.; Dousse, J; Suffczynski, N; Dupuis, A Lemaître, I Sagnes, J Bloch, P Voisin, and P Senellart. Spatial, spectral and polarization properties of coupled micropillar cavities. *Appl. Phys. Lett.*, 99:101103, 2011. (Cited on page 88.)

[170] C Sturm, D Tanese, H S Nguyen, H Flayac, E Galopin, A Lemaître, I Sagnes, D Solnyshkov, A Amo, G Malpuech, and J Bloch. All-optical phase modulation in a cavity-polariton Mach-Zehnder interferometer. *Nat. Commun.*, 5:3278, 2014. (Cited on page 89.)

[171] Sydney G. Davison and Maria Steslicka. *Basic Theory of Surface States (Monographs on the Physics and Chemistry of Materials)*. Clarendon Press, 1996. (Cited on page 90.)

[172] M. Di Liberto, A. Hemmerich, and C. Morais Smith. Topological varma superfluid in optical lattices. *Phys. Rev. Lett.*, 117:163001, 2016. (Cited on pages 91 and 106.)

[173] Congjun Wu, Doron Bergman, Leon Balents, and S. Das Sarma. Flat Bands and Wigner Crystallization in the Honeycomb Optical Lattice. *Phys. Rev. Lett.*, 99(7):070401, aug 2007. (Cited on pages 91 and 95.)

[174] Congjun Wu and S. Das Sarma. p x , y -orbital counterpart of graphene: Cold atoms in the honeycomb optical lattice. *Phys. Rev. B*, 77(23):235107, jun 2008. (Cited on page 91.)

[175] Nicola Marzari, Arash A. Mostofi, Jonathan R. Yates, Ivo Souza, and David Vanderbilt. Maximally localized wannier functions: Theory and applications. *Rev. Mod. Phys.*, 84:1419–1475, Oct 2012. (Cited on page 92.)

[176] Masatoshi Imada, Atsushi Fujimori, and Yoshinori Tokura. Metal-insulator transitions. *Rev. Mod. Phys.*, 70:1039–1263, Oct 1998. (Cited on page 92.)

[177] Y. Tokura and N. Nagaosa. Orbital physics in transition-metal oxides. *Science*, 288(5465):462–468, 2000. (Cited on page 92.)

[178] Sheneve Z. Butler, Shawna M. Hollen, Linyou Cao, Yi Cui, Jay A. Gupta, Humberto R. Gutiérrez, Tony F. Heinz, Seung Sae Hong, Jiaxing Huang, Ariel F. Ismach, Ezekiel Johnston-Halperin, Masaru Kuno, Vladimir V. Plashnitsa, Richard D. Robinson, Rodney S. Ruoff, Sayeef Salahuddin, Jie Shan, Li Shi, Michael G. Spencer, Mauricio Terrones, Wolfgang Windl, and Joshua E. Goldberger. Progress, challenges, and opportunities in two-dimensional materials beyond graphene. *ACS Nano*, 7(4):2898–2926, 2013. (Cited on page 92.)

[179] Jarillo-Herrero Pablo Churchill, Hugh O. H. *Nat. Nano.*, 9:330–331, 2014. (Cited on page 92.)

[180] Likai Li, Yijun Yu, Guo Jun Ye, Qingqin Ge, Xuedong Ou, Hua Wu, Donglai Feng, Xian Hui Chen, and Yuanbo Zhang. Black phosphorus field-effect transistors. *Nat. Nano.*, 9:372–377, 2014. (Cited on page 92.)

[181] Xi Ling, Han Wang, Shengxi Huang, Fengnian Xia, and Mildred S. Dresselhaus. The renaissance of black phosphorus. *Proc. Natl. Acad. Sci. U.S.A.*, 112(15):4523–4530, 2015. (Cited on page 92.)

[182] M V Bollinger, J V Lauritsen, K W Jacobsen, J K Nørskov, S Helveg, and F Besenbacher. One-dimensional metallic edge states in MoS2. *Phys. Rev. Lett.*, 87(19):196803, nov 2001. (Cited on page 92.)

[183] M Trushin, E J. R. Kelleher, and T Hasan. Theory of edge-state optical absorption in two-dimensional transition metal dichalcogenide flakes. *Phys. Rev. B (to be published), preprint available at arXiv:1602.06298*, 2016. (Cited on page 92.)

[184] Chendong Zhang, Yuxuan Chen, Jing-Kai Huang, Xianxin Wu, Lain-Jong Li, Wang Yao, Jerry Tersoff, and Chih-Kang Shih. Visualizing band offsets and edge states in bilayer–monolayer transition metal dichalcogenides lateral heterojunction. *Nature Communications*, 7:10349, jan 2016. (Cited on page 92.)

[185] Shinsei Ryu and Yasuhiro Hatsugai. Zero energy edge states and their origin in particle hole symmetric systems: symmetry and topology. *Phys. C*, 388:90,91, 2003. (Cited on page 92.)

[186] E. Kalesaki, C. Delerue, C. Morais Smith, W. Beugeling, G. Allan, and D. Vanmaekelbergh. Dirac Cones, Topological Edge States, and Nontrivial Flat Bands in Two-Dimensional Semiconductors with a Honeycomb Nanogeometry. *Phys. Rev. X*, 4(1):011010, jan 2014. (Cited on page 92.)

[187] C. Segarra, J. Planelles, and S. E. Ulloa. Edge states in dichalcogenide nanoribbons and triangular quantum dots. *Phys. Rev. B*, 93:085312, Feb 2016. (Cited on page 92.)

[188] Balázs Dóra, Igor F. Herbut, and Roderich Moessner. Occurrence of nematic, topological, and berry phases when a flat and a parabolic band touch. *Phys. Rev. B*, 90:045310, Jul 2014. (Cited on page 95.)

[189] Guanyu Zhu, Jens Koch, and Ivar Martin. Nematic quantum liquid crystals of bosons in frustrated lattices. *Phys. Rev. B*, 93:144508, Apr 2016. (Cited on page 95.)

[190] G Panzarini, L C Andreani, A Armitage, D Baxter, M S Skolnick, V N Astratov, J S Roberts, A V Kavokin, M R Vladimirova, and M A Kaliteevski. Cavity-polariton dispersion and polarization splitting in single and coupled semiconductor microcavities. *Physics of the Solid State*, V41(8):1223–1238, 1999. (Cited on page 97.)

[191] C. L. Kane and T. C. Lubensky. Topological boundary modes in isostatic lattices. *Nat. Phys.*, 10(1):39–45, dec 2013. (Cited on pages 100 and 106.)

[192] M. Milićević, T. Ozawa, G. Montambaux, I. Carusotto, E. Galopin, A. Lemaître, L. Le Gratiet, I. Sagnes, J. Bloch, and A. Amo. Orbital edge states in a photonic honeycomb lattice. *Phys. Rev. Lett.*, 118:107403, Mar 2017. (Cited on page 102.)

[193] A. P. Drozdov, M. I. Eremets, I. A. Troyan, V. Ksenofontov, and S. I. Shylin. Conventional superconductivity at 203 kelvin at high pressures in the sulfur hydride system. *Nature*, 525(7567):73–76, aug 2015. (Cited on page 106.)

[194] Chun-Hong Li, Yu-Jia Long, Ling-Xiao Zhao, Lei Shan, Zhi-An Ren, Jian-Zhou Zhao, Hong-Ming Weng, Xi Dai, Zhong Fang, Cong Ren, and Gen-Fu Chen. Pressure-induced topological phase transitions and strongly anisotropic magnetoresistance in bulk black phosphorus. *Phys. Rev. B*, 95:125417, Mar 2017. (Cited on page 106.)

[195] G. E. Volovik. Topological lifshitz transitions. 2016. (Cited on page 108.)

[196] G. E. Volovik. Quantum phase transitions from topology in momentum space. In *Quantum Analogues: From Phase Transitions to Black Holes and Cosmology*, pages 31–73. Springer Berlin Heidelberg. (Cited on page 108.)

[197] Ling Lu, Zhiyu Wang, Dexin Ye, Lixin Ran, Liang Fu, John D. Joannopoulos, and Marin Soljačić. Experimental observation of weyl points. *Science*, 2015. (Cited on page 108.)

[198] Su-Yang Xu, Chang Liu, Satya K. Kushwaha, Raman Sankar, Jason W. Krizan, Ilya Belopolski, Madhab Neupane, Guang Bian, Nasser Alidoust, Tay-Rong Chang, Horng-Tay Jeng, Cheng-Yi Huang, Wei-Feng Tsai, Hsin Lin, Pavel P. Shibayev, Fang-Cheng Chou, Robert J. Cava, and M. Zahid Hasan. Observation of fermi arc surface states in a topological metal. *Science*, 347(6219):294–298, 2015. (Cited on page 108.)

[199] Hui Li, Hongtao He, Hai-Zhou Lu, Huachen Zhang, Hongchao Liu, Rong Ma, Zhiyong Fan, Shun-Qing Shen, and Jiannong Wang. Negative magnetoresistance in dirac semimetal cd3as2. *Nature Communications*, 7:10301, 2016. (Cited on page 108.)

[200] S. A. Parameswaran, T. Grover, D. A. Abanin, D. A. Pesin, and A. Vishwanath. Probing the chiral anomaly with nonlocal transport in three-dimensional topological semimetals. *Phys. Rev. X*, 4:031035, Sep 2014. (Cited on page 108.)

[201] Alexey A. Soluyanov, Dominik Gresch, Zhijun Wang, QuanSheng Wu, Matthias Troyer, Xi Dai, and B. Andrei Bernevig. Type-II weyl semimetals. *Nature*, 527(7579):495–498, nov 2015. (Cited on pages 109 and 121.)

[202] M. O. Goerbig, J.-N. Fuchs, G. Montambaux, and F. Piéchon. Tilted anisotropic dirac cones in quinoid-type graphene and $\alpha-(\text{BEDT-TTF})_2 i_3$. *Phys. Rev. B*, 78:045415, Jul 2008. (Cited on page 109.)

[203] Hiroki Isobe and Naoto Nagaosa. Coulomb interaction effect in weyl fermions with tilted energy dispersion in two dimensions. *Phys. Rev. Lett.*, 116:116803, Mar 2016. (Cited on page 109.)

[204] Hong-Yan Lu, Armindo S. Cuamba, Shih-Yang Lin, Lei Hao, Rui Wang, Hai Li, YuanYuan Zhao, and C. S. Ting. Tilted anisotropic dirac cones in partially hydrogenated graphene. *Phys. Rev. B*, 94:195423, Nov 2016. (Cited on page 109.)

[205] N. H. Nguyen and J.-C. Charlier. Klein tunneling and electron optics in dirac-weyl fermion systems with tilted energy dispersion, 2017. (Cited on pages 109, 131, and 134.)

[206] Ching-Kit Chan, Netanel H. Lindner, Gil Refael, and Patrick A. Lee. Photocurrents in weyl semimetals. *Phys. Rev. B*, 95:041104, Jan 2017. (Cited on page 109.)

[207] G. E. Volovik. Black hole and hawking radiation by type-ii weyl fermions. *JETP Letters*, 104(9):645–648, Nov 2016. (Cited on page 110.)

[208] Ke Deng, Guoliang Wan, Peng Deng, Kenan Zhang, Shijie Ding, Eryin Wang, Mingzhe Yan, Huaqing Huang, Hongyun Zhang, Zhilin Xu, Jonathan Denlinger, Alexei Fedorov, Haitao Yang, Wenhui Duan, Hong Yao, Yang Wu, Shoushan Fan, Haijun Zhang, Xi Chen, and Shuyun Zhou. Experimental observation of topological fermi arcs in type-ii weyl semimetal mote2. *Nature Physics*, 12:1105 EP –, Sep 2016. (Cited on pages 110 and 121.)

[209] Huaqing Huang, Shuyun Zhou, and Wenhui Duan. Type-ii dirac fermions in the **ptse₂** class of transition metal dichalcogenides. *Phys. Rev. B*, 94:121117, Sep 2016. (Cited on page 110.)

[210] Han-Jin Noh, Jinwon Jeong, En-Jin Cho, Kyoo Kim, B. I. Min, and Byeong-Gyu Park. Experimental realization of type-ii dirac fermions in a pdte₂ superconductor. *Phys. Rev. Lett.*, 119:016401, Jul 2017. (Cited on page 110.)

[211] Georgios G. Pyrialakos, Nicholas S. Nye, Nikolaos V. Kantartzis, and Demetrios N. Christodoulides. Emergence of type-ii dirac points in graphynelike photonic lattices. *Phys. Rev. Lett.*, 119:113901, Sep 2017. (Cited on pages 110 and 131.)

[212] Huaqing Huang, Kyung-Hwan Jin, and Feng Liu. Black hole horizon in a type-iii dirac semimetal zn₂in₂s₅, 2017. (Cited on pages 110 and 131.)

[213] G. Montambaux, F. Piéchon, J.-N. Fuchs, and M. O. Goerbig. Merging of dirac points in a two-dimensional crystal. *Phys. Rev. B*, 80:153412, Oct 2009. (Cited on pages 111, 114, and 115.)

[214] Pierre Delplace. (Cited on page 111.)

[215] J. Kim, S. S. Baik, S. H. Ryu, Y. Sohn, S. Park, B.-G. Park, J. Denlinger, Y. Yi, H. J. Choi, and K. S. Kim. Observation of tunable band gap and anisotropic dirac semimetal state in black phosphorus. *Science*, 349(6249):723–726, 2015. (Cited on page 111.)

[216] Chen Si, Zhimei Sun, and Feng Liu. Strain engineering of graphene: a review. *Nanoscale*, 8:3207–3217, 2016. (Cited on page 112.)

[217] N. Levy, S. A. Burke, K. L. Meaker, M. Panlasigui, A. Zettl, F. Guinea, A. H. Castro Neto, and M. F. Crommie. Strain-induced pseudo–magnetic fields greater than 300 tesla in graphene nanobubbles. *Science*, 329(5991):544–547, 2010. (Cited on page 112.)

[218] Yuhang Jiang, Jinhai Mao, Junxi Duan, Xinyuan Lai, Kenji Watanabe, Takashi Taniguchi, and Eva Y. Andrei. Visualizing strain-induced pseudomagnetic fields in graphene through an hBN magnifying glass. *Nano Letters*, 17(5):2839–2843, apr 2017. (Cited on page 112.)

[219] Alexander Georgi, Peter Nemes-Incze, Ramon Carrillo-Bastos, Daiara Faria, Silvia Viola Kusminskiy, Dawei Zhai, Martin Schneider, Dinesh Subramaniam, Torge Mashoff, Nils M. Freitag, Marcus Liebmann, Marco Pratzer, Ludger Wirtz, Colin R. Woods, Roman V. Gorbachev, Yang Cao, Kostya S. Novoselov, Nancy Sandler, and Markus Morgenstern. Tuning the pseudospin polarization of graphene by a pseudo-magnetic field. *Nano Letters*, 17(4):2240–2245, 2017. (Cited on page 112.)

[220] Grazia Salerno, Tomoki Ozawa, Hannah M Price, and Iacopo Carusotto. How to directly observe Landau levels in driven-dissipative strained honeycomb lattices. *2D Materials*, 2(3):034015, sep 2015. (Cited on page 112.)

[221] Grazia Salerno, Tomoki Ozawa, Hannah M. Price, and Iacopo Carusotto. Propagating edge states in strained honeycomb lattices. *Phys. Rev. B*, 95:245418, Jun 2017. (Cited on page 112.)

[222] Vitor M. Pereira, A. H. Castro Neto, and N. M. R. Peres. Tight-binding approach to uniaxial strain in graphene. *Phys. Rev. B*, 80:045401, Jul 2009. (Cited on page 112.)

[223] J. Nissinen and G. E. Volovik. Type-III and IV interacting weyl points. *JETP Letters*, 105(7):447–452, mar 2017. (Cited on page 121.)

[224] Shin-Ming Huang, Su-Yang Xu, Ilya Belopolski, Chi-Cheng Lee, Guoqing Chang, BaoKai Wang, Nasser Alidoust, Guang Bian, Madhab Neupane, Chenglong Zhang, Shuang Jia, Arun Bansil, Hsin Lin, and M. Zahid Hasan. A weyl fermion semimetal with surface fermi arcs in the transition metal monopnictide taas class. *Nature Communications*, 6:7373 EP –, Jun 2015. Article. (Cited on page 121.)

[225] Zhijun Wang, Dominik Gresch, Alexey A. Soluyanov, Weiwei Xie, S. Kushwaha, Xi Dai, Matthias Troyer, Robert J. Cava, and B. Andrei Bernevig. mote$_2$. *Phys. Rev. Lett.*, 117:056805, Jul 2016. (Cited on page 121.)

[226] R. de Gail, J.-N. Fuchs, M.O. Goerbig, F. Piéchon, and G. Montambaux. Manipulation of dirac points in graphene-like crystals. *Physica B: Condensed Matter*, 407(11):1948 – 1952, 2012. Proceedings of the International Workshop on Electronic Crystals (ECRYS-2011). (Cited on page 128.)

[227] Gilles Montambaux, Lih-King Lim, Jean-Noöl Fuchs, and Frédéric Piéchon. Winding vector: how to annihilate two dirac points with the same charge, 2018. (Cited on page 131.)

[228] A. V. Nalitov, D. D. Solnyshkov, and G. Malpuech. Polariton Z Topological Insulator. *Physical Review Letters*, 114(11):116401, mar 2015. (Cited on page 134.)

[229] Torsten Karzig, Charles-Edouard Bardyn, Netanel H. Lindner, and Gil Refael. Topological Polaritons. *Physical Review X*, 5(3):031001, jul 2015. (Cited on page 134.)

[230] Zheng Wang, Yidong Chong, J D Joannopoulos, and Marin Soljacic. Observation of unidirectional backscattering-immune topological electromagnetic states. *Nature*, 461(7265):772–775, 2009. (Cited on page 134.)

[231] Babak Bahari, Abdoulaye Ndao, Felipe Vallini, Abdelkrim El Amili, Yeshaiahu Fainman, and Boubacar Kanté. Nonreciprocal lasing in topological cavities of arbitrary geometries. *Science*, 2017. (Cited on page 134.)

[232] L. H. Haddad and Lincoln D. Carr. The nonlinear Dirac equation in Bose-Einstein condensates: II. Relativistic soliton stability analysis. *arXiv:1402.3013*, page 31, feb 2014. (Cited on page 134.)

[233] X. Chen, Z.-X. Gu, Z.-C.and Liu, and X.-G. Wen. Symmetry-protected topological orders in interacting bosonic systems. *Science*, 338(6114):1604–1606, 2012. (Cited on page 134.)

[234] M. Hafezi, M. D. Lukin, and J. M . Taylor. Non-equilibrium fractional quantum hall state of light. *New Journal of Physics*, 15(6):063001, 2013. (Cited on page 134.)

[235] Huaqing Huang, Kyung-Hwan Jin, and Feng Liu. Black hole horizon in a type-iii dirac semimetal $zn_2in_2s_5$, 2017. (Cited on page 135.)

[236] C. A. Downing, D. A. Stone, and M. E. Portnoi. Zero-energy states in graphene quantum dots and rings. *Phys. Rev. B*, 84:155437, 2011. (Cited on page 135.)

[237] O. Ovdat, Jinhai Mao, Yuhang Jiang, E. Y. Andrei, and E. Akkermans. Observing a scale anomaly and a universal quantum phase transition in graphene. *Nature Communications*, 8(1), sep 2017. (Cited on page 135.)